Dissertation

submitted to the

Combined Faculties of the Natural Sciences and Mathematics

of the Ruperto-Carola-University of Heidelberg, Germany

for the degree of

Doctor of Natural Sciences

Put forward by

Maximilian, Bopp

born in: Heidelberg

Oral examination: 13th of June 2018

Air-Flow and Stress Partitioning over Wind Waves in a Linear Wind-Wave Facility

Referees: Prof. Dr. Bernd Jähne

Prof. Dr. Kurt Roth

Abstract

In this thesis the dynamics of the air sided boundary layer above wind induced water waves was investigated by velocity measurements. Within the scope of this study a measurement technique based on particle tracking was developed, which enables to measure the flow directly above the water surface down to the viscous boundary layer with high accuracy. At the big linear wind-wave facility in Marseille, France, experiments with different wind speeds ($u_{10} = 3 - 15.5\,\mathrm{m/s}$) and different wave conditions (pure wind waves and mechanically generated waves) were performed. In addition the water elevation was measured using laser induced fluorescence, which allows the use of wave following coordinates and phase dependent averaging of the velocity fields. Turbulent, wave coherent and viscous stress contribution to the total drag were determined. The pressure induced momentum transport was indirectly estimated by measurering the total momentum flux and closing the momentum balance. For the first time measurements of the complete high resolved stress partitioning from inside the viscous boundary layer ($< 1\,\mathrm{mm}$) to approximately $25\,\mathrm{cm}$ above the mean water level were accomplished for high wind speeds and large waves. It was found that directly at the water surface the viscous shear decreases from $70\,\%$ of the total stress at $3\,\mathrm{m/s}$ to only $10\,\%$ at $15.5\,\mathrm{m/s}$. Additionally, the viscous shear at the wave crest is larger than the mean and strongly depends on the wave steepness.

Zusammenfassung

In dieser Arbeit wurde die Dynamik der luftseitigen Grenzschicht über windinduzierten Wasserwellen anhand von Geschwindigkeitsmessungen untersucht. Eine im Rahmen der Arbeit entwickelte Messtechnik, bei der kleinste Partikel mit einer Kamera verfolgt werden, ermöglichte es mit sehr hoher räumlicher Auflösung direkt über der Wasseroberfläche bis in den viskosen Bereich hinein die Strömung zu vermessen. Am großen linearen Wind-Wellenkanal in Marseille, Frankreich wurden Experimente mit verschiedenen Windgeschwindigkeiten ($u_{10} = 3 - 15.5\,\mathrm{m/s}$) und unterschiedlichen Wellen (reine windinduzierte und mechanisch erzeugte Wellen) durchgeführt. Die Wellenauslenkung wurde mit Hilfe von laserinduzierter Fluoreszenz gemessen, was die Verwendung von gekrümmten Koordinaten und eine phasenabhängige Mittelung der Geschwindigkeitsfelder ermöglichte. Dadurch konnte der turbulente, der wellenkorrelierte und der viskose Anteil der Schubspannung höhenabhängig ermittelt werden. Der druckinduzierte Anteil der Schubspannung wurde durch Messung der gesamten Schubspannung indirekt abgeschätzt. Zum ersten Mal wurden Messungen der gesamten höhenabhängigen Aufteilung des Impulstransports von der viskosen Grenzschicht ($< 1\,\mathrm{mm}$) bis zu einer Höhe von $25\,\mathrm{cm}$ über großen Wasserwellen bei solch hohen Windgeschwindigkeiten präsentiert. Es zeigt sich, dass unmittelbar an der Wasseroberfläche der viskose Anteil der Schubspannung von $70\,\%$ bei $3\,\mathrm{m/s}$ auf nur $10\,\%$ bei $15.5\,\mathrm{m/s}$ absinkt. Außerdem ist die viskose Schubspannung am Wellenberg größer als ihr Mittelwert und hängt stark von der Wellensteilheit ab.

Contents

1 Introduction

1.1 Transport processes at the air-sea interface

The ocean and the atmosphere are two major environmental compartments, which cannot be considered separately, as they are connected by the water surface. Wind controls the boundary layer between those two global systems, where exchange of momentum, heat and mass takes place. Liss (2014) gives a broad overview of this interdisciplinary field of research concerning the interaction processes between atmosphere and ocean.

Wind blowing over the sea is the main driving force for all physical processes close to the water surface. The air flow is usually faster than the water, therefore momentum is transferred from the atmosphere to the ocean and surface waves are generated. Due to viscous shear and pressure forces at the surface, energy is transferred and waves grow until their energy loss due to friction equals the input. The knowledge of all mechanisms responsible for generation, interaction and decay of waves increased in the last century starting with first descriptions (Stokes, 1849) over fundamental theories presented by Miles (1957) and Phillips (1957) and parametrizations of the wave spectrum like those of Hasselmann et al. (1976) to many numerical and experimental studies (e.g. Toba, 1972; Wanninkhof et al., 2009; Caulliez, 2013; Zakharov et al., 2015).

Additionally, the wind and the momentum transport control the efficiency of transport processes like heat and gas transfer due to the generation of turbulence, thinning of boundary layers, surface renewal events and other effects. Jähne et al. (1979) made the approach, that the transfer rate of gases and heat represented by a transfer velocity is in first order proportional to the friction velocity in water, which is a quantifies the vertical momentum transfer. During the last forty years, many studies have been performed investigating the connection of the transfer of heat and gas with wind, waves, wave breaking, turbulence, bubbles, spray, rain, surfactants, foam and many more (Jähne et al., 1987; Wanninkhof et al., 2009; Nightingale, 2009; Garbe et al., 2014). But due to this complexity and non linearity many aspects are still not fully understood.

For gas exchange as well as for wave dynamics the partitioning of the momentum transport to different pathways is essential. Pressure forces at the water surface are for example less crucial for mass transport, because viscous shear is controlling the thickness of the mass boundary layer, which is the bottle neck for mass transfer (Liss, 1973; Jähne et al., 1987). The larger the tangential stress, the thinner the boundary layer and the higher the transfer rates. For waves, air sided pressure at the water surface contributes significantly by pushing the wave crests and the viscous stress only partly contributes to momentum input into the waves (Papadimitrakis, 2005).

On the other hand waves play an important role in the kinematics and dynamics of the boundary layer and thereby influence the drag (Donelan et al., 1995; Jones and Toba, 2001; Sullivan and McWilliams, 2010). Short capillary waves induce small scale roughness of the surface, long gravity waves are responsible for air flow separation and wave coherent stresses. Together with events like wave breaking, spray production

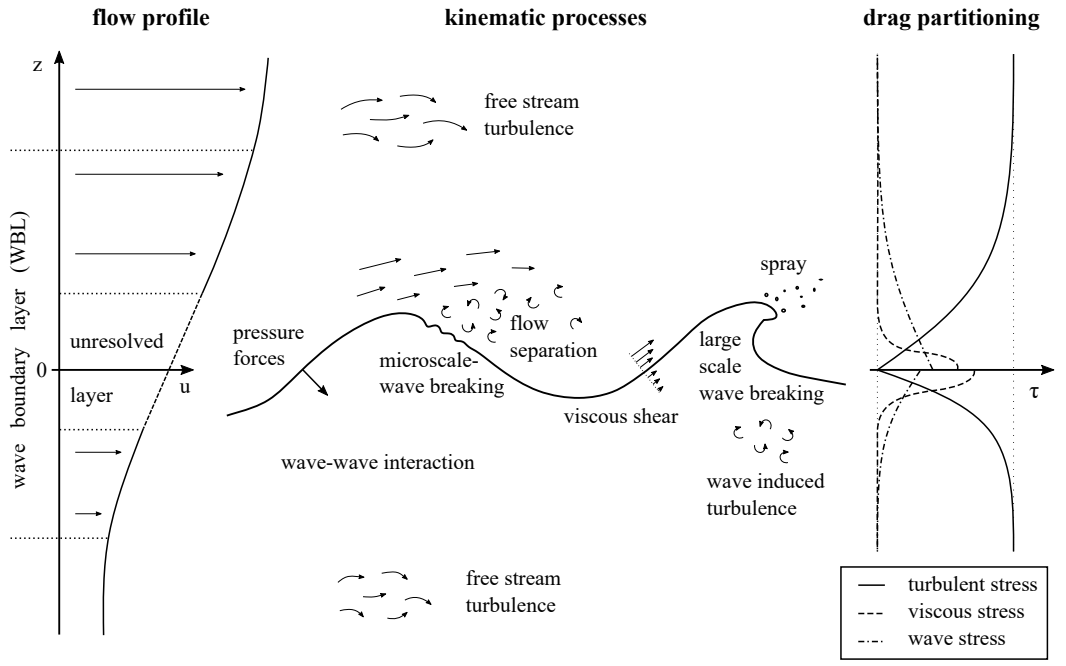

Figure 1.1: Sketch of flow profiles, kinematic processes and the drag partitioning at the wind driven water surface. Waves influence the region above and below the water surface, which is called the wave boundary layer (WBL). Here various processes take place and the drag splits into turbulent, viscous and wave stress, where the latter consists of pressure forces and wave coherent fluxes. Outside the WBL only free stream turbulence occurs carrying the full drag.

and others, the sea state influences the total amount of wind induced stress and its partitioning in water as well as in air. Besides the flow profile and some processes in figure 1.1 also this partitioning into turbulent stress, viscous stress and wave stress (form drag) is sketched, where the latter is defined as the sum of pressure forces and wave coherent fluxes. Inside the wave boundary layer (WBL) the turbulent stress reduces with decreasing distance from the interface, and dependent on the wave state the other stresses increase. Even if a large number of studies brought substantial insights, there is still a big knowledge gap relating the coupling between wind and waves.

1.2 Measuring momentum transport

Already in the first half of the 20^{th} century experiments have been performed concerning the drag above waves (a comprehensive historical overview is given by Jones and Toba, 2001). Charnock (1955) introduced the first parametrization of the surface drag, which was derived from logarithmic wind profiles measured by precise anemometers. Using the same method many studies followed, which resulted in a large number of parametrizations also considering the wave state (e.g. Kitaigarodskii and Volkov, 1965;

Stewart, 1974). The first direct measurements of Reynolds stress above the ocean were performed by Weiler and Burling (1967) using hot wires in X-configuration, whereby the eddy covariances could be measured. Acoustic measurement techniques further extended the capabilities and during the last decades optical measurement techniques like laser doppler anemometry (LDA) and particle imaging velocimetry (PIV) allowed for measurements with higher precision, even though it is very difficult to operate them at the open sea (Donelan et al., 2006; Sutherland and Melville, 2015).

In laboratory wind wave flumes measurements much closer to the water surface in the so called unresolved layer are possible and as another big advantage the conditions like wind speed and fetch can be controlled. Additionally, the momentum balance can be used to measure surface drag. While in linear tanks, where a logarithmic wind profile forms (Kawamura et al., 1981; Troitskaya et al., 2012; Zavadsky and Shemer, 2012), the input of momentum yields to a slightly tilted water level (Donelan et al., 2004). In annular facilities the water starts rotating and the surface drag can be determined by relating the water bulk velocity to the stress at the walls (Jähne et al., 1979; Ilmberger, 1981; Nielsen, 2004; Bopp, 2014) – here secondary currents influence the wind profile and the profile method fails.

While the literature contains a large number of studies focusing on the total drag and its dependencies on wave parameters (e.g. Taylor and Yelland, 2001; Drennan et al., 2003; Fairall et al., 2003; Drennan et al., 2005; Jian et al., 2011; Edson et al., 2013), direct measurements of the stress partitioning inside the WBL are rare. This is caused by technical difficulties of measurements below the highest wave crests, where the operation of fixed positioned flow and pressure sensors is not possible.

By observing streamlines of hydrogen bubbles inside laboratory waves Okuda et al. (1976) estimated the shear at the water surface, after what a series of publications followed focusing on the flow structure of short wind waves (Okuda et al., 1977; Kawamura et al., 1981; Okuda, 1982a,b, 1983, 1984; Yoshikawa et al., 1988).

Peirson (1997) investigated the water flow below wind driven water waves using PIV-techniques. He showed the significant increase of the wave form drag with wave development for wind speeds up to $u_{10} = 13\,\mathrm{m/s}$ (extrapolated wind speed to $10\,\mathrm{m}$ reference height) and short fetches $< 4.4\,\mathrm{m}$ (see Banner and Peirson, 1998). The results have been confirmed in further experiments and it could be shown, that aqueous near-surface turbulence is generated by wind shear and wave breaking (Peirson and Banner, 2003; Siddiqui and Loewen, 2010; Peirson et al., 2014).

Measurements in air are more challenging, because the velocities are much higher and the viscous boundary layer is thinner. The first 2D PIV velocity fields over mechanically generated waves have been obtained by Reul et al. (1999) and showed airflow separation past wave crests. Following experiments showed the turbulent flow structure above waves (Shaikh and Siddiqui, 2010; Troitskaya et al., 2010; Belden and Techet, 2011) and confirmed that above a certain level the drag is fully represented by turbulent stress (Troitskaya et al., 2011).

Veron et al. (2007) achieved the first direct phase resolved estimations of the viscous

stress using PIV in air, which has its maximum at the windward side of the crest and drops nearly to zero at the lee side, due to air flow separation. By repeatedly plunging a hot wire anemometer into the water Grare et al. (2013) determined the viscous and form drags for several wind wave conditions. The recent study by Buckley and Veron (2016), where combined PIV and laser induced fluorescence (LIF) methods have been used, analyzes the turbulent velocity fields above waves by meaningful phase averages and shows the influence of wave age and flow separation on wave-coherent and turbulent quantities in the airflow (see also Buckley and Veron, 2017). The use of wave following coordinates, first introduced by Benjamin (1959), makes it possible to clarify how wave coherent fluxes contribute.

Furthermore, simulations like direct numerical simulations (DNS) or large eddy simulations (LES) complemented the experimental studies at the water side (Teixeira, 2011) as well as in air (Sullivan et al., 2000; Hara and Sullivan, 2015).

1.3 Scope and structure of this thesis

This study focuses on the partitioning of momentum transfer in the air-sided WBL, which was investigated by a large number of experiments at different wind-wave conditions.

The necessary theoretical considerations are shown in chapter 2, which describes the basics of fluid dynamics, the theory of waves and air-sided kinematics in the boundary layer. The third chapter gives an overview of the used measurement techniques and their fundamentals, which were mainly represented by imaging techniques like a newly developed method of particle streak velocimetry (PSV). In chapter 4 all experiments are described, which were performed at the large linear IRPHE-Luminy wind wave tank in Marseille, France. A detailed description of the measurement setup is also given there. The next chapter 5 explains the full procedure of data processing from raw images to physical quantities, which is dominated by the newly developed PSV-technique. How waves are analyzed and wave following coordinates are determined is addressed in chapter 6. All results are presented in chapter 7. Wave properties like spectra, phase speed, wave height and steepness could be determined for all experiments (section 7.1). Time series of the measured 2D wind velocity are shown (section 7.2) and the overall friction velocity is obtained by logarithmic wind profiles (section 7.3). Phase dependent velocity fields are shown (section 7.4) and the successfully obtained partitioning of momentum transport is presented (section 7.5). Finally, the results are summarized and discussed in chapter 8.

2 Theory

This chapter collects the theoretical basics necessary for treating the air-side transport of momentum above water waves. It gives an overview of the relevant physical processes and mathematical descriptions. After starting with some substantial descriptions of fluid dynamics the theory for surface waves in water is outlined, which plays an important role for the momentum transport in air. This air sided vertical momentum transport is treated in the last part of this section, where the momentum equations and the occurring stresses are described as well in fixed as in wave following coordinates. There is no claim to completeness of this broad field of research and for more detailed information it is referred to pertinent text books like Kundu et al. (2012) for general fluid dynamics, Phillips (1977) and Massel (2013) for wave dynamics and Schlichting and Gersten (2006) for boundary layer dynamics.

For reasons of legibility Einstein's notation or Einstein's summation convention is used in most cases.

2.1 General fluid dynamics

2.1.1 Continuity equation

In an Newtonian fluid, which can be described by a velocity vector u_i and its density ρ, mass conservation has to be fulfilled. This basic conservation law is generally expressed in differential form:

$$\frac{\partial \rho}{\partial t} + \frac{\partial}{\partial x_i}\left(\rho u_i\right) = 0. \tag{2.1}$$

The temporal change of the mass in an infinitesimal fluid parcel is controlled by the loss through its boundaries, written by the spacial derivative of ρu_i. In an incompressible medium all derivatives of the density vanish and the equation reduces to:

$$\frac{\partial u_i}{\partial x_i} = 0 \tag{2.2}$$

2.1.2 Momentum equations

Derived from the conservation of momentum the acceleration of a fluid parcel can be described by the Navier-Stokes momentum equation (NSE):

$$\rho \frac{Du_j}{Dt} = \rho\left(\frac{\partial u_j}{\partial t} + \frac{\partial}{\partial x_i}\left(u_i u_j\right)\right) = -\frac{\partial p}{\partial x_j} + \rho g_j + \mu \frac{\partial^2 u_j}{\partial {x_i}^2}. \tag{2.3}$$

The change of momentum expressed by the temporal derivative and an advection term balances all forces, here represented by the pressure p, gravity with the gravitational constant g and viscous stresses controlled by the viscosity μ. This form of the NSE

requires incompressibility and all pressure forces are separated from the pure viscous momentum transport. In a Newtonian fluid this viscous term can be expressed by the viscous stress tensor:

$$\mu \frac{\partial^2 u_j}{\partial {x_i}^2} = \mu \frac{\partial}{\partial x_i} \left(\frac{\partial u_j}{\partial x_i} + \frac{\partial u_i}{\partial x_j} \right) = \frac{\partial}{\partial x_i} \tau_{\mathrm{visc},ij}, \tag{2.4}$$

with

$$\tau_{\mathrm{visc},ij} = \mu \left(\frac{\partial u_j}{\partial x_i} + \frac{\partial u_i}{\partial x_j} \right). \tag{2.5}$$

Its components $\tau_{\mathrm{visc},ij}$ can be seen as an expression for the viscous transport of i-momentum in negative j-direction.

It often is favourable to write the momentum equations in dimensionless form. Therefore scaling variables like the scaling length l_{sc}, the velocity scale u_{sc} and the rotation or oscillation frequency ω_{sc} are introduced. By normalization of all variables

$$x_i^+ = x_i / l_{\mathrm{sc}}, \quad u_i^+ = u_i / u_{\mathrm{sc}}, \quad t^+ = t\,\omega_{\mathrm{sc}}, \quad p^+ = (p - p_0)/\rho {u_{\mathrm{sc}}}^2, \quad g_i^+ = g_i / g \tag{2.6}$$

the NSE is transformed dimensionless:

$$\left[\frac{\omega_{\mathrm{sc}} l_{\mathrm{sc}}}{u_{\mathrm{sc}}} \right] \frac{\partial u_j^+}{\partial t^+} + \frac{\partial}{\partial x_i^+} \left(u_i^+ u_j^+ \right) = -\frac{\partial p^+}{\partial x_j^+} + \left[\frac{g\, l_{\mathrm{sc}}}{{u_{\mathrm{sc}}}^2} \right] g_j^+ + \left[\frac{\mu}{\rho\, u_{\mathrm{sc}} l_{\mathrm{sc}}} \right] \frac{\partial^2 u_j^+}{\partial {x_i^+}^2}. \tag{2.7}$$

All information about dimensions is carried by three dimensionless groups of parameters shown in [,]-brackets, which are controlling the differential equations and thereby the structure of the flow. These groups have the following names and interpretations:

$$\mathrm{St} = \text{Strouhal number} \equiv \frac{\text{unsteady acceleration}}{\text{advective acceleration}} \propto \frac{\omega_{\mathrm{sc}} l_{\mathrm{sc}}}{u_{\mathrm{sc}}} \tag{2.8}$$

$$\mathrm{Re} = \text{Reynolds number} \equiv \frac{\text{inertia force}}{\text{viscous force}} \propto \frac{\rho\, u_{\mathrm{sc}} l_{\mathrm{sc}}}{\mu} \tag{2.9}$$

$$\mathrm{Ri} = \text{Richards number} \equiv \frac{\text{inertia force}}{\text{gravity force}} \propto \frac{{u_{\mathrm{sc}}}^2}{g\, l_{\mathrm{sc}}} \tag{2.10}$$

The Strouhal number represents the fraction of unsteady and advective acceleration and becomes important when flow unsteadiness arises. The Reynolds number, maybe the most common dimensionless number, deals the fraction of inertia and viscous force and relates the scale of the flow to its kinematic viscosity, which is important for the flow regime – only in high Re flows turbulence occurs. The Richards number is represented by the inertia and gravity forces and gives information about the influence of gravity to the flow like in stratification flows or surface waves.

2.1.3 Bernoulli equation

In many fluid mechanical problems the Bernoulli equation helps to find an analytical solution. It can be derived from the NSE and energy considerations and for constant viscosity, irrotational, unsteady, constant density flow it is in integrated form:

$$\frac{\partial \phi}{\partial t} + \frac{1}{2}\left|\frac{\partial \phi}{\partial x_i}\right|^2 + \frac{p}{\rho} + g\, x_z = \text{constant}, \tag{2.11}$$

where the fluid velocity is expressed by the velocity potential with $u_i \equiv \partial\phi/\partial x_i$.

2.1.4 Turbulence

A flow is called turbulent, if it contains unpredictable, irregular and chaotic fluctuations, where energy is transferred by nonlinear interactions from larger to smaller spinning flow structures, called eddies. The size of these eddies ranges from the width of the turbulent region to very small scales, where the action of viscosity becomes so large, that kinetic energy is transferred to heat – it is dissipated. This big range of chaotic velocity structures makes mixing and diffusion of momentum, heat or mass much more effective than it is in an equivalent laminar flow with no turbulence.

Since the end of the 19th century turbulence is a leading topic of fluid mechanics and many studies have been performed to understand this nonlinear unpredictable process. Monin and Yaglom (2007) give a comprehensive overview of this large field and also describes its historical evolution.

One context found early by Osborne Reynolds is the connection of the appearance of turbulence to the dimensionless number $\mathrm{Re} = \rho\, u_{\mathrm{sc}} l_{\mathrm{sc}}/\mu$ (see equation 2.9), which was later named the Reynolds number. Below a threshold value Re_{c} no turbulence occurs and above the flow regime changes from laminar to turbulent. These critical Reynolds numbers depend on the boundary conditions of the flow, for example in a pipe flow it is $\mathrm{Re}_{\mathrm{c}} \approx 2.5, 10^3$ (Prandtl, 1957).

Beside fluctuations the flow contains mean properties, which can be identified by the Reynolds decomposition. All instant quantities q such as velocity, temperature, pressure, are expressed by a mean part $\overline{q}$ and its fluctuations $q^{'}$:

$$q = \overline{q} + q^{'}. \tag{2.12}$$

Assuming stationary flow, what means in case of turbulent flow no temporal changes of the mean quantities ($\partial\overline{q}/\partial t = 0$), this Reynolds decomposition can be applied to the NSE (equation 2.3). Temporal averaged this yields

$$\frac{\partial}{\partial x_i}\Bigg(\underbrace{\rho\,\overline{u}_i\overline{u}_j}_{\text{advection}}\Bigg) = \frac{\partial}{\partial x_i}\Bigg(\underbrace{-\rho\,\overline{u_i^{'}u_j^{'}}}_{\tau_{\mathrm{turb},ij}} \quad \underbrace{-p\delta_{ij}}_{\text{press. forces}} \quad + \underbrace{\mu\left(\frac{\partial \overline{u}_j}{\partial x_i} + \frac{\partial \overline{u}_i}{\partial x_j}\right)}_{\tau_{\mathrm{visc},ij}}\Bigg) \tag{2.13}$$

where all fluctuating quantities except for the correlation term $\overline{u_i' u_j'}$ cancel out. In this formulation the density of air ρ and the kinematic viscosity μ are treated as constant and the total pressure $p_{\mathrm{total}} = p + \rho_{\mathrm{a}} g z$ is expressed by the sum of the dynamic pressure p and the atmospheric pressure $\rho g z$. Thereby no gravity forces are present anymore. The correlation term describes the transport of momentum due to fluctuations and together with a negative sign and the density ρ it is called turbulent stress $\tau_{\mathrm{turb},ij}$.

In order to find a solution for the mean velocity field near a boundary the Reynolds correlations $\overline{u_i' u_j'}$ can be set in relation to the mean flow velocity $\overline{u}_i$. In analogy to the molecular-motion-based laminar momentum transport an eddy-motion-based turbulent viscosity $\mu_{\mathrm{turb,\,a}}$ can be introduced:

$$-\rho_{\mathrm{a}} \overline{u_i' u_j'} = \mu_{\mathrm{turb,\,a}} \left(\frac{\partial \overline{u}_j}{\partial x_i} + \frac{\partial \overline{u}_i}{\partial x_j} \right). \tag{2.14}$$

Approaches like the mixing lengths model (Prandtl, 1957) or the Kolmogorov-scaling (Kolmogorov, 1941) have been developed in order to close the mean-flow momentum equation.

2.1.5 Transport of heat and mass

Beside velocity, pressure and density also concentration of mass and temperature are important quantities in a flow. In laminar conditions the transport is performed by molecular diffusion, which can be described by Fick's law for mass and Fourier's law for temperature or heat:

$$\text{mass:} \qquad j_{c,i} = -D \frac{\partial c}{\partial x_i} \tag{2.15}$$

$$\text{heat:} \qquad j_{\mathrm{heat},i} = -\lambda_{\mathrm{heat}} \frac{\partial T}{\partial x_i} = -\Xi_{\mathrm{heat}} \frac{\partial c_p \rho T}{\partial x_i}. \tag{2.16}$$

The flux j_i is proportional to the gradient, where D is called the diffusion constant, λ_{heat} the thermal conductivity number and $\Xi_{\mathrm{heat}} = \lambda_{\mathrm{heat}} / c_p \rho$ the thermal diffusivity. Describing the behavior of these transport processes in flow dimensionless numbers like the Schmidt number

$$\mathrm{Sc} = \frac{\nu}{D} \tag{2.17}$$

and the Prandtl number

$$\mathrm{Pr} = \frac{\nu}{\Xi} \tag{2.18}$$

give the relation to viscous fluxes of momentum, which are in analogy – the shear stress is proportional to the gradient of velocity (compare equation 2.5). Here the kinematic viscosity $\nu = \mu / \rho$ is used, also called the momentum diffusivity.

Similar to momentum transport turbulence increases the efficiency of transport, so also for heat and mass turbulent diffusivities can be posted, which are defined by the correlation of velocity fluctuations with temperature or mass concentration fluctuations.

2.1.6 Coordinate transformations

The Cartesian coordinates, here denoted as (x, y, z, t), form the most simple coordinate system. In the context of this work x is directed in mean horizontal wind direction and y is the horizontal crosswind component. The third component z is directed vertical upward with $z = 0$ at the mean water surface.

In fluid dynamics often other coordinates systems are used, which are following surfaces for example. These are defined by a transformation mapping the Cartesian coordinates (x, y, z, t) to the new coordinates (x^*, y^*, z^*, t). By the transformation function

$$x_i^* = x_i^*(x, y, z, t) \qquad \text{or} \qquad x_i = x_i(x^*, y^*, z^*, t) \tag{2.19}$$

the new coordinates of local points or vectors can be calculated (Schlichting and Gersten, 2006, p. 77). For transforming the fluid mechanical equations the chain rule for partial derivatives has to be used. Anderson et al. (2012) give a detailed explanation of the transforming rules and how the basic equation can be expressed in the new coordinates. The partial derivatives become

$$\frac{\partial}{\partial x_i} = \frac{\partial x_k^*}{\partial x_i} \frac{\partial}{\partial x_k^*} \tag{2.20}$$

and the differential expressions can be written by the following matrix multiplication:

$$\begin{aligned} \begin{pmatrix} dx^* \\ dy^* \\ dz^* \end{pmatrix} &= \begin{pmatrix} \frac{\partial x^*}{\partial x} & \frac{\partial x^*}{\partial y} & \frac{\partial x^*}{\partial z} \\ \frac{\partial y^*}{\partial x} & \frac{\partial y^*}{\partial y} & \frac{\partial y^*}{\partial z} \\ \frac{\partial z^*}{\partial x} & \frac{\partial z^*}{\partial y} & \frac{\partial z^*}{\partial z} \end{pmatrix} \begin{pmatrix} dx \\ dy \\ dz \end{pmatrix} \\ \text{or} \quad \begin{pmatrix} dx \\ dy \\ dz \end{pmatrix} &= \begin{pmatrix} \frac{\partial x}{\partial x^*} & \frac{\partial x}{\partial y^*} & \frac{\partial x}{\partial z^*} \\ \frac{\partial y}{\partial x^*} & \frac{\partial y}{\partial y^*} & \frac{\partial y}{\partial z^*} \\ \frac{\partial z}{\partial x^*} & \frac{\partial z}{\partial y^*} & \frac{\partial z}{\partial z^*} \end{pmatrix} \begin{pmatrix} dx^* \\ dy^* \\ dz^* \end{pmatrix} \end{aligned} \tag{2.21}$$

with

$$\begin{aligned} \begin{pmatrix} \frac{\partial x^*}{\partial x} & \frac{\partial x^*}{\partial y} & \frac{\partial x^*}{\partial z} \\ \frac{\partial y^*}{\partial x} & \frac{\partial y^*}{\partial y} & \frac{\partial y^*}{\partial z} \\ \frac{\partial z^*}{\partial x} & \frac{\partial z^*}{\partial y} & \frac{\partial z^*}{\partial z} \end{pmatrix} &= \begin{pmatrix} \frac{\partial x}{\partial x^*} & \frac{\partial x}{\partial y^*} & \frac{\partial x}{\partial z^*} \\ \frac{\partial y}{\partial x^*} & \frac{\partial y}{\partial y^*} & \frac{\partial y}{\partial z^*} \\ \frac{\partial z}{\partial x^*} & \frac{\partial z}{\partial y^*} & \frac{\partial z}{\partial z^*} \end{pmatrix}^{-1} \\ &= J \begin{pmatrix} \frac{\partial y}{\partial y^*}\frac{\partial z}{\partial z^*} - \frac{\partial y}{\partial z^*}\frac{\partial z}{\partial y^*} & \frac{\partial x}{\partial z^*}\frac{\partial z}{\partial y^*} - \frac{\partial x}{\partial y^*}\frac{\partial z}{\partial x^*} & \frac{\partial x}{\partial y^*}\frac{\partial y}{\partial z^*} - \frac{\partial x}{\partial z^*}\frac{\partial y}{\partial y^*} \\ \frac{\partial y}{\partial z^*}\frac{\partial z}{\partial x^*} - \frac{\partial y}{\partial x^*}\frac{\partial z}{\partial z^*} & \frac{\partial x}{\partial x^*}\frac{\partial z}{\partial z^*} - \frac{\partial x}{\partial z^*}\frac{\partial z}{\partial x^*} & \frac{\partial x}{\partial z^*}\frac{\partial y}{\partial z^*} - \frac{\partial x}{\partial x^*}\frac{\partial y}{\partial z^*} \\ \frac{\partial y}{\partial x^*}\frac{\partial z}{\partial y^*} - \frac{\partial y}{\partial y^*}\frac{\partial z}{\partial x^*} & \frac{\partial x}{\partial y^*}\frac{\partial z}{\partial x^*} - \frac{\partial x}{\partial x^*}\frac{\partial z}{\partial y^*} & \frac{\partial x}{\partial x^*}\frac{\partial y}{\partial y^*} - \frac{\partial x}{\partial y^*}\frac{\partial y}{\partial x^*} \end{pmatrix}. \end{aligned} \tag{2.22}$$

So the partial derivatives of the transformed coordinates can be determined by differentiating the expressions of the Cartesian coordinates. The Jacobian J, defined by

$$J = \frac{\partial(x^*, y^*, z^*)}{\partial(x, y, z)} = \begin{vmatrix} \frac{\partial x^*}{\partial x} & \frac{\partial x^*}{\partial y} & \frac{\partial x^*}{\partial z} \\ \frac{\partial y^*}{\partial x} & \frac{\partial y^*}{\partial y} & \frac{\partial y^*}{\partial z} \\ \frac{\partial z^*}{\partial x} & \frac{\partial z^*}{\partial y} & \frac{\partial z^*}{\partial z} \end{vmatrix} \tag{2.23}$$

and

$$J = 1/J^{-1} = 1\Big/\frac{\partial(x, y, z)}{\partial(x^*, y^*, z^*)} = 1\Bigg/\begin{vmatrix} \frac{\partial x}{\partial x^*} & \frac{\partial x}{\partial y^*} & \frac{\partial x}{\partial z^*} \\ \frac{\partial y}{\partial x^*} & \frac{\partial y}{\partial y^*} & \frac{\partial y}{\partial z^*} \\ \frac{\partial z}{\partial x^*} & \frac{\partial z}{\partial y^*} & \frac{\partial z}{\partial z^*} \end{vmatrix}, \tag{2.24}$$

describes the metrics and can be determined if analytical expressions are available – independent of the direction.

These transformations can be applied to the basic equations for fluid dynamics, like the continuity equation or the NSE. For expressing temporal derivatives of transformed coordinates, the transformed velocity vector U_i is introduced:

$$U_i = \frac{1}{J}\left(u_k \frac{\partial x_i^*}{\partial x_k} + \frac{\partial x_i^*}{\partial t}\right). \tag{2.25}$$

By the temporal derivative also accelerated mappings are considered. The continuity equation becomes

$$\frac{\partial U_i}{\partial x_i^*} = 0 \tag{2.26}$$

and the NSE

$$\frac{1}{J}\rho\frac{\partial u_j}{\partial t} + \frac{\partial}{\partial x_i^*}\left(\rho\, U_i\, u_j + p\,\frac{1}{J}\frac{\partial x_i^*}{\partial x_j} - \tau_{\mathrm{visc},jk}\frac{1}{J}\frac{\partial x_i^*}{\partial x_k}\right) = 0. \tag{2.27}$$

These equations balance the Cartesian components of momentum regarded in the transformed coordinate system. The variables u_j, p and $\tau_{\mathrm{visc},jk}$ are the same as before, except they are now functions of the new coordinates (x^*, y^*, z^*, t) (Hara and Sullivan, 2015). Dividing by the Jacobian J hereby keeps the metrics constant. More details and explanations can be found at Anderson et al. (2012).

2.2 Surface waves

This section gives a broad overview of the theory of water waves, explains the basic equations and describes the main processes. For all following considerations homogeneity in y-direction is assumed, which only partly represents the real situation at open waters. Nevertheless the theory of 2D-waves is not much different to three dimensional waves and for more information it is referred to text books like Kinsman (1965), Phillips (1977) or Massel (2013).

2.2.1 Wave equations

The basic equation for a water wave is given by the Laplace equation:

$$\Delta\phi_u = \frac{\partial^2\phi_u}{\partial x^2} + \frac{\partial^2\phi_u}{\partial z^2} = 0 \tag{2.28}$$

It is derived by inserting the velocity potential (with $\vec{u} = \vec{\nabla}\phi_u$) in the continuity equation for incompressible fluids (equation 2.2). In order to solve this equation the boundary conditions (BC) are necessary (Kundu et al., 2012). At the bottom ($z = -h$) the normal velocity component vanishes, which defines the first BC written in form of the velocity potential:

$$\frac{\partial\phi_u}{\partial z}\Big|_{z=-h} = 0. \tag{2.29}$$

At the free surface ($z = \eta$) the total derivative of the surface elevation η at location $\vec{x}$ can be written as:

$$\frac{d\eta}{dt} = w\big|_{z=\eta} = \frac{\partial\phi_u}{\partial z}\Big|_{z=\eta} = \frac{\partial\eta}{\partial t} + \vec{u}\left(\frac{\partial\eta}{\partial x}\right) = \frac{\partial\eta}{\partial t} + \frac{\partial\phi_u}{\partial x}\frac{\partial\eta}{\partial x}\Big|_{z=\eta} \tag{2.30}$$

On a dynamically free surface the pressure can only differ by the surface tension γ. The pressure at the surface can be written as $p = p_0 - \gamma\,\partial^2\eta/\partial x^2$. With Bernoulli's equation (2.11) where the constant and p_0/ρ is integrated in ϕ_u it is:

$$\frac{\partial\phi_u}{\partial t} + \frac{1}{2}\rho_\mathrm{w}\left(\vec{\nabla}\phi_u\right)^2 + g\,\eta - \frac{\gamma}{\rho_\mathrm{w}}\frac{\partial^2\eta}{\partial x^2} = 0 \tag{2.31}$$

Neglecting the quadratic term this leads to the dynamical BC:

$$\frac{\partial\phi_u}{\partial t} = -g\,\eta + \frac{\gamma}{\rho_\mathrm{w}}\frac{\partial^2\eta}{\partial x^2} \tag{2.32}$$

2.2.2 Linear waves

First the surface elevation is assumed to be small, so there the BC (equation 2.30) becomes to $\partial\phi_u/\partial z|_{z=\eta} \approx \partial\eta/\partial t$. Together with the BC at the bottom (2.29) and the dynamical BC (2.32) the Laplace equation (2.28) can be solved for a sinusoidal water elevation and velocity functions:

$$\eta(x,t) = a\cos(kx - \omega(k)t) \tag{2.33}$$

$$\phi_u(x,z,t) = \frac{a\,\omega(k)}{k}\frac{\cosh(k(z+h))}{\sinh(kh)}\sin(kx - \omega(k)t) \tag{2.34}$$

$$u(x,z,t) = a\,\omega(k)\frac{\cosh(k(z+h))}{\sinh(kH)}\cos(kx - \omega(k)t) \tag{2.35}$$

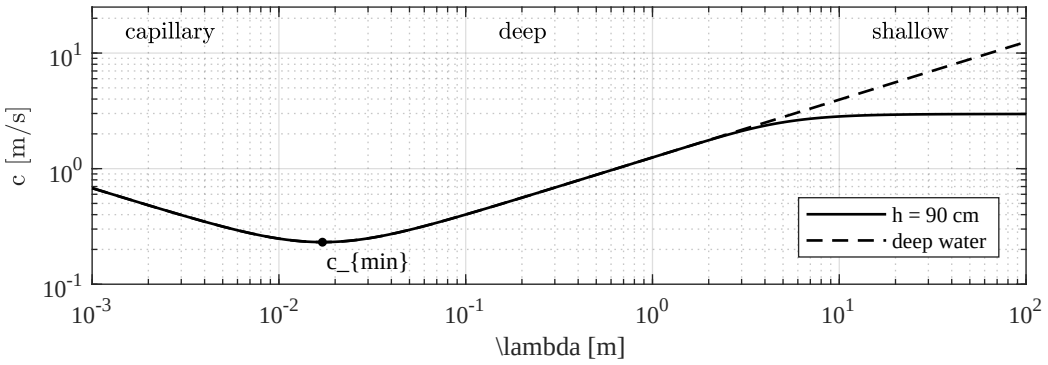

Figure 2.1: Dispersion relation for surface waves in clean water with $\gamma = 0.073$ N/m. While the dashed line represents deep water ($h \gg \lambda$), the solid line shows the relation at water height $h = 90$ cm. The minimum phase speed $c_{\min}$ is 23.1 cm/s at a wave length of $\lambda = 1.71$ cm.

$$w(x, z, t) = a\,\omega(k)\frac{\sinh(k(z+h))}{\sinh(kH)}\sin(kx - \omega(k)t) \tag{2.36}$$

Inserted in the dynamical BC (equation 2.32) the phase frequency $\omega(k)$ and thereby the dispersion relation is found to:

$$c(k) = \frac{\omega(k)}{k} = \sqrt{\left(\frac{g}{k} + \frac{\gamma k}{\rho_{\mathrm{w}}}\right)\tanh(kh)}. \tag{2.37}$$

In figure 2.1 the phase velocity c is plotted against the wavelength λ for a finite depth of $h = 90$ cm and deep water ($h \to \inf$). At a wavelength of $\lambda = 1.71$ cm a minimum of 23.1 cm/s is reached. To the left the waves are called capillary, where surface tension is the main restoring force. To the right gravity dominates giving the name gravity waves. Until a certain point c is growing proportional to $\lambda^{1/2}$, than the influence of the water depth h becomes significant and c approximates a constant value of $\sqrt{gh}$.

2.2.3 Finite amplitude waves

So far the quadratic term in the dynamical BC has been neglected, which has in consequence, that the following linear equations show waves propagating unchanged in form. For finite amplitude waves in a dispersive medium this terms yields small changes, which end in different Fourier components propagating at different speeds (compare Kinsman, 1965; Kundu et al., 2012).

Stokes' waves

Stokes (1849) showed an approximation of possible forms of finite amplitude gravity waves in deep water, where the nonlinear steepening cancels out the dispersive

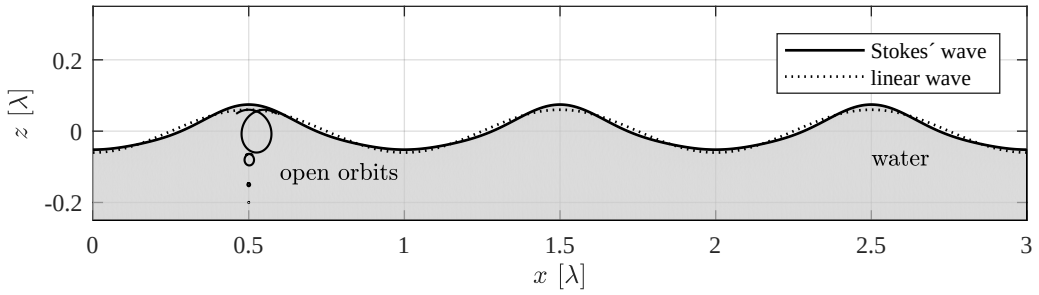

Figure 2.2: Illustration of the surface form of a stokes wave - an approximation of a finite amplitude deep water gravity wave. The black line shows the surface elevation of the first three terms with an amplitude of $a = 0.06\,\lambda$. By the dashed line the linear wave with the same amplitude is drawn.

steepening and so the wave form keeps constant.

This wave is called the *Stokes' wave* and follows the equation:

$$\begin{aligned} \eta(x,t) &= a\cos(k(x-c\,t)) + \\ &\quad \frac{1}{2}\,k\,a^2\cos(2k(x-c\,t)) + \frac{3}{8}\,k^2\,a^3\cos(3k(x-c\,t)) + ... \end{aligned} \tag{2.38}$$

with the speed of propagation

$$c(k) = \sqrt{\frac{g}{k}(1 + k^2a^2 + \ ...\ )} \quad . \tag{2.39}$$

The form changes from a sinusoidal to steeper wave crests and flatter wave troughs, which is illustrated in figure 2.2. As a results the orbits of a fluid parcel are no longer closed circles, so averaging in time yields a slight forward creep in the direction of propagation. This mean velocity is called the *Stokes drift* $\overline{u_{\mathrm{L}}}$ and depends exponentially on depth. For deep water gravity waves it is

$$\overline{u}_{\mathrm{L}} = a^2\,\omega k e^{2\,k\,z}. \tag{2.40}$$

Crapper's waves

For the regime of short wavelengths, where surface tension is the dominant restoring force, Crapper (1957) found an exact solution for progressive capillary waves. Here points at the surface are described by the x- and z-position, which depend on the wave phase ϕ:

$$\begin{aligned} x(\phi) &= \frac{1}{k}\left(\frac{\phi}{k} - \frac{4\,A\sin(\phi)}{1 + A^2 + 2\,A\,\cos(\phi}\right) \\ z(\phi) &= \frac{4}{k}\left(1 - \frac{1 + A\cos(\phi)}{1 + A^2 + 2\,A\,\cos(\phi}\right) \end{aligned} \tag{2.41}$$

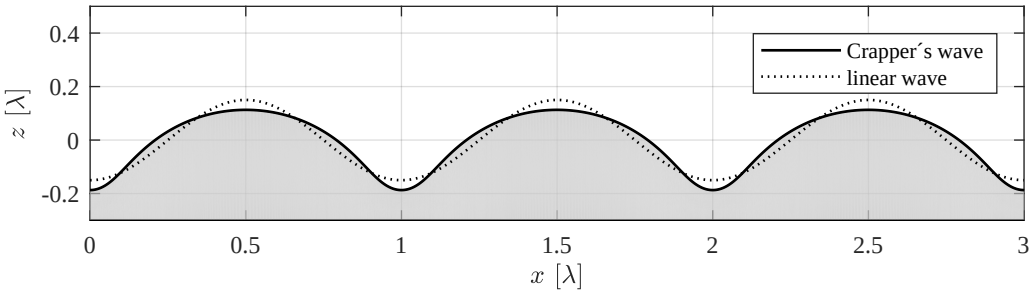

Figure 2.3: Illustration of the surface form of a Crapper's wave - an exact solution of a finite amplitude capillary wave. The black line shows the surface elevation with an amplitude of $a = 0.15\,\lambda$. By the dashed line the linear wave with the same amplitude is drawn.

and

$$A = \frac{2}{k\,a}\left(\sqrt{1+\frac{k^2a^2}{4}}-1\right). \tag{2.42}$$

The dispersion relation is:

$$c(k) = \sqrt{\frac{\gamma\,k}{\rho_\mathrm{w}}}\left(1+\frac{k^2\,a^2}{4}\right)^{-\frac{1}{4}}. \tag{2.43}$$

The amplitude a is defined as half the distance of the crests to the troughs. The surface form, which is illustrated for $a = 1.5\,\lambda$ in figure 2.3, shows the opposite of Stokes' gravity waves: flatten crests and steeper troughs. This solution holds for amplitudes up to $a < 0.365\,\lambda$, where the surface comes in contact with itself.

2.2.4 Statistical properties of wave fields

Only in rare cases a wavy water surface can be described by a single wave with a certain amplitude and frequency. Usually a superposition of many different wave modes with different amplitudes is present. Only with statistical considerations the complete wave field can be captured. In the following, some statistical descriptions and parameters for complex wave fields are presented.

Energy spectra

The total wave energy can be split in a potential and a kinetic part. The mean potential energy density E_pot of a gravity wave is described by the temporal or spacial averaged integration of the gravity force acting on the water column from zero water level to the water elevation η

$$\overline{E_\mathrm{pot}} = \overline{E_\mathrm{grav}} = \overline{\int_0^\eta \rho_\mathrm{w}\,g\,z\,dz} = \frac{1}{2}\,\rho_\mathrm{w}\,g\,\overline{\eta^2}. \tag{2.44}$$

For capillary waves an influence by surface tension has to be taken into account:

$$\overline{E_{\text{pot}}} = \overline{E_{\text{grav}}} + \overline{E_{\text{surf}}} = \frac{1}{2}\,\rho_{\text{w}}\,g\,\overline{\eta^2} - \frac{\gamma}{2\,\rho_{\text{w}}}\overline{\eta\frac{\partial^2\eta}{\partial x^2}}. \tag{2.45}$$

To get the mean kinetic energy an integration of the wave motion can be done:

$$\overline{E_{\text{kin}}} = \overline{\int_{-H}^{\eta} \frac{1}{2}\rho_{\text{w}}\,u^2\,dz}. \tag{2.46}$$

Since the water wave is a harmonic system, in spatial or temporal mean the kinetic and potetntial energy are equal. So the total energy yields to

$$\overline{E_{\text{total}}} = \overline{E_{\text{kin}}} + \overline{E_{\text{pot}}} = 2\,\overline{E_{\text{pot}}} = \rho_{\text{w}}\,g\,\overline{\eta^2} - \frac{\gamma}{\rho_{\text{w}}}\overline{\eta\frac{\partial^2\eta}{\partial x^2}} \tag{2.47}$$

In fact the wave field always exists of a combination of several waves with different wavelengths containing different amounts of energy. With knowledge of the surface elevation $\eta(x, y, t)$ the energy distribution can be calculated by use of spectral analysis (Phillips, 1977). The surface can be entirely expressed in Fourier space by

$$\eta(x, y, t) = \frac{1}{(2\pi)^3}\iiint \hat{\eta}(k_x, k_y, \omega)e^{i(k_x x + k_y y - \omega t)}\,dk_x\,dk_y\,dt, \tag{2.48}$$

which means, that the energy spectra can be expressed by the squared Fourier modes, respectively. It is distinguished between different forms of reduced spectra, where partly integration over the variables k or ω has been conducted. The *wavenumber (power density) spectrum* is given by:

$$\Psi(k_x, k_y) = |\hat{\eta}(k_x, k_y)|^2 \qquad \text{with} \qquad E = \rho_{\text{w}}\iint \Psi(k_x, k_y)dk_x dk_y \tag{2.49}$$

and the *frequency (power density) spectrum* by:

$$\Phi'(\omega) = |\hat{\eta}(\omega)|^2. \tag{2.50}$$

Because ω is often defined positive and $\Phi'(\omega)$ is symmetric in a stationary wave field, it is:

$$\Phi(\omega) = \begin{cases} 2\cdot\Phi'(\omega) & \text{for} \quad \omega \geq 0 \\ 0 & \text{for} \quad \omega < 0 \end{cases} \qquad \text{with} \qquad E = \rho_{\text{w}}\int \Phi(\omega)d\omega. \tag{2.51}$$

Momentum

The momentum M of a single wave can be expressed by the energy divided by the phase speed: $M = \frac{E}{c}$. Therefore the total momentum of a wave field can be written as the integral over the energy density spectrum divided by the speed of propagation $c = \omega(k)/k$:

$$\vec{M} = \rho_{\text{w}}\iint \frac{\vec{k}}{\omega(k)}\,\Psi(k_x, k_y)\,dk_x dk_y. \tag{2.52}$$

Wave height

While the energy spectrum gives detailed information about the distribution over all wavelengths, in many cases only the height of waves – meaning the distance from peak to peak – is of interest. While one single wave has a wave height doubled the amplitude, for wave fields with spread amplitude spectra only averaged values can be defined. The literature provides a large number of different definitions and notations, which is summarized by Holthuijsen (2007) and Massel (2013).

One common definition is the significant wave height, which represents the mean wave height of the highest third. For wind waves close to wind-wave equilibrium this can be expressed as four times the root-mean-square wave elevation (a_{rms}):

$$H_{\mathrm{s}} = 4\sqrt{\overline{\eta^2}} = 4\, a_{\mathrm{rms}}. \tag{2.53}$$

It's important to note the fact, that expression 2.53 holds only for wave fields with amplitude distributions close to the Rayleigh distribution (Caulliez, 2013). For other distributions the wave height must be calculated by measuring the height of each individual wave and taking the average. A single stokes wave with constant amplitude for example leads to $H_{\mathrm{s}} \approx 2.8\, a_{\mathrm{rms}}$, where no difference between the highest third and the mean wave height is present.

So in many situations the mean wave height of all waves, also called the dominant wave height H_{d}, could be a more meaningful parameter to describe and compare wave fields. In case of wind waves near equilibrium it is $H_{\mathrm{d}} \approx 2.5\, a_{\mathrm{rms}}$ (Massel, 2013). For a single stokes wave it is $H_{\mathrm{d}} \approx 2.8\, a_{\mathrm{rms}}$.

Wave steepness

In order to describe the wave height in relation to the wave length λ often the wave steepness ϵ is used as parameter, which is classically written as:

$$\epsilon = ak = \frac{a\, 2\pi}{\lambda} = \frac{\pi H}{\lambda} = \frac{\pi H}{cT}. \tag{2.54}$$

Here k is the wave number, H is the distance from peak to peak, T is the wave period and c is the phase velocity.

Such a wave steepness also can be calculated for wave spectra, where ϵ has to be averaged. The average over all waves is called the dominant wave steepness $\epsilon_{\mathrm{d}} = \overline{\epsilon}$ in the context of this work. Similar to the significant wave height, also the significant wave steepness ϵ_{s} is a commonly used parameter describing the steepness of the highest third. For waves close to equilibrium it can be estimated directly from the frequency spectrum S_{η_t} of the temporal derivative of the water elevation $\eta_t = \partial\eta/\partial t$:

$$\epsilon_{\mathrm{s}} = \frac{2}{c_{\mathrm{p}}}\sqrt{\int S_{\eta_t}(f)\, df}. \tag{2.55}$$

By this definition also phase coupling between the dominant wave and frequency modulations close to the spectral peak (Caulliez et al., 2008) is regarded. The integration or summation is conducted around the peak from 0.5 to 1.5 f_{peak}.

Mean square slope

In situations, where the small scale roughness of the surface is important, as it is for gas exchange, the significant wave height is not sensible enough. Here only the large surface elevations contribute and it can not be differentiated between a big smooth single wave and rough wind wave with lots of small ripples. In this case the mean square slope (mss) can be used as a parameter indicating the roughness of the surface.

2.2.5 Wave breaking

If the energy density rises, a wave becomes steeper and steeper until a certain point is reached, where the fluid parcels near the crest are unable to follow the wave motion. Then the surface form looses its stability and the wave starts breaking. The processes connected with wave breaking are strongly nonlinear and many different situations have to be considered. A summary of this still actual research field can be found in Massel (2013). The criteria for predicting wave breaking can be classified into three categories: „(1) geometric criteria based on local wave shape and global wave steepness; (2) kinematic criteria based on particle and phase velocities; and (3) dynamic criteria based on acceleration at the crest, momentum and energy growth rate and higher harmonic energy evolution.” (Wu and Nepf, 2002)

In the 19th century already, Stokes (1849) supposed a maximum angle between both sides of a crest of 120° for stable gravity waves, which could be established with calculations by Michell (1893). He showed, that the maximum amplitude of a stokes wave is 0.07 times the wavelength λ, which is usually expressed by the wave steepness ak. During the last decades a big number of threshold values determined by laboratory and field measurements appeared in the literature, all in the same range as the value given by Michell (1893).

Kinematic criteria are dealing with the fluid velocity $|\vec{u}|$ in direction of propagation, which must be equal or higher than the phase velocity c. In this case the wave overtakes itself and starts breaking. By this approach the effect of shear influencing the breaking becomes more obvious. Shear currents near the surface are increasing the particle velocity, which reduces the threshold of breaking especially for small waves and high shear stresses (e.g. Banner and Song, 2002; Phillips, 1985; Song and Banner, 2002).

As an example for a dynamical criterion the downward acceleration of a fluid parcel should become bigger than the restoring force, which equals g for gravity waves. For Stokes waves of second order this leads to a maximum amplitude of $a \geq 0.07\lambda$ or a maximum wave steepness of $(ak)_{\max} \approx 0.44$ coinciding with Michell (1893). At the ocean or in big laboratory wave tanks mostly waves of different wavelengths are present,

where the small waves are riding on top of the big ones. Thereby the real accelerations of the fluid parcels could differ from its single modes, which affects the breaking and leading to phase dependent breaking.

For capillary waves the different regime of restoring forces also changes the breaking characteristics, which is subject of actual studies (see Peirson et al., 2014).

2.2.6 Wind waves and growth rates

From an intuitive point of view the connection between wind and waves is rather clear: the higher the wind speed the bigger the waves, because wind pushes the waves. But looking closer to the dependency of this wind induced wave growth and trying to understand the physical processes becomes very complex. In the middle of the last century Phillips (1957) and Miles (1957) came out with two different and independent works building the base for the following research. In respective publications like Kinsman (1965), Phillips (1977) and Massel (2013) the achievements of the last century in this field is summarized. Without going into detail only some main concepts and dependencies are shown in the following subsection.

Regarding the process of wave growing due to wind first small waves are produced. By nonlinear wave wave interaction and due to wave breaking energy this transformed to bigger waves ending in an equilibrium wave spectrum, where all the input energy is dissipated. This spectrum strongly depends on wind speed, on water depth and the presence of surfactants.

Energy transport equation

The wind is putting energy and momentum in form of pressure forces and shear stress through the water surface, which partly ends up in energy and momentum input to waves. At the same time waves are dissipating energy by viscosity and wave breaking. Additionally, energy and momentum is transferred by nonlinear interaction processes between waves with different wavelengths. This context can be expressed by the energy momentum equation (Jones and Toba, 2001):

$$\frac{d\Psi}{dt} = \frac{\partial \Psi}{\partial t} + (\vec{u} + \vec{c}_{\mathrm{gr}}) \cdot \vec{\nabla}\Psi = s_{\mathrm{in}} + s_{\mathrm{nl}} - s_{\mathrm{diss}}. \tag{2.56}$$

The total change of the spectral wave energy Ψ (equation 2.49) is expressed by the time derivative and transport term, where $\vec{u}$ is the current velocity and c_{gr} is the group velocity. On the right side we have the energy input source function s_{in}, the nonlinear interaction source function s_{nl} and the dissipation source function s_{diss}. In integrated form the dissipation term vanishes and S_{in} and S_{diss} are also spectral integrated:

$$\frac{dE}{dt} = \frac{\partial E}{\partial t} + (\vec{u} + \vec{c}_{\mathrm{gr}}) \cdot \vec{\nabla}E = S_{\mathrm{in}} - S_{\mathrm{diss}}. \tag{2.57}$$

The energy fluxes between wind and waves (equation 2.56) and the resulting growth rate β_{wave}, which often is written in a dimensionless spectral form

$$\beta_{\mathrm{wave}} = \frac{1}{\omega\,\Phi(\omega)}\frac{\partial\Phi}{\partial t}, \tag{2.58}$$

is subject of several studies like Donelan et al. (2006) and Melville and Fedorov (2015), where a big number of parametrizations came out (Bole and Hsu, 1969; Peirson and Garcia, 2008; Reutov and Troitskaya, 1995; Shemdin and Hsu, 1967; Troitskaya and Rybushkina, 2008).

Momentum transport equation

Similar to the energy balance an equation for the wave momentum $\vec{M}$ (equation 2.52) could be set to

$$\frac{d\vec{M}}{dt} = \frac{\partial\vec{M}}{\partial t} + (\vec{u} + \vec{c}_{\mathrm{gr}}) \cdot \left(\vec{\nabla}\vec{M}\right) = \tau_{\mathrm{in}} - \tau_{\mathrm{diss}}. \tag{2.59}$$

Here τ_{in} is the total momentum input to wave motion and τ_{diss} is the momentum transfer from waves to the mean current due to friction and wave breaking. How τ_{in} is connected to the stress situation at the surface is topic of actual research (Peirson and Garcia, 2008; Grare et al., 2013) – the total wind induced stress contributes also to mean currents.

Wave age

Intuitively the momentum and energy input functions depend on the difference of wind speed to phase speed of the waves. If the wave moves with the same speed as the wind, all pressure forces shrink towards zero. In cases of old waves on the ocean, which generated long before and where the wind has been calmed down the phase velocity can exceed the wind speed. Then the wind input function becomes negative and the wave is damped by the air flow. To describe this connection the dimensionless parameter wave age is introduced, which is the fraction of this two velocities c_{p}/u. As the wind speed u is height dependent, many different notations of the wave age are present in the community. Using the reference wind speed u_{10} at 10 m height or the air sided friction velocity $u_{*,a}$ are common. While a low value indicates a young wave, high values indicate old waves, which had enough time to grow close to equilibrium. After Sullivan and McWilliams (2010) at a wave age of $c_{\mathrm{p}}/u_{10} \approx 1.2$ or $c_{\mathrm{p}}/u_{*,a} \approx 30$ the energy input equals the dissipation and the equilibrium is reached. In this context it should be pointed out, that for shallow water waves – this is the case for bigger waves in wind wave facilities with finite depths – the wave age for equilibrium is much lower than on the ocean, especially for higher wind speeds. Here the phase speed has a maximum (compare to figure 2.1) and no long waves are generated.

2.3 Air-sided vertical momentum transport above the water surface

Flux of momentum in a fluid can be realized by two processes: At the one hand momentum can be transported by advection – the inflow to an infinitesimal fluid parcel has a different momentum than the outflow. At the other hand forces can also contribute, which are mostly defined as stresses using stress tensors τ_{ij}. As a common way the advective transport, especially turbulent transport, is also written as such a stress tensor (compare section 2.1.4) and the different contributions can be included to one τ_{ij}. Regarding the mean air-sided vertical momentum transport above the water surface only one component of this stress tensor is of interest, τ_{xz} describes the horizontal stress acting vertically. The flux of horizontal momentum in z-direction $j_{\mathrm{m},xz}$ then equals the negative stress component:

$$j_{\mathrm{m},xz} = -\tau_{xz}. \tag{2.60}$$

The opposite sign comes from the notation of τ, which is defined as the stress acting on a surface with $f_i = \tau_{ji} n_j$, where $\vec{n}$ is the surface normal.[1]

Regarding the momentum transport above the water surface it is suitable to characterize this shear stress τ_{xz} by a quantity with the dimension of a velocity. This velocity u_* is called the friction velocity and it is (Roedel and Wagner, 2017):

$$|\tau_{xz}| = \rho u_*^2 \qquad \text{or} \qquad u_* = \sqrt{|\tau_{xz}|/\rho}. \tag{2.61}$$

As the fluids densities above and below the water surface differ two different friction velocities exist, $u_{*,a}$ in air and $u_{*,w}$ in water, respectively. They can be transformed by the factor $\sqrt{\rho_a/\rho_w}$.

2.3.1 Flat surface

We start with the most simple case, a flat surface without waves. This is a well known regime described by the law of the wall and plays a big role also in other fields with no connection to ocean dynamics. Above a certain height the Reynolds number exceeds the critical value and the flow becomes fully turbulent. To analyze the momentum transport we consider the NSE in its averaged form after applying the Reynolds decomposition (equation 2.13). We assume stationary mean flow in time and in horizontal direction and no mean vertical flow ($\overline{u}_z = 0$), which is caused by a constant sea level. Then inside the constant flux layer the equation reduces to

$$0 = \frac{\partial}{\partial z}\Bigg(\underbrace{-\rho_{\mathrm{a}}\, \overline{u_x' u_z'}}_{\tau_{\mathrm{turb},xz}} + \underbrace{\mu_{\mathrm{a}} \frac{\partial \overline{u_x}}{\partial z}}_{\tau_{\mathrm{visc},xz}} \Bigg), \tag{2.62}$$

[1] The literature provides different notations of τ with opposite signs, here the notation common in fluid mechanics is used, see Kundu et al. (2012).

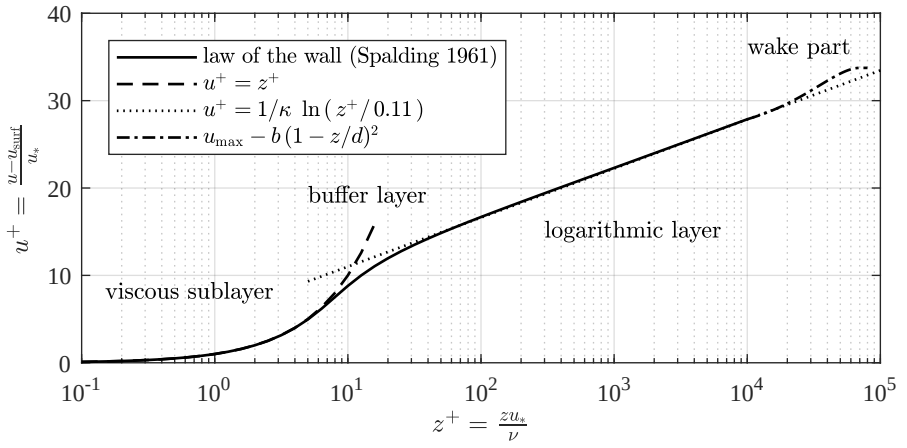

Figure 2.4: Law of the wall in dimensionless form. The dashed line shows the linear velocity behavior (equation 2.63) valid for the viscous sublayer $z^+ < 5$. Dotted the logarithmic velocity profile (equation 2.64) is drawn, valid for the logarithmic layer giving good results for $z^+ > 30$. The buffered layer between is well described by the experimental found equation (2.66), which describes the complete profile from viscous to fully turbulent regimes. Above the logarithmic layer the wake part begins, where the flux of momentum decreases and the velocity profile can be approximated by a quadratic function.

where only the z-derivative of the turbulent and viscous stress terms ($\tau_{\mathrm{turb},xz}$ and $\tau_{\mathrm{visc},xz}$) remains. Here the total shear $\tau_{xz} = \tau_{\mathrm{turb},zx} + \tau_{\mathrm{visc},zx}$ is constant in height. Inside the viscous boundary layer all fluctuations are dissipated directly and τ consists only of the viscous part. Solving this equation yields a linear function in z or z^+ (dimensionless height with $z^+ = z\,u_{*,a}/\nu_a$):

$$u^+(z^+) = z^+ \qquad \text{or} \qquad u_x(z) - u_{\mathrm{surf}} = \frac{{u_{*,\mathrm{a}}}^2}{\nu_{\mathrm{a}}} z, \tag{2.63}$$

where u_{surf} is the surface velocity and ν_a is the kinematic viscosity of air. Here $u^+ = (u_x - u_{\mathrm{surf}})/u_*$ is the dimensionless velocity. Far above the viscous sublayer the effect of molecular viscosity can be neglected and by using the turbulent viscosity with the mixing length model (Prandtl, 1957) the logarithmic velocity profile can be deduced:

$$u^+(z^+) = \frac{1}{\kappa} \ln\left(\frac{z^+}{0.11}\right) \qquad \text{or} \qquad u_x(z) = \frac{u_{*,\mathrm{a}}}{\kappa} \ln\left(\frac{z}{z_0^{\mathrm{smooth}}}\right). \tag{2.64}$$

κ is the van Karman constant, which has been experimentally determined to 0.41 (Schlichting and Gersten, 2006). The integration constant z_0 represents the roughness length. For an aerodynamically smooth surface experiments show the dependency (Fairall et al., 2003):

$$z_0^{\mathrm{smooth}} = 0.11\,\frac{\nu_{\mathrm{a}}}{u_{*,\mathrm{a}}}. \tag{2.65}$$

Bridging these two regimes, the viscous sublayer (equation 2.63) and the logarithmic layer (equation 2.64), Spalding (1961) experimentrally found an equation describing the complete velocity profile. It is given in implicit form:

$$z^+ = u^+ + 0.11\left(\mathrm{e}^{\kappa u^+} - 1 - \kappa u^+ - \frac{1}{2}(\kappa u^+)^2 - \frac{1}{6}(\kappa u^+)^3 - \frac{1}{24}(\kappa u^+)^4\right). \quad (2.66)$$

In figure 2.4 these equations are showed. Actual measurements confirm these equations like Buckley and Veron (2016), who measured the air flow above a flat water surface.

In the outer part of the turbulent layer the flow changes to free flow, where the magnitude of the total stress is decreasing. This leads to the so called wake part of the velocity profile, which varies from the logarithmic law and depends on the Reynolds number. In figure 2.4 an examplary parametrization by a quadratic function is plotted, where d represents the boundary layer thickniss and b is an experimental parameter. Generally the wake part begins at larger distances to the boundary for larger Reynolds numbers.

2.3.2 Wavy surface

If the air flow has a sufficient velocity, waves are developing influencing the flow, which also influences the momentum transport. At the one hand the surface topology increases the generation of turbulence, which ends up in an increased shear. At the other hand a wave coherent momentum flux occurs, which can be pointed out by using a triple decomposition of a quantity q. Beside the mean component $\overline{q}$ the fluctuating component is further decomposed in the phase dependent $\widetilde{q}$ and the real turbulent perturbation $q^{'}$ (Anis and Moum, 1995; Buckley and Veron, 2016):

$$q = \overline{q} + \widetilde{q} + q^{'} \quad (2.67)$$

$$\text{with} \qquad \langle q(x,y,z,t)\rangle_t = \overline{q}(x,y,z) \quad (2.68)$$

$$\text{and} \qquad \langle q(x,y,z,t)\rangle_{t,\phi=\text{const.}} = \overline{q}(x,y,z) + \widetilde{q}(x,y,z,\phi). \quad (2.69)$$

Inserting this triple decomposition to the momentum equation (2.13) and taking a phase dependent mean (denoted by $\langle\,\rangle = \langle\,\rangle_{t,\phi=\text{const.}}$) it yields:

$$\frac{\partial}{\partial x_i}\Bigg(\underbrace{\rho_\mathrm{a}(\overline{u}_i\overline{u}_j + \overline{u}_i\widetilde{u}_j + \widetilde{u}_i\overline{u}_j)}_{\text{advection}}\Bigg) = \quad (2.70)$$

$$\frac{\partial}{\partial x_i}\Bigg(\underbrace{-\rho_\mathrm{a}\widetilde{u}_i\widetilde{u}_j}_{\widetilde{\tau}_{\text{wave},ij}} \quad \underbrace{-\rho_\mathrm{a}\left\langle u_i^{'}u_j^{'}\right\rangle}_{\widetilde{\tau}_{\text{turb},ij}} \quad \underbrace{-p\delta_{ij}}_{\widetilde{\tau}_{\text{press},ij}} + \underbrace{\mu_\mathrm{a}\tfrac{\partial}{\partial x_i}(\overline{u}_j + \widetilde{u}_j)}_{\widetilde{\tau}_{\text{visc},ij}}\Bigg).$$

After averaging all phases (denoted by a line) the equation reduces to:

$$\frac{\partial}{\partial x_i}\Bigg(\underbrace{\rho_\mathrm{a}\,\overline{u}_i\overline{u}_j}_{\text{advection}}\Bigg) = \frac{\partial}{\partial x_i}\Bigg(\underbrace{-\rho_\mathrm{a}\overline{\widetilde{u}_i\widetilde{u}_j}}_{\overline{\tau}_{\mathrm{wave},ij}}\ \underbrace{-\rho_\mathrm{a}\overline{u_i'u_j'}}_{\overline{\tau}_{\mathrm{turb},ij}}\ \underbrace{-p\delta_{ij}}_{\overline{\tau}_{\mathrm{press},ij}} + \underbrace{\overline{\mu_\mathrm{a}\frac{\partial}{\partial x_i}(\overline{u}_j)}}_{\overline{\tau}_{\mathrm{visc},ij}}\Bigg). \tag{2.71}$$

The notation of the phase averaged and global averaged shear stresses is $\widetilde{\tau}$ and $\overline{\tau}$, respectively. The global average can be determined by averaging $\widetilde{\tau}$ over all phases.

Regarding the vertical transfer of horizontal momentum and again assuming a constant water level and stationary flow, the global averaged equation becomes:

$$0 = \frac{\partial}{\partial z}\Bigg(\underbrace{-\rho_\mathrm{a}\overline{\widetilde{u}_x\widetilde{u}_z}}_{\overline{\tau}_{\mathrm{wave},xz}}\ \underbrace{-\rho_\mathrm{a}\overline{u_x'u_z'}}_{\overline{\tau}_{\mathrm{turb},xz}} + \underbrace{\mu_\mathrm{a}\frac{\partial\overline{u}_x}{\partial z}}_{\overline{\tau}_{\mathrm{visc},xz}}\Bigg). \tag{2.72}$$

Compared with equation 2.62 an additional term occurs representing the wave induced advection. It needs to be said, that this equation only holds above the uppermost wave crest. Below, problems in taking the mean along a constant vertical height z occur because of the presence of two different liquids. Here curvilinear coordinates can be used, as it is described in the next section 2.3.3.

The total transfer of horizontal momentum in vertical direction τ_{xz} can be split into three parts: the wave induced shear $\tau_{\mathrm{wave},xz}$, the turbulent shear stress $\tau_{\mathrm{turb},xz}$ and the viscous stress $\tau_{\mathrm{visc},xz}$ (Veron et al., 2007).

$$\tau_{xz} = \tau_{\mathrm{wave},xz} + \tau_{\mathrm{turb},xz} + \tau_{\mathrm{visc},xz} \tag{2.73}$$

Logarithmic wind profile

At a certain height above the uppermost crest the wave induced shear and the viscous shear converge to zero and only the turbulent part remains. Inside the WBL (compare to figure 1.1), where the total vertical momentum transport is constant in height, a logarithmic wind profile is formed.

$$u_x(z) = \frac{u_{*,\mathrm{a}}}{\kappa}\ln\left(\frac{z}{z_0^{\mathrm{rough}}}\right). \tag{2.74}$$

The equation equals the logarithmic profile of a smooth surface (2.64) with the only difference, that the roughness length z_0 is added by an additional term (Fairall et al., 1996):

$$z_0^{\mathrm{rough}} = 0.11\,\frac{\nu_\mathrm{a}}{u_{*,\mathrm{a}}} + \alpha_\mathrm{ch}\frac{{u_{*,\mathrm{a}}}^2}{g}. \tag{2.75}$$

This rough flow component was first introduced by Charnock (1955) who gave the Charnock coefficient α_ch its name. During half of the last century a big number of

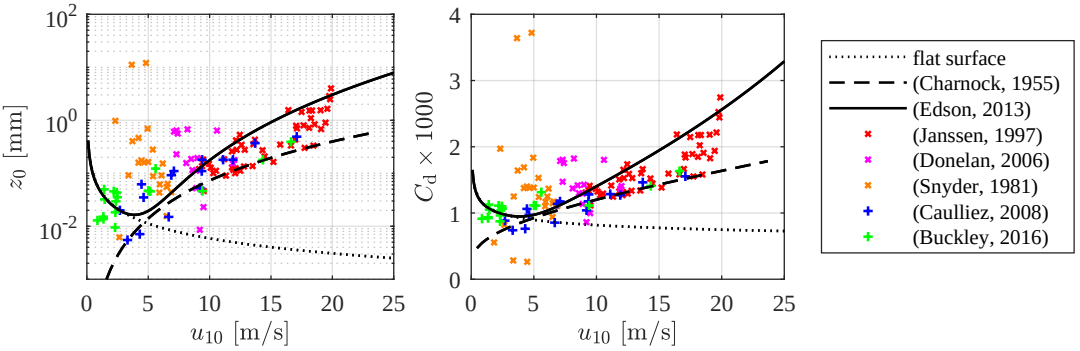

Figure 2.5: Roughness length z_0 (**right**) and drag coefficient C_d (**left**) against the reference wind speed at 10 m height u_{10}. With the dotted line the aerodynamical smooth case is plotted. Parametrizations of wavy water are shown by the solid (Edson et al., 2013) and the dashed (Charnock, 1955) black line. By crosses measurements at open ocean (Snyder et al., 1981; Janssen, 1997; Donelan et al., 2006) are plotted and pluses are showing laboratory measurements (Caulliez et al., 2008; Buckley and Veron, 2016).

parametrizations of z_0^{rough} or α_{ch} have been postulated for the wavy water surface (Jones and Toba, 2001). Many depend on wave age u_*/c_p (Kitaigarodskii and Volkov, 1965; Hsu, 1974), some also depend on wave steepness or significant wave height (Jian et al., 2011) and others only take the reference wind speed u_{10} into account (Edson et al., 2013).

Drag coefficient

Another parameter describing the momentum transport over the wavy water surface is given by the drag coefficient C_d. It is calculated by the relation of the shear stress τ and the density times the reference wind speed u_{10} squared:

$$C_\mathrm{d} = \frac{\tau}{\rho\, {u_{10}}^2} = \frac{{u_{*,\mathrm{a}}}^2}{{u_{10}}^2} = \kappa^2 \left(\ln\left(\frac{10}{z_0^{\mathrm{rough}}}\right)\right)^{-2}. \tag{2.76}$$

C_d can be expressed by the squared friction velocity divided by ${u_{10}}^2$. The roughness length z_0^{rough} and C_d can be converted by $z_0^{\mathrm{rough}} = 10\exp(-\kappa\sqrt{C_\mathrm{d}})$.

As for z_0 a large convolution of measurements and parametrizations have been published during the last decades, where one main topic was the dependency on the wave state. A small selection is showed in figure 2.3.2, where z_0 and C_d is plotted against u_{10}. While lines are representing parametrizations, single data points are measurements. A large scattering as well for open ocean measurements (crosses) and laboratory measurements (pluses) is demonstrating the complexity. Above $u_{10} \approx 4$ m/s z_0 and C_d rise with increasing wind speed, which can be explained by the wave state becoming more rough. Recent studies by Donelan (2018) show an upper limit for very

high wind speeds above $u_{10} \approx 30\,\text{m/s}$, where the drag coefficient starts decreasing again.

2.3.3 Considerations in curvilinear coordinates

At heights below the highest crests it is better to make momentum considerations along layers, which have no intersects with the water surface (Benjamin, 1959). Such layers following the surface geometry can be received by setting a constant value of the vertical component z^* in curvilinear coordinates. At $z^* = 0$ this layer is representing the water surface.

Mapping functions

For the mapping function a large number of transformations with different approaches could be found in the literature. One option is to use conformal (or angle-preserving) mapping. Such orthogonal curvilinear coordinates have been first applied on a single sinusoidal water elevation by Benjamin (1959). Al-Zanaidi and Hui (1984) supplemented the transformation by using Stokes waves of second order. Further, the transformation is able to follow a random surface without loosing orthogonality, if the complete Fourier spectrum of the surface elevation is taken into account (Buckley and Veron, 2016; Troitskaya and Rybushkina, 2008).

Using a conformal transformation, which has to modify the horizontal coordinate yields to complex calculations. An easier approach has been already used for numerical considerations by Chalikov (1978). The horizontal coordinates remain unchanged and only the z-component is modified. By subtracting a term $f(\vec{x}^*, t)$ depending on the position in curvilinear coordinates this yields a system following the surface for $z^* = 0$ (e.g. Hara and Sullivan, 2015; Troitskaya et al., 2011). The only necessity is $f(\vec{x}^*, t)|_{z^*=0} = \eta(x, t)$ – for vanishing z^* the function is describing the surface elevation. The transformation is

$$\begin{aligned} x^* &= x \\ y^* &= y \\ z^* &= z - f(\vec{x}^*, t) \end{aligned} \tag{2.77}$$

and thereof the determinant of the Jacobian and the differentials become (see section 2.1.6)

$$J = 1 \Big/ \begin{vmatrix} 1 & 0 & 0 \\ 0 & 1 & 0 \\ \frac{\partial f}{\partial x} & 0 & 1+\frac{\partial f}{\partial z^*} \end{vmatrix} = \left(1 + \tfrac{\partial f}{\partial z^*}\right)^{-1} \tag{2.78}$$

$$\begin{pmatrix} \frac{\partial x^*}{\partial x} & \frac{\partial x^*}{\partial y} & \frac{\partial x^*}{\partial z} \\ \frac{\partial y^*}{\partial x} & \frac{\partial y^*}{\partial y} & \frac{\partial y^*}{\partial z} \\ \frac{\partial z^*}{\partial x} & \frac{\partial z^*}{\partial y} & \frac{\partial z^*}{\partial z} \end{pmatrix} = \frac{1}{\left(1+\frac{\partial f}{\partial z^*}\right)} \begin{pmatrix} 1+\frac{\partial f}{\partial z^*} & 0 & 0 \\ 0 & 1+\frac{\partial f}{\partial z^*} & 0 \\ -\frac{\partial f}{\partial x} & 0 & 1 \end{pmatrix}$$

$$= \begin{pmatrix} 1 & 0 & 0 \\ 0 & 1 & 0 \\ -\left(1+\frac{\partial f}{\partial z^*}\right)^{-1} \frac{\partial f}{\partial x} & 0 & \left(1+\frac{\partial f}{\partial z^*}\right)^{-1} \end{pmatrix} \tag{2.79}$$

In this work two functions f are applied. Once a simple shift of the vertical coordinate by the surface elevation is conducted by setting f equal $\eta(x,t)$. Than an exponential declining shift is realized by multiplying an exponential term on each mode in Fourier space, respectively. Thereby all waves are considered according to their wave length. Long gravity waves are declining more slowly than short ripples. How strong they are declining can be controlled by the parameter σ_d. The two functions are defined by:

$$\text{simple shift:} \qquad f(x,t) = \eta(x,t) \tag{2.80}$$

$$\text{declining shift:} \qquad f(x,z^*,t) = \sum_n a_n \cos(k_n x - \phi_n)\, e^{-\sigma_\mathrm{d} k_n z^*} \tag{2.81}$$

From a fluid mechanical view the simple shift coordinate transformation is not sufficient, because the wind is not effected by the waves at higher layers. The transformed coordinates also should approach the fixed Cartesian coordinates with growing distance to the water surface, which is fulfilled by the declining shift.

Figure 2.3.3 shows a demonstration of the simple shifted (equation 2.80) and the exponential declining (equation 2.81) transformation with two different parameters. The difference is clearly visible. While the lines of constant z^* for the simple shifted case (red dots) keep the shape of the water surface, the transformed vertical coordinates of declining transformations follow the surface near the water and converge the Cartesian coordinates for larger heights. Even at a distance to the water surface of half a wavelength, the deviation becomes negligible for $\sigma_\mathrm{d} = 1$. For the lower value of $\sigma_\mathrm{d} = 0.5$ the declining is more slowly.

Averaged momentum equation

Similar to the consideration in the upper section the triple decomposition (equation 2.67) can be applied on all quantities of the NSE written in transformed coordinates in general form (equation 2.27). First, the phase dependent mean is taken:

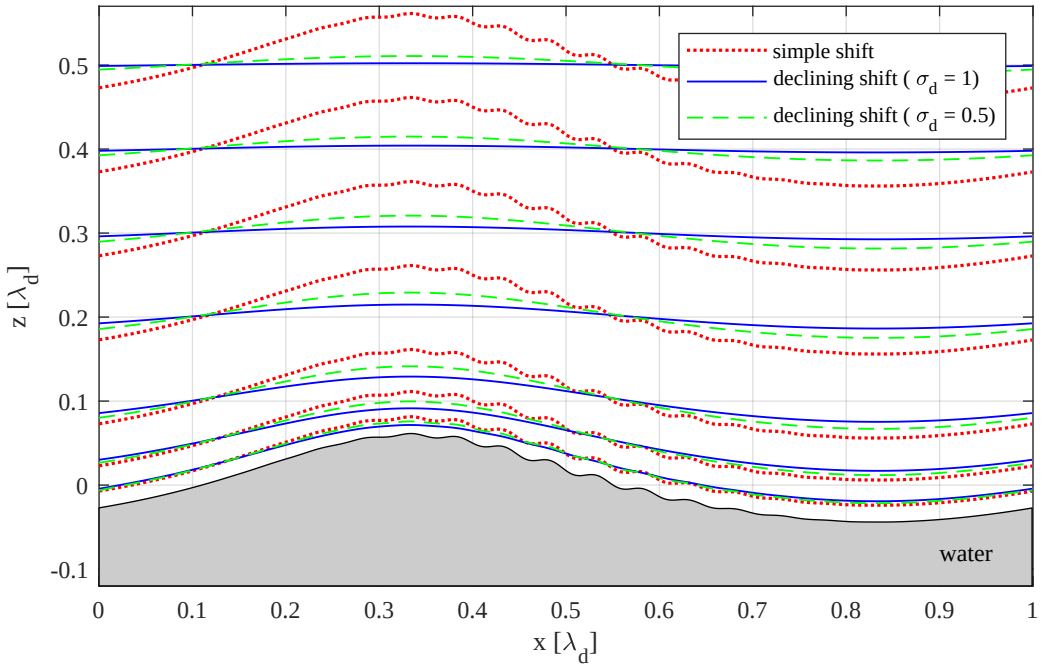

Figure 2.6: Demonstration of curvilinear coordinates above a water wave. The black line and the gray area below show the surface of a simulated wave. Lines of constant z^* are plotted above. With red dots the simple shifted coordinates are visualized. The blue lines show constant z^* for the declining shift transformation.

$$\frac{\partial}{\partial x_i^*}\Bigg(\underbrace{\rho_\mathrm{a}(\overline{U}_i\overline{u}_j+\overline{U}_i\widetilde{u}_j+\widetilde{U}_i\overline{u}_j)}_{\text{advection}}\Bigg)= \tag{2.82}$$
$$\frac{\partial}{\partial x_i^*}\Bigg(\underbrace{-\rho_\mathrm{a}\widetilde{U}_i\widetilde{u}_j}_{\widetilde{\tau}_{\mathrm{wave},ji^*}}\ \underbrace{-\rho_\mathrm{a}\left\langle U_i'u_j'\right\rangle}_{\widetilde{\tau}_{\mathrm{turb},ji^*}}\ \underbrace{-\left\langle\frac{1}{J}\,p\,\frac{\partial x_i^*}{\partial x_j}\right\rangle}_{\widetilde{\tau}_{\mathrm{pres},ji^*}}+\underbrace{\left\langle\frac{1}{J}\,\tau_{\mathrm{visc},jk}\frac{\partial x_i^*}{\partial x_k}\right\rangle}_{\widetilde{\tau}_{\mathrm{visc},ji^*}}\Bigg).$$

Global averaging yields:

$$\frac{\partial}{\partial x_i^*}\Bigg(\underbrace{\rho_\mathrm{a}\overline{U}_i\overline{u}_j}_{\text{advection}}\Bigg)= \tag{2.83}$$
$$\frac{\partial}{\partial x_i^*}\Bigg(\underbrace{-\rho_\mathrm{a}\overline{\widetilde{U}_i\widetilde{u}_j}}_{\overline{\tau}_{\mathrm{wave},ji^*}}\ \underbrace{-\rho_\mathrm{a},\overline{U_i'u_j'}}_{\overline{\tau}_{\mathrm{turb},ji^*}}\ \underbrace{-\overline{\frac{1}{J}\,p\,\frac{\partial x_i^*}{\partial x_j}}}_{\overline{\tau}_{\mathrm{pres},ji^*}}+\underbrace{\overline{\frac{1}{J}\,\tau_{\mathrm{visc},jk}\frac{\partial x_i^*}{\partial x_k}}}_{\overline{\tau}_{\mathrm{visc},ji^*}}\Bigg).$$

Due to the mean, wave dependent and turbulent parts $\overline{U}_i$, $\widetilde{U}_i$ and U_i' of the transformed

velocity vector U_i and due to the partial derivatives of the mapped coordinates the equations differ from their form in Cartesian coordinates (equation 2.70 and 2.71). Now all terms between the clamps are expressing the transport of j-momentum across a unit area with constant x_i^*, phase dependent or averaged, respectively.

Partitioning of momentum transfer

The mean transport of horizontal momentum across a layer with constant z^* if of interest, so only the terms of $\frac{\partial}{\partial z^*}(\ )$. The phase dependent mean is:

$$\frac{\partial}{\partial z^*}\Bigg(\underbrace{\rho_\mathrm{a}(\overline{U}_z\overline{u}_x+\overline{U}_z\widetilde{u}_x+\widetilde{U}_z\overline{u}_x)}_{\text{advection}}\Bigg)= \frac{\partial}{\partial z^*}\Bigg(\underbrace{-\rho_\mathrm{a}\widetilde{U}_z\widetilde{u}_x}_{\widetilde{\tau}_{\mathrm{wave},xz^*}}\ \underbrace{-\left\langle\frac{1}{J}\,p\,\frac{\partial z^*}{\partial x}\right\rangle}_{\widetilde{\tau}_{\mathrm{pres},xz^*}} \underbrace{-\rho_\mathrm{a}\left\langle U_z'u_x'\right\rangle}_{\widetilde{\tau}_{\mathrm{turb},xz^*}} + \underbrace{\left\langle\frac{1}{J}\,\tau_{\mathrm{visc},xx}\frac{\partial z^*}{\partial x}\right\rangle+\left\langle\frac{1}{J}\,\tau_{\mathrm{visc},xz}\frac{\partial z^*}{\partial z}\right\rangle}_{\widetilde{\tau}_{\mathrm{visc},xz^*}}\Bigg) \tag{2.84}$$

and the total mean is:

$$0=\frac{\partial}{\partial z^*}\Bigg(\underbrace{-\rho_\mathrm{a}\overline{\widetilde{U}_z\widetilde{u}_x}}_{\overline{\tau}_{\mathrm{wave},xz^*}}\ \underbrace{-\overline{\frac{1}{J}\,p\,\frac{\partial z^*}{\partial x}}}_{\overline{\tau}_{\mathrm{pres},xz^*}}\ \underbrace{-\rho_\mathrm{a}\overline{U_z'u_x'}}_{\overline{\tau}_{\mathrm{turb},xz^*}}+\underbrace{\overline{\frac{1}{J}\,\tau_{\mathrm{visc},xx}\frac{\partial z^*}{\partial x}}+\overline{\frac{1}{J}\,\tau_{\mathrm{visc},xz}\frac{\partial z^*}{\partial z}}}_{\overline{\tau}_{\mathrm{visc},xz^*}}\Bigg). \tag{2.85}$$

Thereby follows, that as well the phase dependent as the total transport consist of four parts. Compared to the equation in Cartesian coordinates an additional term containing the pressure occurs. This pressure is defined as a field and consists not only at the water surface. Moreover, the viscous shear stress has to be supplemented by a projection of $\tau_{\mathrm{visc},xx}$. All advection terms in the phase dependent equation (2.85) do not contribute to the total momentum transport and therefore don't have to be regarded.

The total shear τ_{xz^*} through a wave following plane, which also can be expressed by the density times the friction velocity $u_{*,\mathrm{a}}$ squared, is

$$\tau_{xz^*}=\underbrace{\tau_{\mathrm{pres},xz^*}+\tau_{\mathrm{wave},xz^*}}_{\tau_{\mathrm{form},xz^*}}+\tau_{\mathrm{turb},xz^*}+\tau_{\mathrm{visc},xz^*}=\rho_\mathrm{a}\,u_{*,\mathrm{a}}^2. \tag{2.86}$$

The sum of the two wave-induced terms $\tau_{\mathrm{wave},xz^*}$ and $\tau_{\mathrm{pres},xz^*}$ is named the wave induced stress (see Hara and Sullivan, 2015) or the form drag $\tau_{\mathrm{form},xz^*}$ (compare to Jones and Toba, 2001). As these parts of shear stress are functions of the transformed coordinate z^* the dependency on this in particular is important and might differ for various wind-wave conditions. Generally near the surface, turbulence shrinks against zero and the momentum transport is carried only by $\tau_{\mathrm{form},xz^*}$ and $\tau_{\mathrm{visc},xz^*}$. Far away from the surface the regime can be assumed as fully turbulent and all influences by waves can be neglected. Here the total shear stress is dominated by $\tau_{\mathrm{form},xz^*}$.

Applying the coordinate transformation of equation (2.77) the pressure and the viscous term can be written as:

$$\begin{aligned} \tau_{\mathrm{pres},xz^*} &= \left(1+\tfrac{\partial f}{\partial z^*}\right) p \left(1+\tfrac{\partial f}{\partial z^*}\right)^{-1} \tfrac{\partial f}{\partial x} \\ &= p\,\tfrac{\partial f}{\partial x} \end{aligned} \tag{2.87}$$

$$\begin{aligned} \tau_{\mathrm{visc},xz^*} &= -\left(1+\tfrac{\partial f}{\partial z^*}\right) \tau_{\mathrm{visc},xx} \left(1+\tfrac{\partial f}{\partial z^*}\right)^{-1} \tfrac{\partial f}{\partial x} + \\ &\qquad \left(1+\tfrac{\partial f}{\partial z^*}\right) \tau_{\mathrm{visc},xz} \left(1+\tfrac{\partial f}{\partial z^*}\right)^{-1} \\ &= \tau_{\mathrm{visc},xz} - \tau_{\mathrm{visc},xx}\,\tfrac{\partial f}{\partial x} \end{aligned} \tag{2.88}$$

So both depend on the incline of the layer of constant z^* expressed by the derivative of f. For the calculation of the two other terms the transformed velocity vector perpendicular to the layer of constant z^* has to be determined:

$$\begin{aligned} U_z &= -\left(1+\tfrac{\partial f}{\partial z^*}\right) u_x \left(1+\tfrac{\partial f}{\partial z^*}\right)^{-1} \tfrac{\partial f}{\partial x} + \\ &\qquad \left(1+\tfrac{\partial f}{\partial z^*}\right) u_z \left(1+\tfrac{\partial f}{\partial z^*}\right)^{-1} - \left(1+\tfrac{\partial f}{\partial z^*}\right) \left(1+\tfrac{\partial f}{\partial z^*}\right)^{-1} \tfrac{\partial f}{\partial t} \\ &= u_z - u_x \tfrac{\partial f}{\partial x} - \tfrac{\partial f}{\partial t}. \end{aligned} \tag{2.89}$$

On this the triple decomposition of equation (2.67) giving $\overline{U_z}$, $\widetilde{U_z}$ and U_z' can be applied whereby the turbulent and wave coherent advective momentum transport can be determined.

Condition at the surface

For wave dynamics only the limiting case at the water surface is of interest, because here all the momentum and energy is transferred from air to water. Using curvilinear coordinates with only modifying the vertical component (equation 2.77) at the surface the shift function f has to equal the surface elevation η. Due to the no slip condition at the boundary the horizontal velocity component u_x is equal to the horizontal surface velocity u_{surf}. The vertical component of the velocity can be expressed by the temporal derivative of the water elevation ($u_z = \partial\eta/\partial t$). Applying these boundary conditions to U_z (equation 2.89) it can be simplified as

$$U_z\big|_{\mathrm{surf}} = u_z - u_x \tfrac{\partial \eta}{\partial x} - \tfrac{\partial \eta}{\partial t} = -u_{\mathrm{surf}} \tfrac{\partial \eta}{\partial x} \tag{2.90}$$

and inserting into the NSE (in this case no triple decomposition is used) it yields

$$\overline{\tau}_{\mathrm{surf}} = -\rho\,\overline{{u_{\mathrm{surf}}}^2 \tfrac{\partial \eta}{\partial x}} + \overline{p\,\tfrac{\partial \eta}{\partial x}} + \overline{\tau}_{\mathrm{visc},xz^*}. \tag{2.91}$$

3 Measurement techniques

3.1 Velocity measurements in air

For velocity measurements a wide choice of techniques is available. Small probes like Pitot tubes or hot-wire anemometers measure fluids properties like pressure or heat transport and by this, the flow velocity can be determined indirectly. Other methods like rotating cup anemometers are able to measure the mechanical influence of the flow on the instrument directly. A large group of measurement techniques, are optical methods using small particles in the air acting as tracers.

While the latter method is described in the next section 3.2, in the following the most common instrument, the Pitot tube is briefly sketched. Even if particle imaging techniques represent the dominant method in this study, the reference wind speed during all experiments were logged by a Pitot tube.

Pitot tube

Pitot tubes are measuring the pressure difference between the stagnation pressure at a small tube directed into the flow and the static pressure. From this dynamic pressure the flow velocity can be determined by using the Bernoulli equation (2.11) (see Durst, 2006).

L-shaped Pitot tubes are often used, which have an opening at the top and on the sides. Connected independently to a differential pressure transducer the dynamical pressure is measured. Due to the construction only a weak dependency on the flow direction is present. Dependent on the length of the tubes, connecting the holes with the differential pressure transducer, the response time of the measurements is rather long. In most cases no turbulent fluctuations can be resolved and so this instrument is approved for measuring average wind velocity with no changes in direction.

As a robust and not expensive measurement technique they are installed in many wind-wave facilities, often placed at a reference position for controlling the magnitude of the wind speed. Also mean wind profiles are measured by Pitot tubes mounting them on translation bars. A big disadvantage is the restricted usability in the presence of waves – if the holes come in contact with water no measurements are possible anymore.

3.2 Particle imaging techniques

The basic principle of all particle imaging techniques is simple: the fluid is seeded with small particles, which follow the flow and represent the fluids velocity. These particles are illuminated to make them visible and their movement is observed with a camera, whereby the fluids velocity is determined. Since many particles can fit into one image, flow fields can be retrieved.

During the last decades a large number of methods has been developed, which make use of particle imaging to investigate flows. In general they can be grouped into three categories according to the seeding density (Adrian, 1991). Low particle densities (first group) allow tracking single particles, which is commonly called particle tracking velocimetry (PTV). This can be realized in different ways, by multiple single frames or multiple illumination pulses in single frames, by long illuminations in single frames leading to particle streaks (also called particle streak velocimetry – PSV) and many more including modifications and combinations. The second group is represented by all particle imaging velocimetry methods (PIV) with medium seeding densities. The particles are separated in the image, but too close for distinct tracking. Looking at small image regions (interrogation windows) the velocity is retrieved by statistically considering many particles. If the seeding is so dense, that no single particles can be resolved, laser speckle velocimetry (LSV) can be applied. By analyzing random interference patterns (speckles) the fluid velocity is determined.

In the following a short description of the measurement techniques used in this work are given. The criteria for good seeding materials are outlined in section 3.2.1. Section 3.2.2 briefly describes statistical PIV, which was used by Alexander Kandaurov for measuring the air-flow simultaneously with the PSV-measurements. The basics of PSV are given in section 3.2.3, where also the modified method used for the current measurements is detailed.

For a review on particle imaging techniques and their historical evolution it is referred to textbooks like Raffel et al. (2007) and Adrian and Westerweel (2011).

3.2.1 Tracking characteristics of particles

Fluid mechanical properties

It is clear, that the seeding particles in air must be very small to follow the air flow. Since the air velocity is determined indirectly by the particles' velocity, errors may be produced, if the air- and particle's velocity differ (Melling, 1997). One source for such an error are gravitational forces. If the density of the fluid and the particles do not match, which is usually the case for seeding in air, gravity leads to a downward velocity of the particles. Assuming spherical particles in a viscous medium at low Reynolds number, this velocity u_g can be estimated using Stokes' drag law – gravitational force equals viscous friction:

$$u_\mathrm{g} = d_\mathrm{particle}^2 \frac{\rho_\mathrm{particle} - \rho_\mathrm{a}}{18\mu_\mathrm{a}}\, g, \tag{3.1}$$

where ρ_particle and ρ_a are densities of the particle and air, respectively, μ_a is the dynamic viscosity and g is the gravitational constant. Inserting typical values like $\rho_\mathrm{particle} = 10^3\,\mathrm{kg/m^3}$ and $d_\mathrm{particle} < 10\,\mu\mathrm{m}$ this leads to a downward velocity of $u_\mathrm{g} < 0.05\,\mathrm{cm/s}$, which can be neglected regarding the air flow above waves with wind speeds in order of m/s.

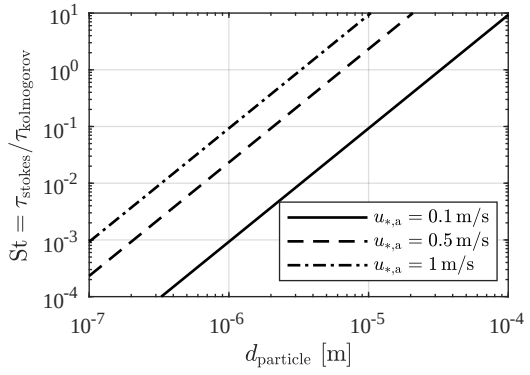

Figure 3.1: Estimation of the Stokes number $\mathrm{St} = \tau_{\mathrm{stokes}}/\tau_{\mathrm{kolmogorov}}$ for particles in dependency on their size $d_{\mathrm{particles}}$. The different lines represent different friction velocities $u_{*,\mathrm{a}}$. The Kolmogorov time scale $\tau_{\mathrm{kolmogorov}}$ has been estimated for wall bounded shear flow inside the transition layer from laminar to turbulent.

Similarly a particle response time τ_{stokes} (relaxation time) can be derived from Stokes' Law. It represents the time constant of the particle acceleration, if there is a velocity lag between the particle and the fluid (Raffel et al., 2007).

$$\tau_{\mathrm{stokes}} = \frac{\rho_{\mathrm{particle}}}{\rho_{\mathrm{a}}} \frac{d^2_{\mathrm{particle}}}{18\,\nu_{\mathrm{a}}}. \tag{3.2}$$

In order that the particles can follow the flow and act as a tracer, τ_{particle} has to be significant smaller than the typical time scale of the flow structures. For turbulent flow, these time scales can be described by the Kolmogorov microscala (Kundu et al., 2012, p. 568):

$$\tau_{\mathrm{kolmogorov}} = \frac{l_{\mathrm{kolmogorov}}}{u_{\mathrm{kolmogorov}}} = \sqrt{\frac{\nu_{\mathrm{a}}}{\epsilon_{\mathrm{turb}}}} \tag{3.3}$$

with the turbulent energy dissipation rate $\epsilon_{\mathrm{turb}} \approx \overline{u'w'}\partial u/\partial z$.

In order to get the dimension of the maximum turbulent energy dissipation rate in the air flow near the water surface we consider shear flow at a rigid wall. Using the logarithmic law of the wall (section 2.3.1), in the transition region from viscous to turbulent layer ($z^+ = z\,\nu/u_* \approx 12$) the largest values of ϵ_{turb} are present:

$$\epsilon_{\mathrm{turb}} = \overline{u'w'}\frac{\partial u}{\partial z} = u_*^2\,\frac{u_*}{\kappa z} = u_*^2\,\frac{u_*^2}{\kappa\,z^+\,\nu}, \tag{3.4}$$

which leads to a minimum Kolmogorov time scale of:

$$\tau_{\mathrm{kolmogorov}} \approx \sqrt{\frac{z^+\,\kappa\,\nu^2}{u_*^4}} = \sqrt{\kappa\,z^+}\,\frac{\nu}{u_*^2} \approx 2.2\frac{\nu}{u_*^2}. \tag{3.5}$$

In figure 3.1 the Stokes number $\mathrm{St} = \tau_{\mathrm{stokes}}/\tau_{\mathrm{kolmogorov}}$ dependent on the particle size d_{particle} is plotted for different values of the friction velocity. At $\mathrm{St} < 1$ the particles are resolving all the flow structures.

During all measurements performed in this study the friction velocities were below $1\,\mathrm{m/s}$ (see section 7.3) and the used particles are in the order of $1\,\mu\mathrm{m}$ (see section 4.3), thus St was about 0.1 in maximum.

Light scattering properties

Since the particles are tracked by a camera, they have to scatter (or emit in case of fluorescence particles) enough light to be visible. As described above, for air sided measurements the particles must have sizes in the order of μm, which is mostly much smaller than the camera resolution. This causes, that the brightness of a particle directly scales with their diameter squared. The larger the diameter, the larger the effective area and the brighter the particle.

The scattered light at spherical particles bigger than the wavelength of the light can be described by Mie's scattering theory. A detailed description of light scattering by small particles, which depends on the observation angle, gives van de Hulst (1981). Raffel et al. (2007) shows some polar distributions of the scattered light intensity, which can differ in the order of magnitudes for different angles, especially for small particles $< 1\,\mu$m. Bigger particles have more homogeneous scattering distributions, hence they are more suitable as seeding for particle imaging.

In general a compromise has to be found: The particles must be small enough to have suitable fluid mechanical properties and big enough to be visible.

3.2.2 Statistical PIV

Statistical PIV has become a standard measurement method in fluid dynamics. This extents to flow measurements close to the water surface, in water (e.g. Peirson, 1997; Siddiqui et al., 2001; Siddiqui and Loewen, 2010; Peirson et al., 2014), as well as in air (e.g. Reul et al., 1999,Troitskaya et al., 2011,Buckley and Veron, 2016).

The PIV-records are divided in small subareas (interrogation areas or interrogation windows) and for each the correlating subarea in the next illumination is tried to be found. The displacement vector quantifies the mean velocity of the fluid inside this small area, where many particles are considered leading to statistically fewer wrong correlations. Modern high speed cameras allow very high frame rates, by what even for high velocities two separate images can be correlated, which is done by applying the cross-corrletaion (see appendix A.4.5). By iterative multigrid methods outliers can be found (Scarano and Riethmuller, 1999; Westerweel and Scarano, 2005) and by assuming an isotropic two-dimensional Gauss peak function of the correlation function sub-pixel accuracy can be retrieved (Fincham and Spedding, 1997; Raffel et al., 2007; Kähler et al., 2012.

Kandaurov et al. (2014) details the modified PIV-method used for the measurements performed within in the scope of the experiments of this study. Transforming the images by the use of the detected water elevation enables measurements closer to the water surface.

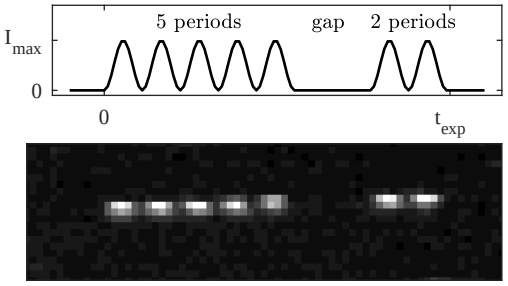

Figure 3.2: Top: illumination signal for PSV consisting of a harmonic, where the 6^{th} and the 7^{th} period are set to zero. **Bottom:** Example of a streak image, representing a particle illuminated by the upper signal and moving from left to right during the exposure time, which is fitted to the illumination signal.

3.2.3 Particle streak velocimetry (PSV)

While standard statistical PIV needs very high sampling rates, PSV makes the approach of extracting all the information out of one single image. Already about thirty years ago a large number of ideas appeared, how this could be realized (Adrian, 1991). The basic idea is to extract the movement of a particle during one exposure of the camera from the light trace seen in the image, which was already realized thirty years ago (Hesselink, 1988) for water flows. Using a constant illumination for example, the streak length is directly connected to the particles velocity. For multiple single illumination pulses single dots appear, whose distances are analysed. For all these methods low seeding densities are needed, because the single streaks have to be separated.

PTV and PSV have been applied in many studies investigating the flow close the air-water interface. Hering et al. (1997) and Hering et al. (1998) for example applied a combined method at the water side, where even at relatively high seeding densities Lagrangian flow fields were obtained. The problem of corresponding was solved by extracting the orientation from the streaks (caused by long exposure times) and by using this information for the tracking algorithm.

At the air side, where velocities are much higher, Eger (2012) made PSV measurements in a small wind-wave facility. Here the streak length was determined directly by innovative image processing, leading to velocity measurements very close to water surface.

If the illumination is modulated in time, the particles seen by a camera generate streaks, which are also modulated in brightness. This can be used to achieve more precise measurements. Voss et al. (2012) for example used a harmonic intensity function for PSV-measurements in water, whereby the Hilbert transform (A.4.3) leaded to position dependent velocities along the streak.

in this study as illumination function a harmonic (shifted cosine) was used. The illumination signal and an example of a resulting modulated streak image are shown in figure 3.3. The signal consists of nine periods of a shifted negative cosine, where the illumination was set to zero during the 6^{th} and the 7^{th} period, denoted as the gap in figure 3.3. Thereby it could be made use of the advantages of the periodicity, like frequency analysis by Fourier decomposition, without losing the information of the flow direction. The streak image at the bottom in figure 3.3 represents the light trace

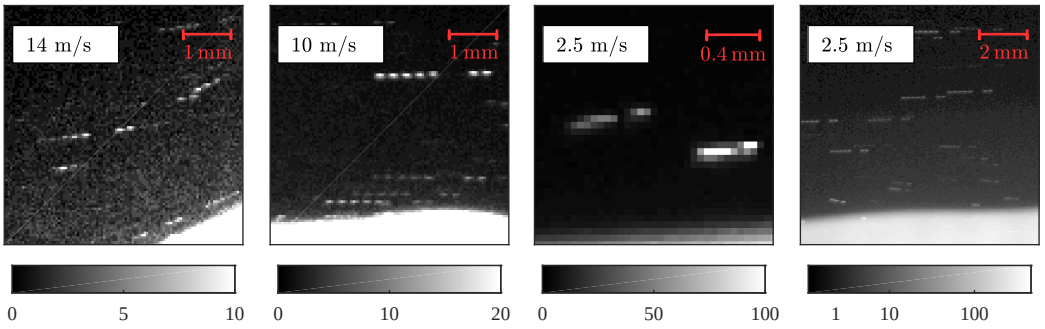

Figure 3.3: Extracts of example images of PSV recorded at different wind speeds during the experiments in Marseille 2016. High velocities lead to less bright streaks. This was compensated by larger gain levels of the cameras, whereby also the noise level increased. Especially at 14 m/s wind speed no measurements were able. At wind speeds ≤ 12 m/s the methods worked properly, even very close to the water surface, which is represented by the white space. At short streaks (third image) the fine structure of the harmonic is not resolved anymore, but the gap provides still structure leading to good measurements.

of a particle moving from left to right during the exposure time, which was fitted to the illumination signal. The frequency of the harmonic (PSV-frequency) and thereby the length of such an illumination signal was chosen dependently on the wind velocity, ranging from 6 kHz (1.5 ms) to 26 kHz (0.35 ms).

Figure 3.3 shows some examples of images recorded during the experiments in Marseille 2016 (see chapter 4). The white spaces are the water surface, where a fluorescent dye was added in order to enable the detection of the water surface (see section 3.3.3). The different images are recorded at different wind speeds, where different gain levels of the cameras where used. The faster the particles, the shorter the time a particle crosses over a pixel and the less bright the streak. This was compensated by increasing the cameras' amplification (gain), which leads to higher noise level. Especially, at 14 m/s wind speed the signal to noise ratio was so low, that no robust measurements where possible. At lower wind speeds with better SNRs the particle streaks are clearly visible and the evaluation worked properly.

The PSV-frequency was chosen in a way, that the free stream velocity could be resolved, being the case, if the streak length at the images is smaller than the FOV. Close to the surface the wind speed decreases, leading to very short streaks (compare the third image in figure 3.3). Here another strength of the chosen illumination signal becomes relevant. Due to the illumination gap, the streaks' intensity is still structured, even if the PSV-frequency itself cannot be resolved (compare the sampling theorem in the appendix A.4.1). Thereby even these short streaks yield good measurements. A detailed description of the evaluation method is given in section 5.1.

3.3 Measuring waves

During the experiments in sum three methods for measuring wave properties were used. While the laser slope gauge and the wave wires were operated by Guillemette Caulliez and are only playing a minor part in this study, the height measurements by laser induced fluorescence (LIF) provided all the wave data necessary for the investigation of the air flow. In the following these three techniques are briefly introduced.

3.3.1 Laser slope gauge

If light passes the interface between water and air, dependent on the angle of incidence refraction occurs, which is used to determine the inclination of the water surface. A vertical laser beam coming from above is diverted by passing the water surface and ends on an instrument, existing of a diffusion screen and a position sensing diode. By the use of special big lenses (frensel lens) an optical telecentric setup can be realized, where the total wave elevation does not influence the measurement (e.g. Lange et al., 1982).

During the experiments the laboratory-made slope measuring system based on this method was used, which has been calibrated carefully. More details on the instrument is given by Caulliez and Guérin (2012).

3.3.2 Wave wires

Wave wires represent a standard method for determining time series of the wave elevation at a single point, in wind-wave facilities as well as at the open ocean. The capacity of a wire, which is partly immersed to water, changes according to the water height. By special electronic circuits this capacity can be measured in time and with accurate calibrations a measurement of the water elevation is realized. The wave wires used during the experiments were the same, as in other studies at the large IRPHE-Luminy wind wave facility in Marseille, see Caulliez et al. (2008) and Caulliez (2013).

3.3.3 Height measurements by LIF

While wave wires measure the surface elevation only at one point, methods using LIF can provide measurements along an extended line. The principle of the technique is simple: a fluorescent dye is added to the transparent water, which absorbs the laser light and directly emits light of lower energy. By spreading the laser beam to a sheet the water shines along a line, which is observed by a camera. By image processing and careful calibration the water elevation along this line can be determined.

During the last decades this method became standard for wind-wave experiments (Caulliez, 2013; Schwarz, 2016; Buckley and Veron, 2017). The setup used in this study is described in detail in section 4.2 and the evaluation process is briefly explained in section 5.3.

4 Setup, calibration and experiments

In this chapter the experiments and their realizations are outlined. After a short description of the wind-wave facility (section 4.1), where all experiments were performed, the optical measurement setup is shown in section 4.2. The new method of seeding generation is described in 4.3. For high spacial accuracy of the measurements the cameras have been calibrated, which is treated in section 4.4. The last section 4.5 gives some information on the experiments itself and their conditions.

4.1 Marseille wind-wave-tank

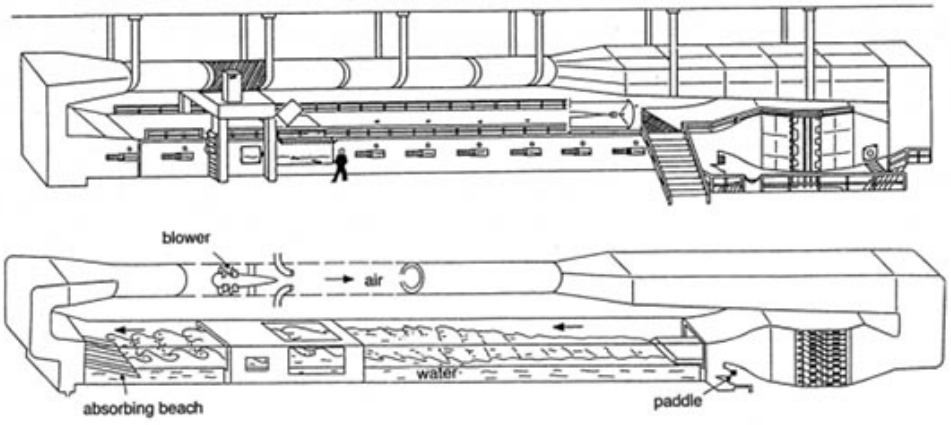

Figure 4.1: Sketch of the large IRPHE-Luminy wind wave facility in Marseille, France. Wind is blown over a 40 m long water tank. The special design provides clean aerodynamical flow and a constant flux air boundary layer forms above the water surface (Giovanangeli et al., 2006).

All measurements included in this study took place at the large IRPHE-Luminy wind wave facility in Marseille, France. In a closed surrounding wind is blown over a water tank, which causes the generation of waves travelling in wind direction along the facility. In such laboratory conditions the physical processes at the interface between water and air can be investigated, which strongly depend on the connection between wind and waves.

Figure 4.1 shows a sketch of the laboratory and the large linear wind-wave facility. The water tank is 40 m long, 2.6 m wide and has an averaged depth of 0.9 m. Below the inlet of the airflow a submerged mechanical wave generator is installed. It is made of oscillating plates controlled by an electrohydaulic motor. The frequency and amplitude can be controlled independently and many different wave regimes can be achieved in the tank. At the end of the facility a tilted perforated metal plate (wave absorber) forces

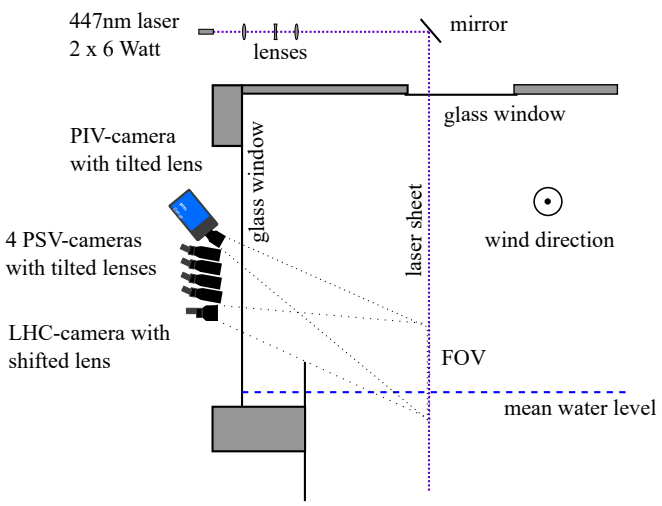

Figure 4.2: Sketch of the optical setup. In sum 6 cameras (1 PIV-camera, 4 PSV-cameras and 1 LHC-camera) were placed outside the facility and looked through a glass window. Their field of view is aligned with a vertical laser sheet, which is realized by 2×6 Watt laser diodes, three lenses (two spherical and one cylindrical) and a mirror.

wave breaking and thereby prevents wave reflections. More detailed information on the geometry is given by Caulliez et al. (2008) and Caulliez (2013).

The wind blowing in the tunnel of 1.5 m height above the water channel is generated by an axial fan placed in the air recirculation duct, which is positioned above. The geometry is specially designed to achieve low-turbulence homogeneous flow at the entrance of the wind-wave part and a constant flux air boundary layer can be reached. Wind speeds in the center of the facility as high as 14 m/s can be reached.

At a fetch of approximately 28 m, two large high quality glass windows, one on each side, enable the optical access for measurements. Additionally for this study a small glass window has been installed in the ceiling.

As supported measurements capacitive wave probes and a single-point laser slope gauge were operated close to the optical measurement region.[2]

4.2 Optical setup

The optical measurements of wave elevation and air flow have been placed at one of the big glass windows at a fetch of approximately 28 m. Figure 4.2 shows a sketch of the setup, where six cameras and a blue laser sheet were in use.

This laser sheet has been created by two 447 nm 6 Watt laser diodes close together, which were focused, widened and aligned by three lenses (two spherical and one cylindrical) and a mirror to a horizontal line along-wind direction with ≈ 20 mm length and ≈ 2 mm in thickness. By a self designed current source the laser intensity could be controlled with a reaction time of $\approx 1\ \mu$s. Thereby the high speed periodic intensity modulation needed for the new PSV-method could be realized.

The PSV-measurements were made using four Basler acA1920-155um cameras

[2]These measurements have been operated by Guillemette Caulliez.

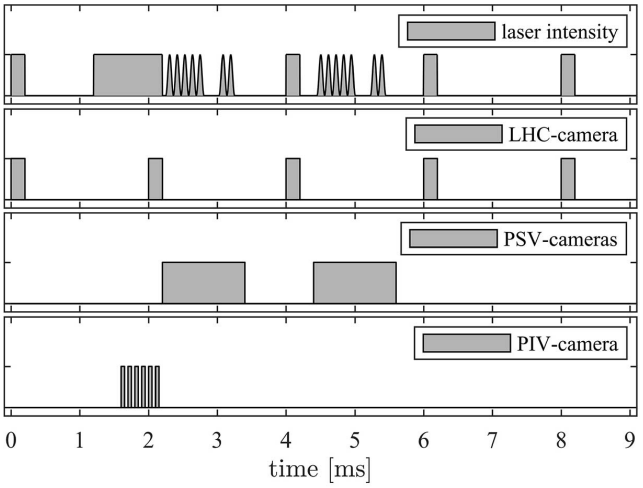

Figure 4.3: Schematic view of the trigger timings for all cameras and lasers. The laser intensity was synchronized to the LHC-camera (500 Hz), the PSV-cameras (two images every 20 ms) and the PIV camera (6 images at $5 - 20$ kHz every 20 ms). During the exposure of PSV the laser was modulated by a cosine including a gap. Only the first 9 ms are shown. The pattern repeats every 20 ms.

(155 fps at 1920×1200 pixels, 5.86 m pixel size) by mounting them on top of each other. Four Nikon 135 mm 1:2.8 lenses result in individual field of views (FOV) around 9 cm in height with ≈ 50 μm/pixel in resolution . The cameras are mounted such that their individual FOVs overlap slightly, so that the overall field of view around 36 cm high and 6 cm width. The horizontal width of FOV was adapted to the width of the laser sheets. By use of adapters, Scheimpflug-optics (Scheimpflug, 1906) was applied. Due to tilting the lens relative to the camera sensor, the focal plane also tilts. Thereby the cameras could be mounted looking downward at an angle around $20°$ without loosing focus at the edges despite of an open aperture.

For standard-PIV measurements, which were made by Alexander Kandaurov, the pco.Dimax high speed camera (1279 fps at full resolution with 2016×2016 pixels, 11 μm pixel size) have been used with a 105 mm 1:2.0 Nikon lens – also in Scheimpflug configuration. A FOV of around 30 cm with a resulting scale of ≈ 150 μm/pixel was achieved. By reducing the horizontal component of the FOV to 1.3 cm, frame rates up to 20 kHz were possible and very high velocities could be measured.

The images for detecting the water surface using laser induced fluorescence (LIF) were recorded by an additional Basler acA1920-155um camera, reffered to in the following as laser height camera (LHC). Here the lens (35 mm 1:1.8 Minolta) was shifted against the center of the sensor, whereby the field of view also shifted. In this way a FOV from lowest trough to highest crest of the waves could be achieved, also without loosing focus despite of an open aperture. The resulting LHC-resolution was 183 μm/pixel and by adapting the FOV to the width of the laser sheet (2 cm) frame rates of 500 Hz could be achieved. The fluorescent dye pyranine was added to the water, which absorbs blue and emits green light (emission and absorption spectra are given by Kräuter, 2015). In order to prevent direct reflections of the laser light into the camera due to wave breaking or floating bubbles, which can affect the detection of the water surface, a green band pass filter was mounted in front of the LHC-camera.

The use of different cameras and especially, the new PSV-technique made it necessary

to trigger and thereby synchronize all cameras and the laser. Figure 4.3 demonstrates the triggering system, which was realized by a micro-controller (Arduino Uno) and a function generator. The uppermost plot shows a time series of the laser signal, below the exposure times of the several cameras are shown, respectively. The LHC-camera was operating continuously at $500\,\mathrm{Hz}$ with an exposure time of $\approx 0.2\,\mathrm{ms}$, where the laser was switched on at full power. PSV and PIV were operated with a base frequency of $50\,\mathrm{Hz}$, so the signals shown in figure 4.3 repeated every $20\,\mathrm{ms}$ – here only the first $9\,\mathrm{ms}$ of such a sequence are shown. The exposures of the PSV-cameras were synchronized to the PSV-laser-signal, which consists of a harmonic nine periods long, where the sixth and seventh period are switched off (see section 3.2.3). In each $20\,\mathrm{ms}$ ling sequence two PSV-images were recorded as close together as possible. The purpose was to track the individual particles and try to find them in next image. But it turned out, that most of the particles left the laser sheet or were too fast, so this method was not further pursued. The PIV-camera took six images at a very high frame rate ($5 - 20\,\mathrm{kHz}$) every $20\,\mathrm{ms}$ ($50\,\mathrm{Hz}$).

4.3 Seeding generation

PIV as well as PSV needs particles suspended in air, which are small enough to follow the flow and big enough, that they scatter enough light to be visible for the cameras. In this study a new method of seeding generation has been developed, where the advantage of a chemical acid-base reaction was taken. Ammonia (base) and hydrochloric acid have the reaction product ammonium chloride, which is a neutral salt (Binnewies et al., 2016). If this reaction takes place in gaseous state, very small particles of ammonium chloride condense, because the salt cannot stay in the gaseous state.

$$\mathrm{NH_{3\ (gas)}} + \mathrm{HCl_{(gas)}} \longrightarrow \mathrm{NH_4Cl_{(solid)}} \tag{4.1}$$

It turned out that those small particles have excellent properties for particle imaging velocimetry. They are very small, have nearly spherical geometry and reflect light in all directions. Figure 4.4 shows an image of sedimented particles taken by an electron-microscope[3], which quantifies the particle size to the order of $1\,\mu\mathrm{m}$. It seems some of them are connected, but it is unclear if this represents their state in air. Independently, they have very good seeding properties, because of their very small size (see section 3.2.1).

During the experiments the generation took place in a setup, which consists of two wash bottles and a 1 liter plastic bottle (see the sketch in figure 4.5). Clean air is flushed through the wash bottles filled with high concentrated solutions of $\mathrm{NH_3}$ and HCl, respectively, where it is saturated. By two thin tubes this saturated air is led to the plastic bottle (mixing bottle), where the reaction takes place. Inside the bottle low

[3]This record was made with the support from Nikon.

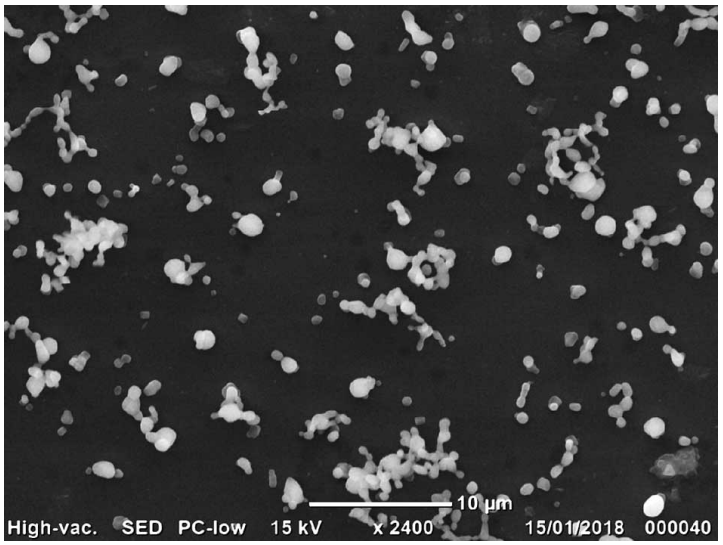

Figure 4.4: Image by an electron-microscope showing ammonium chloride particles settled down on a plate. Their size is of the order of $1\,\mu$m and their geometry is close to spheres. Some of them seem to be connected, but it is not clear, if this phenomenon only occurs due to sedimentation, or whether they are also connected while they are floating in air.

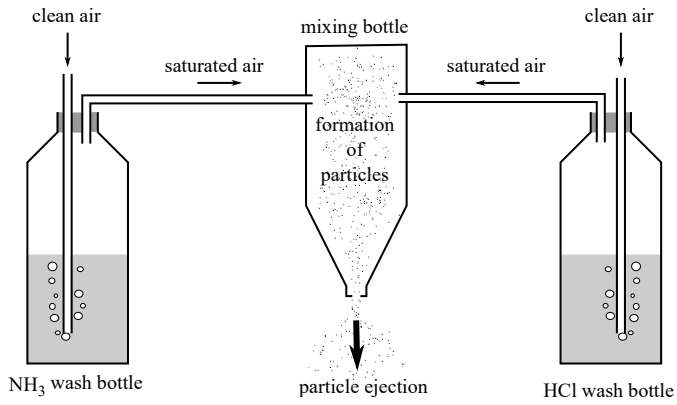

Figure 4.5: Sketch of the setup for particle generation. Clean air is flushed through two wash bottles, where it saturates with NH_3 and HCl, respectively. In a plastic bottle the reaction takes place, the particles form and are then ejected to the facility.

turbulent flow conditions are present, which seems to provide more a homogenous size distribution. The air flowing out is now saturated with many small particles. By controlling the incoming air flux rates the reaction is optimized. The saturation pressure of ammonia is 14 times higher than for chloride acid, so the air flux of HCl has to be 14 times higher.

The plastic bottle was positioned downwind of the measurement section inside the facility, whereby an homogeneous particle density could be achieved. The particles had to pass the full recirculation flume and arrived perfectly distributed at the laser sheet. By controlling the total incoming air flux the particle density could be controlled.

4.4 Calibration

As different cameras have been used a careful calibration was necessary, which maps the image coordinates to the real world. One big advantage is that all detected structures,

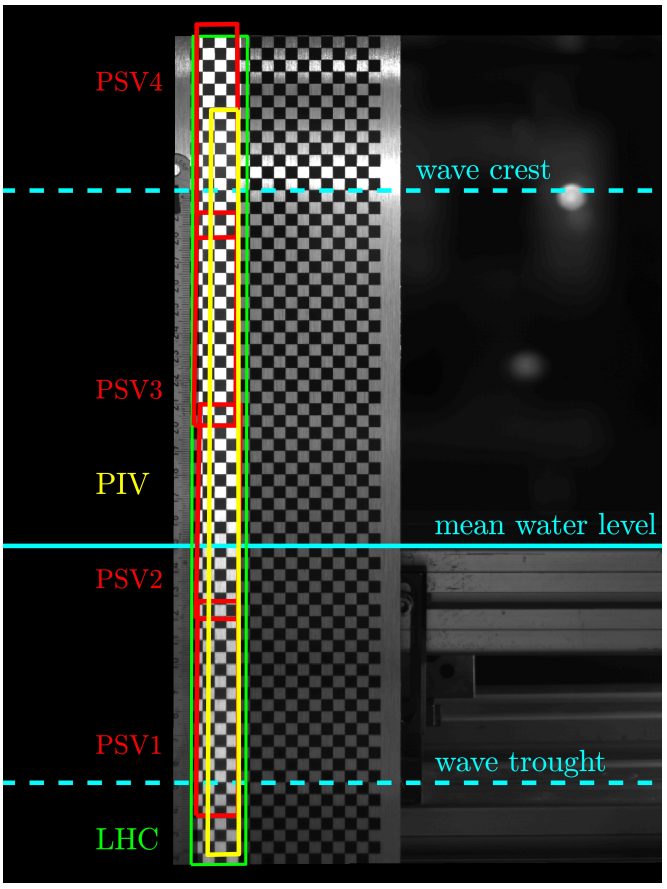

Figure 4.6: Image of the used calibration target. A checkerboard pattern (5 mm square size) was printed on an aluminum covered plate (aludibond). As indicator of the absolute position a metal ruler was glued to the left boarder. The FOV of the different cameras are shown by colored rectangles (LHC in green, PSV in red and PIV in yellow). Additionally, the mean water surface as well as the extrema of the water elevation are drawn by blue lines. The calibration target was aligned as good as possible with the laser sheet, which corresponds to the brighter region at the left side of the target.

the wave height as well as the particle streaks, are located in a thin plane defined by the laser sheet. Therefore 2D-mapping is sufficient and there is no need of 3D techniques like triangulation (for more information on 3D vision see Song, 2013).

The calibration target used during the experiments is shown in figure 4.6. A checkerboard pattern with 5 mm squares was printed on a plate covered by aluminum (aludibond). The image shown in figure 4.6 was recorded by the LHC-camera by reading out the full sensor. Despite looking slightly downwards, there is nearly no distortion visible, which was achieved by shifting the lens relative to the sensor as mentioned above. For PSV- and PIV-records this is not the case due to Scheimpflug optics (tilting the lens). Here the width of FOV slightly changes with height. The several FOV are shown in different colors (LHC in green, PSV in red and PIV in yellow) in figure 4.6. Additionally the mean water level as well as the extrema of the water elevation observed during all experiments is drawn in blue. The slightly brighter region shows the position of the laser sheet, which was aligned as good as possible with the calibration target.

To map the image plane (X, Y) to the object plane in real world coordinates (x, z) (x is in wind direction and z points vertical upward) the following mapping function

was used (Raffel et al., 2007):

$$x = \frac{a_{11}X + a_{12}Y + a_{13} + a_{14}X^2 + a_{15}Y^2 + a_{16}XY}{a_{31}X + a_{32}Y + a_{33} + a_{34}X^2 + a_{35}Y^2 + a_{36}XY} \tag{4.2}$$

$$z = \frac{a_{21}X + a_{22}Y + a_{23} + a_{24}X^2 + a_{25}Y^2 + a_{26}XY}{a_{31}X + a_{32}Y + a_{33} + a_{34}X^2 + a_{35}Y^2 + a_{36}YX} \tag{4.3}$$

$$a_{33} = 1.$$

While the linear parts fully account for the perspective projection (the mapping preserves the straightness of lines), the nonlinear parts also correct geometric distortions due to imperfect lenses. Thereby $6 \times 3 - 1 = 17$ parameters ($a_{11}...a_{36}$) fully describe the mapping and since they are known the position of each pixel can be mapped to the real world.

The corner points of all squares seen by a camera have been used to derive all 17 parameters using a Levenberg-Marquard method, which is more robust for this application than a linear least squares method (Raffel et al., 2007). By this mapping function the real positions at the checkerboard could be reprojected with errors in order of 10% of the resolution (PSV: $\approx 50\,\mu$m/pixel, LHC: $\approx 183\,\mu$m/pixel, PIV: $\approx 150\,\mu$m/pixel).

4.5 Experiments

All experiments treated in this study took place in June 2016 within the framework of the european ASIST-project[4], which focuses on the interaction processes at the wind driven water surface. Besides the measurements presented in this work also other techniques were employed simultaneously. Transfer rates of heat were measured by active thermography (Kunz, 2017; Kunz and Jähne, 2018) and transfer velocities of mass were measured by use of a mass spectrometer – a large set of species of gases and volatile species have been used with different solubilities. Gas transfer velocities were measured with the method described in Krall and Jähne (2014) and are not yet published. Additionally bubble size distributions were measured by Flothow (2017) at least for the high wind speed conditions.

A large number of single experiments was conducted with different wind speeds, different wave conditions (pure wind and mechanically generated waves) and fresh water as well as modeled salt water, where not all of them are included in this study. For example all experiments, where butanol was added to the water were excluded here. Butanol changes the bubble coalescence mechanisms such, that it behaves similar to salt water (modeled salt water), which is relevant for the transfer rates of water controlled

[4] Air-Sea Interaction under Stormy and Hurricane Conditions: Physical Models and Applications to Remote Sensing (ASIST), coorperation of University of Keele (UK), Université d'Aix Marseille (France), Ruprecht-Karls-Universität Heidelberg (Germany) and Institute of Applied Physics Nizhny Novgorod (Russia).

gases. For waves and thereby also for the airflow above no significant differences could be observed (see Schwarz, 2016).

#	u_{ref} [m/s]	f_{paddle} [Hz]	f_{p} [Hz]	a_{rms} [cm]	mss [%]
1	14	–	1.45	2.45	9.20
4	14	0.9	n.a.	n.a.	n.a.
5	14	1.3	n.a.	n.a.	n.a.
7	12	–	1.54	2.03	8.14
8	12	0.9	n.a.	n.a.	n.a.
9	10	–	1.69	1.61	6.54
10	10	0.9	n.a.	n.a.	n.a.
11	10	1.3	n.a.	n.a.	n.a.
13	8	–	1.80	1.09	4.51
14	8	0.9	n.a.	n.a.	n.a.
15	6	–	1.95	0.80	2.95
17	6	0.9	n.a.	n.a.	n.a.
18	6	1.3	n.a.	n.a.	n.a.
20	5	–	2.13	0.62	2.21
21	4	–	2.40	0.44	1.77
22	3	–	3.09	0.26	1.41
23	2.5	–	3.64	0.18	1.12

Table 4.1: Overview of experimental conditions included in this study. The conditions are numbered (#), missing numbers in the table are conditions not regarded in this study. The wind speed at the free stream reference position u_{ref} was measured by a pitot-tube. f_{paddle} is the frequency of the mechanical wave generator. The peak frequency f_{p} of the elevation spectrum and the root mean square wave height a_{rms} were measured by capacitive wave wires and the mean square slope mss (sum of both directions) was measured by a single point laser slope gauge. At some conditions no wave measurements are available up to now (n.a.).

Table 4.1 gives an overview of all conditions included in this study. Each single experiment was given an experiment-number (#), numbers missing in table 4.1 correspond to conditions not regarded here. The wind speed at the reference position (close to the air-sided free stream velocity in the flume, measured by a pitot-tube) ranges from 2.5 to 14 m/s and is shown in the second column. For some experiments the mechanical wave generator has been used, the paddle-frequency f_{paddle} is shown in the third column of table 4.1. The wave amplitude was chosen as high as possible. Thereby three wave regimes could be achieved: First there are pure wind waves, where the wave generator was switched off (denoted as –). Secondly, conditions with 0.9 Hz paddle frequency represent long waves, which were nearly two dimensional along the compete facility. Here the highest wave amplitude was found, but the wave form was still stable. By the 1.3 Hz paddle wave (short paddle wave) a regime could be achieved, where a lot of wave breaking of the dominant wave occurred along the fetch. The waves were not two

dimensional anymore and unstable.

Also given in table 4.1 are some of the measured wave properties, which were obtained by the capacitive wave wires and the single point laser slope gauge (see section 3.3.1). f_p is the peak frequency of the amplitude spectrum, a_rms is the root mean square wave height and mss is the mean square slope in sum of both directions.

All measurements have been performed after the wind was running for at least 30 minutes, so equilibrium conditions can be assumed.

In sum for nearly all conditions the wave elevation and the flow was measured for 30 minutes. With wave periods shorter than one second, thereby at least 1800 single waves were observed, which leads to representative statistics. During performing the measurements at 5 m/s problems occurred, which have been recognized later. So here only 4.5 minutes of measurements are available.

5 Data processing

For nearly all measurements performed in the context of this work imaging techniques have been used. The flow velocities have been measured with a new particle tracking method based on particle streak velocimetry. For this, a complete procedure of image and data processing has been developed. In this section all evaluation steps are described, starting from a raw image and ending in velocity vectors and the surface elevation in real world coordinates.

First, the particle streaks are detected in a raw image and their properties are extracted. This is done by an algorithm written in *Matlab*. For each particle streak, the position in the image, the direction and a wavelength is determined – all in pixel coordinates. This wavelength is coupled with the periodic illuminating laser signal and is proportional to the length of the streak. Additionally two parameters are outputted, whereby the goodness of the respective value could be valued. In order to proof the goodness of the algorithm, a big number of artificial streak images with different properties has been generated and the algorithm was tested. Through simulating different image qualities, an estimation of the measurement accuracy was possible. By using the camera calibration and the frequency of the illumination function, a velocity vector in real world coordinates can be determined.

5.1 PSV-algorithm

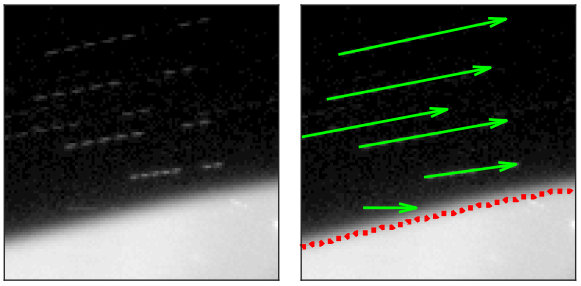

Figure 5.1: Result of the PSV-algorithm. From a recorded raw image (left) the surface (red) and the velocity vectors (green) are determined using image processing. Even dark streaks close to the water surface can be measured successfully.

On each recorded PSV-image the new developed PSV-algorithm has been applied. The procedure can be split into six steps. First some preprocessing is done separating the background from the streaks. Second the local orientation within the image is estimated by use of the structure tensor. Next all streaks are detected, composed if necessary and an 1D gray-value profile is extracted, giving the position $(X, Y)_{\mathrm{streak}}$ and direction ϕ_{streak} of each streak (step 3 and 4). In a fifth step, a first estimation of the streak wavelength $\lambda_{\mathrm{streak}}$ is performed through spectral analysis, which is used to improve the calculation time of the last step. Finally, the highest correlation of the gray-value

profile with modeled streak profiles is found, resulting in a good measure of the streak wavelength $\lambda_{\mathrm{streak}}$ and thereby the velocity. An illustration of the whole procedure is given in figures 5.2 to 5.5. An example of the results in form of the detected water surface and velocity vectors is shown in figure 5.1. All figures used for demonstration are measurements recorded during the measurements in Marseille (see chapter 4) at a reference wind speed of $8\,\mathrm{m/s}$ with pure wind waves. The algorithm works rather independently of the wind speed, merely the recording conditions like the frequency of the illumination function have to be adapted.

5.1.1 Step 1 - preprocessing

In order to generate the background image, first a median filter is applied to the raw image. The filter mask has to be large enough to disperse the streaks and small enough to maintain the surface, which has significantly higher gray values and a smooth boundary. Through the optical setup, the streaks could be depicted with very good resolution and sharpness yielding streak thicknesses not bigger than two pixels. Therefore a mask of $7 \times 7\,\mathrm{pixels}$ was sufficient. Next the initial image is compared with the obtained median image and all pixels with differences bigger than the noise level are replaced by the median. This background image is smoothed by binomial filtering and shows no discredited values, as is the case for the simple median image. A big advantage of using such a symmetric filter system is the conservation of the position of the water surface. Using minimum filters, as it is done in many other PIV-methods, would lead to a shift of the surface height and an exact extraction of the water height becomes difficult.

The surface extraction is done in two steps. First a simple threshold provides an estimation of the surface position, if present in the image. The smooth boundary, which originates mainly from the width of the laser sheet and the high camera resolution, allows further considerations. In a small region around this detected position, the maximum of the vertical gradient of the gray-values is found, which leads to a good measure of the surface height.

On the one hand, this water height is stored and considered during later analysis. On the other hand, it is a necessary information to generate meaningful particle images, where only streaks representing particles in the air are included. Structures arising from dirt in the water can be successfully excluded. In order to obtain these particle images, the initial images are subtracted by the background images and all gray-values below the detected water surface are set to zero.

5.1.2 Step 2 - direction field by structure tensor

Before detecting the streaks the direction is obtained. In this way it is possible to separate streaks with distances smaller than the gap between their two parts. For getting a direction field over a full image, the structural tensor (see appendix A.4.4) is applied on the slightly smoothed particle image. Before the angle of orientation is gained by

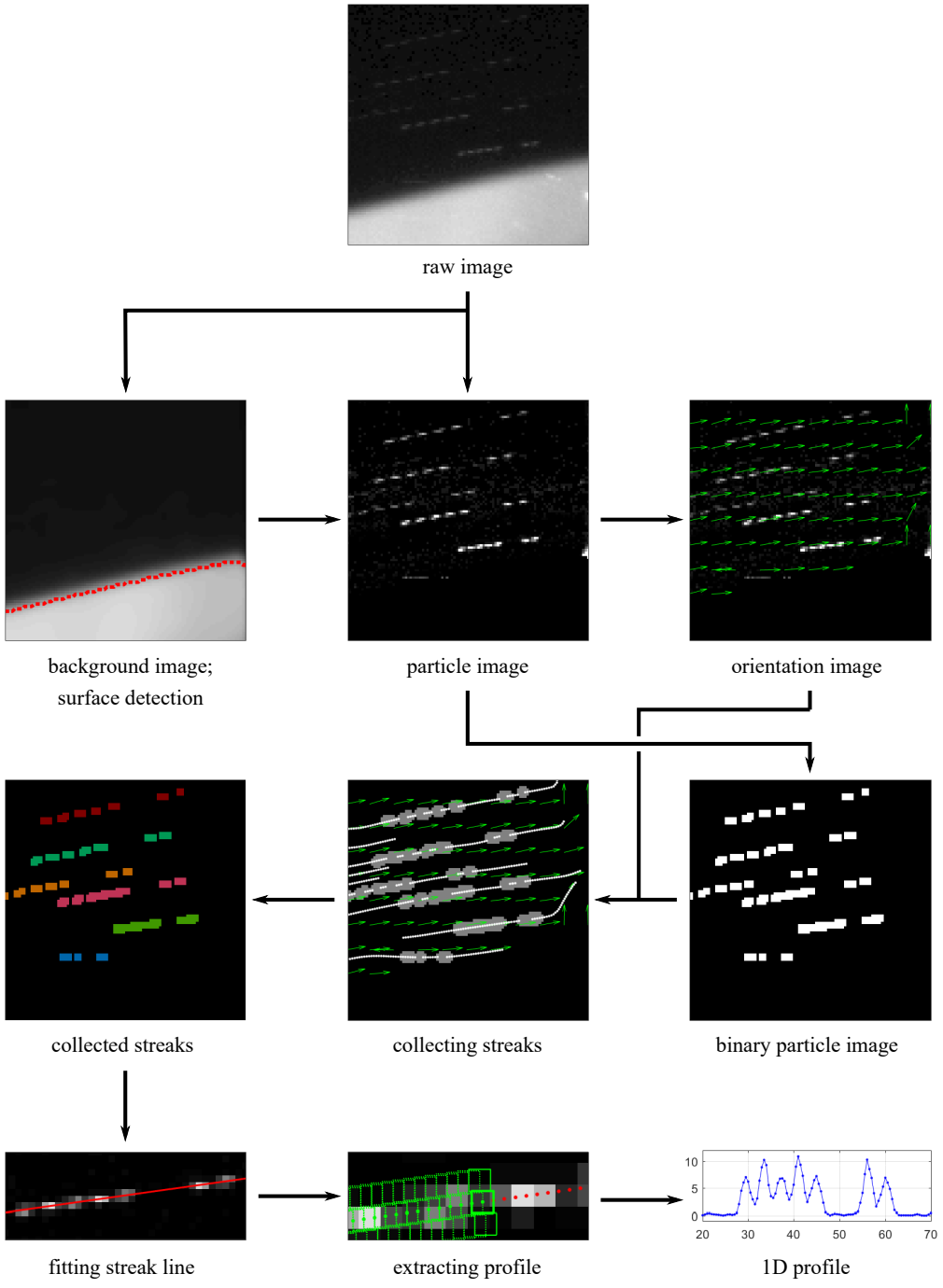

Figure 5.2: Illustration of the first four steps of the new developed PSV-algorithm. From the raw image a background image is derived by using a median filter, where the surface elevation (red dotted line) can be detected. Subtracting this background image from the raw image leads to a particle image, from which the orientation (green arrows) is gained with the structural tensor and the binary particle image is found by applying a simple threshold. Using the orientation, the single detections of one streak are collected and through a linear fit, a straight line (red line) describing the streak is obtained. Along this line the gray-values are extracted, respectively resulting in a 1D gray-value profile.

taking the inverse tangent, the entries of the structural tensor have to be smoothed significantly. For this, a Gaussian filter with a big mask and a rather small variance was used. This leads to meaningful orientations in the absence of the streaks and exact results in their immediate surrounding. An example of a direction field is shown by green arrows in the orientation image of figure 5.2.

5.1.3 Step 3 - detection and connection of particle streaks

Identifying the streak of one particle and extracting an intensity profile is one of the main tasks of the PSV-algorithm. The gap between the first five and the last two intensity maxima of a streak is a challenge for image processing, especially because the length of this gap could be bigger than the distance between two single streaks. Hence a simple threshold detection combined with a dilatation filter was proved to be unsuccessful. The single maxima are well detected, but split in individual objects. Long streaks result in seven short detections, at shorter streaks these detections can be connected leading to two or even one elongated detection. By use of the orientation gained from the structural tensor, these single objects could be assigned to the light trace of one particle.

First a single threshold detection is applied to the particle image. Due to the background correction, already pixels with values bigger than $\approx 3\,\mathrm{dn}$ ($g_i > 3$ applied on $8\,\mathrm{Bit}$ images) can be identified as streaks. As a result we obtain a binary particle image where all connected "true" pixels represent objects and are labelled. The example in figure 5.2 illustrates this step and the separation of one streak into single objects. While longer streaks in the top part of the image are generating seven detections, the shorter ones below yield fewer.

In order to identify all detections belonging to one streak, the orientation image is used. Starting at one single object all detections along a path according to the local orientation are collected. For this, steps with $0.5\,\mathrm{pixels}$ are made in the direction of the local orientation. Running in both directions – forward and backward – up to a certain length, all detections belonging to the light trace of one particle are collected. Therefore the binary particle image is dilated a bit. If a new detection is added, the path position is corrected by its mean position, whereby small errors of the direction field are corrected. The small image in figure 5.2 named "collecting streaks" shows this procedure. The small white connected dots are representing all steps along such a path, the dilated binary particle image is represented in in gray. In the lefthand image the resulting collected streaks are illustrated with different colors. Each equal colored areas belongs to the same streak. As long as the streaks in the dilated binary image are not touching each other, reasonable results are obtained.

5.1.4 Step 4 - extraction of gray-value profile

After all pixels belonging to a streak are identified, its direction and structure containing the velocity information has to be extracted. For this purpose, the 2D image of a streak

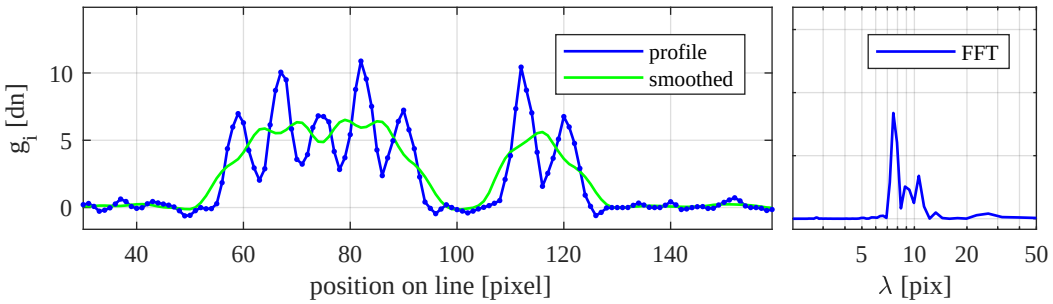

Figure 5.3: 1D gray-value profile and first estimation of the streak wave length by FFT (step 5). The blue line in the left plot represents the extracted gray-value profile along the streak. In green the strongly smoothed signal is depicted. The FFT is applied on the gray-value profile subtracted by the smoothed profile. The spectrum at the right has a significant maximum.

is converted to a 1D gray-value profile. Since this only contains the spatial extend and no longer the direction, the latter has to be an output of this conversion.

First a straight line is determined, which describes the particle path as good as possible. This is implemented by a linear fit of all pixels of the streak weighted with their gray values. Programmed as a matrix multiplication (Lang and Pucker, 2010), this is realized with very small computational costs. One output of this fit is the direction of the streak, whereas it is still unclear whether the particle is moving in positive or negative direction. Such a line is exemplary shown in figure 5.2 by a red line in the image at the lower left corner.

Next, along this line in steps of 0.5 pixels, the gray-values are extracted, respectively. As the image is discrete and the regarded positions are rarely positioned in a pixel's center, the extracted numbers are weighted means of the surrounding pixels. Therefore, a mask of one pixel size is moved along the straight line and accordingly to the overlapping area, the gray values are weighted and averaged. In order to count also streaks, which are slightly curved or are not that sharp, this extraction is also done with a mask with one pixel distance perpendicular to the line (fit) above and below. In figure 5.2 this extracting procedure is illustrated by green squares representing the masks. On the right the resulting 1D gray-value profile is plotted by the blue line. The x-axis corresponds to the position on the fitted line in pixels. From then, on all following considerations are only based on this gray-value profile.

5.1.5 Step 5 - first estimation by FFT

One advantage of the chosen illumination signal composed by two harmonics with five and two periods is the option to use frequency analysis. For this, the frequency spectrum of the gray-value profile is calculated using an FFT-algorithm. Its maximum then is a first estimation of the wave length $\lambda_{\mathrm{streak}}$.

Before the FFT is applied, the strongly smoothed profile is subtracted. Thereby no modes with big wave lengths are visible in the spectrum and the maximum leads to a

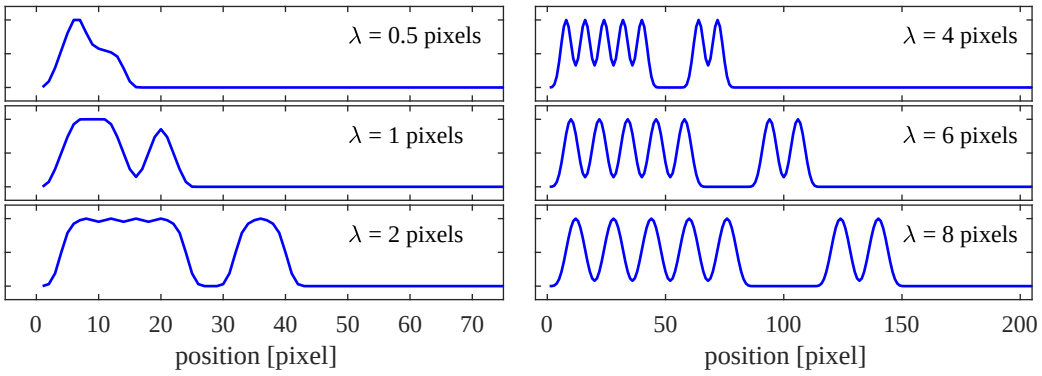

Figure 5.4: Model profiles with different wave lengths. The illumination signal has been projected onto a discrete array with 0.5 pixels in resolution. The stretching of the raw signal leads to signals with different wave lengths. The gained model streaks show the expected structures – smoothing of the harmonics for small wave lengths.

good measure for the wave length. The smoothing was designed in a manner, that it also works for the largest streaks appearing in a measurement. In figure 5.3 the profile, the smoothed profile and the spectrum is shown.

It has to be noted, that this method using spectral analysis has restrictions. If the streak is short and the amplitude of the harmonics shrinks due to the image resolution the procedure yields to wrong results. Thus, the estimated λ_{streak} is only used to optimize the next step. A further disadvantage is the fact, that there cannot be made a distinction of forward or backward movement from the spectrum.

5.1.6 Step 6 - fitting the streak profile

Beside the frequency analysis the knowledge of the illumination signal can be used to determine the wave length of the streak. Therefore model profiles with different wave lengths are generated and the correlation with the extracted profile is regarded. The highest correlation gives a precise measurement for the wave length and by using forward and backward models also the moving direction is detected.

The model profiles are generated by projecting the analytical illumination function (compare section 3.2.3) on discrete values. Thereby each value contains the integral over a length related to the sampling distance. This is in analogy by the light emitted by a moving particle, which is projected to the image sensor. Small shifts of the projected signal can cause aliasing effects yielding different outputs. This could be reduced by lightly smoothing the signal. This smoothing takes place during processing the extracted profiles, too. First due to non-idealized optical imaging and second due to extracting itself, which is done by a one pixel sized mask. A big number of such model profiles with wave lengths from 0 to 20 pixels with steps of 0.05 pixels was generated. In figure 5.5 some examples are plotted. While in all model profiles with big wave lengths the initial function is still present, at smaller wave lengths, high frequencies are more and

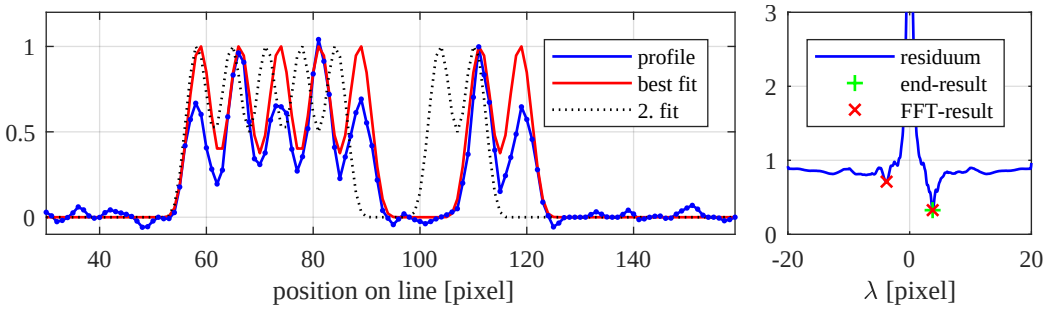

Figure 5.5: Results of fitting the model profile. **Left:** Extracted profile (blue) and best fitting model profile (red). With black dots the model profile with the second best residuum is shown. **Right:** The residuum (blue) obtained for each λ by the cross correlation gives the best fitting model profile by its minimum (green plus). The first estimation from step 5, which can be used to improve performance is plotted with red crosses.

more smoothed out. For $\lambda < 1$ even the gap starts disappearing.

For finding the best correlation of these model profiles g_{model} with the measured one g_{prof}, the cross correlation (see appendix A.4.5) is used. Previously, the extracted profile is normalized by the mean of the highest three values. For each model profile, the maximum of the correlation function is determined and the normalized residuum Θ is calculated:

$$\Theta_{\text{fit}} = \frac{\sum |g_{\text{model},i} - g_{\text{prof},i}|}{\sum g_{\text{model},i}}. \tag{5.1}$$

The minimum of this residuum gives the streak wave length λ_{streak} as a result. By using a three point Gaussian fit around the minimum, the resolution could be increased to sub pixel accuracy. In addition to the residuum of the best fit, also the residuum of the second best fit is outputted and saved. Therewith rules for sorting outliers can be adapted (see section 5.2). In figure 5.5, residuum and the resulting best fit is shown. The starting point of the streak $(X, Y)_{\text{streak}}$ also is outputted.

As mentioned before the fifth step gives a first estimation of λ_{streak}, which can be used to improve the calculation time. This is done by performing the cross correlation only with model profiles in a range around the estimation of the spectral analysis. This only works for big wave lengths, because smaller streaks yield to wrong estimations in step 5. Here the length of a streak, measured by the maximum distance of all detected pixels, is taken into account. Detailed information is given in section 5.2.

The end result of the PSV-algorithm is the detection of the surface and a value of the starting point $(X, Y)_{\text{streak}}$, the direction ϕ_{streak} and wave length λ_{streak} of each streak found in the image. From this, the velocity vector can be derived, which is shown in figure 5.1 in the beginning of this section.

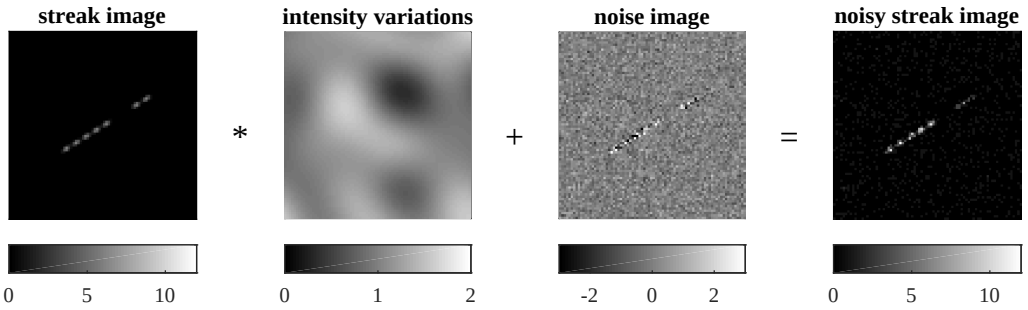

Figure 5.6: Scheme of generating a streak image in order to proof the algorithm. A homogeneous streak image is multiplied with random intensity variations to simulate inhomogeneities in brightness. Then a random white noise image with noise levels depending on the intensity of each pixel is added. Finally, the noisy streak image is converted to an 8 bit image and can be used to verify the algorithm.

5.2 Validation of the PSV-method

In order to proof the correct process of the PSV-algorithm and to get a measure for the accuracy of this technique a big number of model images has been generated. Artificial particle streaks were drawn onto black images and image noise has been added. All steps of the PSV-algorithm were performed on these artificial particle streak images and the output has been compared with the initial streak properties.

5.2.1 Generation of streak images

All streaks can be described by a starting point, a wavelength $\lambda_{\mathrm{streak}}$, an angle ϕ_{streak} and an intensity of brightness I_{streak}. With the objective to generate realistic streak images, a virtual particle is moved across a dark image and with respect to its position, the gray-values of neighboring pixels are increased. This is done reversely to extracting the gray-values along a streak, described in step 4 of the PSV-algorithm (section 5.1). The first image in figure 5.6 shows an example of such a generated streak image.

In fact, the brightness of a particle is not homogeneous along its path, which might be caused by leaving the laser sheet or inhomogeneities in illumination. To simulate this behavior, the streak image is multiplied by an image of low frequent random variations, which are produced by setting random values in the Fourier space and performing the inverse Fourier transform. These images have a mean value of one and the amplitude of the variations can be controlled by a parameter.See the second image in figure 5.6 for an example image.

Next to some large scale variations of the streak brightness, also image noise influences the algorithm. Because of very low light emission of the particles in many records the gray-values of the streaks are close to the background noise. This can cause problems in detecting and collecting the streaks from the binary images (see step 3 in section 5.1). Further noisy images reduce the quality of the extracted profiles, which af-

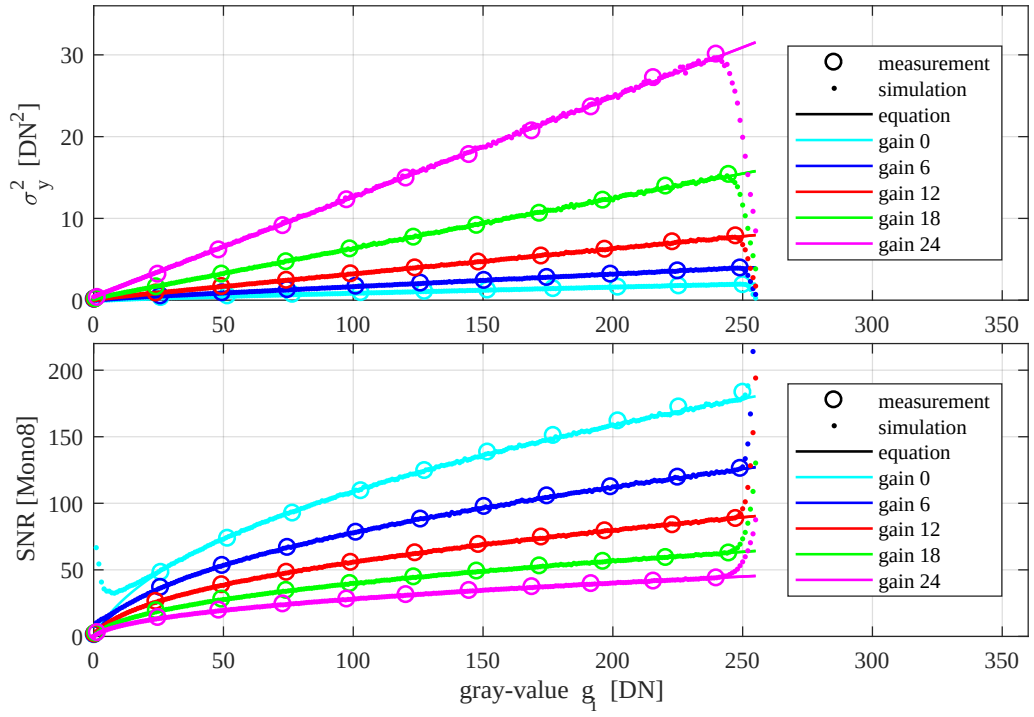

Figure 5.7: Measurements and simulation of camera noise of Basler, acA1920-155um at a wavelength of 466 nm transformed to 8 bit (Jähne and Herrmann, 2015a,b). For different gain levels, shown in different colors, the measurements are displayed as circles. The colored lines show the result for the linear variance by using the characterization shown in table 5.1. With small colored dots the results of modeled noisy images using equation 5.2 are plotted. The upper part shows the variance and the lower part shows the SNR for the full range of an 8 bit-signal.

fects fitting the profile. To simulate realistic images random noise with a linear variance (equation 5.2) was added. The variance of the dark signal $\sigma^2_{y.\mathrm{dark}}$ and the overall system gain K have been extracted from a specification of the used camera model according to the EMVA 1288 standard (EMVA, 2016). Table 5.1 shows the results for different camera intern gain settings, measured at a wavelength of 466 nm. Here, the camera was operated at a data transfer mode of 12 bit. Because all PSV-measurements performed within this work have been performed at 8 bit, all values for $\sigma^2_{y.\mathrm{dark}}$ have been adapted before generating the noise image, which is simply added to the streak image with low frequency variations. The gray value of each pixel of this noise image $g_{i,\mathrm{noise}}$ is set to the sum of a random number representing the noise of the dark signal plus the product of the square root of the gray-value of the streak image g_i and a random number r_{slope}:

$$g_{i,\mathrm{noise}} = r_{\mathrm{dark}} + \sqrt{g_i}\; r_{\mathrm{slope}}. \tag{5.2}$$

For generating r_{dark} and r_{slope}, a function was used, which produces random normal numbers with variances set to σ_d^2 and K, respectively. This method leads to noise representing the statistical fluctuations of a linear pixel, if σ_d^2 is small enough, which is

the case for the used camera. The quantization noise can be added simply by performing all steps in a floating number format and converting the image to 8 Bit in the end. Figure 5.7 shows the results of simulated noisy images, which are generated in this manner. They are plotted besides the results of a camera characterization (Jähne and Herrmann, 2015a,b) and show the good correlation.

Gain	$\sigma^2_{y.\mathrm{dark}}$	K
0 dB	$0.64\,\mathrm{DN}^2$	$0.120 \pm 0.3\,\%$
6 dB	$1.70\,\mathrm{DN}^2$	$0.247 \pm 0.1\,\%$
12 dB	$5.20\,\mathrm{DN}^2$	$0.493 \pm 0.1\,\%$
18 dB	$16.49\,\mathrm{DN}^2$	$0.981 \pm 0.1\,\%$
24 dB	$58.27\,\mathrm{DN}^2$	$1.959 \pm 0.1\,\%$

Table 5.1: Camera noise characterization of Basler, acA1920-155um at a wavelength of 466 nm (Jähne and Herrmann, 2015a,b). The values are measured with a data transfer mode of 12 bit.

For each noise level shown in table 5.1, a large number of model streak images like the example in figure 5.6 have been generated. This was done for the full spectrum of wavelengths $\lambda_{\mathrm{streak}}$, angles ϕ_{streak} and intensities of brightness I_{streak}, which results in a large data set for each noise setting. To simulate the effect of inhomogeneities in streak brightness, this was done for different amplitudes of large-scale variations from no variations to amplitudes up to 100 % of the mean.

5.2.2 Use of first estimation by FFT

In order to reduce the processing time, a first estimation of the streak wavelength λ_{fft} is used to localize the range for fitting the streak profile (compare step 5 and 6 of the PSV-algorithm in section 5.1). In the upper plot of figure 5.8, a histogram of the FFT-results shows how they are distributed in comparison to the initial streak wavelength $\lambda_{\mathrm{streak}}$. The data shown here is the result from random generated model streak images at a large noise level corresponding to gain 18 of the used camera (Basler, acA1920-155um). In this case, no large scale variations were used. The histogram shows a good coincidence for $\lambda_{\mathrm{streak}} > 4$. This can be easily explained by regarding the streak profile at short wavelengths, where the streak frequency becomes more and more invisible. The insufficient sampling smooths the signal and the FFT-result is dominated by the gap (see section 5.5).

The wrong FFT-results for short streak wavelengths require a decision rule, whether a result is trustable or not. Therefor the streak length of connected detections is used. In the lower part of figure 5.8, the mean streaklength is plotted for the different streak wavelengths. It shows, that for short wavelengths ($\lambda_{\mathrm{streak}} < 4$) the streak length is below approx. 40 pixels. The following decision rule is limiting the range of wavelengths for fitting λ_{fit}:

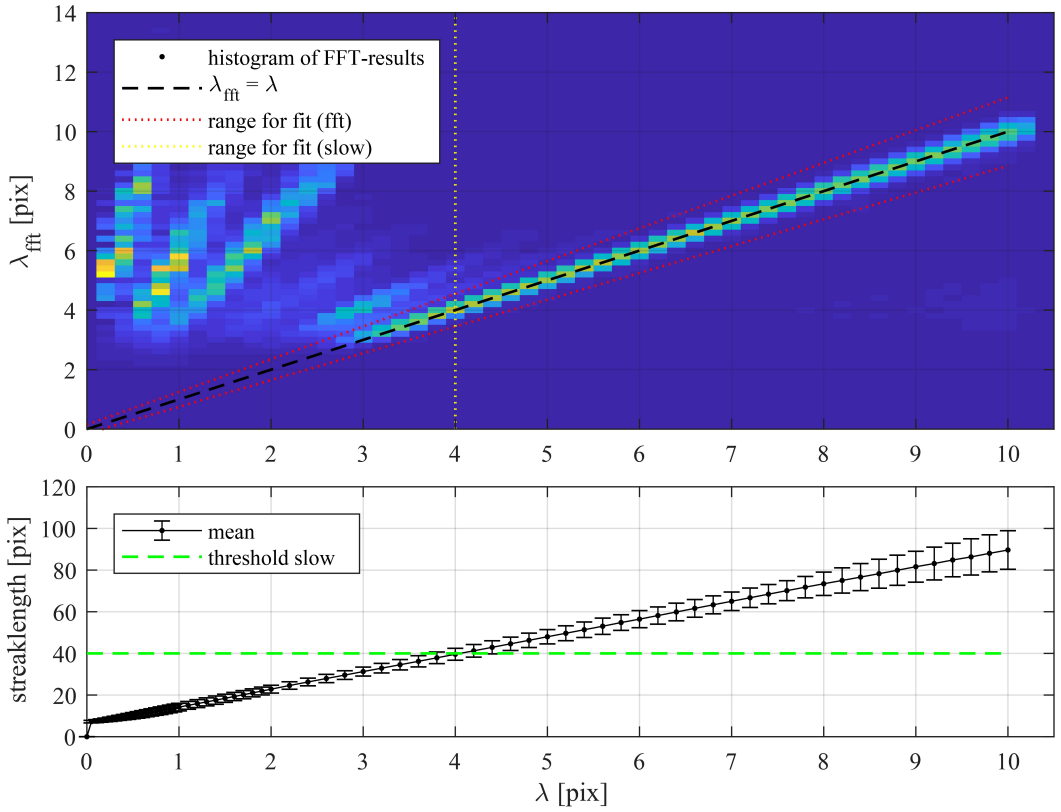

Figure 5.8: FFT-results for model streak images at different noise levels corresponding to gain 18. **Top:** Histogram of the wavelength estimated by FFT for different origin wavelengths. **Bottom:** Mean streak length of connected detections, which is used to define the decision rules. The green and yellow dashed lines illustrate the decision rules for trusting the result.

$$\text{streak length} \leq 40: \quad 0 < \lambda_{\text{fit}} < 4 \text{ and } 0.9\,\lambda_{\text{fft}} < \lambda_{\text{fit}} < 1.1\,\lambda_{\text{fft}} \tag{5.3}$$

$$\text{streak length} > 40: \quad 0.9\,\lambda_{\text{fft}} < \lambda_{\text{fit}} < 1.1\,\lambda_{\text{fft}} \tag{5.4}$$

The range around λ_{fft} is set to $\pm 10\%$, which is indicated by the red dashed lines in the histogramm (figure 5.8). By this rule, the computing time could be reduced significantly, because the fitting of the streaks is the most CPU-intensive step of the algorithm.

5.2.3 Goodness of fit

The PSV-algorithm gives the result for each detected streak: $\lambda_{\text{fit}}, \phi_{\text{fit}}$ and Θ_{fit}, which is the normalized difference between the extracted streak profile and the best fitting model streak profile (equation 5.1). In the following it will be analyzed how this parameter Θ_{fit} gives information about the goodness of the fit. Therefore the large data set of modeled

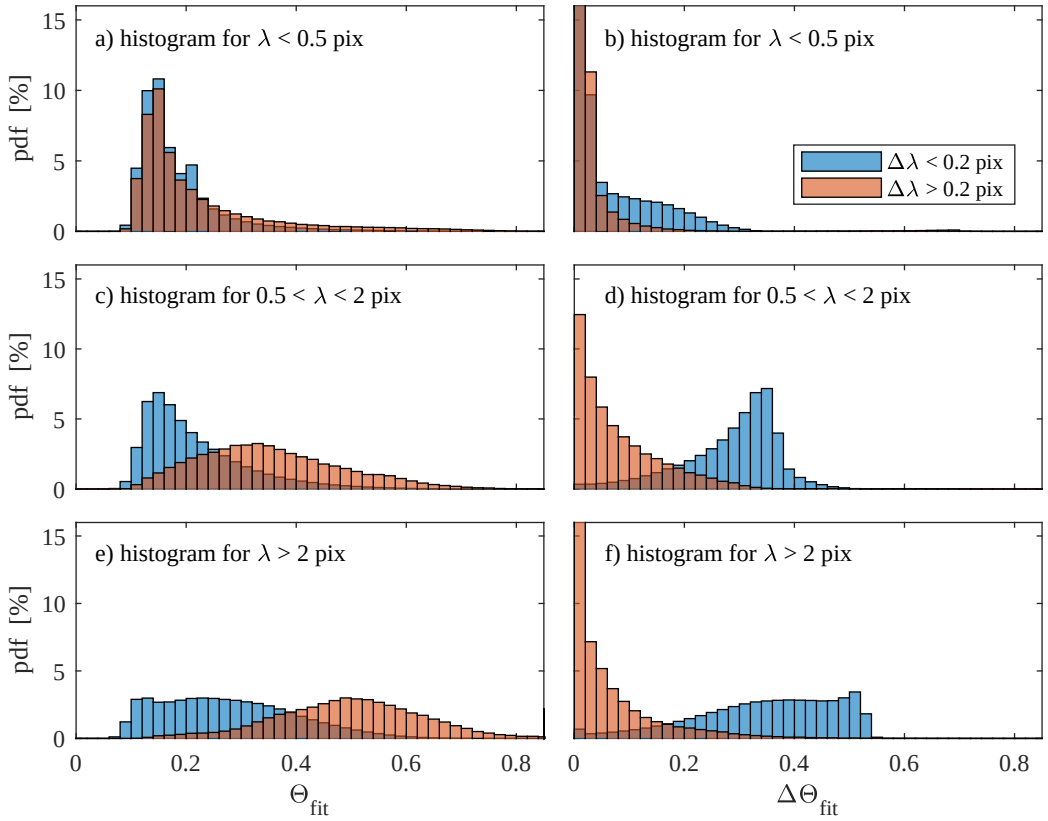

Figure 5.9: Comparison of Θ_{fit} between matches and mismatches for different streak regimes. The data shows histograms for the normalized difference between the extracted streak profile and the best fitting model streak profile for a data set of modeled streaks generated with a noise level corresponding to gain 18 with large intensity variations. While for short streaks with $\lambda_{\mathrm{streak}} \leq 1/2\,\mathrm{pix}$ no significant difference between matches and mismatches can be identified, for larger streaks the distribution of Θ_{fit} splits. Mismatches show much bigger values and can be identified by this.

streaks generated with different noise levels and large intensity variations is considered. While the major part of the fitted streaks show good results with $\lambda_{\mathrm{fit}} \approx \lambda_{\mathrm{streak}}$, there are some outliers completely mismatching. In the following a result is regarded as a mismatch if the deviation exceeds $0.2\,\mathrm{pixels}$.

Due to sampling, the streak profiles can be categorized into three classes. If $\lambda_{\mathrm{streak}}$ exceeds two pixels, all structure of the streak is visible and the profile is comparable with the light signal (compare sampling theorem, appendix A.4.1). With a wavelength of the streak bigger than half a pixel and smaller than two pixels the streak frequency blurs, but the gap still remains. Only if $\lambda_{\mathrm{streak}} \leq 1/2\,\mathrm{pixel}$ holds, no structure remains. These limits splitting the three classes are not strict and the image quality has a big influence. In case of image blurring the values require raising.

Next to the normalized difference of the best fitting model streak Θ_{fit}, the second best fitting model streak is outputted, too. For most of the streak detections, this second

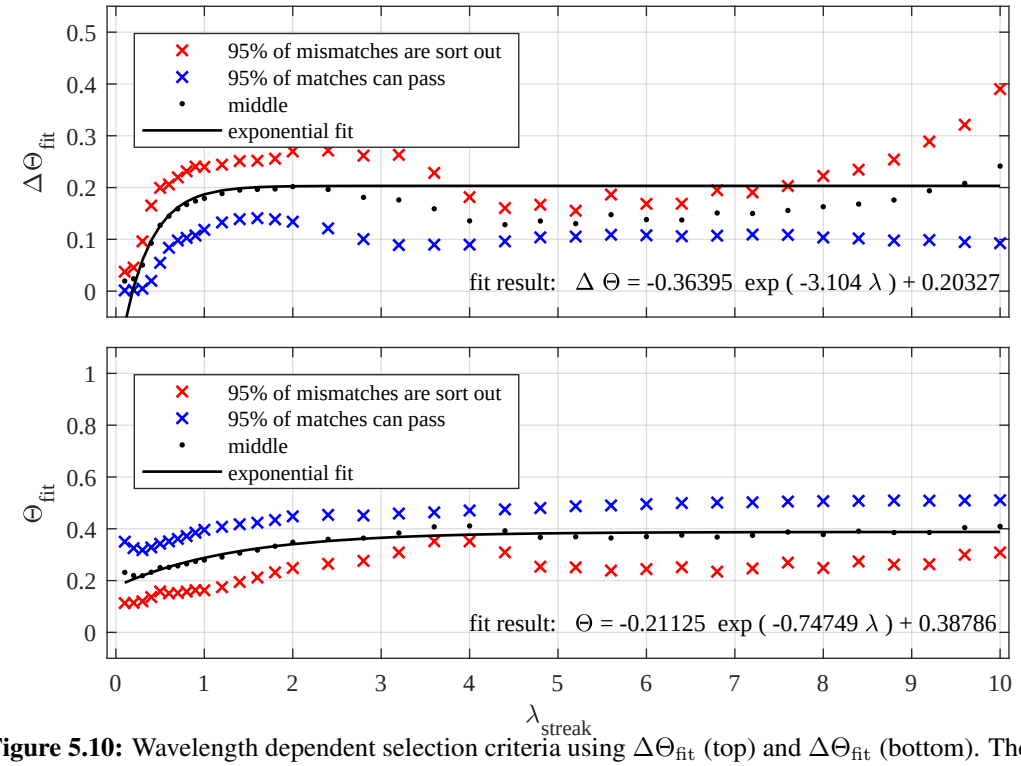

Figure 5.10: Wavelength dependent selection criteria using $\Delta\Theta_{\text{fit}}$ (top) and $\Delta\Theta_{\text{fit}}$ (bottom). The blue crosses show the selection values, where $95\,\%$ of all matches pass the selection, the red ones indicate the values, where $95\,\%$ of all mismatches are sorted out. The black dots show the middle, which was fitted with an exponential function.

best fitting model is represented by the fit with inverse direction, especially if the first estimation by FFT is used. The difference of these two values $\Delta\Theta_{\text{fit}}$ can be used as a second selection criterion. Especially partly pictured streaks, which are often giving wrong results, can be sorted out in that way.

In figure 5.9, the connection of Θ_{fit} and $\Delta\Theta_{\text{fit}}$ to the matching/mismatching is illustrated for the three regimes explained above. The left plots a), c) and e) show histograms of Θ_{fit} for matches in blue and mismatches in red. For wavelengths longer than 0.5 pixels, the distributions show significant differences. Mismatches have higher Θ_{fit} values than matches. Short streaks with $\lambda_{\text{streak}} \leq 1/2$ pixel show the same distribution of Θ_{fit} independent of matching/mismatching. On the right side in figure 5.9, the distributions of the difference between the two bests fits $\Delta\Theta_{\text{fit}}$ is shown. While short streaks behave similarly, mismatching streaks with $\lambda_{\text{streak}} \geq 1/2$ pixel show lower differences than the matching streaks in the same regime. The distributions are clearly separated, which indicates a good selection criterion.

The purpose of this validation is to find rules picking out outliers. The fraction of found mismatches as well as the fraction of the matches, which are not filtered out, should be as high as possible. The differences for respective wavelengths λ_{streak} requires a wavelength dependent treatment. In figure 5.10, a procedure for finding thresholds for

the selection criteria using Θ_{fit} and the difference $\Delta\Theta_{\mathrm{fit}}$ is demonstrated. A collection of different data sets with different noise levels and different intensity variations was used. While the red crosses indicate the levels $95\,\%$ of all mismatches are sort out, the blue ones show the levels where $95\,\%$ of the good matches pass the selection. By black dots the mean is drawn, on what an exponential fit was employed. These two fits give the opportunity to apply a simple selection criterion. Each evaluated detection of a streak has to pass these two rules:

$$\Theta < -0.21125 \exp(-0.74749\,\lambda_{\mathrm{streak}}) + 0.38786 \tag{5.5}$$

$$\Delta\Theta > -0.36395 \exp(-3.104\,\lambda_{\mathrm{streak}}) + 0.20327 \tag{5.6}$$

5.2.4 Resulting accuracy

The generation and evaluation of a large number of model streak images allows to validate the accuracy of the algorithm. First, the selection criteria as defined in the previous section are discussed (see figure 5.9 and 5.10). Here the number of not found mismatches and passed matches is relevant. While the former should be as few as possible, high numbers of the latter are of advantage. The top part of figure 5.11 shows the respective fractions in dependence of $\lambda_{\mathrm{streak}}$. All results are split into four groups depending on the signal to noise ratio (SNR) of the streak image, which are plotted in different colors. Neglecting very short wavelengths, the results appear to be satisfying. The fraction of not found mismatches, plotted by dashed lines, is low for all SNRs. There is a small enhancement for wavelengths between one and two pixels, which carries no weight. The different SNR levels become significant for the fraction of counted matches, displayed with solid lines. While high SNRs result in high numbers, low SNRs reduce the fraction to below 50 %. For wavelengths below 0.3 pixels both fractions indicate the weak spot of the PSV method: for very short streaks the selection criteria seem to fail.

The mean error of the estimated wavelength is regarded in the following. In the central part of figure 5.11, two cases are plotted: the solid line displays the mean error for all matches (difference smaller 0.2 pixels) in dependence of $\lambda_{\mathrm{streak}}$. With dashed lines the mean error for all detections, which passed the selection criteria, are drawn. If the separation of the mismatches works properly, these two data sets show the same results, which is the case for wavelengths bigger than 0.3 pixels. For shorter wavelength the false positive increase the mean error. All in all for wavelengths bigger than 0.3 pixels and SNRs higher than 2, the algorithm provides an accuracy significantly below 0.05 pixels. Only for very short streaks, problems in selection of mismatches can occur, causing a lower accuracy.

Beside the extracted wavelength each streak has a direction, which also contains errors. The algorithm offers two approaches to estimate the direction of the streak: by using the orientation from the structure tensor (step 2) and by using the fitted line

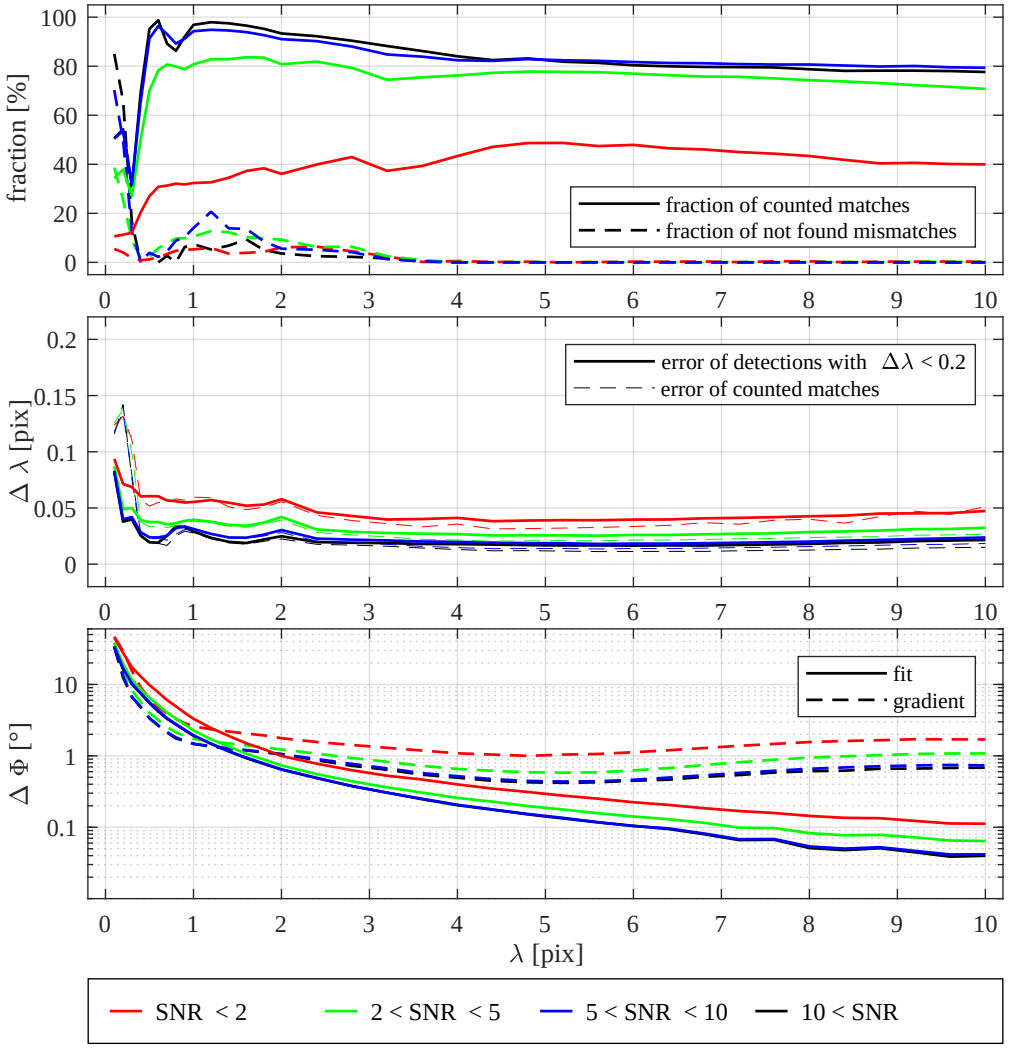

Figure 5.11: Goodness and accuracy of the algorithm applied on simulated PSV-streaks. **Top:** Fraction of counted matches and not found mismatches plotted for different wavelengths $\lambda_{\mathrm{streak}}$. While high rates of counted matches (solid lines) are preferred, the number of not found mismatches should be as low as possible. For streaks with SNR values (indicated by colors) above 2, the selection criteria are performing well, for lower SNR values only few streaks are passing. **Center:** Error for $\lambda_{\mathrm{streak}}$ expressed by the standard deviation, where big outliers with $\Delta\lambda > 0.2$ are excluded. The accuracy depends a on the SNR and drops a little bit for streaks shorter than ≈ 0.3 pixels. But all errors are below a very good level of 0.1 pixels. Without excluding outliers especially at short streaks the errors are bigger. **Bottom:** Accuracy of direction obtained by the linear fit (solid line) and by only using the structural tensor. For streaks longer than ≈ 1.3 pixels, the linear fit yields much better results.

through the streak image (step 4). The third part of figure 5.11 shows the mean error of the calculated angle for both methods in dependence of the streak wavelength and SNRs. The dashed lines illustrate the results by using the orientation from the structure tensor, denoted as gradient. For medium to long streaks the error is between $0.5°$ and $2°$, where higher SNRs give smaller errors. The results gained by fitting a line through the streak image provide much better results in this wavelength region, which are plotted as solid lines. The longer the streak is, the smaller than the errors. For long streaks, the error is smaller $0.1°$. However, this holds only for medium and long streaks. For short streaks, the gradient method yields significantly better results. Since the algorithm needs to calculate the orientation by both methods, the choice of method can be made streak length dependently.

At this place it should be pointed out, that all these simulations and error estimations were performed to proof and to optimize the algorithm. The simulated streak images could differ from real measured images. This can affect the effective accuracy. Statements to the resulting accuracy of the PSV-method can be found in section 5.4.5, where simultaneous measurements with a standard PIV technique are discussed.

5.3 Detection of the water surface from LHC

In all images recorded by the laser height camera (LHC), the surface elevation have been detected. This has been realized within the scope of the bachelor thesis of Schwarz (2016), where a detailed description and information about the data processing can be found. Here only an overview of the procedure is given.

First a position dependent threshold is determined, which is necessary because of intensity variations of the laser sheet. Thereby binary images of the surface are produced by applying $g_i > g_{\mathrm{threshold}}$. Small objects are deleted and holes are closed. The uppermost "true" pixel in a column gives the position of the water surface. Better results could be obtained by using threshold ranges from 90% to 110% and taking the mean. In case of strong variance – this is the case within wave breaking or other conditions effecting the images – these detections are discarded. Next, filtered values are interpolated and smooth fitting in space and time with splines is performed. As the result the surface position is outputted in pixel coordinates.

Figure 5.12 shows an examplary LHC-image and the determined surface position as a red line.

5.4 Real world coordinates and accuracy

The PSV-algorithm and the detection of the water surface from the LHC entirely works in image coordinates. For obtaining measurements in real world coordinates, the image calibration described in section 4.4 is used. Therefore the start and end point of each streak i is transformed to real coordinates yielding to a velocity $(u_{x,i}, u_{z,i})$. The middle

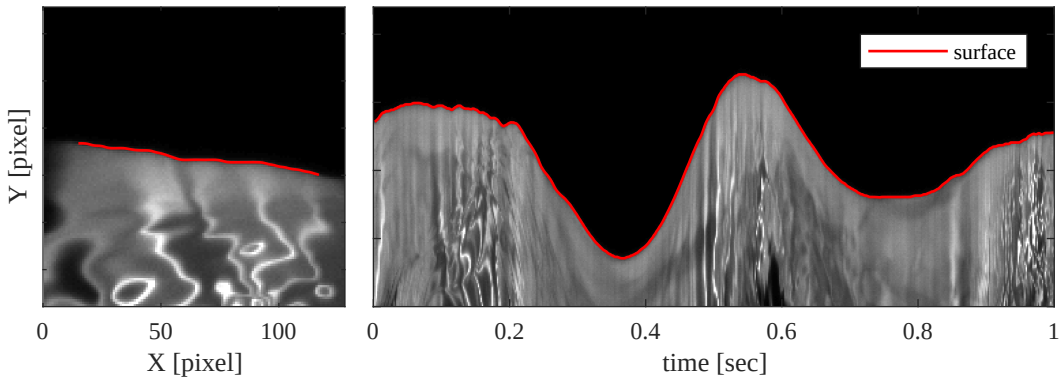

Figure 5.12: Exemplary detection of the water surface of pure wind waves at 6 m/s. **Left:** Extract of one image recorded by LHC and the determined water elevation (red). **Right:** yt-plane of a central column. By the high sampling rate of 500 Hz time series of the water elevation are measured.

of the streak gives the position (x_i, z_i) of the measurement. The same is done for the surface detection.

As four cameras with different fields of view have been used for the PSV measurements (compare chapter 4), the results were composed.

One critical point of all measurements is the accuracy, which has to be regarded before physical interpretations can be made. In this section, the results from different simultaneously recording cameras are compared.

5.4.1 Accuracy of height measurements

The water elevation $\eta(x, t)$ is measured by the laser height camera (LHC) as well as by the cameras used for particle streak velocimetry (PSV). Since they are synchronized in time and by use of the same calibration target, the results can be compared. The images are recorded slightly time-displaced, see the explanation of the used triggering system in section 4.2. Hence for each recorded PSV-image the weighted average of the LHC-measurements before and after the PSV-measurement was calculated giving the height measurement, respectively.

In figure 5.13 histograms of the difference between the height measured by LHC (η_{LHC}) and by PSV-cameras, which see the water surface (η_{PSV}) are shown. The single cameras show individual offsets, which might be caused by misalignment of the laser sheet and the calibration target or by other small calibration errors. This offset is corrected in first order by subtracting on for each camera, respectively. The sum of all corrected detections, illustrated in blue, shows a Gaussian distribution with zero mean, which is indicating only statistical errors after the correction. The error represented by the standard deviation is an indication of the resulting accuracy of the elevation measurements, which can be transferred to all position measurements. With a value of $\sigma \approx 0.06$ mm the achieved accuracy is smaller than the resolution of the LHC with

0.183 mm/pix.

In this context it has to be remarked, that the PSV-images with ≈ 0.05 mm/pix are better resolved and could deliver more accurate measurements than LHC. Especially for determining the relative distance of detected streaks in PSV to the water surface, this higher accuracy is useful.

5.4.2 Projection error

One issue, which has to be considered, is the projection error occurring due to the inclined view of the cameras. For the detection of the water surface – realized by laser induced fluorescence (LIF) – this is no problem. The result is integrated over the thickness of the laser sheet and as long as the laser sheet is constant and has a fixed position, no errors occur.

For the velocity measurements by PIV or PSV, the situation is different. The single particles, which are tracked by the cameras, are much smaller than the thickness of the laser sheet and their position and velocity perpendicular to the laser sheet influences the projection onto the image sensor and thereby the measurement.

The PSV-cameras are mounted with an angle of approximately $20°$ against the horizontal. With the Scheimpflug optics the focal plane could be tilted, but the projection angle still remains. Due to the thickness of the laser sheet (≤ 2 mm), the tilted view of the PSV-cameras can yield to slightly wrong measurements of the height. This possible error can be estimated by the tangents of the inclination and the half width of the laser sheet:

$$\Delta z_{\mathrm{PSV}} \approx 1\,\mathrm{mm} \cdot \tan(\alpha_{\mathrm{incl}}) = 0.364\,\mathrm{mm}. \tag{5.7}$$

As the uncertainty of the y-position is effecting the z-position, the y-velocity is effecting the z-velocity. If the y-component (horizontally cross wind) of a particle's motion is nonzero ($u_y \neq 0$), the observed vertical velocity component $u_{z,\,\mathrm{obs}}$ can be expressed by:

$$u_{z,\,\mathrm{obs}} = u_z + u_y \tan(\alpha_{\mathrm{incl}}). \tag{5.8}$$

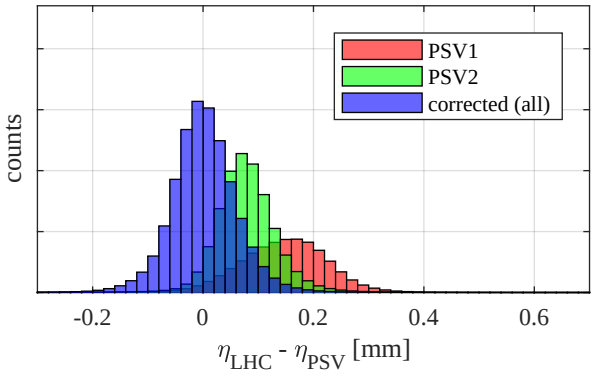

Figure 5.13: Comparison of the measured water elevation by the LHC and the PSV-cameras (6 m/s wind speed and long paddle waves). The histogram shows a Gaussian distribution with $\sigma \approx 0.06$ mm. This error is much smaller than the image resolution of LHC (0.183 mm/pix).

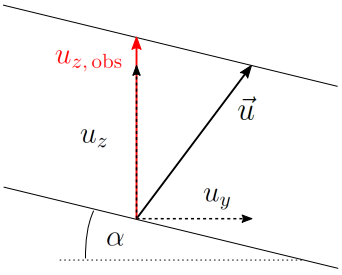

Figure 5.14: Illustration of the projection error due to the inclined observation. The velocity vector $\vec{u}$, which is composed by u_y and u_z yields an observed vertical velocity component $u_{z,\,\mathrm{obs}}$ differing from u_z. Depending on the direction of u_y, this could lead to an enhancement or a reduction. The component in wind direction u_x can be disregarded in this context, because it is perpendicular to the direction of observation (thin black lines).

The tangents of the inclination angle α_{incl} times the horizontal cross wind component is added due to the projection. In figure 5.14, a sketch of an observed velocity is shown.

Within the scope of this work, mainly averaged velocity quantities are considered. Under the assumption of a vanishing mean y-component of the velocity ($\overline{u}_y = 0$) the influence of the projection error is vanishing, too. This holds for single means as well as for averaged products of the velocity components:

$$\overline{u}_{z,\,\mathrm{obs}} = \overline{u}_z + \overline{u_y \tan(\alpha_{\mathrm{incl}})} = \overline{u}_z \tag{5.9}$$

$$\overline{u_{z,\,\mathrm{obs}} u_x} = \overline{u_z u_x} + \overline{u_y u_x \tan(\alpha_{\mathrm{incl}})} = \overline{u_z u_x} \tag{5.10}$$

Thus, it can be followed that as long as there are no mean horizontal flows in cross wind direction, the here used inclined observation yields correct results for averaged quantities. Regarding instantaneous measurements, this effect has to be taken into account.

The effect of this projection error really becomes problematic, if secondary currents occur as it is the case in annular wind wave facilities. Here, stereo measurements can be performed within all three components and so the projection error is avoided.

5.4.3 Exclusion of outliers

As it turned out the PSV-algorithm outputs not only good streak detections. In a certain fraction of all detections, the best fit is not representing the real particle motion and the challenge is to filter them out. The study of generated streak images with random variations yields to a selection criterion (section 5.2.3), which can be applied to find and exclude nearly all bad detections.

Figure 5.15 illustrates histograms of detections measured with different distances to the water surface. Binning is performed in two dimensions, the x-axis is the height $z^* = z - \eta(x,t)$ and the y-axis is the horizontal velocity u_x. The number of counts in each bin is illustrated by colors, from blue (no counts) to yellow (many counts). This way for binning was chosen, because here the long term observation of u_x should yield to a rather smooth profile, similar to the law of the wall. Appearances beside this profile can be considered as wrong. The left plot in figure 5.15 shows an histogram for all detections unfiltered. The big structure is the expected profile. With rising distance

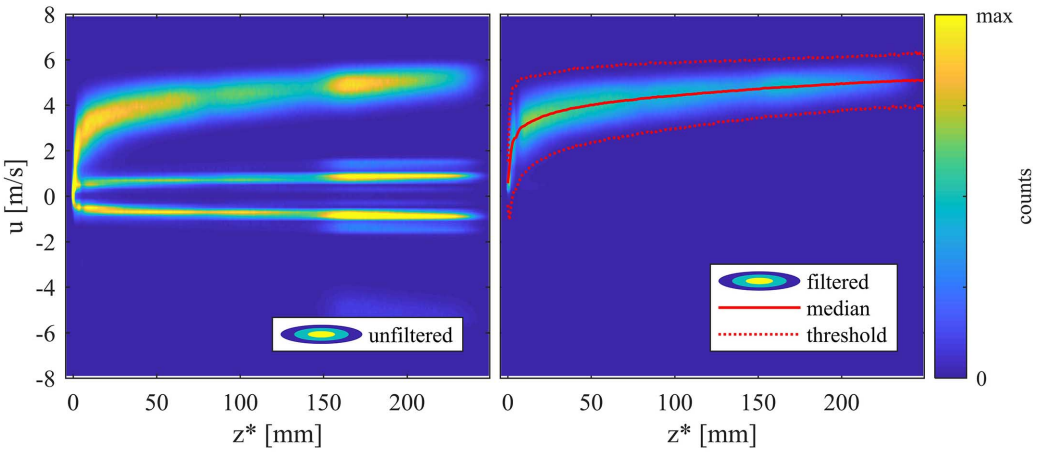

Figure 5.15: Illustration of the filtered wrong PSV-results and excluding single outliers. 2D histograms with horizontal velocity on y-axis and wave following vertical coordinate on x-axis demonstrate the efficiency of the selection criteria. **Left:** The plot of all found detections shows counts around zero at heights, which can be clearly identified as mismatches. **Right:** after filtering according to the selection criteria (section 5.2.3) these structures disappear. Single outliers, which were not found by the first step, can be excluded by use of the median and a threshold expressing the variance at each height.

to the water surface the velocity increases and the width of the structure represents all the turbulent eddies. Around zero there are additional counts, which can be evidently identified as wrong. These detections can be explained by particles, whose path only partly hit the laser sheet causing the streak to be cut. The fitting of the profile function leads to wrong results. Additionally, few counts appear with right magnitude but with negative direction.

At the right of figure 5.15, the remaining values after applying the selection criteria (equation 5.5 and 5.5) are shown. Now nearly all wrong data points have disappeared, indicating good success of the selection process.

A few outliers, which are not visible in the color plots, could not be filtered out. For a simple average, these values do not contribute significantly. But for averaged correlation terms like $\overline{u_x' u_z'}$ they can make a big effect. In order to exclude these, too, a second selection step is performed. For each height, the median (u_{med}) and the range of the middle 50% ($\Delta u_{50\%}$) of all filtered values is calculated. Then all detections with

$$u_{\mathrm{med}} - 2\,\Delta u_{50\%} \leq u_{x,i} \leq u_{\mathrm{med}} + 2\,\Delta u_{50\%} \tag{5.11}$$

are kept and all others are excluded. These boundaries are plotted in the right plot of 5.15 and are clearly outside the dominant profile, so that there is a buffer and it can be assumed, that no meaningful measurements are excluded.

As the profile may depend on the phase of the dominant wave, this second step of selection is performed phase dependently.

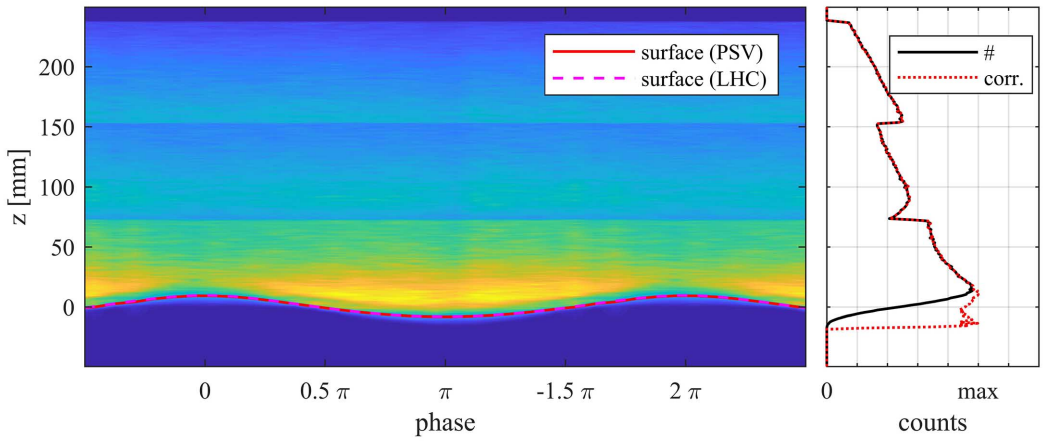

Figure 5.16: Histogram of measurement points in fixed coordinates. **Left:** Colored illustration in dependency on the phase of the dominant wave. The color indicates the number of counts, from zero (blue) to maximum (yellow). The phase dependent averaged surface elevation is plotted by a red (observation from PSV) and pink dashed (observation from LHC) line. **Right:** Phase averaged plot of the height dependent counts of measurements (black line). Clear horizontal structures are visible, which are caused by lens effects of the single PSV-cameras (blurring, vignetting). The normalized height dependent histogram is used for corrected averaged values by weighting the single measurements. The red dotted line illustrates the correction for regions, which are partly under water.

5.4.4 Variances in particle density

A further critical aspect is the distribution of the particles and thereby the distribution of measurements. Successful averaging needs homogeneous distributed measurements. If, for example, the density of measurements in front of the wave crest is higher than behind, the calculated average over all phases of the vertical velocity will be positive, although the real quantity is zero. This means, that in vertical direction as well as phase dependent, the distribution of the measurements should be homogeneous.

In the present case, a homogeneous particle density must not lead to a homogeneous distribution of measurement points. Whether a particle in the laser sheet leads to a successful measurement, depends strongly on the image quality. These can vary due to variances of the illumination (the focusing of the laser sheet can vary with height) or due to lens effects like blurring, vignetting or reflections.Furthermore, quantization effects of the background influences the PSV-algorithm.

Firstly, the effects caused by the lenses and the laser sheet variances are evaluated. Because these must only depend on the position figure 5.16 shows a histogram of all good measurements, which means they passed the selection criterion. The x-direction represents the phase of the dominant wave. Vertically the height in fixed coordinates (distance to mean water level) is plotted. The mean phase dependent surface elevation is plotted with a red line (observation from PSV) and a pink dashed line (measurement by LHC). Clearly visible are horizontal structures, which become more obvious by the phase independent illustration on the right side in figure 5.16. These can be explained by

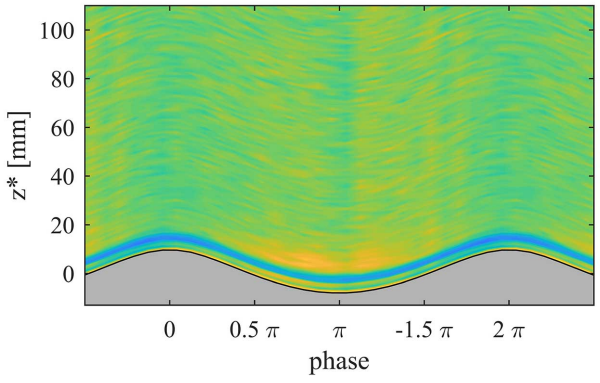

Figure 5.17: Phase dependent histogram of weighted measurements points in wave following coordinates. The blue layer indicates less detections in a certain distance above the water surface, which is caused by an increased background noise in the images due to scattering of the laser induced fluorescent light from the surface. This phase and z^* dependent information is also used for weighting during averaging. This plot shows only an extraction of the full FOV.

the influences of the lenses on the image quality. The dominant steps coincide with the field of views of the single PSV-cameras. The general tendency of fewer measurements with increasing heights can have two causes. On the one hand, the particles could accumulate in the lower part. On the other hand the focusing of the laser sheet could make the same effect. Also the longer streaks caused by higher velocities lead to effectively fewer good detections.

Especially in the boundaries of two cameras this density variations of measurement points could shift the average values, if – as it is done in the evaluation – this average is performed along a layer crossing these borders. To avoid such errors, the single measurements were weighted by the inverse of the normalized density during averaging. At heights which are partly under water the weights are corrected, which is demonstrated by the red dotted line in the right plot in figure 5.16.

Figure 5.17 shows a phase dependent histogram of the measurements points, where the fixed coordinate weighting has been adopted. Here the illustration of the vertical coordinate is z^*, the distance to the actual water surface. For the illustration of the waves, the mean surface elevation at each phase have been added. Now the distribution of measurement points depicts a layer with a significantly reduced number of detections at a constant distance to the water surface, which can be guessed in figure 5.16, too. The reason for this effect is a combination of a light background caused by scattered light from laser induced fluorescence at the surface and the low light operation of the cameras. The images have an enlarged background noise in this region, while more detections are filtered out by the selection criteria. This layer of reduced density also causes an increase in the wave trough, which is an artifact of the weighting along constant fixed height. In order to also avoid effects from these structures this histogram is used for weighting the data points, which is done in dependency of phase and z^*. Thereby the influence of the distribution of measurement points could be reduced to a minimum and for all further considerations these weights are applied.

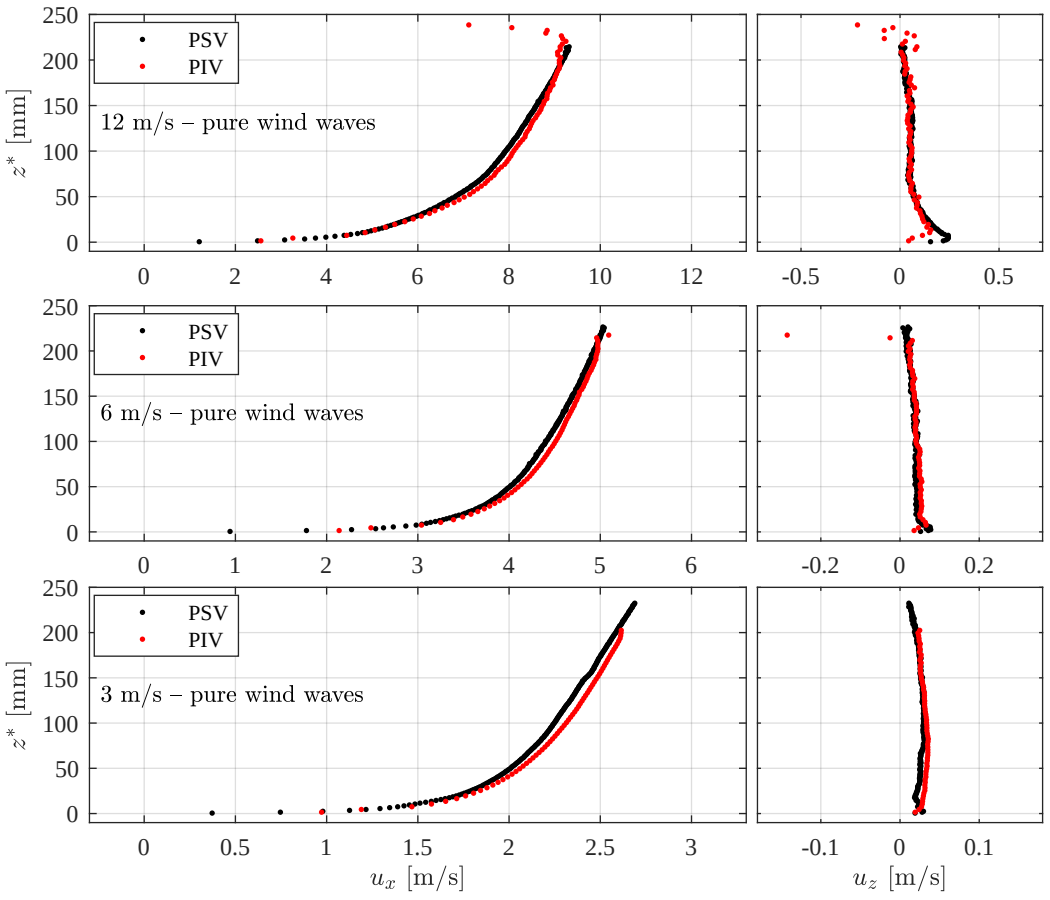

Figure 5.18: Comparison of results obtained by PIV and PSV at different wind speeds and pure wind waves. As vertical coordinate the simple shifted height z^* (distance to actual water surface) was chosen. All points are averages of mean velocities (horizontal at left and vertical at right) with bin sizes of 3 mm for PIV and 1 mm for PSV. Results from PIV are shown in red, results from PSV in black. The mean values show no significant differences.

5.4.5 Comparison of PSV and PIV

The simultaneous measurements with two different methods (standard statistical PIV and PSV) give the opportunity to compare the measured velocities and proof the techniques.

For that purpose vertical profiles of the mean velocity are calculated in simple shift coordinates ($z^* = z - \eta(x,t)$). The PIV-measurements have approximately 3 mm in spacial resolution, therefore the vertical bin size was chosen accordingly.

In figure 5.18 the profiles of $\overline{u}_x$ and $\overline{u}_z$ are plotted for both techniques, respectively. The averaged values obtained by PSV (black dots) and by PIV (red dots) are comparable. Only small deviations up to few percent are visable and range in the accuracy of both methods.

In section 5.2.4 the accuracy of the PSV algorithm has been discussed by using

u_{ref} [m/s]	f_{PSV} [kHz]	Δu_{PSV} [m/s]
2.5	6	0.015
3	6	0.015
4	9	0.023
5	11	0.028
6	13	0.033
8	17	0.043
10	21	0.053
12	26	0.065
14	26	0.065

Table 5.2: Accuracy of PSV-measurements for different wind conditions. The error of each velocity vector is controlled by the PSV-frequency f_{PSV} and the image resolution ($\approx 50\,\mu$m/pixel). In all measurements the theoretical accuracy is lower than 1% of the free stream velocity.

modeled streak images. The result is that the wavelength of the streaks is determined with an uncertainty of $\Delta\lambda \approx 0.05$ pixels. After transforming to real world coordinates, the image resolution and the PSV-frequency f_{PSV} is limiting the accuracy. The larger the frequency the larger the uncertainty of each streak measurement. In order to optimize the settings for each wind condition, different frequencies were used. In combination with the optical resolution ($\approx 50\,\mu$m/pixel), the resulting accuracy Δu_{PSV} can be calculated and is presented in tabular 5.2. So for all conditions the measurements have theoretical accuracies lower than 1% of the free stream wind speed.

6 Wave analysis

Essential for successfully interpreting the measured flow velocities above water waves, the latter have to be analyzed carefully. Besides the measured water elevation also the dynamics of the wave is important. In this section a short description of the work flow of detecting the height in the images recorded by the LHC-camera is given. It is also explained how statistical properties are determined and how the curvilinear wave following coordinates and the dominant wave phase are obtained.

6.1 Statistical properties

For each run of experiments the available height data measured by the LHC (see section 3.3.3 and 5.3) have been used to generate a convolution of the statistical parameters, which are describing the wave field (compare table 4.1).

6.1.1 Frequency spectra

In order to account for statistical variations the whole sequence has been split into parts of $30\,\mathrm{sec}$ and from each the frequency spectrum has been determined using Fourier analysis. Thereafter all single spectra were averaged. Examples of the energy density spectra are shown in section 7.1.1. The peak frequency f_p has been determined by finding the maximum of the frequency spectrum $\Phi(f)$ in each short sequence. The uncertainty of measurement values is representing the standard deviation of the values of all short sequences.

6.1.2 Wave height and period

As a good measure for the mean amplitude of surface waves the root-mean-square wave height $a_\mathrm{rms} = \sqrt{\eta^2}$ was calculated in each short sequence, too. From the standard deviation the uncertainty or rather variations, which are presented in the summary of measurement values (appendix A.2), have been derived.

While for wind waves, which are approximately Rayleigh distributed, from a_rms also the dominant wave height H_d and the significant wave height H_s could be estimated, for paddle waves these assumptions do not hold. To still state these parameters an analysis has been performed extracting the height and period of each individual wave.

An algorithm was written, which detects all zero crossings and all peaks between in a time signal of the wave elevation at a single point. Figure 6.1 shows in the uppermost plot an example of the detected points. From these points the wave height H as the distance from peak to peak as well as the wave period T was determined. Also shown in the lowest plot is the time resolved phase velocity – a description of the method follows in the next section. From all single wave heights H the average quantities H_d

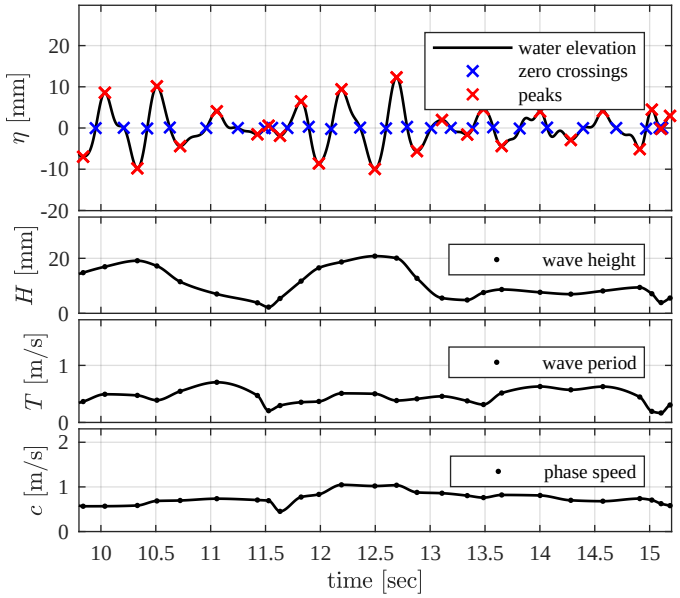

Figure 6.1: Detection of the wave height and wave period of each individual wave at 6 m/s wind speed and pure wind waves. The uppermost plot shows a time signal of the water elevation at a single point (black line). Blue crosses are detected zero-crossings and red crosses are detected peaks (crest or through, respectively). The derived wave height H (distance from peak to peak) and the wave period T are plotted below. The lowest plot shows the time resolved phase speed, which was derived by the time correlation between two signals measured at both ends of the laser sheet.

and H_s are calculated. The uncertainties presented in this work are statistical errors of the mean.

6.1.3 Phase speed

Measuring the height along the laser sheet with width around 2 cm it was possible to determine the phase speed c_p of the dominant wave. This has been done by use of the cross correlation between short sequences measured at the right and the left of the laser sheet. The shift of these two signals provides the phase speed and by use of short sequences temporal resolution could be achieved. The left part of figure 6.2 shows height signals of such a short sequence. The dashed blue line visualizes the shifted left signal, which has the highest correlation with the right signal. This temporal resolution makes it possible to obtain the variance of c, which is illustrated by the histogram at the right side of figure 6.2.

For determining the wave steepness ϵ_s (equation 2.55) of pure wind waves the spectrum of the time derivative of the water elevation S_{η_t} have been calculated and summarized from 0.5 to $1.5\, f_p$. Together with c for each run a value came out. The uncertainty could be derived by Gaussian error propagation.

6.2 Curvilinear coordinates

For the considerations of momentum transport above waves curvilinear coordinates have been introduced (compare section 2.3.3). In the scope of this work only coordinate systems are used, which keep the horizontal coordinate unchanged and only modify the

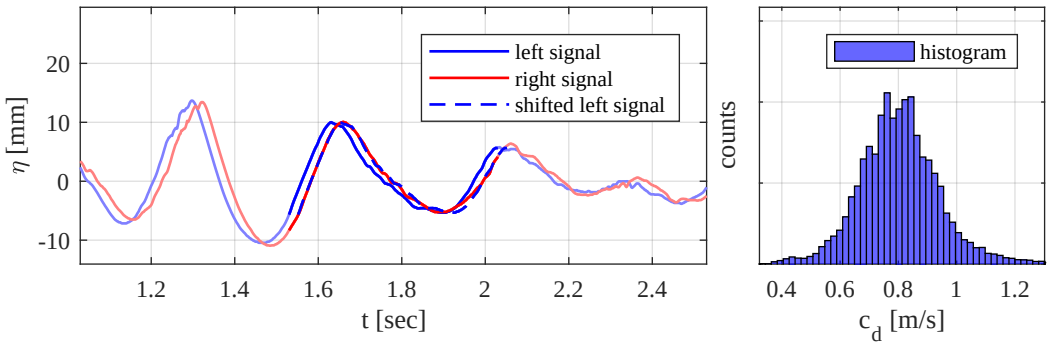

Figure 6.2: Illustration of determining the phase speed shown exemplarily for 6 m/s wind speed and pure wind waves. **Left:** The time series of the water elevation measured at the left side (blue) and the right side (red) of the laser sheet are drawn by solid lines. With saturated colors the region of approximately one period is illustrated, which is regarded for the correlation. The dashed blue line shows the high correlation of the shifted left signal. **Right**: The histogram demonstrates the variation of all values of the phase speed along a time series with 5 min length.

vertical. The z-component is added by a certain value, described by a function f, which depends on position and time. Two different approaches for this function are deployed.

First this function is expressed by the water elevation $\eta(x,t)$ itself yielding to a simple shift independent in height. Therefore all necessary height data is directly measured by the LHC or PSV-cameras.

The second approach – the declining shift – adapts the vertical component dependent on the distance to the water surface and the wave form. This is realized by decomposing the surface elevation $\eta(x,t)$ into several harmonics ($a_n \cos(k_n x - \phi_n)$) and multiplying on each mode an exponential decaying factor $\exp(-k_n z^*)$, which depends on the respective wave number k_n and the new vertical component z^* (equation 2.81). For applying such a transformation first the spacial decomposition of $\eta(x,t)$ has to be conformed for each moment of the time series. The available elevation data contain not more than two centimeters, which is insufficient to identify bigger gravity waves.

Therefore the temporal information of the time series can be used. In the previous subsection the determination of the phase speed is described. By use of this temporal resolved quantity the surface beside the measurement range can be extrapolated. Of course temporal changes of the wave form are neglected, but those become merely critical with bigger distance to the measurement point. For the extrapolation the left and right ends x_{left} and x_{right} of the measured surface line are regarded. The values of $\eta(x,t)$ at time t_0 for $x < x_{\mathrm{left}}$ are calculated by

$$\eta(x,t_0) = \eta(x_{\mathrm{left}},t') \qquad \text{with} \qquad x_{\mathrm{left}} - x = \int_{t_0}^{t'} c_{\mathrm{p}}(t)dt \tag{6.1}$$

and for $x > x_{\mathrm{right}}$ by

$$\eta(x,t_0) = \eta(x_{\mathrm{right}},t') \qquad \text{with} \qquad x_{\mathrm{right}} - x = \int_{t_0}^{t'} c_{\mathrm{p}}(t)dt. \tag{6.2}$$

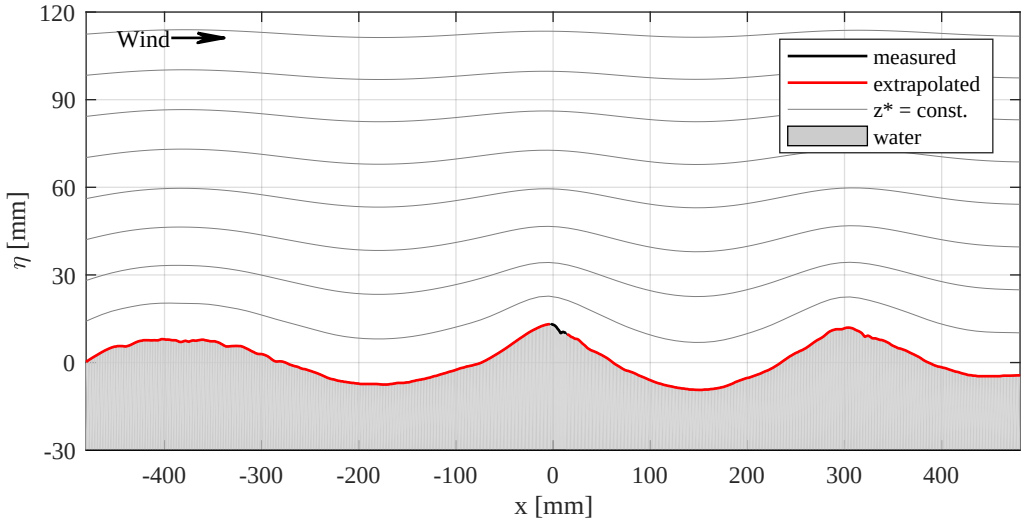

Figure 6.3: Measured and extrapolated surface elevation along the horizontal coordinate x and layers of constant z^* in curvilinear coordinates for pure wind waves at 6 m/s wind speed. The measured (black) and extrapolated (red) water elevation is drawn for a region around the measurement area much bigger than the wave length of dominant wave. Above the water surface the layers of constant z^* for the declining shift coordinate transformation are illustrated by gray lines.

In figure 6.3 such an extrapolation is illustrated by a red line for an exemplary pure wind wave at 6 m/s wind speed. The small black part in the middle shows the measured data. For all wind regimes this method yields reasonable results and no fault extrapolation could be observed, which would lead to inhomogeneities in the wave form.

As the standard method for decomposing a signal into harmonics the Fourier decomposition (see appendix A.4.2) has been used. In order to save calculating time the procedure was applied in two resolution steps. First a Fast Fourier Transform algorithm (FFT) has been employed on the combined height signal (measured and extrapolated) at each time step. Therefore a large region of about 5 m with 1 cm resolution was used, whereby wave length from 2 cm to 5 m are covered. Second a small region around the measurement area of approx. 5 cm with 0.1 mm resolution was regarded. The big structures, which are captured by the first FFT, have been subtracted and again an FFT algorithm was applied. Together all structures expressed by wave lengths down to 0.2 mm are well resolved at and around the measurement area by not just more than 500 modes. By these in the form of $a_n(t)\cos(k_n x - \phi_n(t))$ the declining shift coordinate transform can be realized at each point of the time series t separately. Edge effects, which are unavoidable while using FFT, are concerning only extreme regions.

Also illustrated in figure 6.3 by gray lines are the calculated layers of constant vertical component z^* by use of this harmonics. Figure 6.4 shows a zoomed view of the area around the measurement area.

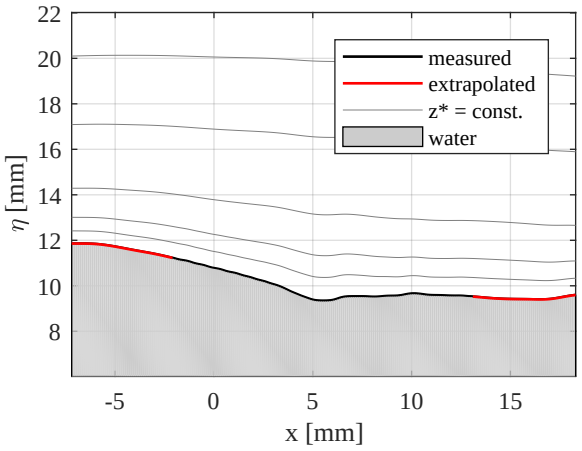

Figure 6.4: Zoomed view of the surface elevation and the obtained curvilinear coordinates of the situation shown in figure 6.3 (6 m/s wind speed and pure wind waves). The measured (black) and extrapolated (red) surface is illustrated by the solid lines. Layers of constant vertical coordinate z^* are drawn with thin gray lines, which are following the surface structure close to the water surface and smooth with bigger height.

6.3 Phase of dominant wave

In order to observe wind wave processes all quantities have to be considered phase dependent. Therefore the dominant wave has to be identified and its phase has to be determined.

For getting the dominant wave a Fourier based band pass filter has been applied on the time series of the measured height data. As range the region between 0.5 and $1.5\ f_\mathrm{p}$ was used. From this signal the Hilbert transform (see appendix A.4.3) provided the local amplitude and phase (Melville, 1983). Thus for each flow measurement and so for each measured velocity vector the phase $\phi_\mathrm{d}(x,t)$ and amplitude $a_\mathrm{d}(x,t)$ of the dominant wave respectively have been obtained and phase averages could be performed. The phase is defined in radians from $-\pi$ to π with $\phi = 0$ at the wave crests and increasing phase in down wind direction. Hence the phase is decreasing with time as it is shown in figure 6.5. Because of edge effects, which render the phase information unreliable (Oppenheim and Schafer, 2010) the first and last seconds of each time series were disregarded.

Figure 6.5 shows a small extraction of a measurement of pure wind waves at 6 m/s. This example has been chosen because of its inhomogeneity. Even for such chaotic wave fields the described method leads to meaningful results. Certainly at regions superposed by two or more modes, which results in very small amplitudes or non-harmonic shapes phase considerations are pointless. But these regions usually are associated with small local amplitudes a_d and so can be identified and excluded for phase averaging.

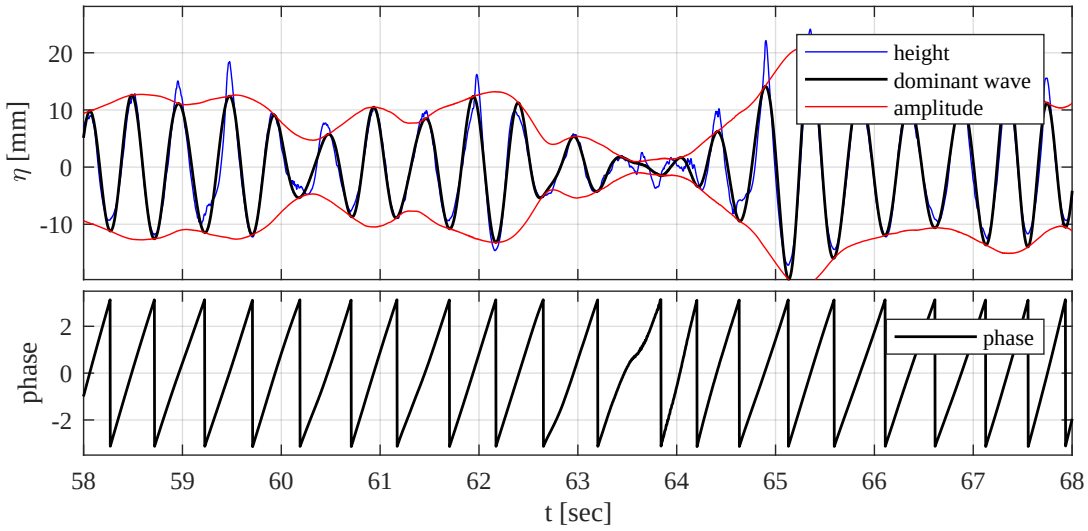

Figure 6.5: Dominant wave and its phase for pure wind waves at 6 m/s. By a Fourier based band pass filter ($0.5\,f_\mathrm{p} < f < 1.5\,f_\mathrm{p}$) the measured time series of the water elevation (blue) is smoothed obtaining the dominant wave (black). The Hilbert transform yields the local amplitude demonstrated by the red line and the local wave phase drawn by the black line in the lower graph. Regions with no clear dominant wave, where no reasonable phase can be extracted, can be identified by low amplitudes.

7 Results

In this chapter all measurements and the obtained results are presented. The first section 7.1 gives a description on the wave conditions and their properties. The initial velocity measurements achieved by the new PSV-method are examplary shown by time series of wind velocity fields in section 7.2. The total drag and the mean wind profile is studied in section 7.3. While section 7.4 shows the structure of the velocity fields by using phase dependent averaging, the last section 7.5 focuses on the momentum transfer and its partioning.

7.1 Wave properties

In the following same key properties of the waves are treated. The intention is to describe the wave field, which is needed for further analysis of the air flow above the waves and the momentum transport.

7.1.1 Wave spectra

A meaningful description of wave fields is given by their frequency spectra Φ (equation 2.51), where the frequency distribution of energy is shown.

Figure 7.1 shows such spectra for a selection of conditions (pure wind waves, short paddle waves and long paddle waves) at different wind speeds. For pure wind waves the spectra show a wide distribution with a peak representing the dominant wave. The peak frequency decreases with increasing wind speed. The higher the wind speed, the higher the wave growth, which leads to longer waves at the point of measurements with $28\,\mathrm{m}$ fetch. A second weak peak appears at the first harmonic of the dominant wave, which coincides with Stokes' theory for finite amplitude gravity waves (see section 2.2.3). As expected with increasing wind speed also the total energy growths.

The $0.9\,\mathrm{Hz}$ of the long paddle was chosen, because at this frequency the dominant wave was stable at all wind speeds, which resulted in a two dimensional single wave. This is exactly what the spectra show. The paddle wave and its harmonics are dominating the spectra and nearly no energy is carried around by modes.

Short paddle waves are between pure wind waves and long paddle waves. Their peak is very close to $1.3\,\mathrm{Hz}$ at all wind speeds. For the highest wind speed a small downward shift is observed. Here the energy distribution varies with increasing wind. For $6\,\mathrm{m/s}$ the paddle wave is dominant besides the peaks the energy density drops significantly. For higher wind speeds the spectra are more smooth. Even if the $1.3\,\mathrm{Hz}$ wave represents the maximum of the spectrum, energy has been transported to adjacent frequencies. This represents the observations during the experiments, where at high wind speeds wave breaking occurred along all fetches, the paddle wave was not stable and a three dimensional wave field was present.

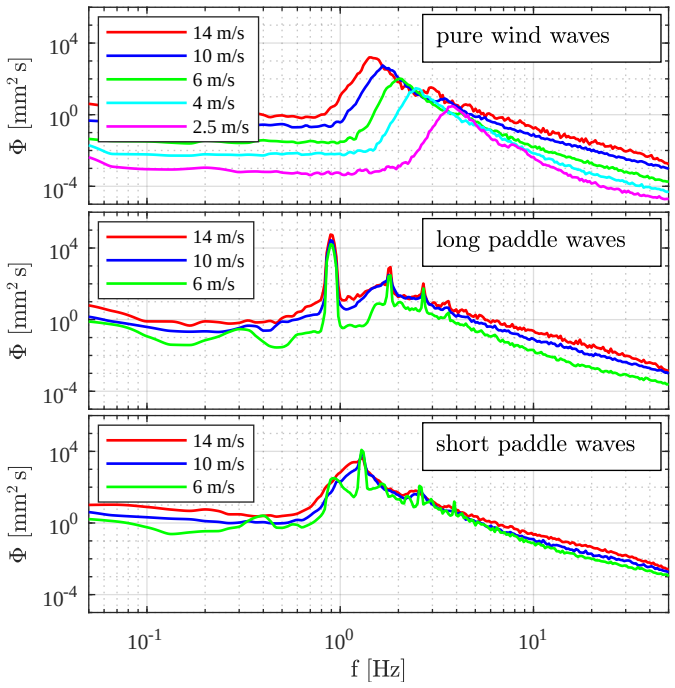

Figure 7.1: Frequency spectra (energy density spectra) for different wave conditions at different wind speeds. Pure wind waves show a smooth spectrum with a peak, which frequency is down shifted with increasing wind speed. The spectra of long paddle waves are dominated by the 0.9 Hz-wave and its harmonics. Short paddle waves (1.3 Hz) are settled in between. The paddle generated mode contains still the most energy, but with increasing wind speed the energy in regions around increases as well.

7.1.2 Wave height

While spectra give good impressions of the composition of wave fields, a quantitative comparison of properties with single values sometimes is more meaningful. As a good parameter the averaged wave height is used here, which was derived from the peak to peak distances measured by LHC (compare section 6.1.2). Figure 7.2 shows the dominant wave height H_d in blue as well as the significant wave height H_s in red for all conditions. Additionally, theoretical expressions using the root mean square wave amplitude a_rms are shown in black and orange.

As expected are all wave heights at conditions with paddle waves larger than for pure wind waves and with increasing wind the wave height growths. Comparing the significant and dominant wave height attention is attracted by the fact, that for wind waves and short paddle waves they are significantly different, while for long paddle waves they are comparable. This underlines the difference between two dimensional stable paddle waves and unstable more chaotic wave fields.

The theoretical calculation of the dominant wave height (shown in black) coincides quite good with the direct observed values. For wind waves and short paddle waves a Rayleigh distribution with $H_\mathrm{d} \approx 2.5\, a_\mathrm{rms}$ was assumed. The long paddle wave was assumed to be a two dimensional Stokes' wave with $H_\mathrm{s} \approx 2.8\, a_\mathrm{rms}$ (see section 2.2.4). For short paddle waves, especially for lower wind speeds, the theoretical values are slightly too low, which indicates a wrong assumption. As the spectrum in figure 7.1 shows, the spectrum of short paddle waves at 6 m/s has not a wide distribution.

For pure wind waves also a theoretical calculation of the significant wave height

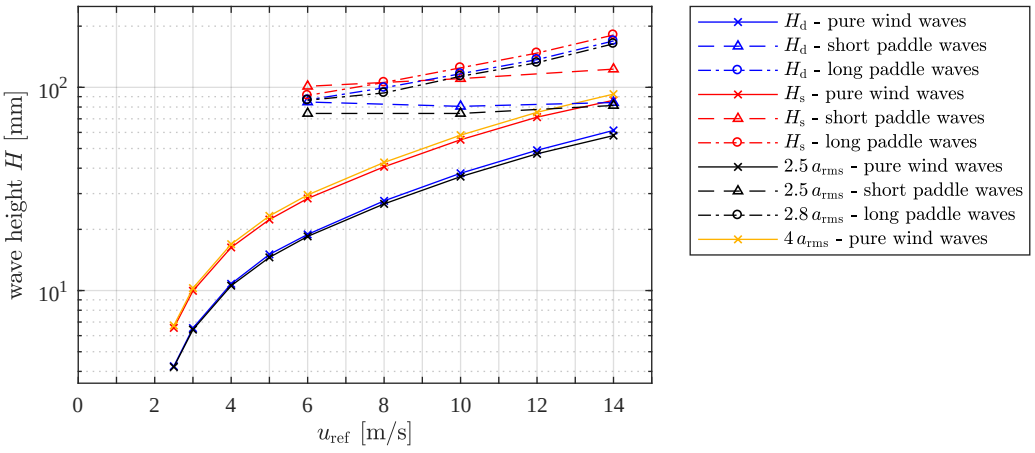

Figure 7.2: Wave height dependent on the reference wind speed for all conditions. Significant wave height H_{s} is shown in red, dominant wave height H_{d} is plotted in blue. Pure wind waves and short paddle waves show significant differences between H_{s} and H_{d}, while there is nearly no difference for long paddle waves. Theoretical calculations using the root mean square wave amplitude a_{rms} are comparable with the direct averages.

with $H_{\mathrm{s}} \approx 4\,a_{\mathrm{rms}}$ is plotted in orange, which also coincides very well.

7.1.3 Phase speed of dominant wave

For calculating the wave steepness as well as the wave age the phase speed of the dominant wave is needed, which was determined by using the time shift of the wave elevation (see section 6.1.3) at both ends of the measured line. Figure 7.3 shows the average values of c for all measured conditions by black symbols. In red the theoretical phase speeds are plotted using the dispersion relation for linear waves (equation 2.37) and the peak frequency of the energy spectrum. For pure wind waves and short paddle waves the theoretical values are below the experimental, which indicates a small drift velocity. Even in a linear facility this is a typical effect – the shear at the air-water interface pushes the water windward and generates a small current in upper layers and a backward flow at the bottom.

For long paddle waves the results differ: The experimental estimations are partly lower than the theoretical calculations, especially for low wind speeds. At the one hand the 0.9 Hz wave has a larger penetration depth, so due to wave motion near the bottom the flow characteristics in the facility might change. But this does not explain the values, which are lower than the linear theory. At the other hand for long paddle waves at lower wind speeds the wave profile differs from the form of a single Stokes' wave, which could influence significantly the phase speed.

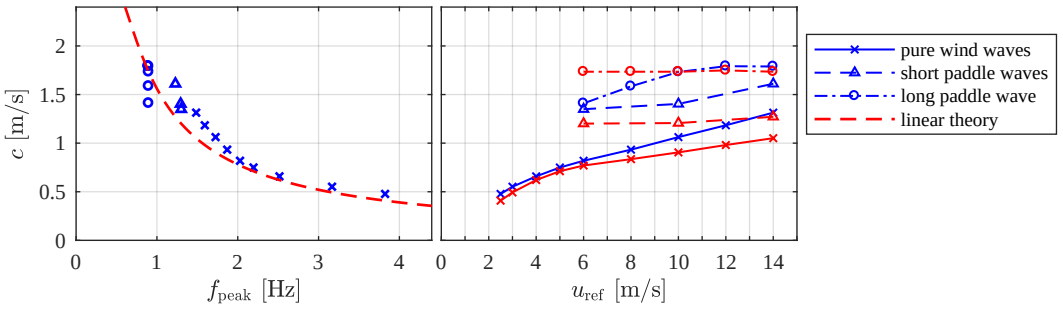

Figure 7.3: Phase speed of dominant wave estimated by correlation. The black symbols represent the measured values for c, while all red data points and the red dashed lines show the linear theory using the peak frequency of the energy density spectrum. Variations indicate mean flow at the upper layers in the tank.

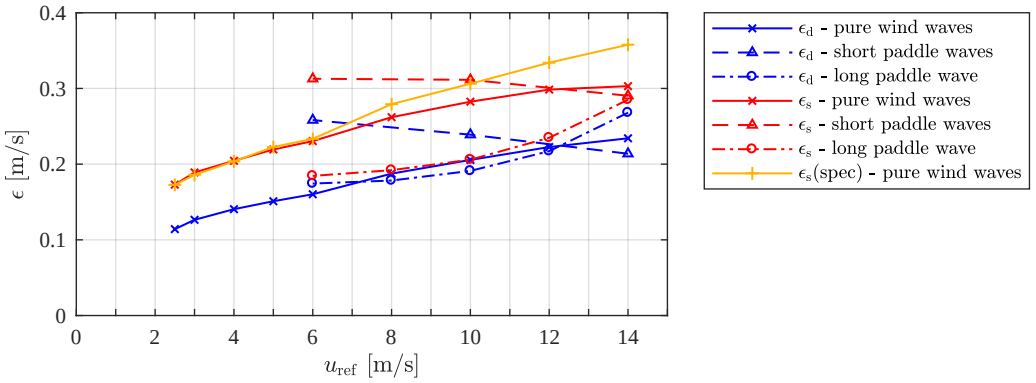

Figure 7.4: Wave steepness ϵ for different wave conditions at different wind speeds. The dominant wave steepness ϵ_d derived from the individual wave heights H, their individual wave period T and the dominant wave speed c, is shown in blue. Representing the mean of the highest third waves the significant wave steepness ϵ_s is plotted in red. For pure wind waves ϵ_s was also derived from the spectrum, which is shown in orange. For pure wind waves and long paddle waves the steepness is increasing for higher wind speeds, but not for short paddle waves.

7.1.4 Wave steepness

The knowledge of the phase speed the measured time series of the water elevation enables an estimation of the wave steepness ϵ (see section 2.2.4). Similar to the two expressions for the wave height (H_s and H_d) the dominant and significant wave steepness ϵ_d and ϵ_s were determined for all experiments. While $\epsilon_\mathrm{d} = \pi\overline{H/(cT)}$ represents the average over all measured waves, ϵ_s accounts only for the highest third.

Figure 7.4 shows the determined values of ϵ_d in blue and ϵ_s in red for all experiments. The different wave regimes are denoted by different symbols. Additionally, the significant wave steepness has been estimated directly from the frequency spectrum S_{η_t} of the temporal derivative of the water elevation (see equation 2.55), which is shown in orange. This formulation was derived under the assumption of a Rayleigh distribution, so only for pure wind waves it is a meaningful estimation. For low wind speeds up to

6 m/s the two methods give nearly the same results. For higher wind speeds the values estimated from the spectra are larger.

Regarding the dependency on the wind speed plotted on the x-axis the steepness increases for pure wind waves and long paddle waves with increasing u_{ref}. Short paddle waves show a different behavior. The significant wave steepness is constant and the dominant wave steepness slightly decreases.

Comparing ϵ_{d} and ϵ_{s} the difference is connected to the distribution of the frequency spectra. Pure wind waves and short paddle waves show a significant difference ($\epsilon_{\mathrm{d}} < \epsilon_{\mathrm{s}}$). The energy is broadly distributed on several wave modes with varying amplitudes, which results in different values for the total average and the average of the highest third. For long paddle wave ϵ_{d} and ϵ_{s} are very close, which demonstrates the homogeneity of this two dimensional single wave.

The significant wave steepness is a good parameter indicating the breaking state of a wave field. The higher ϵ_{s}, the more wave breaking occurs. The high values for short paddle waves and pure wind waves at high wind speeds are indicating high breaking rates, which coincides with the observations during the measurements. Wave fields with $\epsilon_{\mathrm{s}} \approx 0.3$ are including some waves exceeding the breaking criteria $(ak)_{\max} \approx 0.44$.

7.2 Time series of wind velocity

In this section some examples of the single air flow measurements are presented. The following plots (figure 7.5 to 7.7) show 2D velocity fields by blue vectors. In gray the surface elevation measured by the laser height camera is plotted. While the vertical represents the distance to the mean water surface, the x-axis shows the time. By use of the phase velocity the time scaling was chosen in a way, that the relation between the vertical and horizontal axes of the plot equals the relation between z and $x_{\mathrm{extr.}} = -c\,t$. This is also the reason for the inverse direction of the time axis.

Some plots are zoomed in for better investigating some single events like eddies or flow separation (e.g. figure 7.7). In all situations the distribution of the measurements is random and the wave is well sampled, even for short waves as shown in figure 7.5.

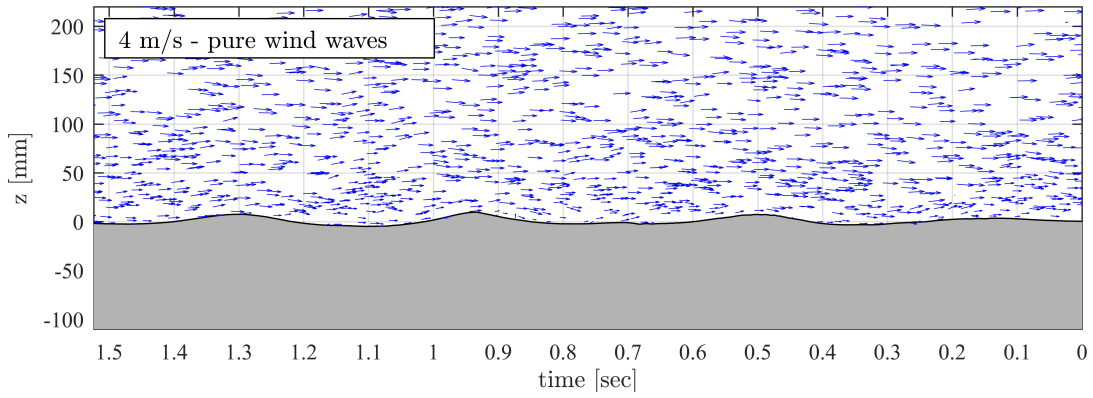

Figure 7.5: Example of measured wind velocity vectors illustrated by blue arrows at 4 m/s free stream wind speed and pure wind waves.

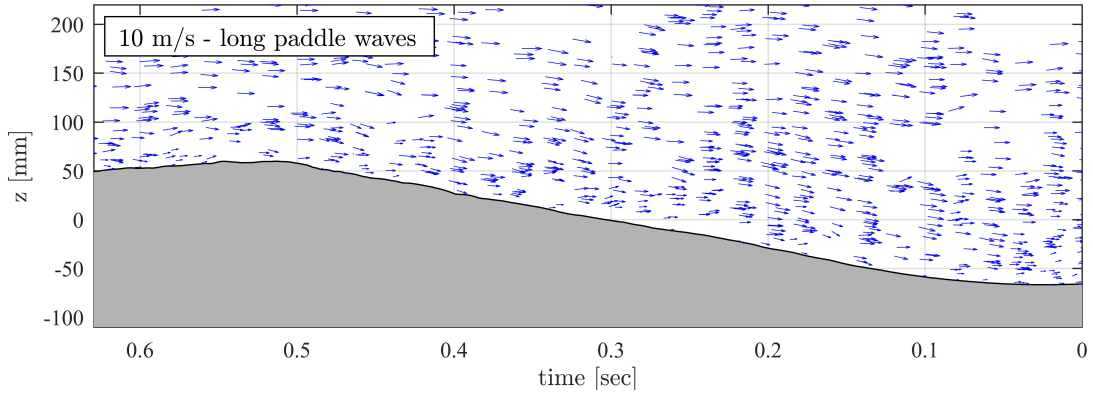

Figure 7.6: Example of measured wind velocity vectors illustrated by blue arrows at 10 m/s free stream wind speed and long paddle waves.

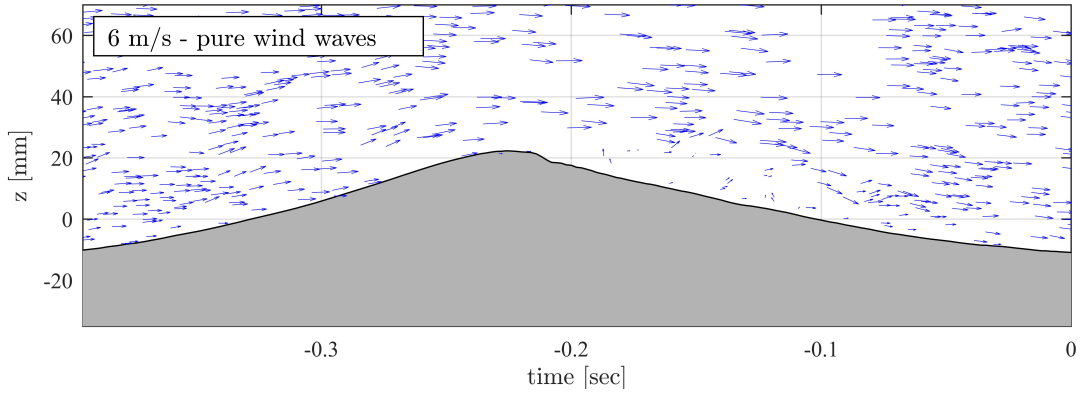

Figure 7.7: Example of measured wind velocity vectors illustrated by blue arrows at 6 m/s free stream wind speed and pure wind waves (zoomed view).

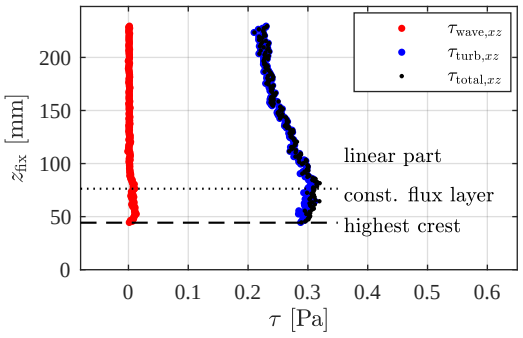

Figure 7.8: Vertical profile of stress in fixed coordinates. The total stress (black) is dominated by the turbulent Reynolds stress (blue) and the wave coherent flux is close to zero. Below ≈ 85 mm the total drag is rather constant, which represents the constant flux layer. Above τ decreases linearly with height.

7.3 Total drag and mean wind profile

In the following the range from the crests up to $\approx$ 230mm height above the mean water surface is considered in fixed coordinates in order to obtain the total momentum transport. Here all the time air is present and simple averages can be performed.

With the measurement of 2D velocity vectors $\vec{u} = (u_x, u_z)$ the total drag τ can be determined by two methods: by fitting the law of the wall in the logarithmic part of the velocity profile or by directly calculating the Reynolds stresses. Both have to be applied inside the constant flux region, which was experimentally found in linear wind wave facilities to be $10 - 15\%$ of the boundary layer thickness δ (Troitskaya and Rybushkina, 2008). For all experiments considered in this study the velocity measurement covers only the lower part of the boundary layer, hence the constant flux layer first has to be identified.

For this purpose the Reynolds flux was calculated and investigated dependent on z. Above the wave crests the viscous shear can be neglected and the total drag is compound by the turbulent shear stress $\tau_{\mathrm{turb},xz} = -\rho\overline{u_z' u_x'}$ and the wave coherent flux $\tau_{\mathrm{wave},xz} = -\rho\overline{\widetilde{u}_z \widetilde{u}_x}$. Figure 7.8 shows $\tau_{\mathrm{wave},xz}$ in blue, $\tau_{\mathrm{wave},xz}$ in red and the sum of both in black for measurements at 10 m/s with pure wind waves. In this case the turbulent part of τ dominates and the wave coherent fluctuations do not contribute significantly. Below ≈ 85 mm the total drag is rather constant, so this can be identified as the constant flux layer. Above τ decreases approximately linearly with height z, which is in agreement with other studies see Troitskaya et al. (2012) and Zavadsky and Shemer (2012).

A measure for the total drag for each condition was demanding. Using the logarithmic wind profile is problematic, because of two reasons. First the highest crest of paddle waves is in the same order of magnitude as the thickness of the constant flux layer (δ_τ), so the fitting region has to be chosen above leading to wrong values. The second reason is the waves themself, which are in the same order of magnitude as the large eddies inside the region of interest. Thereby the assumptions for the derivation of the law of the wall are not fulfilled anymore and it is unclear how this influences the profile.

Even for determining the total drag from the stress profiles the big paddle waves are challenging, because it is hard to identify the constant flux layer. Wave following coordinates can not be used, because due to the transformation of the momentum

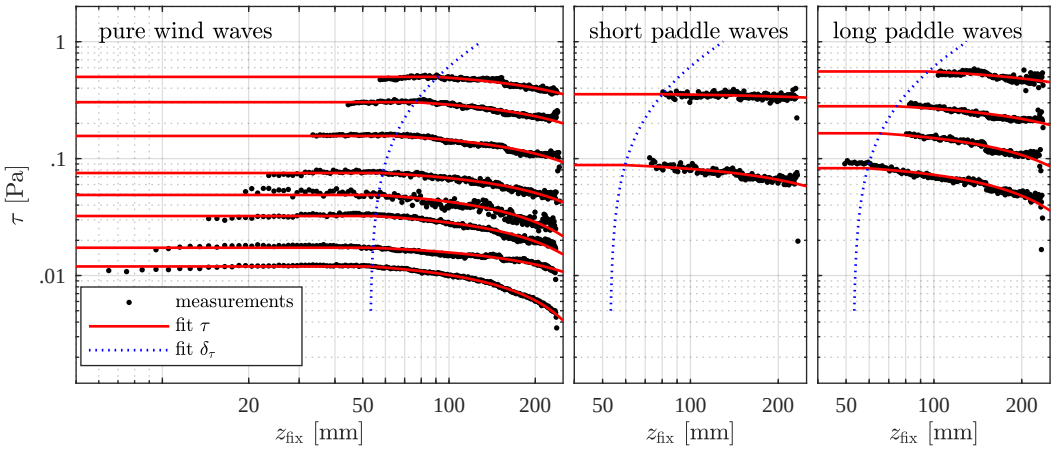

Figure 7.9: Profiles of total stress τ determined in fixed Cartesian coordinate. Black dots show the measured values above the highest crest. The thickness of the constant flux layer δ_τ (blue dotted line) was determined from the measurements above pure wind waves. Using a parametrization of $\delta_\tau(\tau)$ the profiles for paddle wave could be extrapolated into the constant flux layer, which is not resolved. Therby even for this conditions the total stress is determined.

equations pressure forces occur, which contribute to the total shear stress (see section 2.3.3). So without direct pressure measurements curvilinear coordinates do not solve the problem.

In order to determine the total drag despite of big waves the linear part of the stress profiles was also used. Under the assumption, that big waves do not change the thickness of the constant flux layer and δ_τ depends only on τ, the linear part was fitted and extrapolated, if waves are to high. First a parametrization of δ_τ was determined from the measurements at pure wind waves. The left plot in figure 7.9 shows the total stress profiles for all pure wind wave conditions by black dots. The height z measured from the mean water surface is drawn on the x-axis. A clear identification of δ_τ is possible. An linear behavior was obtained

$$\delta_\tau(\tau) = (76.8 \pm 27.5)\,\tfrac{\text{mm}}{\text{Pa}} \cdot \tau + (52.2 \pm 3.4)\,\text{mm}, \tag{7.1}$$

which is drawn in blue. With this dependency of $\delta_\tau(\tau)$ the height dependent two case function

$$\tau_{\text{fit}}(z) = \begin{cases} \tau & \text{for } z < \delta_\tau \\ m\,z + b & \text{for } z > \delta_\tau \end{cases} \tag{7.2}$$

has been fitted to all data sets, where m, b and τ were fitting parameters and so the total stress was determined. The results of this fit are shown by thin red lines in figure 7.9. The curved shape of these linear functions is an artifact of the double logarithmic scale. By this method even for high waves an estimation of τ could be made.

While the total drag and thereby also the friction velocity $u_{*,\text{a}}$ could be successfully determined from the stress profile, the roughness length z_0 (see section 2.3.2) cannot be extracted out of it. For determining z_0 the velocity profile was regarded and with

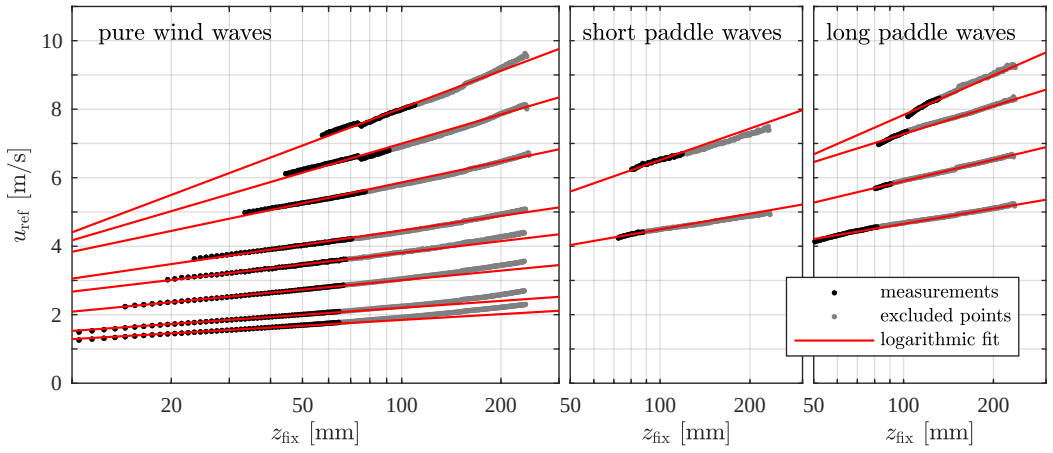

Figure 7.10: Wind profiles for all measurements at different conditions. Logarithmic fits (red line) have been performed to determine the roughness length z_0. $u_{*,\mathrm{a}}$ was fixed by use of the values obtained from the stress profiles. Points above a certain point (shown in gray) are excluded.

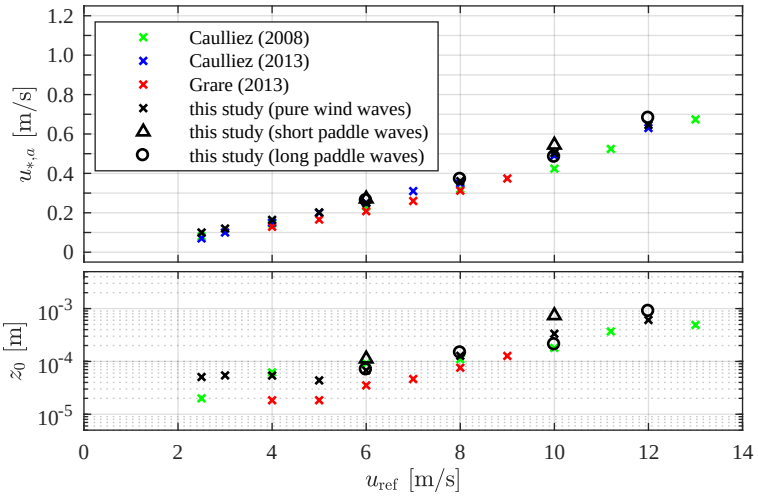

Figure 7.11: Friction velocity $u_{*,\mathrm{a}}$ and roughness length z_0 dependent on the free stream wind speed u_{ref}. The comparison with earlier studies at the same location (colored points) shows coincidence with the results of this study (black). A slight increase of $u_{*,\mathrm{a}}$ and z_0 for short paddle waves can be obtained.

the known $u_{*,\mathrm{a}}$ a logarithmic fit was performed, where the roughness length is the only free parameter. Figure 7.10 shows the velocity profiles and these fits for all measured conditions. The region, where the fits have been applied is marked in black, while gray dots are not considered.

The results of $u_{*,\mathrm{a}}$ and z_0 are presented in figure 7.11 in black, different symbols represent different wave conditions. Also shown are measurements obtained by earlier studies by Caulliez et al. (2008), Caulliez (2013) and Grare et al. (2013), who measured in the same facility at comparable fetch. The measurements coincide within the scattering of the different experiments. A small increase of $u_{*,\mathrm{a}}$ and z_0 for short paddle waves can be obtained.

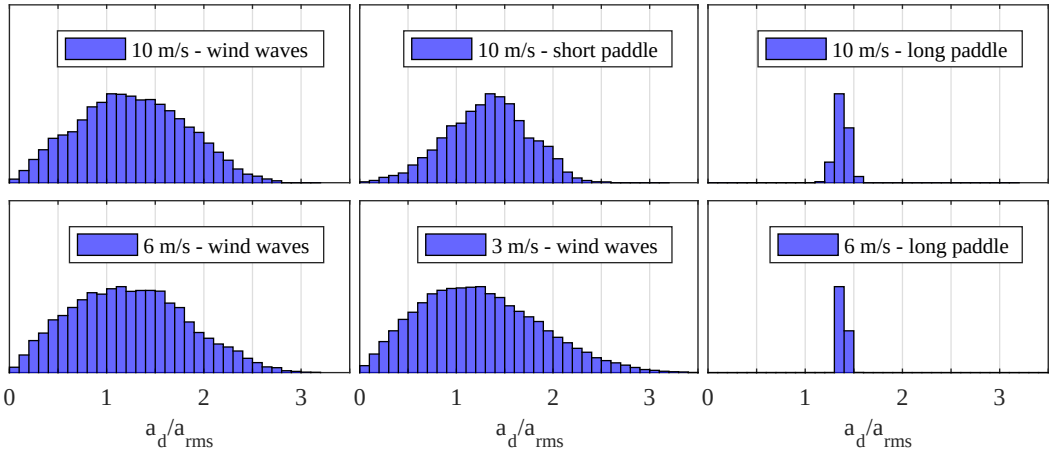

Figure 7.12: Histogram of dominant amplitude obtained by the Hilbert transform of the smoothed wave ($0.5 f_{\mathrm{peak}} - 1.5 f_{\mathrm{peak}}$). While long paddle waves have one sharp peak, short paddle and pure wind waves have a wide distribution, which is especially for wind waves close to the Rayleigh distribution.

7.4 Phase dependent velocity fields

The phase of the dominant wave can be obtained by applying the Hilbert transform on the smoothed wave height-time-signal. Thereby the phase ϕ as well as the dominant amplitude a_{d} is determined for each point in time of a measured sequence (see section 6.3). This enables phase dependent averaging of the velocity vectors, introduced as the triple decomposition (see equation 2.67 to 2.69).

As shown in figure 6.5, this method only gives meaningful results, if the amplitude exceeds a certain value. For long paddle waves this is always fulfilled, but for pure wind waves and short paddle waves regions appear, where the phase extraction leads to wrong results. These regions can be identified by looking at the dominant wave amplitude a_{d}, which drops there significantly. Figure 7.12 shows the distribution of a_{d} normalized by the root mean square wave amplitude a_{rms} for several conditions. Long paddle waves have a single peak at $\approx 1.4\, a_{\mathrm{rms}}$. Pure wind waves have distributions close to the Rayleigh distribution, which agrees with theory (see Massel, 2013). Short paddle waves are something between.

The following two sections show phase dependent mean velocity fields using the triple decomposition. While for long paddle waves a simple phase decomposition was performed, for short paddle and pure wind waves the sequence was split into three classes depending on the the dominant wave amplitude.

The phase dependent averaging was performed by using bins of width $\Delta\phi = \pi/12$ in phase and $\Delta z = 1\,\mathrm{mm}$ in vertical direction. This was applied for fixed coordinates, as well as for wave following coordinates, using the two different mappings described in section 2.3.3. The simple shift coordinate transform (equation 2.80) is adding the actual surface elevation to the vertical coordinate and the declining shift mapping (equation 2.81) considers the Fourier modes of the wave profile leading to wave following

coordinates, which change into Cartesian coordinates with increasing distance to the water surface.

7.4.1 Long paddle waves

Figure 7.13 shows an example of the averaged flow field above a long paddle wave at 12 m/s wind. The left plots show the different velocity components, where the color indicates the magnitude – yellow represents high velocities and blue zero or negative values, respectively. By the black line and gray color below, the mean phase dependent water elevation is plotted. It is illustrated in Cartesian coordinates, even if the binning was performed in wave following coordinates. So the position of each bin represents the mean height z of this bin and the phase, which is drawn on the x-axis. The wave following vertical coordinates z^* of these bins are indicated by thin gray lines in the lower plots, which represent the simple shift and the declining shift mapping, respectively. At the right of figure 7.13, the phase averages are plotted. Here the vertical coordinate represents z^*, the average was performed along layers of constant z^*.

The uppermost plot shows the horizontal velocity component as the sum of the phase averaged $\overline{u}_x$ and the phase dependent part $\widetilde{u}_x$. This illustration shows the structure of the boundary layer, which has higher gradients at the wind ward side of the crest than at the lee side, where the wind speed is significantly smaller. This behavior is typical for air flow separation, the rapid air parcels shoot over the wave crest and are not able to follow the surface form anymore. Additionally, above the crest the velocities are increased in comparison to above the troughs, which is simply due to compression of the flow. The phase averaged profile plotted at the right has a smooth shape and looks similar to a regular boundary flow profile, all phase dependent variations are averaged to zero.

The plot below shows the vertical velocity component also as sum of $\overline{u}_z$ and $\widetilde{u}_z$. Here the upward flow at the windward side and the downward flow at the lee side of the crest is clearly visible. The phase averaged profile shows increased values close to the surface, which first seems to be unrealistic, but will be explained in the following.

The third and forth plot illustrates the transformed velocity components U_z, which represent the flow through layers, of constant wave following coordinate z^*. Regarding the phase averaged profiles $\overline{U}_z$ they are almost zero, independent of the used mapping. This shows, that the increased values of $\overline{u}_z$ are caused by averaging along a curved layer without regarding the horizontal flow components, which are contributing to the mean flux through this layer. Thereby continuity is fulfilled, because the mean surface height is constant and there should be no mean flux downwards.

The color-plots of the phase dependent averages $\overline{U}_z + \widetilde{U}_z$ differ from the pure Cartesian components and depend on the applied mapping. The simple shift (third plot from top) leads to negative values at the windward side and positive values at the lee side, especially with increasing distance to the water surface. Close to the water surface it is close to zero, meaning the flow is following the coordinate z^*. Above, the curved

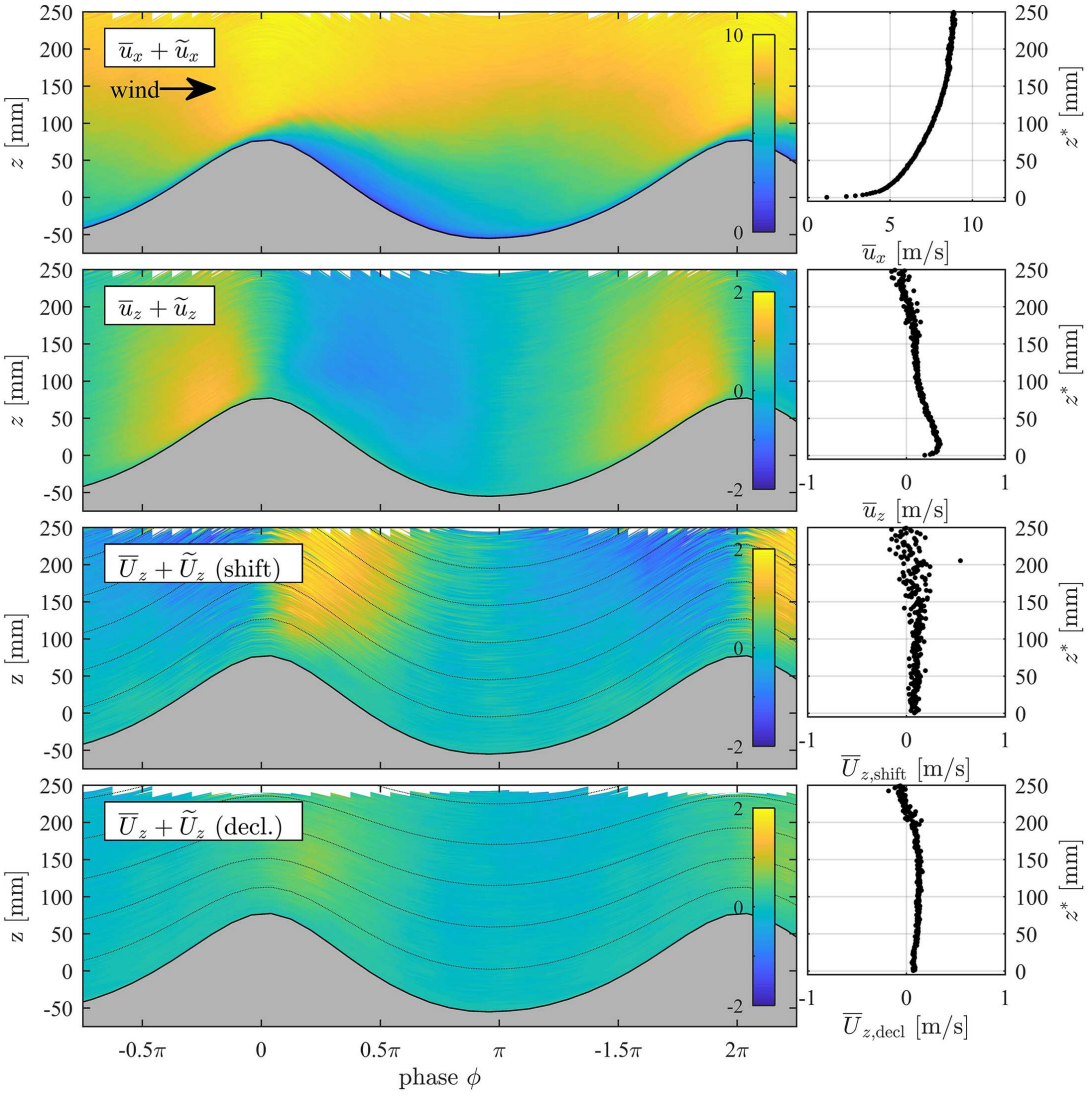

Figure 7.13: Averaged velocity fields at 12 m/s with long paddle waves. The phase dependent average of the respective velocity component is illustrated by color. Yellow indicates high and blue low or negative values. On the right the phase averaged profiles in wave following coordinate z^* are plotted. The horizontal velocity shown in the uppermost plot illustrates the boundary layer close to the water at the windward side of the crest. At the lee side, the velocities are much lower caused by flow separation. The comparison of the vertical Cartesian velocity u_z with the transformed velocity components U_z depicts the influence of the mapping. The declining shift transformation represents better the mean flow, than the simple shift.

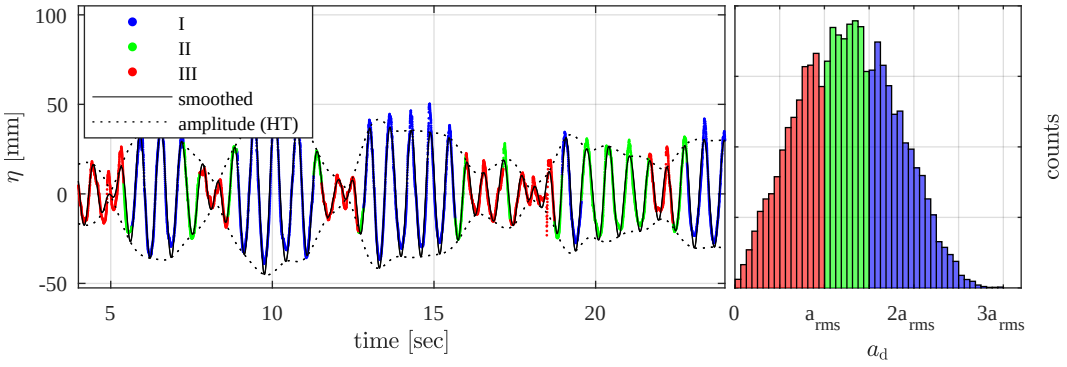

Figure 7.14: Binning in three amplitude classes exemplary for 12 m/s and pure wind waves. The measured sequence is separated in three classes with equal number of counts. Colors indicate the different classes: blue for class I (high amplitude waves), green for class II (medium waves) and red for class III (low amplitude waves). At the right the distribution of the dominant amplitude a_d is shown, which is used as selection criterion.

layers are not representing the flow anymore, which leads to increased magnitudes. The transformed vertical components with declining shift have much smaller magnitudes. Hence these coordinates describe the mean flow above waves better .

Similar behaviors were observed for the other long paddle wave conditions at lower wind speeds, where the air flow separation is less pronounced, but the characteristic of the flow is the same.

7.4.2 Short paddle waves and wind waves

In order to apply phase averaging on the air flow above pure wind waves and short paddle waves the sequences are split into three classes using the dominant wave amplitude a_d. These classes are chosen to achieve equal number of counts, so class I represents the third of the high amplitude waves, class II the medium and class III the low amplitude waves. Figure 7.14 shows an example of a time series of the wave elevation, where the separation in those three classes is illustrated by colors. While the colored dots represent the measured wave elevation, the smoothed signal on which the Hilbert transform have been applied is drawn by a black line. The smoothing in Fourier space only maintains the dominant modes around the peak frequency of the energy spectrum. This causes deviations in comparison to the real signal, especially at the peaks and for short waves. For that reason, the dominant amplitude a_d is only used for classifying and not for wave analysis.

Figure 7.14 shows the averaged velocity fields for a wind speed of 12 m/s and pure wind waves. The figure is similar structured as figure 7.13 (averaged phase dependent velocity field over long paddle waves), with the difference that the three classes are shown separately. The vertical coordinate represents the height in fixed coordinates (color plots) or wave following coordinates (profiles), respectively. The phase of the

dominant wave is drawn on the x-axis, while for class III (low amplitude waves) no phase binning is applied. Here the method to extract the phase is not working robustly.

The structure of the velocity fields, shown in figure 7.15, is comparable to those above long paddle waves, even if the magnitude of the mean wave elevation is significantly lower. The regions of low horizontal velocities behind the wave crest is smaller in class II than in class I, the same is the case, for the upward and downward velocities on both sides of the crest. Also for this condition the declining shift mapping gives minimum magnitudes of $\overline{U}_z + \widetilde{U}_z$, the velocity component through layers of constant z^*.

Comparing all wind-wave conditions, the structure of the velocity fields differs only in magnitudes. Overview plots of all measurements are shown in the appendix (Reference), where the horizontal and vertical Cartesian velocity fields are illustrated by color-plots. In general the flow characteristics scale with the wave heights: the higher the waves, the more pronounced the flow separation. With increasing wave height also the wave coherent flow structures are ranging to larger distances to the water surface (see appendix A.3).

7.5 Partitioning of momentum transfer

The previous section shows the characteristics of the air flow above gravity waves, which is more a qualitative observation. This section focuses on the partition of the momentum transfer into turbulent Reynolds stresses, wave coherent fluxes, viscous shear and pressure forces, which is strongly connected to the flow structures.

7.5.1 Turbulent and wave coherent fluxes

First the turbulent and wave coherent fluxes are investigated. These can be directly determined by calculating $\widetilde{\tau}_{\mathrm{turb},xz^*} = -\rho_\mathrm{a} \left\langle U_z' u_x' \right\rangle$ and $\widetilde{\tau}_{\mathrm{wave},xz^*} = -\rho_\mathrm{a} \widetilde{U}_z \widetilde{u}_x$, which leads to phase and height resolved stress fields. Phase averaging leads to $\overline{\tau}_{\mathrm{turb},xz^*}$ and $\overline{\tau}_{\mathrm{wave},xz^*}$ representing the averaged flux through a layer of constant wave following heigh z^*. Here, the considerations in wave following coordinates are used (see section 2.3.3), because fixed coordinates are not meaningful at heights below the highest crest. It has to be noted, that different mappings lead to different results, which will be shown in detail in section 7.5.3 and is also indicated by the velocity fields presented in the previous section 7.4. In this section only the declining shift mapping is used, which best describes the averaged flow.

Exemplary measurements at a wind speed of $12\,\mathrm{m/s}$ above long paddle waves are shown in figure 7.16. The color-plots illustrate the phase dependent turbulent flux (top) and wave coherent flux (bottom). Yellow indicates positive stresses representing downward momentum transport, blue indicates negative stresses representing upward momentum transport. At green regions the stress is close to zero. Similar to the velocity plots, the vertical coordinates represent the fixed coordinate z, layers of constant wave

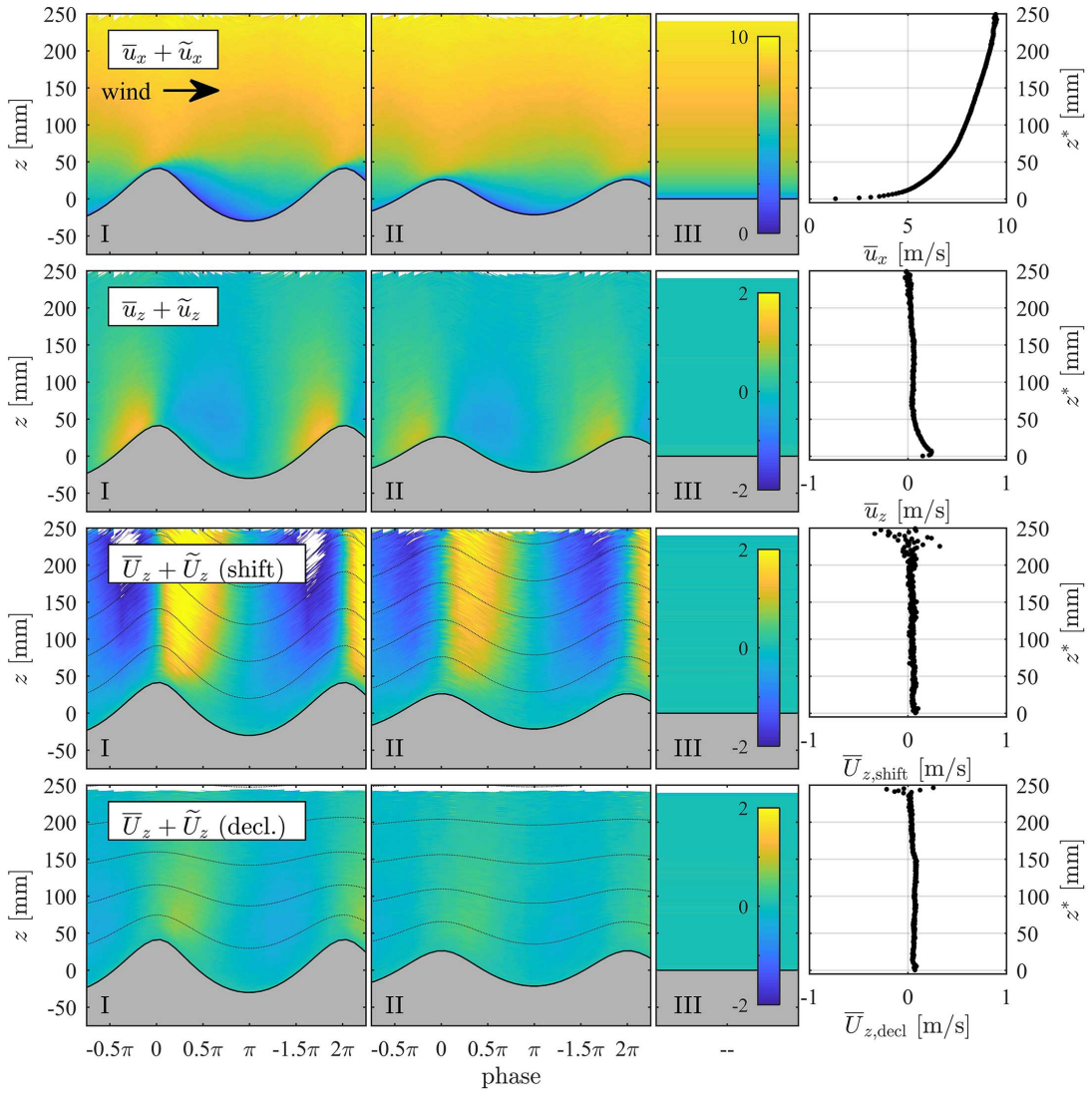

Figure 7.15: Averaged velocity fields at 12 m/s with pure wind waves. The magnitude phase dependent average of the respective velocity component is illustrated by color. Yellow indicates high and blue low or negative values. On the right the phase averaged profiles in wave following coordinate z^* are plotted. The horizontal velocity shown in the uppermost plot illustrates the boundary layer close to the water at the windward side of the crest. The magnitudes of the varying structures (air flow separation, thinning of the boundary layer at the windward side, up- and downward velocities) are less pronounced for medium waves (class II) than for high waves (class I). For low amplitude waves (class III) no phase separation is applied.

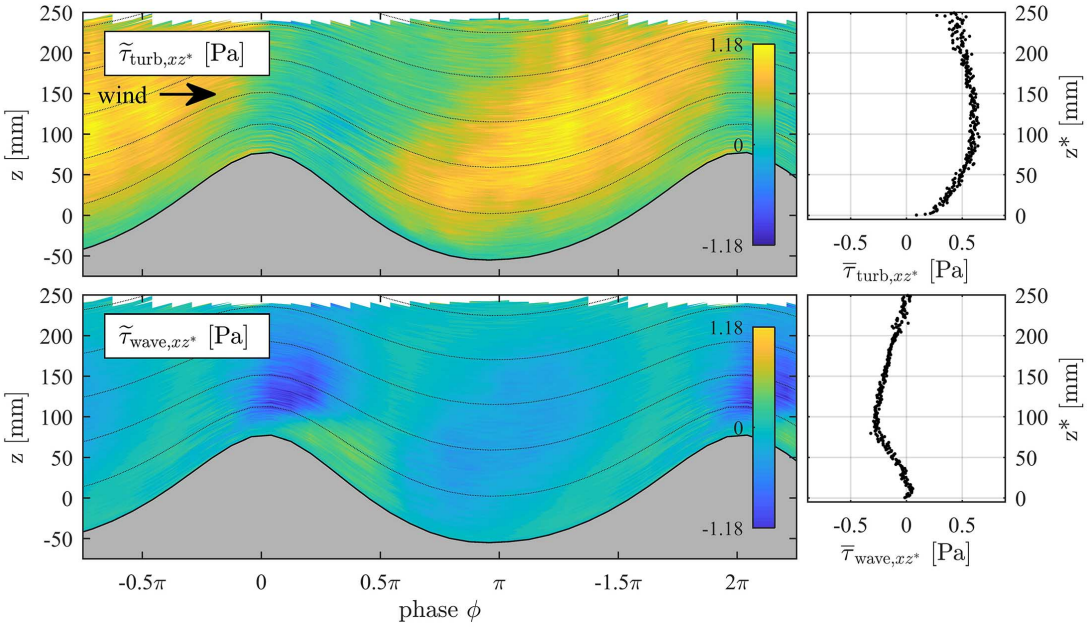

Figure 7.16: Turbulent and wave coherent stress distribution at 12 m/s wind speed with long paddle waves. Color indicates the magnitude of $\widetilde{\tau}_{\mathrm{turb},xz^*}$ and $\widetilde{\tau}_{\mathrm{wave},xz^*}$, respectively. At the right phase averaged profiles along layers of constant wave following coordinate z^* show positive values for turbulent and negative values for wave coherent fluxes.

following coordinates ($z^* = \text{const.}$) are represented by thin gray lines.

The distribution of turbulent stress $\widetilde{\tau}_{\mathrm{turb},xz^*}$ ranges from zero right behind the crests to positive values above the troughs and at the windward side of the crests. Close to the water surface $\widetilde{\tau}_{\mathrm{turb},xz^*}$ drops to zero, where the gradient at the wind ward side seems to be higher than at the lee side. The phase averaged profile plotted at the right has its maximum at a height of $z^* \approx 100\,\mathrm{mm}$, which coincides with the thickness of the constant flux layer determined in section 7.3. Its magnitude is around half of the maximum of all phase dependent turbulent stresses.

The wave coherent momentum flux shows negative values right above the crests and a slightly positive region, where flow separation occurs. Everywhere else $\widetilde{\tau}_{\mathrm{wave},xz^*}$ is around zero. The strong negative region can be explained by fast flow overshooting the wave, which is not able to follow the surface profile. Thereby momentum is carried upwards. This is also present in the phase averaged profile, which is mostly negative.

By comparing the different measurements at varying wind-wave conditions, in general the magnitude of the effects is scaling with the wind speed and the amplitude of the waves (see appendix A.3).

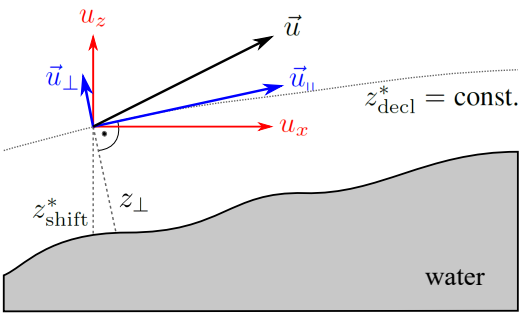

Figure 7.17: Decomposition of a velocity vector $\vec{u}$ near the water surface into a component $\vec{u}_\parallel$ parallel to a layer of constant wave following coordinate z^* and a perpendicular component $\vec{u}_\perp$.

7.5.2 Estimation of viscous stresses

To investigate the momentum transport above surface waves correctly using wave following coordinates is essential. The viscous shear stress acting on a layer of constant wave following coordinate z^* is $\tau_{\mathrm{visc},xz^*}$, which can be expressed by the Cartesian components $\tau_{\mathrm{visc},xx}$, $\tau_{\mathrm{visc},xz}$ of the viscous stress tensor and the derivative of the mapping function $\partial f/\partial x$ (see equation 2.88).

If the stress is aligned with the layer of a constant z^*, $\tau_{\mathrm{visc},xz^*}$ equals its magnitude $\tau_{\mathrm{visc},\parallel}$. The x-length of a transformed infinitesimal fluid parcel is stretched, which compensates the partitioning of $\tau_{\mathrm{visc},\parallel}$ into $\tau_{\mathrm{visc},xx}$ and $\tau_{\mathrm{visc},xz}$. A more detailed derivation is added in the appendix (A.1). In this case it is sufficient to determine the viscous stress component parallel to such layers of constant z^*, which is expressed by

$$\tau_{\mathrm{visc},xz^*} = \tau_{\mathrm{visc},\parallel} = \mu \frac{\partial u_\parallel}{\partial z_\perp}, \tag{7.3}$$

where μ is the kinematic viscosity, $u_\parallel$ is the parallel part of a velocity vector and $z_\perp$ denotes the normal distance to the water surface. The only assumption is, that there are no stress contributions perpendicular to this layer of constant z^*, which is fulfilled, if $u_\perp$ is zero. Figure 7.17 sketches the decomposition of a vector $\vec{u}$ (black) into a parallel and perpendicular part (blue).

Viscous stress is defined by velocity gradients, which cannot be determined directly by the measurements made in this study, where only randomly distributed velocity vectors are available. The only way to still measure viscous stress is to consider averaged velocity profiles and calculate the gradient, which results in an averaged viscous shear. In equation 7.3 the parallel velocity has to be replaced by an average, the structure of the equation keeps the same.

To obtain this averaged parallel shear stress close to the water surface phase dependent profiles of $u_\parallel$ against $z_\perp$ were regarded. The up and downward velocity of the surface was corrected by subtracting the elevation speed $\partial\eta/\partial t$. In figure 7.18 an example of such a profile is presented. Also shown there is a profile of $u_\perp$ against $z_\perp$, which satisfies the assumption of $u_\perp \approx 0$ in the regarded region. The single gray points represent the single measurements, the black dots are averages with $\Delta z = 0.1\,\mathrm{mm}$

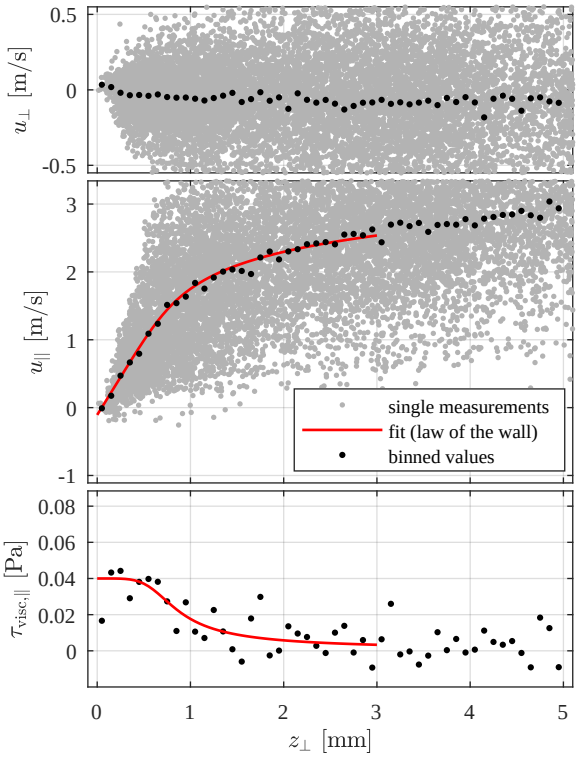

Figure 7.18: Velocity profiles and viscous shear profiles close to the water surface, measured at 6 m/s free stream wind speed and long paddle waves. Gray dots show the single measurements and black dots represent averaged values with bins of 0.1 mm width. The top plot shows the perpendicular velocity component $u_\perp$, which is on average close to zero. The averaged profile of the parallel component $u_\parallel$ against the distance to the water surface (middle plot) shows a linear shape very close to the water surface. With increasing $z_\perp$ the profile transitions to turbulent and becomes more flat. With a red line a numerical fit using the law of wall is shown, which fits the shape of the averaged data points. The plot at the bottom shows the viscous shear $\tau_{\mathrm{visc},\parallel}$ calculated from the gradient of the averaged profile (black) and as result of the fit (red).

bin size. Very close to the water below approximately 0.5 mm a linear behavior of the mean profile is present in this example. Above 0.5 mm the profile becomes more flat indicating the transition to the turbulent regime. The first approach to obtain the viscous shear is to look at the gradient of this averaged profile. The resulting values already slightly smoothed are presented by black dots in the third plot at the bottom of figure 7.18. Despite of large scattering the values show the expected shape (see 2.3.1): maximum at the water surface and dropping to zero with increasing distance to the surface.

Close to the water surface inside the viscous boundary layer the flow can be regarded as smooth. The roughness elements of the water surface represented by waves with wavelengths ranging from centimeters to meters are larger than the regarded thickness of < 5 mm. Thus the law of the wall in its implicit formulation (equation 2.66) well describes the velocity profile. In order to achieve a robust method and also make use of the transition from laminar to turbulent flow, this implicit formulation was fitted numerically to the data. This fitting was performed in two steps, a first estimation of the individual stress and a second fit, where the regarded region was limited to $z^+ < 30$. The dimensionless vertical coordinate z^+ needed for the second step (compare sectio 2.3.1) was estimated from the results of the first step. In figure 7.18 the result of this fit is plotted by a red line, which coincides with the binned values. Also the resulting stress profile shown in the plot at the bottom is positioned between the scattered points.

By this method the phase dependent viscous stress inside the boundary layer could be

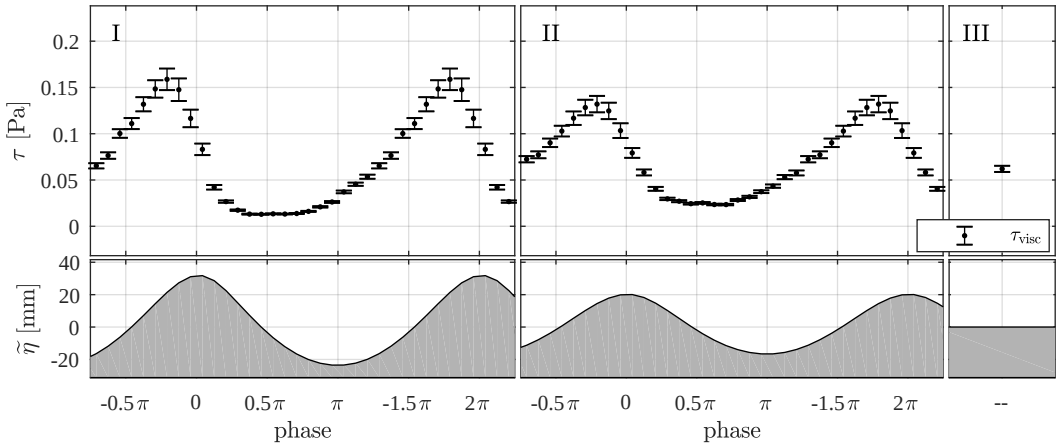

Figure 7.19: Phase dependent distribution of viscous shear $\widetilde{\tau}_{\mathrm{visc},\parallel}$ directly above the water surface at 10 m/s and pure wind waves. Slightly shifted in phase a strong dependency on the dominant phase is present. Class I (high amplitudes) shows much higher variations than class II (medium waves).

measured for all conditions, even for high wind speeds up to 12 m/s, where the viscous part in the boundary layer is in the order of 0.1 mm.

Figure 7.19 shows the measured phase dependent values of $\widetilde{\tau}_{\mathrm{visc},\parallel}$ (obtained by fitting the law of the wall for each phase independently) for such a high wind speed condition at 12 m/s above pure wind waves. The black dots show the results of the fit, representing the viscous shear stress directly at the surface and inside the viscous boundary layer. By numerically fitting, an uncertainty was obtained, which is demonstrated by black error bars. The wave elevation is illustrated by the phase averaged wave profile for each wave amplitude class, respectively. In class III, which represents low amplitude waves, no phase binning was performed. $\widetilde{\tau}_{\mathrm{visc},\parallel}$ shows high phase dependent variations, especially above large waves in class I. At the windward side of the crest the maximum is reached and directly behind the crest $\widetilde{\tau}_{\mathrm{visc},\parallel}$ drops. This coincides very well with the observed flow field and can be explained by flow separation. Also the turbulent stress shows a similar distribution close to the water surface – high values at the windward side, low values at the lee side.

The phase dependent results for all conditions are presented in the overview plots in the appendix (A.3). The general conclusion is: the higher the waves, the higher the variances. The phase dependent distribution of $\widetilde{\tau}_{\mathrm{visc},xz^*}$ is comparable to the results of measurements in water (e.g. Okuda, 1982a; Peirson and Garcia, 2008), which also show large enhancements right before the crests.

For the exchange of mass and heat through the interface as well as for wave growth it is important how the total stress is partitioned directly at the water surface. Even if the pressure was not measured, the relation of the viscous stress $\overline{\tau}_{\mathrm{visc},\parallel}$ averaged over all phases to the total stress $\tau = \rho_{\mathrm{a}} {u_{*,\mathrm{a}}}^2$ derived by the total stress profiles in fixed coordinates (section 7.3) shows the partitioning, because the wave coherent and

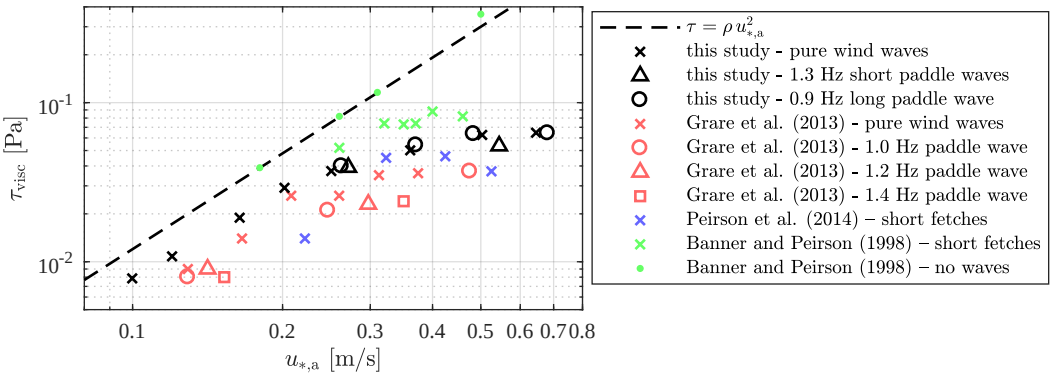

Figure 7.20: Averaged viscous shear stress τ_{visc} against the air sided friction velocity $u_{*,\mathrm{a}}$. All measurements of this study (black symbols) are significantly below the reference (black dashed line). With increasing friction velocity τ_{visc} seems to saturate below $0.08\,\mathrm{Pa}$. Measurements above short paddle waves show slightly lower values than for pure wind waves and long paddle waves. Measurements of other studies show the same behavior with more scattering.

turbulent stress vanishes.

Figure 7.20 shows the results of $\overline{\tau}_{\mathrm{visc},\parallel}$ (denoted as τ_{visc} in the following) against the air sided friction velocity $u_{*,\mathrm{a}}$ (see section 7.3). The reference of $\tau = \rho_{\mathrm{a}} {u_{*,\mathrm{a}}}^2$ is plotted by the black dashed line. All conditions show significantly lower values as the reference. With increasing friction velocity also the difference increases and the τ_{visc} seems to reach saturation below $0.08\,\mathrm{Pa}$. The different wave conditions (pure wind waves, short paddle waves and long paddle waves), which are illustrated by different symbols are showing slightly different values. Especially short gravity waves have lower values of τ_{visc}. All uncertainties are in the range of few percent, so they are not plotted.

By red symbols measurements performed by Grare et al. (2013) are shown. They have been measured at the same location in the same wind-wave facility by using a hot wire anemometer, which was repeatedly plunged into the water. Different symbols again denote different wave conditions also using paddle waves. This data points are significantly lower than those measured in this study and showing larger scattering. By blue and green crosses the viscous shear stress measured in water at short fetches by Banner and Peirson (1998) and Peirson et al. (2014) is plotted. The green dots also measured by Banner and Peirson (1998) at very short fetches, where no waves were present, are very close to the reference, so here all the shear is transported by viscosity. This large scattering gives reason to assume, that the relation of τ_{visc} and τ is strongly connected to the wave state. But as usual for experimental investigations systematical errors can not be excepted.

7.5.3 Height dependent momentum budget

Using wave following coordinates the turbulent, the wave coherent and the viscous stress contributions could be obtained from the air side velocity measurements above

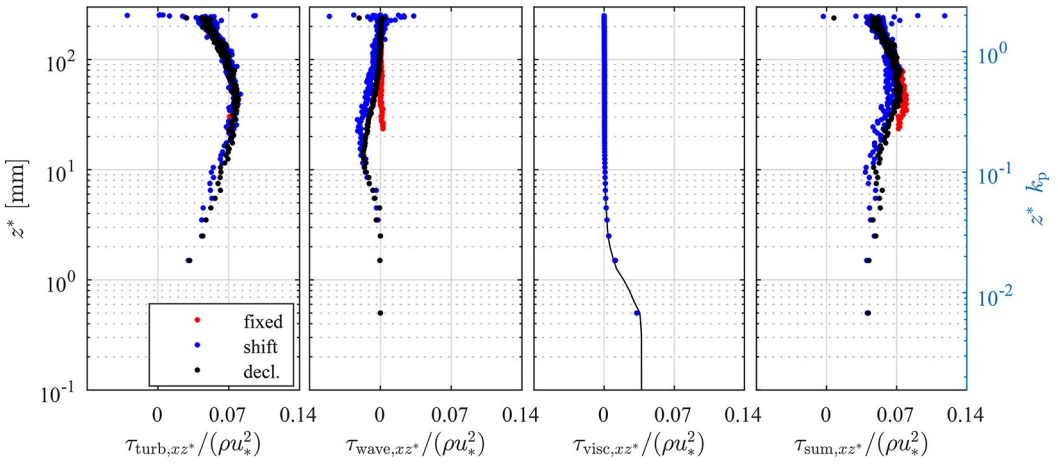

Figure 7.21: Influence of different mappings on the single stress contributions demonstrated for a condition at 6 m/s and pure wind waves. Results obtained in fixed coordinates above the highest crest are shown in red, in simple shift wave following coordinates in blue and in declining shift coordinates in black. While the profiles of turbulent and viscous stress are very similar, the wave coherent fluxes give slightly different results, which also affects the sum of all three. Declining shift coordinates have less scattering than simple shift coordinates.

water waves. So except for pressure forces, all contributions to the momentum budget are available and can be studied in dependency on the wave following coordinate z^*. Additionally, the assumption of a constant total drag τ inside the constant flux layer with its thickness δ_τ and its estimation from considerations in fixed coordinates (see section 7.3) gives the opportunity to close this height dependent momentum balance.

In section 7.4, where phase dependent velocity fields are presented, it is outlined, how different mappings lead to different transformed velocity vectors U_z. Since these are used to determine the turbulent and wave coherent fluxes $\tau_{\mathrm{turb},xz^*}$ and $\tau_{\mathrm{wave},xz^*}$, different mappings also lead to different values of phase averaged stress contributions. This can be simply explained: These phase averaged stresses are representing momentum fluxes through layers of constant z^*. Different mappings lead to different layers and thereby also the stress contributions change.

In figure 7.21 the height dependent phase averaged stresses $\overline{\tau}_{\mathrm{turb},xz^*}$, $\overline{\tau}_{\mathrm{wave},xz^*}$, $\overline{\tau}_{\mathrm{visc},xz^*}$ and the sum of all three $\overline{\tau}_{\mathrm{sum},xz^*}$ are shown for the two used mappings, simple shift in blue and declining shift in black. Additionally the results obtained in fixed coordinates are shown in red, where z^* equals z. While $\overline{\tau}_{\mathrm{turb},xz^*}$ and $\overline{\tau}_{\mathrm{visc},xz^*}$ are nearly independent on mapping (if no points of a color are visible, they are hidden by the others), $\overline{\tau}_{\mathrm{wave},xz^*}$ varies significantly, which also leads to different results of the sum of all three. Comparing the single profiles, the declining shift mapping leads to less scattering. A possible explanation for that could be, that here the layers of constant z^* better follow the mean flow and thereby lead to more robust estimates, so for all following considerations only the declining shift mapping is used.

While the vertical axes in figure 7.21 represent the wave following coordinate z^*

in mm (scale shown at the left), an additionally scale of the wave following height normalized by the wave number of the spectral peak k_p is shown at the right in blue color. This scaling gives the opportunity to compare the stress partitioning above water waves with different wavelengths. Such a comparison is presented in figure 7.22 and 7.23, where the stress partitions normalized by the total drag τ is shown. The different contributions are plotted by different colors and are divided by τ, which was derived from stress profiles in fixed coordinates (see section 7.3) and is also shown as a black line. The wave number k_p was estimated from the peak frequency of the energy spectrum and the measured phase velocity c.

The green dots in figure 7.22 and 7.23 represent the sum of turbulent, wave coherent and viscous stress contributions. While the turbulent stress in some conditions exceeds the total drag (black lines), the sum is significantly smaller close the water surface and matches τ with increasing height. From the difference between $\overline{\tau}_{\mathrm{sum},xz^*}$ and τ an estimation of the contribution of pressure forces $\overline{\tau}_{\mathrm{pres},xz^*}$ was made, which is shown in orange and closes the momentum budget. For all conditions $\overline{\tau}_{\mathrm{pres},xz^*}$ has its maximum close to the surface, where the turbulent and wave coherent stresses drop to zero. With increasing height $\overline{\tau}_{\mathrm{pres},xz^*}$ decreases and is close to zero at a normalized height of $z^*k_\mathrm{d} \approx 1$. At some high wind speed conditions with paddle waves the pressure contribution also decreases at $z^*k_\mathrm{d} \approx 0.1$, where also $\overline{\tau}_{\mathrm{wave},xz^*}$ changes. While for all conditions the wave coherent fluxes show negative values at the region between 0.1 and 1 and are close to zero above and below, only these conditions show positive values around 0.1. This effect only occurs for high wind speeds relatively large waves. For lower wind speeds no such effect can be observed.

In general the stress partitions agree with other studies. Hara and Sullivan (2015) showed by direct numerical simulations, that stress partition profiles have the same characteristics at conditions with low wind speeds. Their profiles also show negative values of $\overline{\tau}_{\mathrm{wave},xz^*}$ between $z^*k_\mathrm{d} \approx 0.1$ and $z^*k_\mathrm{d} \approx 1$ and the structure of the pressure stress profile is very similar to the results obtained in this study.

Buckley and Veron (2016) (continued in Buckley and Veron, 2017) presented profiles of wave coherent stresses having also positive regions below $z^*k_\mathrm{d} \approx 0.1$, especially for very high wave ages. These were realized by low wind speeds ($u_{10} < 6\,\mathrm{m/s}$) and mechanically generated long waves (f_p ranging from 0.5 to 1.2). At this regime the positive regions are found below the critical height z_c, where the mean flow velocity equals the phase speed. In order to compare this effect with the measurements of this study, the critical height z_c is plotted in figure 7.22 and 7.23 by black dotted lines. But in contrary to Buckley and Veron (2016) z_c is significantly below the region of positive $\overline{\tau}_{\mathrm{wave},xz^*}$, which is probably caused by the high wind speeds. In comparison to Buckley and Veron (2016) the amplitudes of the paddle waves were much larger (factor 2-3) and the wind speeds over these were significantly higher.

Regarding the phase dependent stress distribution in general (see overview plots in the appendix A.3) the positive regions of $\overline{\tau}_{\mathrm{wave},xz^*}$ appear right behind the crests, where sheltering effects are present. So this effect probably is connected to the strength of air

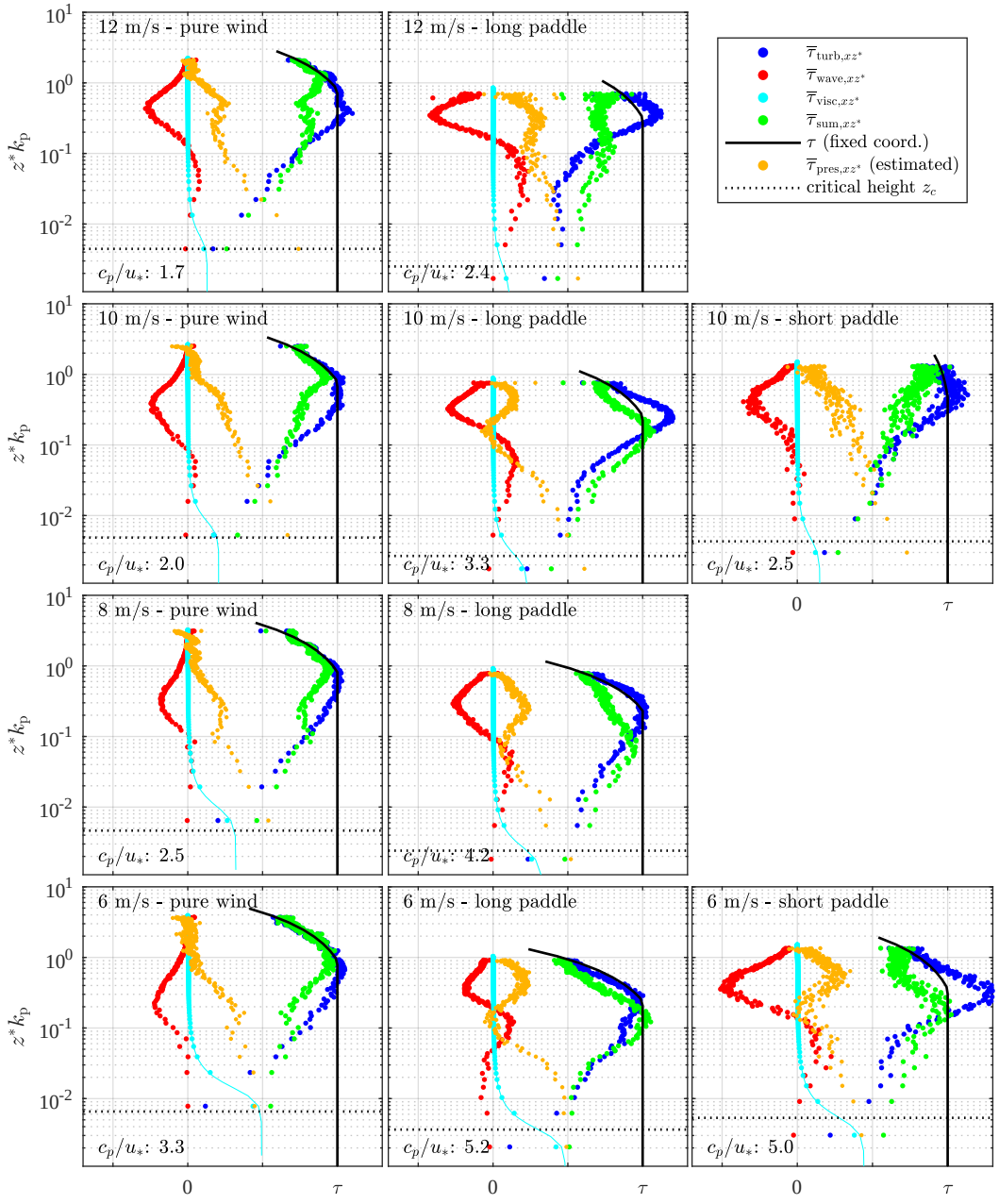

Figure 7.22: Profiles of stress partitioning dependent on the normalized height $z^* k_\mathrm{p}$ for all conditions at wind speeds from 6 to 12 m/s. The directly measured contributions by turbulent stress $\overline{\tau}_{\mathrm{turb},xz^*}$ (blue), wave coherent flux $\overline{\tau}_{\mathrm{wave},xz^*}$ (red) and viscous shear $\overline{\tau}_{\mathrm{visc},xz^*}$ (cyan), as well as the sum of these three $\overline{\tau}_{\mathrm{sum},xz^*}$ (green) are shown. By the black line the height dependent total stress τ is shown, which was derived in fixed coordinates above the crests. The pressure contribution $\overline{\tau}_{\mathrm{pres},xz^*}$ (orange) is estimated by the difference between the sum of the measured contributions to the total stress. The critical height z_c ($\overline{u}_z(z_\mathrm{c}) = c$) is drawn by the black dotted line and is close to the viscous sublayer for all conditions. While $\overline{\tau}_{\mathrm{turb},xz^*}$ and $\overline{\tau}_{\mathrm{wave},xz^*}$ drop to zero close to the water surface, $\overline{\tau}_{\mathrm{visc},xz^*}$ and $\overline{\tau}_{\mathrm{pres},xz^*}$ are maximal and decrease with height.

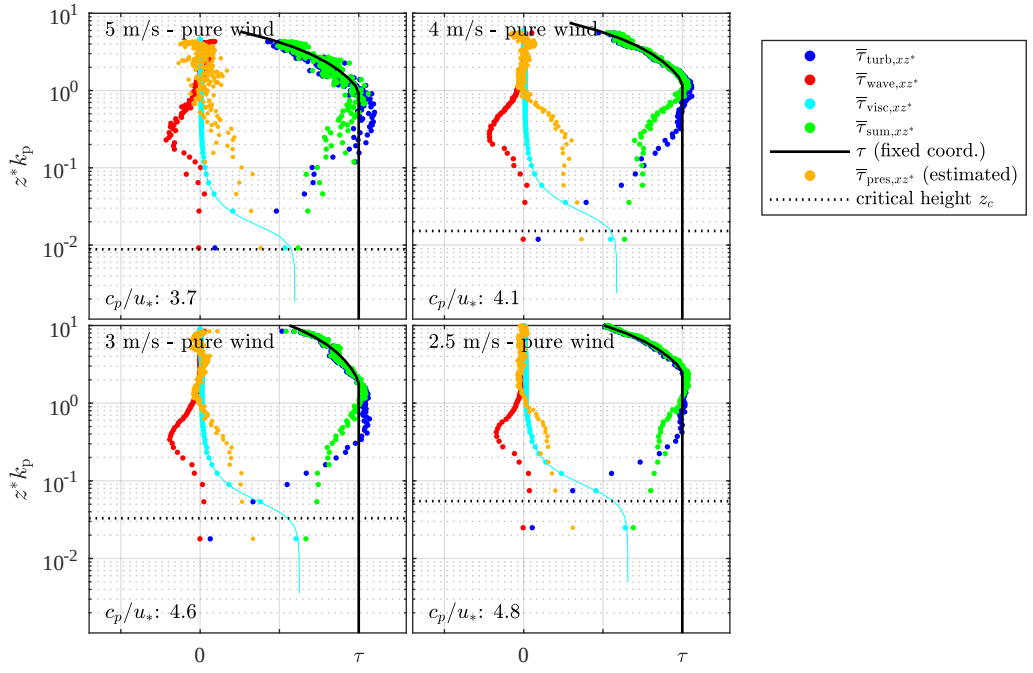

Figure 7.23: Profiles of stress partitioning dependent on the normalized height $z^* k_\mathrm{p}$ for all conditions at wind speeds from 2.5 to 5 m/s. The profiles have similar shapes to conditions at higher wind speeds and pure wind waves, which are shown in figure 7.22 (same notation).

flow separation and the resulting flow structures above high waves at high wind speeds.

7.5.4 Dependency on wind-wave properties

In the following it is outlined, how the partition of the surface drag is related to the wind-wave properties. For this, the relation of the pure viscous shear $\overline{\tau}_{\mathrm{visc},xz^*}$ (simply denoted as τ_visc) to the total drag $\tau = \rho_\mathrm{a} {u_{*,\mathrm{a}}}^2$ is presented against different wind and wave properties. For gas transfer as well as for wave dynamics, the situation directly at the surface is predominantly important, so no height dependency is regarded. As shown in section 7.5.3, the turbulent and wave coherent stresses are dropping towards zero with decreasing height, so here the total momentum transport is represented by viscous shear and pressure forces.

The separation of the measured sequences into three classes of different wave amplitudes allows a closer evaluation of the dependency of the partitioning on the wave properties. Figure 7.24 shows the normalized shear stress $\tau_\mathrm{visc}/\rho u_*^2$ against the wind forcing (reference wind speed at the left and friction velocity at the right). The different paddle conditions are represented by different symbols and the three classes are shown by color. Black circles show measurements at long paddle wave, where no classification has been performed. The variances at same wind speeds u_ref caused by different paddle conditions are relativized in the depiction against u_*. Comparing the three classes,

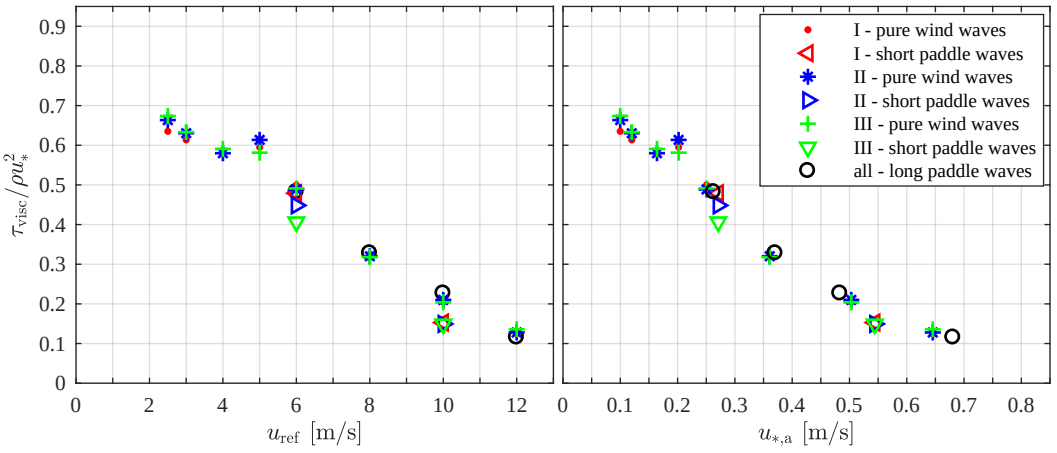

Figure 7.24: Stress partition as relation between viscous shear τ_{visc} and total stress ρu_*^2 against the wind forcing. Different conditions are represented by different symbols, amplitude classifying by colors. Plotting against the friction velocity u_* shows a more clear dependency than for the free stream reference velocity u_{ref}.

slightly increased values are observed above higher amplitudes (class I). In general, the relation decreases steadily with increasing wind forcing.

In figure 7.25, the partition for the three wave amplitude classes and for different wind-wave conditions is plotted against the measured wave properties ϵ (wave steepness), H (wave height) and c/u_* (wave age). The friction velocity is illustrated by the color of the symbols. Blue colors represent low and yellow high values. All three plots show only very low dependencies, which are significantly smaller than the dependencies on u_*. Based on this observation it can be supposed, that the partition is dominated by the wind forcing represented by the friction velocity. But it has to be noted, that the regarded wave conditions are only in a narrow range and also strongly dependent on u_*. The situation might change for other waves states like very old waves or very short fetches. Here, fetch dependent observations are needed and would deliver better insights.

Another aspect being of big importance for the dynamic of gas transfer as well as for waves is the phase dependent distribution of the viscous stress τ_{visc}. How this is connected to some wind-wave properties is illustrated in figure 7.26. As a quantitative description of the distribution, the maximum and minimum values of τ_{visc} normalized to the mean of τ_{visc} are plotted in red and blue, respectively. Again different symbols represent the different classes at the varying conditions. Here a clear dependency on the wave steepness ϵ is present, while wave height H, wave age c/u_* and friction velocity u_* are showing big variations. The minimum values of τ_{visc} are decreasing from high values around $0.8\,\tau_{\mathrm{visc}}$ at low wave steepness down close to zero. The maxima are ranging from slightly above τ_{visc} up to $3\,\tau_{\mathrm{visc}}$ showing a clear increase for higher values of ϵ. Here the classification has a big influence, so in class III (low amplitudes) the span width between minimum and maximum is much lower than in class I (high amplitudes).

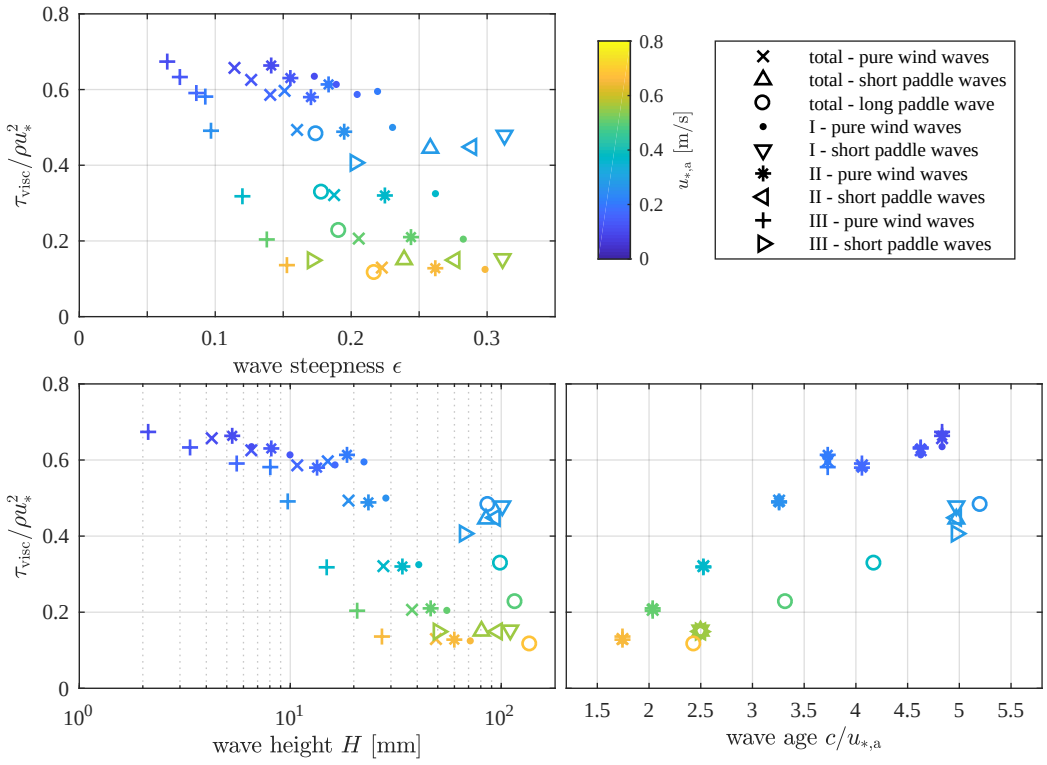

Figure 7.25: Stress partition as relation between viscous shear τ_{visc} and total stress $\rho {u_*}^2$ against wave properties. The color represents the friction velocity u_* and different conditions and classes are shown by different symbols. Only slow dependencies on the different wave properties are present, which are all less pronounced than the dependency on u_*.

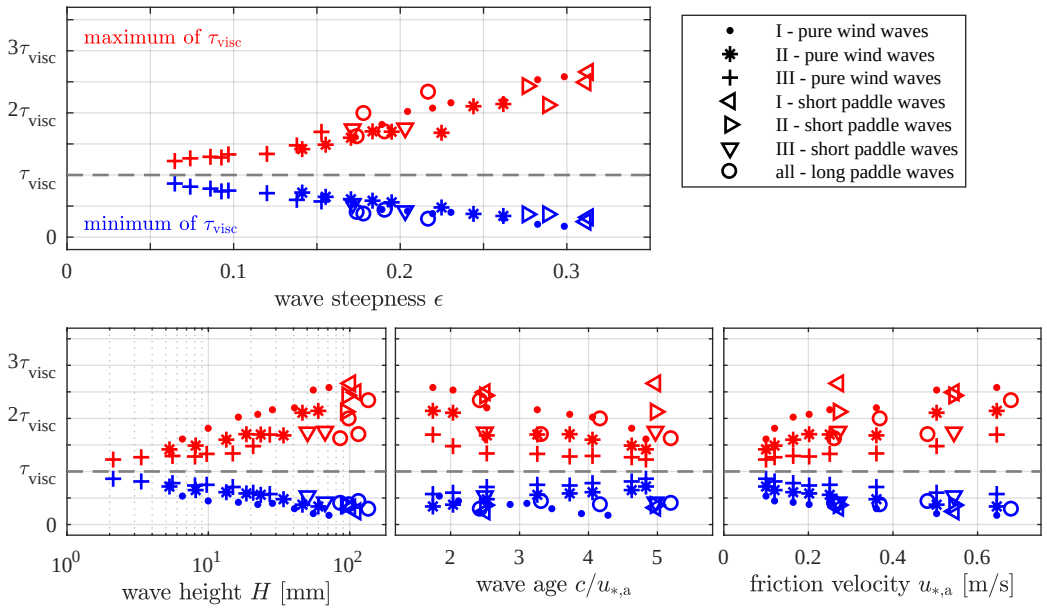

Figure 7.26: Dependency of the span between the normalized maximum (red) and minimum (blue) magnitudes of viscous stresses on several wind-wave conditions. Different conditions and classes are represented by different symbols. The plotting against the wave steepness ϵ shows the clearest dependency: The steeper the waves, the larger the normalized span width of τ_{visc}.

8 Conclusion and outlook

8.1 Conclusion

Investigating the wind induced stress partitioning above water waves requires air sided velocity measurements, which are of high spacial resolution and do not influence the flow. Within the scope of this thesis, a modified PSV-method was developed, where small particles are illuminated by laser light, which is modulated in intensity (section 3.2). By observing the particles by a camera and applying image processing the determination of the particle velocity from only one exposure is possible (section 5.1). Thereby no expensive high speed cameras are needed and the use of camera arrays becomes applicable. Additionally, this method allows the measurement of velocities with high spacial accuracy down to 3-5 pixels, which is better than many statistical PIV-methods (about 8 pixels).

As tracking material small crystals of ammonium chloride were directly generated by an acid-base reaction in the air (section 4.3). With sizes of about $1\,\mu$m they are following the air flow and are big enough to scatter enough light. Their big advantage in comparison to other seeding materials is their disappearance after hitting the water surface, because the salt is simply solved.

Detecting the surface elevation by the use of laser induced fluorescence (section 3.3) and measuring the air velocity by PSV allowed the investigation of the air flow ranging from the viscous boundary layer above the water surface up to heights of minimum twice the wave height. By using an array of four small cameras the field of view was extended to approximately $36\,$cm with a spacial resolution about $50\,\mu$m/pixel (section 4.2). A big set of experiments was performed at the large IRPHE-Luminy linear wind-wave facility in Marseille (France), which has optimal flow characteristics (section 4.1). By applying wind speeds from 2.5 to $12\,$m/s a large range of different values of $u_{*,*}$ was investigated at a fetch of $28\,$m. Additional experiments with large mechanically generated waves with wave heights up to $19\,$cm were performed. For the first time air sided velocity measurements at such wind-wave conditions were realized, which resolve the whole boundary layer up to $23\,$cm and also having a resolution high enough, to resolve the viscous boundary layer (section 4.5).

For all conditions the wave state was characterized by determining the energy spectra and wave parameters like wave height, wave steepness and phase speed (section 7.1). The total vertical momentum transport (drag), which is constant below a certain height (constant flux layer), could be directly determined by calculating the Reynolds stresses from the velocity measurements in fixed coordinates above the crests, where no pressure forces have to be regarded and thereby the momentum balance is closed (section 7.3). For some conditions the wave height exceeded the thickness of the constant flux layer, so here the stress profiles were extrapolated and an estimation of the total drag made possible.

The time resolved measurements of the surface elevation at high frequency ($500\,$Hz)

enabled the determination of wave following coordinates and the extraction of the phase of the dominant wave (section 6.2 and 6.3). Thereby averaged phase dependent velocity fields could be obtained, which characterized the air flow above gravity waves at different wind-wave conditions (section 7.4). Classifying waves using their amplitude enabled the phase dependent averaging also for inhomogeneous pure wind waves, where different wave heights and wavelengths are present.

By using wave following coordinates and transforming the momentum equation (section 2.3) the stress contribution from turbulent, wave coherent and viscous stress could be obtained dependently on the vertical wave following coordinate (section 7.5.1 and 7.5.2). Even for high wind speeds up to $12\,\mathrm{m/s}$ the phase dependent viscous shear distribution could be measured. By fitting the law of the wall on the velocity profile a very robust method was found leading to meaningful results despite of very thin viscous boundary layers.

While turbulent, wave coherent and viscous stresses could be determined directly from the velocity measurements, the pressure forces were indirectly estimated from the difference to the total drag. Thereby the height dependent momentum budget could be closed and the complete phase averaged stress partitions at the different wind-wave conditions could be received, which is presented for the first time in this study (section 7.5.3). Up to now the full height dependent stress partition was only received from direct numerical simulations (Hara and Sullivan, 2015) and there are no measurements available covering such high wind speeds and large waves. Normalizing these vertical stress profiles by the wave number of the dominant wave allowed to compare the different experiments. In general at all conditions the turbulent stress decreases and the viscous stress and the pressure forces increase with closer distance to the water surface. For all conditions the pressure forces are close to zero at a height of approximately the wavelength of the dominant wave divided by two π ($z^* k_\mathrm{p} \approx 1$). While turbulent stresses, viscous stresses and pressure forces show completely positive values, the wave coherent stress shows partly negative values. The structure of the profiles of wave coherent and pressure stress strongly depends on the wave state. Especially, for large mechanically generated waves a regime occurs, where the wave coherent flux changes its direction into positive, which also influences the profile of pressure contributions.

Compared to other studies the results of this height dependent stress partitions coincide within the scope of the overlapping wind-wave states. The characteristics for pure wind wave conditions are very similar to the results obtained by numerical simulations (Hara and Sullivan, 2015) and also other experimental studies by Buckley and Veron (2016) and Buckley and Veron (2017) deliver comparable results for pure wind waves and long paddle waves at low wind speeds, even if they are do not show the complete stress partition. So by this thesis new insights to the stress partition above wind waves are presented, especially for high wind speeds above large gravity waves.

The partition of stress into viscous shear and pressure forces directly at the surface is important for transport processes of mass and heat, as well as for the dynamics of waves. The relation of phase averaged viscous shear to total drag have been showed to

have a clear dependency on the wind forcing represented by the friction velocity (7.5.4). The performed experiments indicate, that the connection to the friction velocity is much stronger than on wave parameters like wave height, wave steepness and wave age. But for clarifying this dependency additional experiments covering a broader range of wave states are needed.

Also important for exchange processes of heat and gas, as well as for wave growth, is the phase distribution of viscous shear along the surface, which has been shown to strongly depend on wave steepness and not directly on u_*. At steep waves close to the crests the viscous shear can have magnitudes three times larger than the phase averaged mean and directly behind the crests it can drop close to zero.

8.2 Outlook

As it is usual for new measurement techniques the PSV-method can be further developed. Even if the imaging processing delivers already good results, maybe other approaches like machine learning could further optimize the extracting of the velocity from the images. Also the quality of the images can be improved. More laser power leads to brighter particle streaks and so higher velocities can be measured. Better optical resolution enables measurements closer to the water surface. By enlarging the field of view in horizontal direction flow paths can be observed and single events like eddies or air flow separation can be better investigated.

Additionally, the use of stereo imaging enables the measurements of 3D velocity vectors by PSV. Thereby also measurements in annular wind-wave facilities can be performed, where secondary currents occur and the horizontal cross wind component is needed to close the momentum budget. Such measurements have been already performed in 2016 at the large annular wind-wave facility in Heidelberg (Aeolotron), but have to be evaluated.

Measurements above very young waves (short fetch) and very old waves at different wind speeds would extent the investigated conditions of this study, which cover more over medium fetches. While annular wind-wave facilities are known for the opportunity to measure at nearly infinite fetches, they also can be used to investigate very young waves. After starting the wind from zero to a constant level the waves begin to rise with time. With the knowledge of the intrinsic phase speed this time can be translated into a fetch length and thereby fetches from zero to very long distances could be obtained. By measuring the flow above the water surface during many of such experiments the connection between the partition of momentum transfer and the wave state can be further investigated.

Bibliography

R. Adrian. Particle-imaging techniques for experimental fluid mechanics. *Annual Review of Fluid Mechanics*, 23:261–304, 1991. doi: 10.1146/annurev.fl.23.010191.001401.

R. J. Adrian and J. Westerweel. *Particle Image Velociimetry*. Cambridge, 2011.

M. A. Al-Zanaidi and W. H. Hui. Turbulent airflow over water waves-a numerical study. *Journal of Fluid Mechanics*, 148(1):225–246, 1984. doi: 10.1017/S0022112084002329.

D. Anderson, J. C. Tannehill, and R. H. Pletcher. *Computational fluid mechanics and heat transfer*. CRC Press, 2012.

A. Anis and J. N. Moum. Surface wave turbulence interactions. scaling ϵ(z) near the sea surface. *Journal of Physical Oceanography*, 25:2025–2045, Sept. 1995. doi: 10.1175/1520-0485(1995)025<2025:SWISNT>2.0.CO;2.

M. L. Banner and W. L. Peirson. Tangential stress beneath wind-driven air-water interfaces. *Journal of Fluid Mechanics*, 364:115–145, 1998. doi: 10.1017/S0022112098001128.

M. L. Banner and J. B. Song. On determining the onset and strength of breaking for deep water waves. part ii: Influence of wind forcing and surface shear. *Journal of Physical Oceanography*, 32:2559–2570, Sept. 2002. doi: 10.1175/1520-0485-32.9.2559.

J. Belden and A. H. Techet. Simultaneous quantitative flow measurement using piv on both sides of the air-water interface for breaking waves. *Experiments in Fluids*, 50 (1):149–161, 2011.

T. B. Benjamin. Shearing flow over a wavy boundary. *Journal of Fluid Mechanics*, 6 (2):161–205, 1959. doi: 10.1017/S0022112059000568.

M. Binnewies, M. Finze, M. Jäckel, P. Schmidt, H. Willner, and G. Rayner-Canham. *Allgemeine und Anorganische Chemie*. SpringerLink : Bücher. Springer Spektrum, Berlin, Heidelberg, 3. aufl. 2016 edition, 2016. doi: 10.1007/978-3-662-45067-3.

J. Bole and E. Hsu. Response of gravity water waves to wind excitation. *Journal of Fluid Mechanics*, 35(04):657–675, 1969. doi: 10.1017/S0022112069001364.

M. Bopp. Flow conditions in water and air in the annular wind-wave tank in heidelberg (aeolotron). Masterthesis, Institut für Umwelphysik, Univeristät Heidelberg, Germany, 2014. doi: 10.11588/heidok.00016962.

M. P. Buckley and F. Veron. Structure of the airflow above surface waves. *Journal of Physical Oceanography*, 46(5):1377–1397, 2016. doi: 10.1175/JPO-D-15-0135.1.

M. P. Buckley and F. Veron. Airflow measurements at a wavy air-water interface using PIV and LIF. *Experiments in Fluids*, 58(11):1–20, 2017.

G. Caulliez. Dissipation regimes for short wind waves. *Journal of Geophysical Research: Oceans*, 118(2):672–684, 2013. doi: 10.1029/2012JC008402.

G. Caulliez and C.-A. Guérin. Higher-order statistical analysis of short wind wave fields. *Journal of Geophysical Research: Oceans (1978-2012)*, 117(C6), June 2012. ISSN 2156-2202. doi: 10.1029/2011JC007854.

G. Caulliez, V. Makin, and V. Kudrayavtsev. Drag of the water surface at very short fetches: observations and modelling. *Journal of Physical Oceanography*, 38:2038–2055, 2008. doi: 10.1175/2008JPO3893.1.

D. V. Chalikov. The numerical simulation of wind-wave interaction. *Journal of Fluid Mechanics*, 87(3):561–582, 1978. doi: 10.1017/S0022112078001767.

H. Charnock. Wind stress on a water surface. *Q.J.R. Meteorol. Soc*, 81:639–640, 1955. doi: 10.1002/qj.49708135027.

G. D. Crapper. An exact solution for progressive capillary waves of arbitrary amplitude. *Journal of Fluid Mechanics*, 2:532–540, 1957. doi: 10.1017/S0022112057000348.

M. Donelan, F. Dobson, S. Smith, and R. Anderson. Reply. *Journal of Physical Oceanography*, 25:1908–1912, 1995. doi: 10.1175/1520-0485(1995)025<1908:R>2.0.CO;2.

M. Donelan, B. Haus, N. Reul, W. Plant, M. Stiassnie, H. Graber, O. Brown, and E. Saltzman. On the limiting aerodynamic roughness of the ocean in very strong winds. *Geophysical Research Letters*, 31(18), 2004. doi: 10.1029/2004GL019460.

M. A. Donelan. On the decrease of the oceanic drag coefficient in high winds. *Journal of Geophysical Research*, 123:1485–1501, 2018. doi: 10.1002/2017JC013394.

M. A. Donelan, A. V. Babanin, I. R. Young, and M. L. Banner. Wave-follower field measurements of the wind-input spectral function. Part II: Parameterization of the wind input. 36:1672–1689, 2006. doi: 10.1175/JPO2933.1.

W. Drennan, P. Taylor, and M. Yelland. Parameterizing the sea surface roughness. *Journal of Physical Oceanography*, 35:835–848, 2005. doi: 10.1175/JPO2704.1.

W. M. Drennan, H. C. Graber, D. Hauser, and C. Quentin. On the wave age dependence of wind stress over pure wind seas. *Journal of Geophysical Research: Oceans*, 108 (C3):8062, 2003. doi: 10.1029/2000JC000715.

F. Durst. *Grundlagen der Strömungsmechanik*. SpringerLink : Bücher. Springer Berlin Heidelberg, Berlin, Heidelberg, 2006. doi: 10.1007/978-3-540-31324-3.

J. B. Edson, V. Jampana, R. A. Weller, S. P. Bigorre, A. J. Plueddemann, C. W. Fairall, S. D. Miller, L. Mahrt, D. Vickers, and H. Hersbach. On the exchange of momentum over the open ocean. *Journal of Physical Oceanography*, 43:1589–1610, 2013. doi: 10.1175/JPO-D-12-0173.1.

P. Eger. Messung der Luftströmung über kleinskaligen Wasserwellen mittels Particle Streak Velocimetry in einem linearen Wind-Wellen-Kanal. Bachelor thesis, Institut für Umweltphysik, Fakultät für Physik und Astronomie, Universität Heidelberg, 2012.

EMVA. Emva standard 1288 release 3.1, Dec. 2016.

C. Fairall, E. Bradley, J. Hare, A. Grachev, and J. Edson. Bulk parameterization of air-sea fluxes: updates and verification for the COARE algorithm. *Journal of Climate*, 16:571–591, 2003. doi: 10.1175/1520-0442(2003)016<0571:BPOASF>2.0.CO;2.

C. W. Fairall, E. F. Bradley, D. P. Rogers, J. B. Edson, and G. S. Young. Bulk parameterization of air-sea fluxes for tropical ocean-global atmosphere coupled-ocean atmosphere response experiment. *Journal of Geophysical Research: Oceans*, 101(C2):3747–3764, 1996. doi: 10.1029/95JC03205.

A. M. Fincham and G. R. Spedding. Low cost, high resolution DPIV for measurement of turbulent fluid flow. *Experiments in Fluids*, 23:449–462, 1997. doi: 10.1007/s003480050135.

L. Flothow. Bubble characteristics from breaking waves in fresh water and simulated seawater. Master's thesis, Institut für Umweltphysik, Fakultät für Physik und Astronomie, Universität Heidelberg, 2017. doi: 10.11588/heidok.00023754.

C. S. Garbe, A. Rutgersson, J. Boutin, B. Delille, C. W. Fairall, N. Gruber, J. Hare, D. Ho, M. Johnson, G. de Leeuw, P. Nightingale, H. Pettersson, J. Piskozub, E. Sahlee, W. Tsai, B. Ward, D. K. Woolf, and C. Zappa. Transfer across the air-sea interface. In P. S. Liss and M. T. Johnson, editors, *Ocean-Atmosphere Interactions of Gases and Particles*, pages 55–112. Springer, 2014. doi: 10.1007/978-3-642-25643-1_2.

J.-P. Giovanangeli, C. Kharif, and E. Pelinovski. Experimental study of the wind effect on focusing of transient wave groups. *ArXiv Physics e-prints*, 2006.

L. Grare, W. L. Peirson, H. Branger, J. W. Walker, J.-P. Giovanangeli, and V. Makin. Growth and dissipation of wind-forced, deep-water waves. *Journal of Fluid Mechanics*, 722:5–50, 2013. doi: 10.1017/jfm.2013.88.

T. Hara and P. P. Sullivan. Wave boundary layer turbulence over surface waves in a strongly forced condition. *Journal of Physical Oceanography*, 45(3):868–883, Mar. 2015. doi: 10.1175/JPO-D-14-0116.1.

K. Hasselmann, W. Sell, D. B. Ross, and P. Müller. A parametric wave prediction model. *Journal of Physical Oceanography*, 6(2):200–228, 1976.

F. Hering, Wierzimok, and C. Leue. Particle tracking velocimetry beneath water waves. Part I: visualization and tracking algorithms. *Experiments in Fluids*, 23(6):472–482, 1997. doi: 10.1007/s003480050137.

F. Hering, D. Wierzimok, C. Leue, and B. Jähne. Particle tracking velocimetry beneath water waves. part II : water waves. *Experiments in Fluids*, 24(1):10–16, 1998. doi: 10.1007/s003480050145.

L. Hesselink. Digital image processing in flow visualization. *Annual Review of Fluid Mechanics*, bf 20:421–485, 1988. doi: 10.1146/annurev.fl.20.010188.002225.

L. H. Holthuijsen. *Waves in Oceanic and Coastal Waters*. Cambdridge Univ. Press, 2007.

S. A. Hsu. A dynamic roughness equation and its application to wind stress determination at the air-sea interface. *Journal of Physical Oceanography*, 4(1):116–120, Jan. 1974. doi: 10.1175/1520-0485(1974)004<0116:ADREAI>2.0.CO;2.

J. Ilmberger. Impulsübertrag und Strömungsverhältnisse in einem runden Wind-Wasser Kanal. Diplomarbeit, Institut für Umweltphysik, Fakultät für Physik und Astronomie, Universität Heidelberg, 1981.

B. Jähne, K. O. Münnich, and U. Siegenthaler. Measurements of gas exchange and momentum transfer in a circular wind-water tunnel. *Tellus*, 31:321–329, 1979. doi: 10.1111/j.2153-3490.1979.tb00911.x.

J. A. M. Janssen. Does wind stress depend on sea-state or not? A statistical error analysis of hexmax data. *Boundary-Layer Meteorology*, 83:479–503, 1997. doi: 10.1023/A:1000336814021.

B. Jähne. *Digitale Bildverarbeitung und Bildgewinnung*. Springer Vieweg, Berlin, 2012. doi: 10.1007/978-3-642-04952-1.

B. Jähne and H. Herrmann. EMVA 1288 datasheet Basler acA1920-155um, 0 dB gain, Nov. 2015a.

B. Jähne and H. Herrmann. EMVA 1288 datasheet Basler acA1920-155um, 12 dB gain, Nov. 2015b.

B. Jähne, K. O. Münnich, R. Bösinger, A. Dutzi, W. Huber, and P. Libner. On the parameters influencing air-water gas exchange. *Journal of Geophysical Research*, 92: 1937–1950, Feb. 1987. doi: 10.1029/JC092iC02p01937.

S. Jian, Z. Zhong, L. Ruijie, L. Yan, and S. Wenyu. Dependence of sea surface drag coefficient on wind-wave parameters. *Acta Oceanologica Sinica*, 30:14–24, 2011. doi: 10.1007/s13131-011-0101-z.

I. S. F. Jones and Y. Toba. *Wind Stress over the Ocean*. Cambridge University Press, Cambridge,UK, 2001.

C. J. Kähler, S. Scharnowski, and C. Cierpka. On the resolution limit of digital particle image velocimetry. *Experiments in Fluids*, 52(6):1629–1639, Jun 2012. doi: 10.1007/s00348-012-1280-x.

A. A. Kandaurov, Y. I. Troitskaya, D. A. Sergeev, M. I. Vdovin, and G. A. Baidakov. Average velocity field of the air flow over the water surface in a laboratory modeling of storm and hurricane conditions in the ocean. *Izvestiya, Atmospheric and Oceanic Physics*, 50(4):399–410, Jul 2014. doi: 10.1134/S000143381404015X.

H. Kawamura, K. Okuda, S. Kawai, and Y. Toba. Structure of turbulent boundary layer over wind waves in a wind wave tunnel. *Tohoku Geophysical Journal*, 28:69–86, 1981.

B. Kinsman. *Wind Waves: Their Generation and Propagation on the Ocean Surface*. Prentice-Hall, Englewood Cliffs, 1965.

S. A. Kitaigarodskii and Y. A. Volkov. On the roughness parameter of the sea surface and the calcuation of momentum flux in the near-water layer of the atmosphere. *Izvestiya Atmospheric and Oceanic Physics*, 1(12):566–574, 1965.

A. N. Kolmogorov. The local structure of turbulence in compressible turbulence for very large Reynolds numbers. *Compt.Rend.Akad.Nauk SSSR*, 30:301, 1941.

K. E. Krall and B. Jähne. First laboratory study of air-sea gas exchange at hurricane wind speeds. *Ocean Science*, 10:257–265, 2014. doi: 10.5194/os-10-257-2014.

C. Kräuter. *Visualization of air-water gas exchange*. Dissertation, Institut für Umweltphysik, Fakultät für Physik und Astronomie, Universität Heidelberg, 2015.

P. K. Kundu, I. M. Cohan, and D. R. Dowling. *Fluids Mechanics*. Academic Press, imprint of Elsevier, 2012.

J. Kunz. *Active Thermography as a Tool for the Estimation of Air-Water Transfer Velocities*. PhD thesis, Institut für Umweltphysik, Fakultät für Physik und Astronomie, Univ. Heidelberg, 2017.

J. Kunz and B. Jähne. Investigating small scale air-sea exchange processes via thermography. *Front. Mech. Eng.*, 2018. doi: 10.3389/fmech.2018.00004.

C. B. Lang and N. Pucker. *Mathematische Methoden in der Physik*. Spektrum Akademischer Verl., Heidelberg, 2. aufl., korr. nachdr. edition, 2010. doi: 10.11588/heidok.00022903.

P. A. Lange, B. Jähne, J. Tschiersch, and I. Ilmberger. Comparison between an amplitude-measuring wire and a slope-measuring laser water wave gauge. *Review of Scientific Instruments*, 53(5):651–655, 1982. doi: 10.1063/1.1137036.

P. S. Liss. Processes of gas exchange across an air–water interface. *Deep-Sea Research*, 20:221–238, 1973. doi: 10.1016/0011-7471(73)90013-2.

P. S. Liss, editor. *Ocean-atmosphere interactions of gases and particles*. Springer earth system sciences. Springer Open, Heidelberg, 2014.

S. Massel. *Ocean Surface Waves: Their Physics and Prediction*. Advanced series on ocean engineering. World Scientific, 2013.

A. Melling. Tracer particles and seeding for particle image velocimetry. *Meas. Sci. Technol.*, 8:1406 – 1416, 1997.

W. K. Melville. Wave modulation and breakdown. *Journal of Fluid Mechanics*, 128: 489, 1983.

W. K. Melville and A. V. Fedorov. The equilibrium dynamics and statistics of gravity-capillary waves. *Journal of Fluid Mechanics*, 767:449–466, March 2015. doi: http://dx.doi.org/10.1017/jfm.2014.740.

J. H. Michell. Xliv. the highest waves in water. *The London, Edinburgh, and Dublin Philosophical Magazine and Journal of Science*, 36(222):430–437, 1893. doi: 10.1080/14786449308620499.

J. W. Miles. On the generation of surface waves by shear flows. *Journal of Fluid Mechanics*, 3:185–204, 1957. doi: 10.1017/S0022112057000567.

A. S. Monin and A. M. Yaglom. *Statistical Fluid Mechanics, Volume I*. Dover Publications, 2007.

R. Nielsen. *Gasaustausch - Entwicklung und Ergebnis eines schnellen Massenbilanzverfahrens zur Messung der Austauschparameter*. Dissertation, Institut für Umweltphysik, Fakultät für Physik und Astronomie, Universität Heidelberg, 2004.

P. D. Nightingale. Air-sea gas exchange. In C. L. Quéré and E. S. Saltzman, editors, *Surface Ocean: Lower Atmosphere Processes*, volume 187 of *Geophysical Monograph Series*, chapter 6, pages 69–97. American Geophysical Union, 2009. doi: 10.1029/2008GM000774.

K. Okuda. The internal structure of short wind waves. Part I: On the internal vorticity structure. *Journal of the Oceanographical Society of Japan*, 38:28–42, 1982a. doi: 10.1007/BF02113819.

K. Okuda. Internal flow structure of short wind waves. Part II The streamline pattern. *Journal of the Oceanographical Society of Japan*, 38:313–322, 1982b. doi: 10.1007/BF02114536.

K. Okuda. Internal flow structure of short wind waves. Part III Pressure distributions. *Journal of the Oceanographical Society of Japan*, 38:331–338, 1983. doi: 10.1007/BF02111029.

K. Okuda. Internal flow structure of short wind waves. Part IIII The generation of flow in excess of the phase speed. *Journal of the Oceanographical Society of Japan*, 40: 46–56, 1984. doi: 10.1007/BF02071208.

K. Okuda, S. Kawai, M. Tokuda, and Y. Toba. Detailed observation of the wind-exerted surface flow by use of flow visualization methods. *Journal of the Oceanographical Society of Japan*, 32:53–64, 1976. doi: 10.1007/BF02107372.

K. Okuda, S. Kawai, and Y. Toba. Measurement of skin friction distribution along the surface of wind waves. *Journal of Oceanography*, 33(4):190–198, 1977. doi: 10.1007/BF02109691.

A. V. Oppenheim and R. W. Schafer. *Discrete-Time Signal Processing*. Pearson, Upper Saddle River, NJ, 3 edition, 2010.

Y. Papadimitrakis. Momentum and energy exchange across an air-water interface. Partitioning (into waves and currents) and parameterization. *Deep Sea Research Part II: Topical Studies in Oceanography*, 52(II):1270–1286, May 2005. doi: 10.1016/j.dsr2.2005.03.006.

W. L. Peirson. Measurement of surface velocities and shears at a wavy air-water interface using particle image velocimetry. *Experiments in Fluids*, 23:427–437, 1997. doi: 10.1007/s003480050131.

W. L. Peirson and M. L. Banner. Aqueous surface layer flows induced by microscale breaking wind waves. *Journal of Fluid Mechanics*, 479:1–38, 2003. doi: 10.1017/S0022112002003336.

W. L. Peirson and A. W. Garcia. On the wind-induced growth of slow water waves of finite steepness. *Journal of Fluid Mechanics*, 608(-1):243–274, 2008. doi: 10.1017/S002211200800205X.

W. L. Peirson, J. W. Walker, and M. L. Banner. On the microphysical behaviour of wind-forced water surfaces and consequent re-aeration. *Journal of Fluid Mechanics*, 743:399–447, 2014. doi: 10.1017/jfm.2013.681.

O. M. Phillips. On the generation of waves by turbulent wind. *Journal of Fluid Mechanics*, 2:417–445, 1957. doi: 10.1017/S0022112057000233.

O. M. Phillips. *The Dynamics of the Upper Ocean*. Cambridge University Press, 2 edition, 1977.

O. M. Phillips. Spectral and statistical properties of the equilibrium range in wind-generated gravity waves. 4:426–434, 1985. doi: 10.1017/S0022112085002221.

L. Prandtl. *Strömungslehre*. Vieweg, 1957.

M. Raffel, C. E. Willert, S. T. Wereley, and J. Kompenhans. *Particle Image Velocimetry: A Practical Guide*. Springer-Verlag, Heidelberg, Berlin, 2 edition, 2007. doi: 10.1007/978-3-540-72308-0.

N. Reul, H. Branger, and J.-P. Giovanangeli. Air flow separation over unsteady breaking waves. *Physics of Fluids*, 11:1959–1961, July 1999. doi: 10.1063/1.870058.

V. P. Reutov and Y. I. Troitskaya. Nonlinear growth rate of wind water waves and their excitation near the stability threshold. *Radiophysics and Quantum Electronics*, 38: 133–136, Mar. 1995. doi: 10.1007/BF01037885.

W. Roedel and T. Wagner. *Physik unserer Umwelt: Die Atmosphäre*. SpringerLink : Bücher. Springer Spektrum, Berlin, Heidelberg, 5. aufl. 2017 edition, 2017. doi: 10.1007/978-3-662-54258-3.

F. Scarano and M. L. Riethmuller. Iterative multigrid approach in PIV image processing with discrete window offset. *Experiments in Fluids*, 26:513–523, 1999.

T. Scheimpflug. Der Photospektrograph und seine Anwendungen. *Photographische Korrespondenz*, (43):516, 1906.

H. Schlichting and K. Gersten. *Grenzschicht-Theorie*. Springer-Verlag, Heidelberg, Germany, 10 edition, 2006. doi: 10.1007/3-540-32985-4.

K. Schwarz. Spatio-temporal measurements of water-wave height and slope using laser-induced fluorescence and splines. Bachelor's thesis, Institut für Umweltphysik, Universität Heidelberg, Germany, 2016. doi: 10.11588/heidok.00021977.

N. Shaikh and K. Siddiqui. An experimental investigation of the near surface flow over air-water and air-solid interfaces. *Physics of Fluids*, 22(2):025103, 2010. doi: 10.1063/1.3313929.

O. Shemdin and E. Hsu. Direct measurement of aerodynamic pressure above a simple progressive gravity wave. *Journal of Fluid Mechanics*, 30(2):403–416, 1967. doi: 10.1017/S0022112067001508.

K. Siddiqui and M. Loewen. Phase-averaged flow properties beneath microscale breaking waves. *Boundary-Layer Meteorology*, 134(3):499–523, Mar. 2010. doi: 10.1007/s10546-009-9447-6.

M. H. K. Siddiqui, M. R. Loewen, C. Richardson, W. E. Asher, and A. T. Jessup. Simultaneous particle image velocimetry and infrared imagery of microscale breaking waves. *Phys.Fluids*, 13:1891–1903, 2001. doi: 10.1063/1.1375144.

R. L. Snyder, F. W. Dobson, J. A. Elliott, and R. B. Long. Array measurements of atmospheric pressure fluctuations above surface gravity waves. *Journal of Fluid Mechanics*, 102(-1):1–59, 1981. doi: 10.1017/S0022112081002528.

J.-B. Song and M. L. Banner. On determining the onset and strength of breaking for deep water waves. part i: Unforced irrotational wave groups. *Journal of Physical Oceanography*, 32(9):2541–2558, 2002. doi: 10.1175/1520-0485(2002)032<2541:ODTOAS>2.0.CO;2.

Z. Song. *Handbook of 3D machine vision*. CRC Press, Boca Raton, FL, 2013.

D. B. Spalding. A Single Formula for the "Law of the Wall". *Journal of Applied Mechanics*, 28:455, 1961. doi: 10.1115/1.3641728.

R. W. Stewart. The air-sea momentum exchange. *Boundary-Layer Meteorology*, 6: 151–167, 1974. doi: 10.1007/BF00232481.

G. G. Stokes. On the theory of oscillatory waves. *Trans. Camb. Philos. Soc.*, 8:441, 1849.

P. P. Sullivan and J. C. McWilliams. Dynamics of winds and currents coupled to surface waves. *Annual Review of Fluid Mechanics*, 42:19–42, 2010. doi: 10.1146/annurev-fluid-121108-145541.

P. P. Sullivan, J. C. McWilliams, and C.-H. Moeng. Simulation of turbulent flow over idealized water waves. *Journal of Fluid Mechanics*, 404:47–85, 2000.

P. Sutherland and W. K. Melville. Field measurements of surface and near-surface turbulence in the presence of breaking waves. *American Meteorological Society*, 45 (4):943–965, April 2015. doi: http://dx.doi.org/10.1175/JPO-D-14-0133.1.

P. K. Taylor and M. J. Yelland. The dependence of sea surface roughness on the height and steepness of the waves. *Journal of Physical Oceanography*, 31:572 – 590, 2001. doi: 10.1175/1520-0485(2001)031<0572:TDOSSR>2.0.CO;2.

M. Teixeira. A linear model for the structure of turbulence beneath surface water waves. *Ocean Modelling*, 36(1):149–162, 2011. doi: 10.1016/j.ocemod.2010.10.007.

Y. Toba. Local balance in the air-sea boundary processes I. On the growth process of wind waves. *Journal of the Oceanographical Society of Japan*, 28:109–121, 1972. doi: 10.1007/BF02109772.

Y. Troitskaya, D. Sergeev, O. Ermakova, and G. Balandina. Statistical parameters of the air turbulent boundary layer over steep water waves measured by the PIV technique. *Journal of Physical Oceanography*, 41:1421–1454, 2011. doi: 10.1175/2011JPO4392.1.

Y. Troitskaya, D. Sergeev, A. Kandaurov, G. Baidakov, M. Vdovin, and V. Kazakov. Laboratory and theoretical modeling of air-sea momentum transfer under severe wind conditions. *Journal of Geophysical Research - Oceans*, 117:C00J21, 2012. doi: 10.1029/2011JC007778.

Y. I. Troitskaya and G. V. Rybushkina. Quasi-linear model of interaction of surface waves with strong and hurricane winds. *Izvestiya Atmospheric and Oceanic Physics*, 44:621–645, Oct. 2008. doi: 10.1134/S0001433808050083.

Y. I. Troitskaya, D. A. Sergeev, Ermakova, O. S., and B. G. N. Fine structure of the turbulent atmospheric boundary layer over the water surface. *Izvestiya Atmospheric and Oceanic Physics*, 46:109–120, 2010. doi: 10.1134/S0001433810010147.

H. C. e. van de Hulst. *Light scattering by small particles*. Dover Publications, New York, 1981.

F. Veron, G. Saxena, and S. Misra. Measurements of the viscous tangential stress in the airflow above wind waves. *Geophysical Research Letters*, 34:L19603, 2007. doi: 10.1029/2007GL031242.

B. Voss, J. Stapf, A. Berthe, and C. S. Garbe. Bichromatic particle streak velocimetry bpsv. *Experiments in Fluids*, 53(5):1405–1420, 2012. doi: 10.1007/s00348-012-1355-8.

R. Wanninkhof, W. E. Asher, D. T. Ho, C. Sweeney, and W. R. McGillis. Advances in quantifying air-sea gas exchange and environmental forcing. *Annual review of marine science*, 1:213–244, 2009. doi: 10.1146/annurev.marine.010908.163742.

H. S. Weiler and R. W. Burling. Direct measurements of stress and spectra of turbulence in the boundary layer over the sea. *Journal of the Atmospheric Sciences*, 24(6):653–664, 1967. doi: 10.1175/1520-0469(1967)024<0653:DMOSAS>2.0.CO;2.

J. Westerweel and F. Scarano. Universal outlier detection for PIV data. *Experiments in Fluids*, 39:1096–1100, 2005. doi: 10.1007/s00348-005-0016-6.

C. H. Wu and H. M. Nepf. Breaking criteria and energy losses for three-dimensional wave breaking. *Journal of Geophysical Research - Oceans*, 107(C10):3177, 2002. doi: 10.1029/2001JC001077.

I. Yoshikawa, H. Kawamura, K. Okuda, and Y. Toba. Turbulent structure in water under laboratory wind waves. *Journal of the Oceanographical Society of Japan*, 44(3): 143–156, 1988. doi: 10.1007/BF02302621.

V. E. Zakharov, S. I. Badulin, P. A. Hwang, and G. Caulliez. Universality of sea wave growth and its physical roots. *Journal of Fluid Mechanics*, 780:503–535, 2015. doi: 10.1017/jfm.2015.468.

A. Zavadsky and L. Shemer. Characterization of turbulent airflow over evolving water-waves in a wind-wave tank. *Journal of Geophysical Research: Oceans*, 117(C11), 2012. doi: 10.1029/2011JC007790.

A Appendix

A.1 Stress on a tilted surface

A stress $\tau_{\parallel}$ parallel to a layer of inclination α is considered in two dimensions (x and z). The resulting stress tensor τ_{ij} in Cartesian coordinates can be expressed by a simple rotation of the coordinate system. With the two dimensional rotation matrix $\mathbf{D}$ for the stress tensor follows (see Kundu et al., 2012):

$$\begin{aligned}
\begin{pmatrix} \tau_{xx} & \tau_{xz} \\ \tau_{xz} & \tau_{zz} \end{pmatrix} &= \mathbf{D}^{\mathrm{T}} \cdot \begin{pmatrix} 0 & \tau_{\parallel} \\ \tau_{\parallel} & 0 \end{pmatrix} \cdot \mathbf{D} \\
&= \begin{pmatrix} \cos(\alpha) & \sin(\alpha) \\ -\sin(\alpha) & \cos(\alpha) \end{pmatrix} \cdot \begin{pmatrix} 0 & \tau_{\parallel} \\ \tau_{\parallel} & 0 \end{pmatrix} \cdot \begin{pmatrix} \cos(\alpha) & -\sin(\alpha) \\ \sin(\alpha) & \cos(\alpha) \end{pmatrix} \\
&= \begin{pmatrix} -2\tau_{\parallel}\cos(\alpha)\sin(\alpha) & \tau_{\parallel}\left(\cos^2(\alpha) - \sin^2(\alpha)\right) \\ \tau_{\parallel}\left(\cos^2(\alpha) - \sin^2(\alpha)\right) & 2\tau_{\parallel}\cos(\alpha)\sin(\alpha) \end{pmatrix}
\end{aligned} \tag{A.1}$$

Using curvilinear coordinates $(x^*, z^*) = (x, z - f(x, z^*, t))$ following the inclined layer (see section 2.1.6 and 2.3.3), the rotation angle can be expressed by the x-derivative of the transformation function f:

$$\tan(\alpha) = \frac{\partial f}{\partial x} \tag{A.2}$$

The stress component in curvilinear coordinates τ_{xz^*} then represents the stress along the horizontal side of an infinitesimal area element (volume element if considered in three dimensions), which is aligned with the inclined layer. It becomes (compare to equation 2.88):

$$\begin{aligned}
\tau_{xz^*} &= \tau_{xz} - \tau_{xx}\frac{\partial f}{\partial x} \\
&= \tau_{\parallel}\left(\cos^2(\alpha) - \sin^2(\alpha)\right) + 2\tau_{\parallel}\cos(\alpha)\sin(\alpha)\tan(\alpha) \\
&= \tau_{\parallel}\underbrace{\left(\cos^2(\alpha) - \sin^2(\alpha) + 2\sin^2(\alpha)\right)}_{=1} \\
\Rightarrow \qquad \tau_{xz^*} &= \tau_{\parallel}
\end{aligned} \tag{A.3}$$

The inclination of the layer enlarges the x-side of the infinitesimal area (volume) element expressed in curvilinear (in this study wave following) coordinates. So the stress acting on this line has to be integrated and this effect compensates the reduction by composing the stress into a horizontal and vertical part.

This evidence was performed for a stress $\tau_{\parallel}$ independent on its physical origin and it is valid for τ_{visc}, as well as for other kind of stresses.

A.2 Summary of measurement values

Tables A.1 to A.3 show all results of the considered results obtained during the experiments in Marseille 2016. Uncertainties fewer than $1\,\%$ are not listed.

#	class	u_{ref} [m/s]	f_{peak} [Hz]	a_{rms} [mm]	$\overline{H}$ [mm]	c [m/s]	ϵ	z_0 [mm]	τ [Pa]	τ_{visc} [Pa]
7	all	12.0	1.59	18.8	49.0	1.18	.22	$.609 \pm .006$	$.4999 \pm .0149$	$.0647 \pm .0049$
	I				71.3		.30			$.0624 \pm .0050$
	II				59.9		.26			$.0639 \pm .0051$
	III				27.2		.15			$.0680 \pm .0048$
9	all	10.0	1.73	14.5	37.8	1.06	.21	$.334 \pm .006$	$.3038 \pm .0083$	$.0627 \pm .0035$
	I				55.2		.28			$.0622 \pm .0037$
	II				46.3		.24			$.0638 \pm .0036$
	III				20.8		.14			$.0619 \pm .0033$
13	all	8.0	1.87	10.7	27.6	.93	.19	$.128 \pm .002$	$.1562 \pm .0033$	$.0502 \pm .0026$
	I				40.7		.26			$.0508 \pm .0028$
	II				34.0		.22			$.0500 \pm .0025$
	III				14.9		.12			$.0497 \pm .0023$
15	all	6.0	2.03	7.3	18.9	.82	.16	$.067 \pm .001$	$.0753 \pm .0011$	$.0372 \pm .0019$
	I				28.4		.23			$.0377 \pm .0019$
	II				23.5		.19			$.0368 \pm .0019$
	III				9.7		.10			$.0370 \pm .0018$
20	all	5.0	2.20	5.8	15.1	.75	.15	$.044 \pm .000$	$.0489 \pm .0010$	$.0292 \pm .0025$
	I				22.4		.22			$.0291 \pm .0026$
	II				18.6		.18			$.0300 \pm .0025$
	III				8.0		.09			$.0284 \pm .0023$
21	all	4.0	2.52	4.2	10.8	.66	.14	$.054 \pm .000$	$.0323 \pm .0004$	$.0189 \pm .0004$
	I				16.3		.20			$.0190 \pm .0004$
	II				13.4		.17			$.0187 \pm .0004$
	III				5.6		.09			$.0191 \pm .0004$
22	all	3.0	3.17	2.6	6.5	.55	.13	$.054 \pm .001$	$.0173 \pm .0002$	$.0108 \pm .0001$
	I				10.0		.19			$.0106 \pm .0001$
	II				8.1		.16			$.0109 \pm .0001$
	III				3.3		.07			$.0109 \pm .0001$
23	all	2.5	3.82	1.7	4.2	.48	.11	$.051 \pm .001$	$.0120 \pm .0001$	$.0079 \pm .0001$
	I				6.6		.17			$.0076 \pm .0001$
	II				5.3		.14			$.0079 \pm .0001$
	III				2.1		.06			$.0081 \pm .0001$

Table A.1: Overview table of all measurements performed with pure wind waves. Each measurement is named by a number #, missing numbers were not evaluated in this study. u_{ref} is the free stream wind speed at a reference position, f_{peak} is the peak frequency of the energy spectrum, a_{rms} is the root mean square wave elevation, $\overline{H}$ is the averaged wave height, c is the intrinsic phase velocity of the dominant wave, ϵ is the wave steepness, z_0 is the roughness length concerning the wind profile, τ is the total drag inside the constant flux layer and τ_{visc} is the averaged viscous shear directly at the water surface.

#	class	u_{ref} [m/s]	f_{peak} [Hz]	a_{rms} [mm]	$\overline{H}$ [mm]	c [m/s]	ϵ	z_0 [mm]	τ [Pa]	τ_{visc} [Pa]
11	all	10.0	1.29	29.4	80.6	1.40	.24	$.738 \pm .006$	$.3554 \pm .0068$	$.0535 \pm .0073$
	I				110.4		.31			$.0543 \pm .0079$
	II				95.8		.28			$.0531 \pm .0073$
	III				50.3		.17			$.0529 \pm .0066$
18	all	6.0	1.30	29.7	84.7	1.35	.26	$.112 \pm .001$	$.0881 \pm .0025$	$.0392 \pm .0029$
	I				101.2		.31			$.0422 \pm .0030$
	II				93.6		.29			$.0395 \pm .0030$
	III				66.9		.20			$.0358 \pm .0026$

Table A.2: Overview table of all measurements performed with short paddle waves with paddle frequency $f_{\mathrm{paddle}} = 1.3\,\mathrm{Hz}$. Similar notation as in table A.1 is used.

#	class	u_{ref} [m/s]	f_{peak} [Hz]	a_{rms} [mm]	$\overline{H}$ [mm]	c [m/s]	ϵ	z_0 [mm]	τ [Pa]	τ_{visc} [Pa]
8	all	12.0	.89	47.2	136.9	1.79	.22	$.893 \pm .008$	$.5561 \pm .0249$	$.0644 \pm .0037$
	I				147.4		.23			–
10	all	10.0	.90	40.1	116.6	1.73	.19	$.209 \pm .003$	$.2805 \pm .0108$	$.0636 \pm .0017$
	I				124.7		.21			–
14	all	8.0	.90	33.5	99.5	1.58	.18	$.146 \pm .001$	$.1647 \pm .0069$	$.0540 \pm .0018$
	I				105.7		.19			–
17	all	6.0	.90	30.8	86.7	1.41	.17	$.070 \pm .002$	$.0828 \pm .0025$	$.0399 \pm .0011$
	I				91.2		.18			–

Table A.3: Overview table of all measurements performed with long paddle waves with paddle frequency $f_{\mathrm{paddle}} = 0.9\,\mathrm{Hz}$. Similar notation as in table A.1 is used.

A.3 Overview plots

In the following the resulting flow and stress fields measured conditions are illustrated by overview plots. The structure of the velocity plots is the same as described in section 7.4. The turbulent and wave coherent stress distributions are explained in section 7.5.1 and the phase dependent viscous stress at the surface is adressed in section 7.5.2.

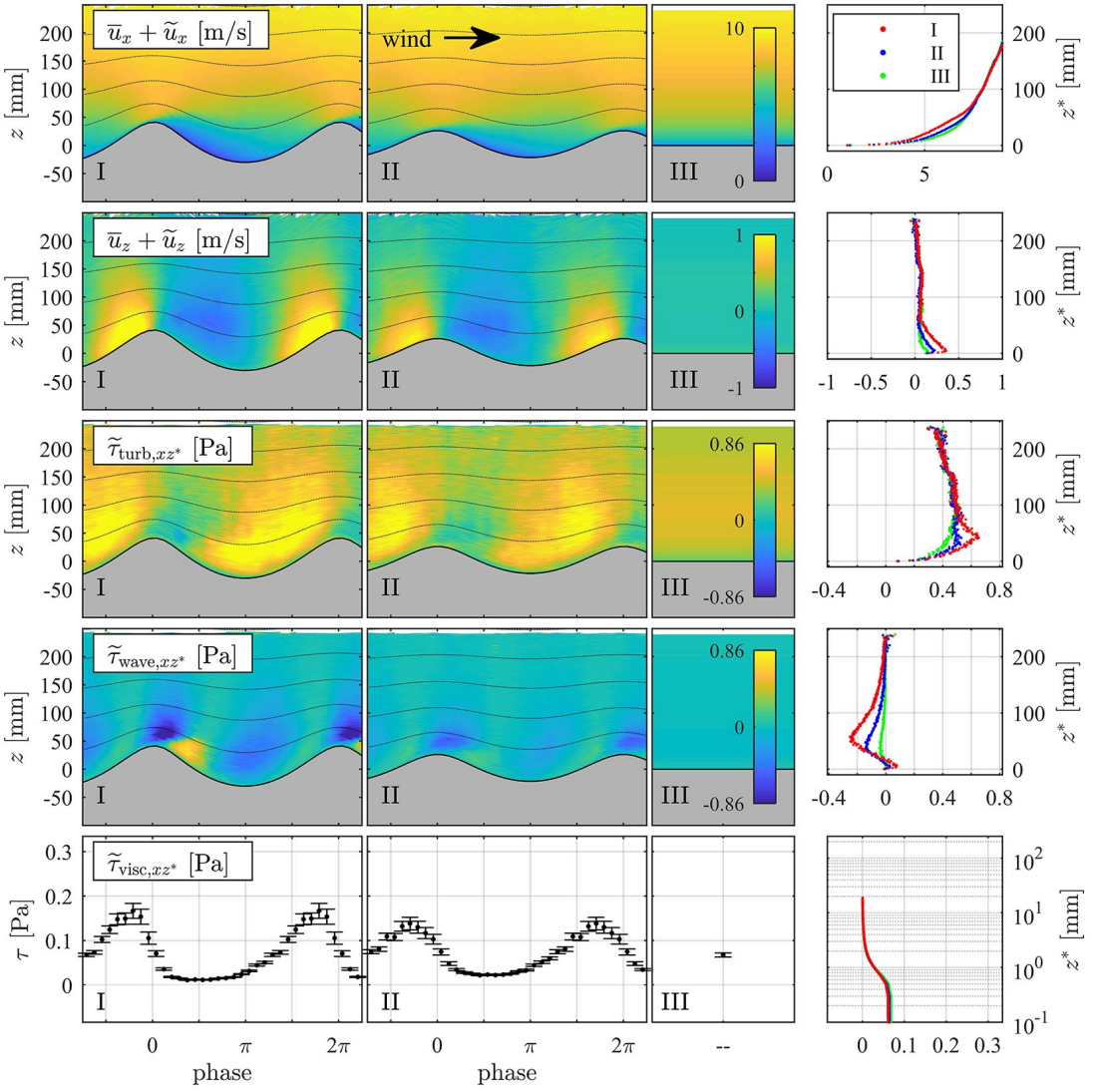

Figure A.1: Overview plot for condition 7 – 12 m/s, pure wind waves. Phase dependent velocity and stress distributions on the left and phase averaged profiles on the right. All data are separated into the three wave amplitude classes.

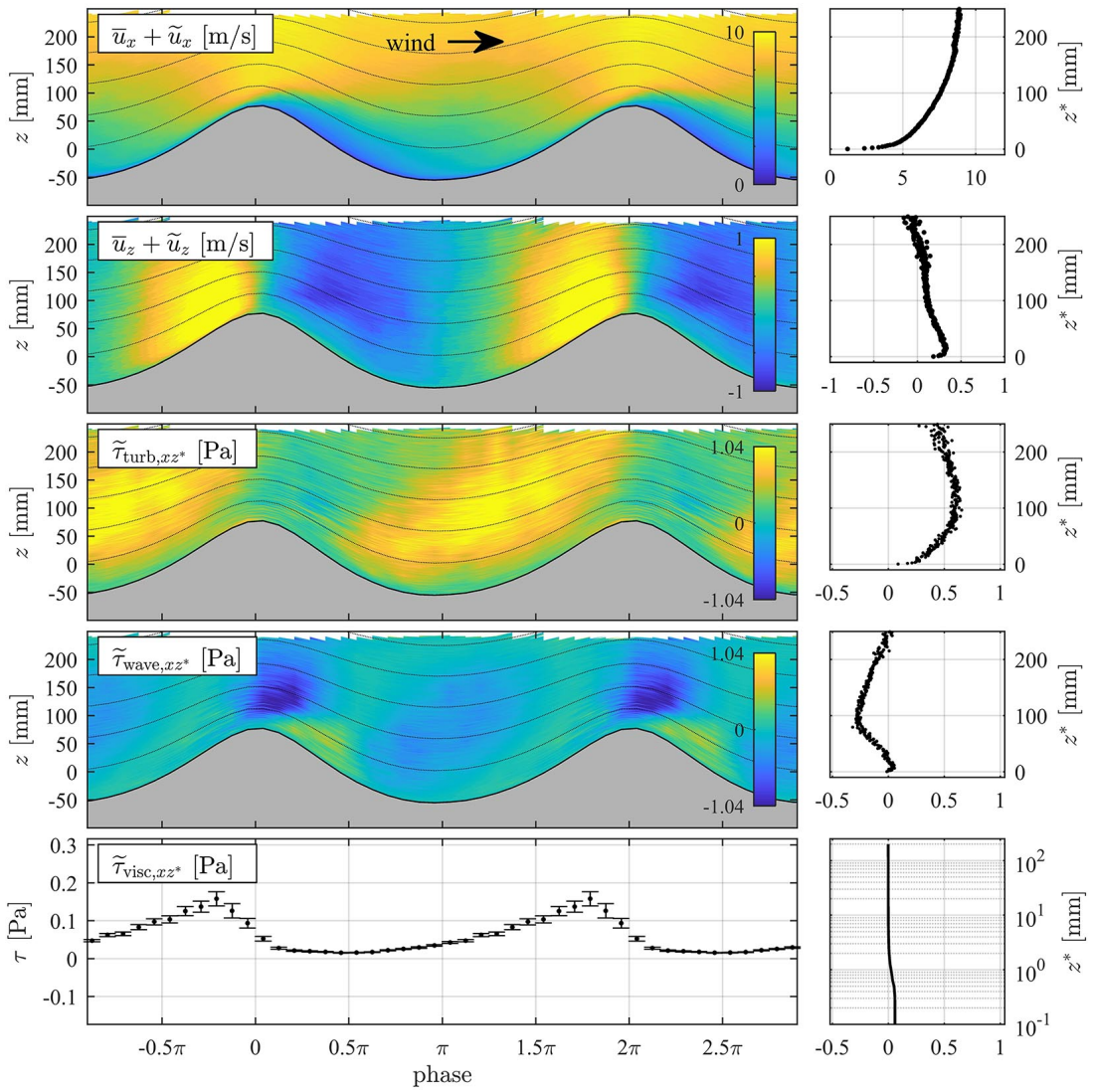

Figure A.2: Overview plot for condition 8 – 12 m/s, long paddle waves. Phase dependent velocity and stress distributions on the left and phase averaged profiles on the right.

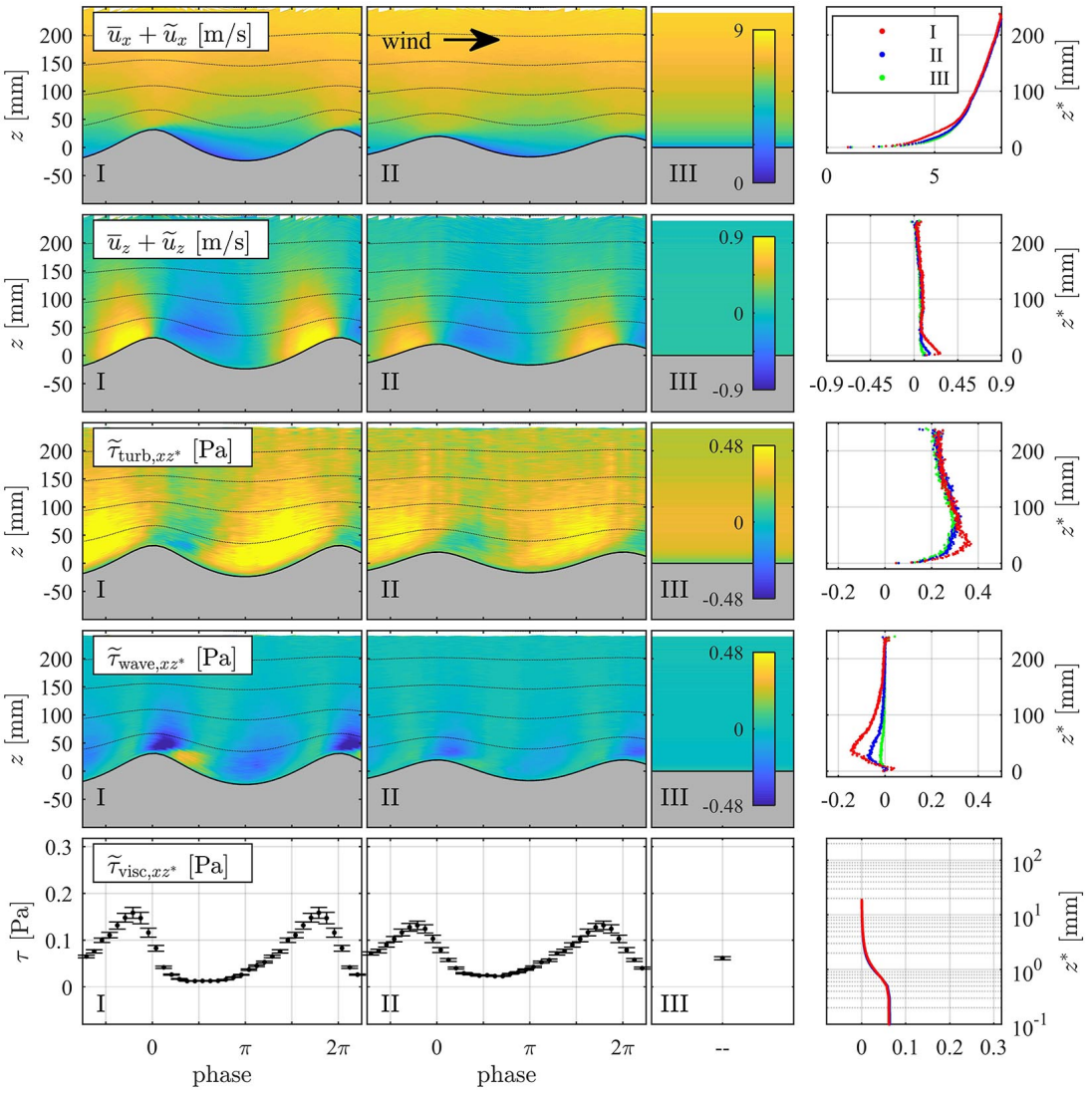

Figure A.3: Overview plot for condition 9 – 10 m/s, pure wind waves. Phase dependent velocity and stress distributions on the left and phase averaged profiles on the right. All data are separated into the three wave amplitude classes.

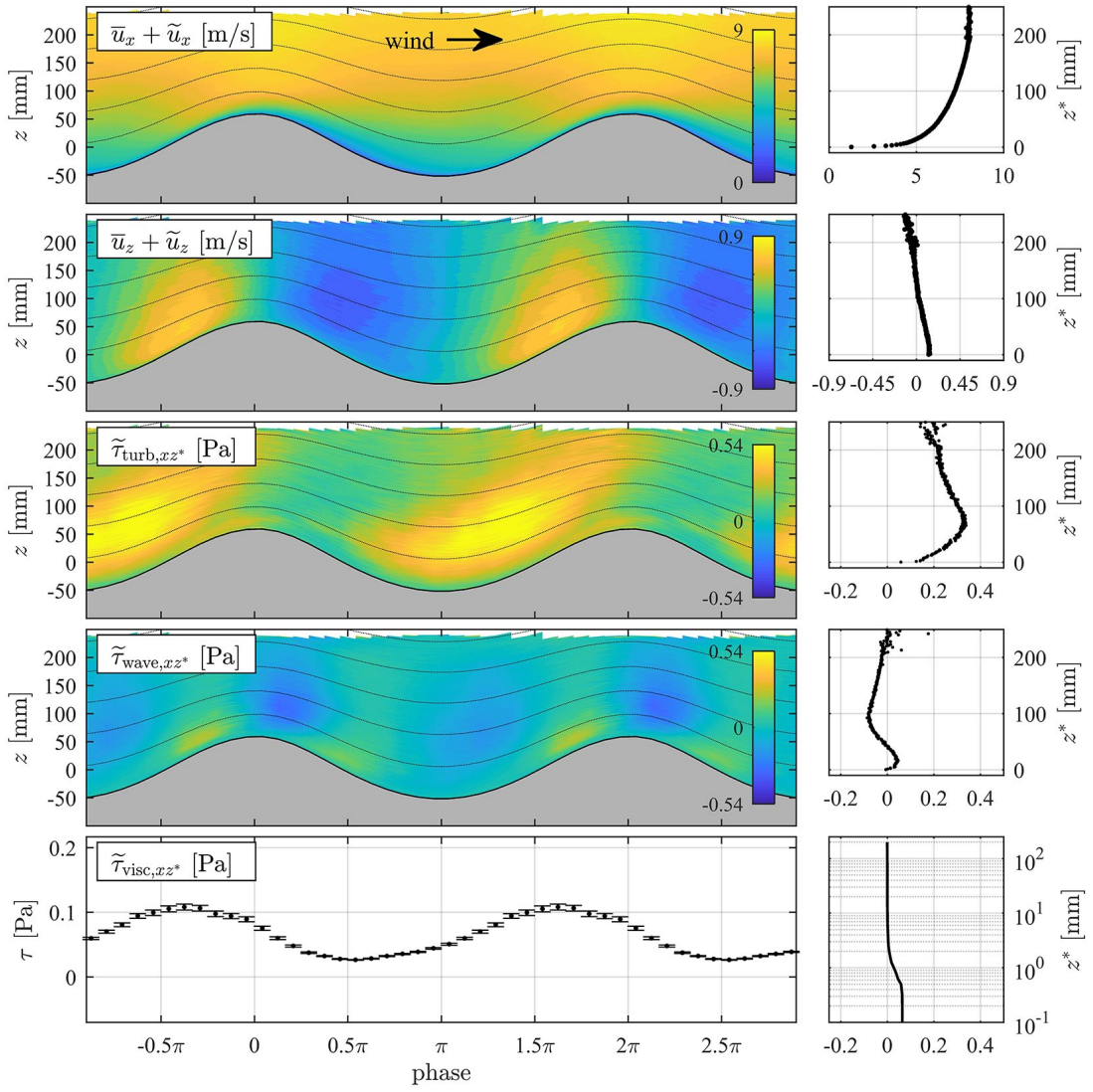

Figure A.4: Overview plot for condition 10 – 10 m/s, long paddle waves. Phase dependent velocity and stress distributions on the left and phase averaged profiles on the right.

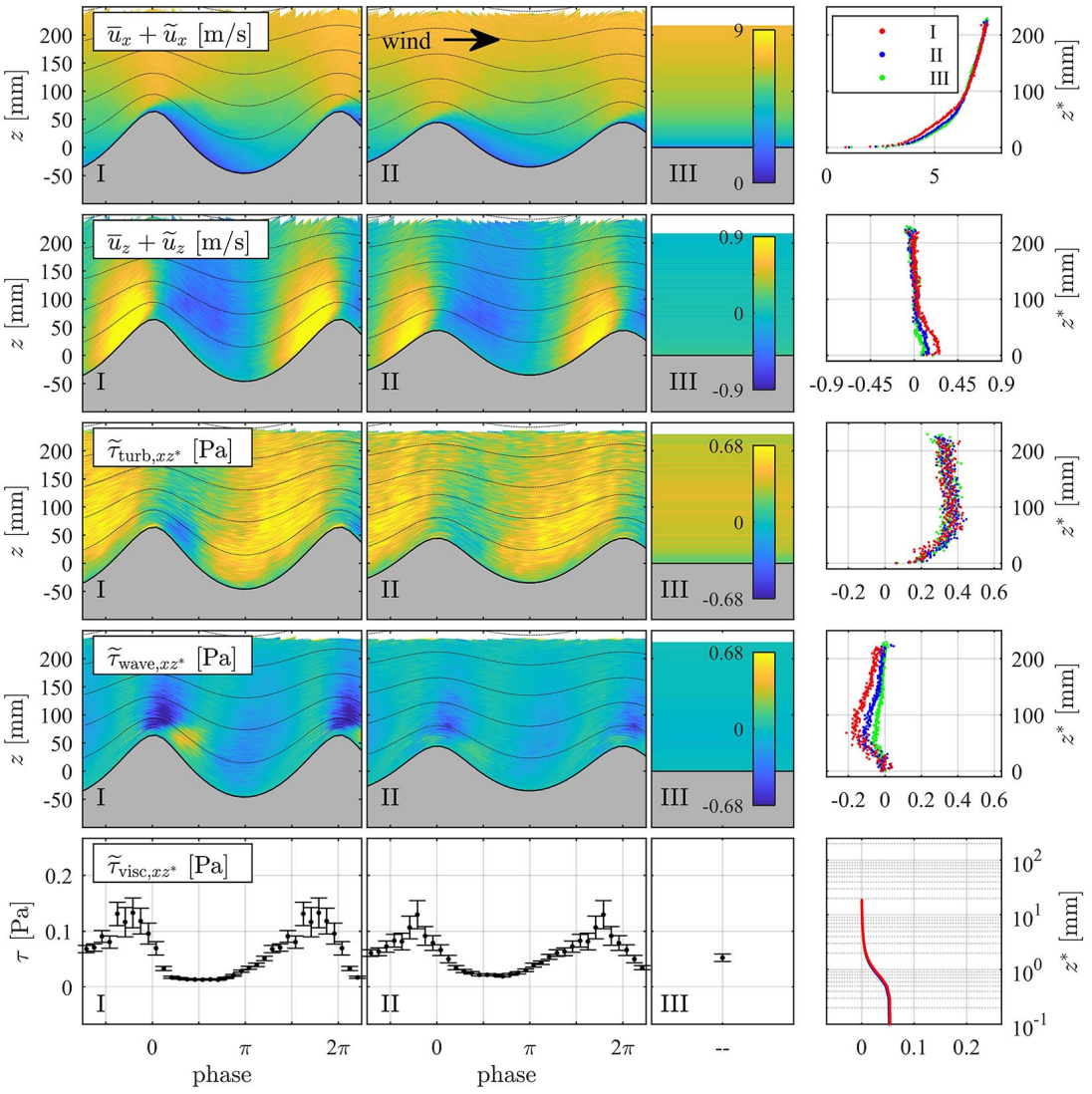

Figure A.5: Overview plot for condition 11 – 10 m/s, short paddle waves. Phase dependent velocity and stress distributions on the left and phase averaged profiles on the right. All data are separated into the three wave amplitude classes.

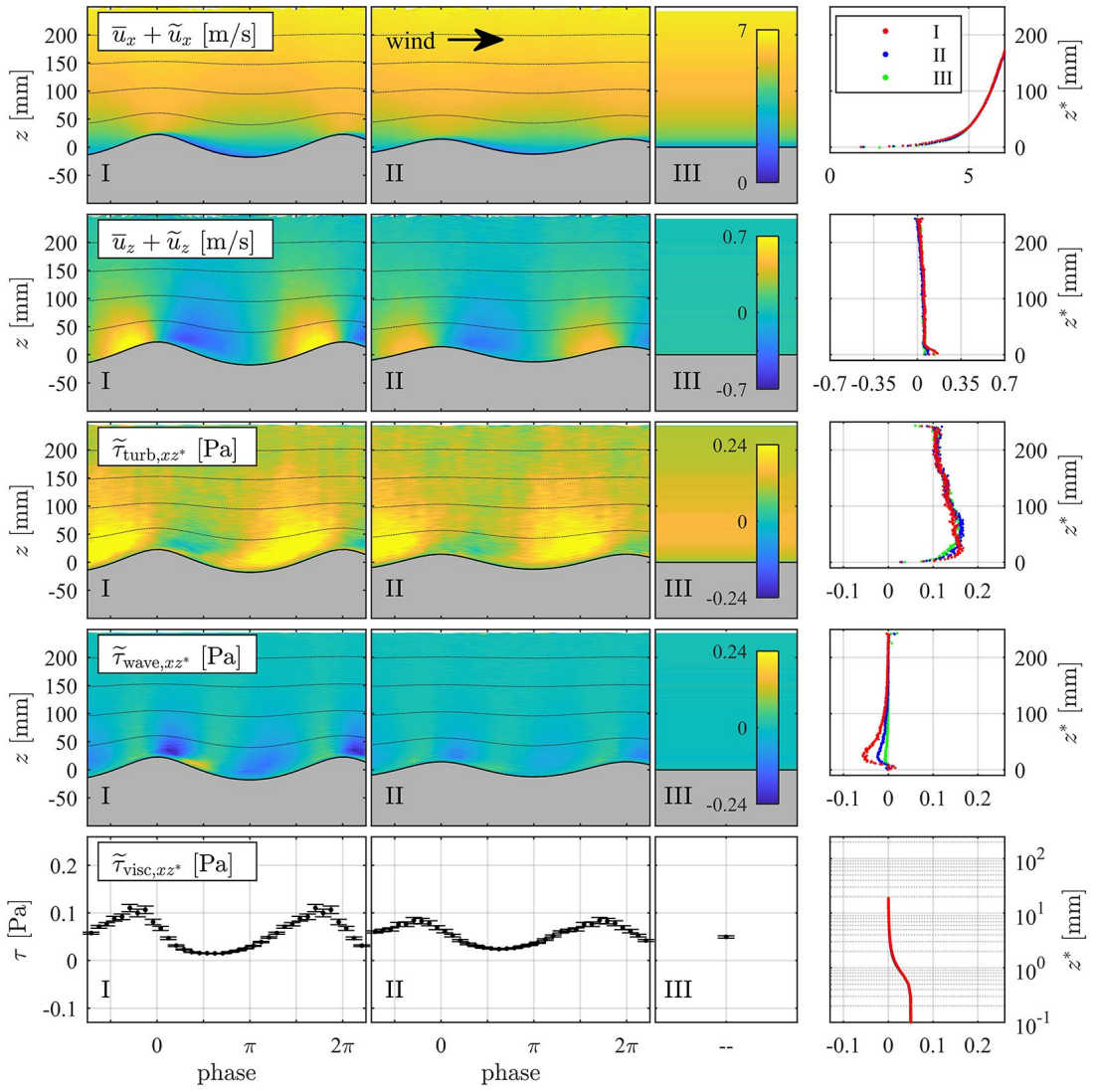

Figure A.6: Overview plot for condition 13 – 8 m/s, pure wind waves. Phase dependent velocity and stress distributions on the left and phase averaged profiles on the right. All data are separated into the three wave amplitude classes.

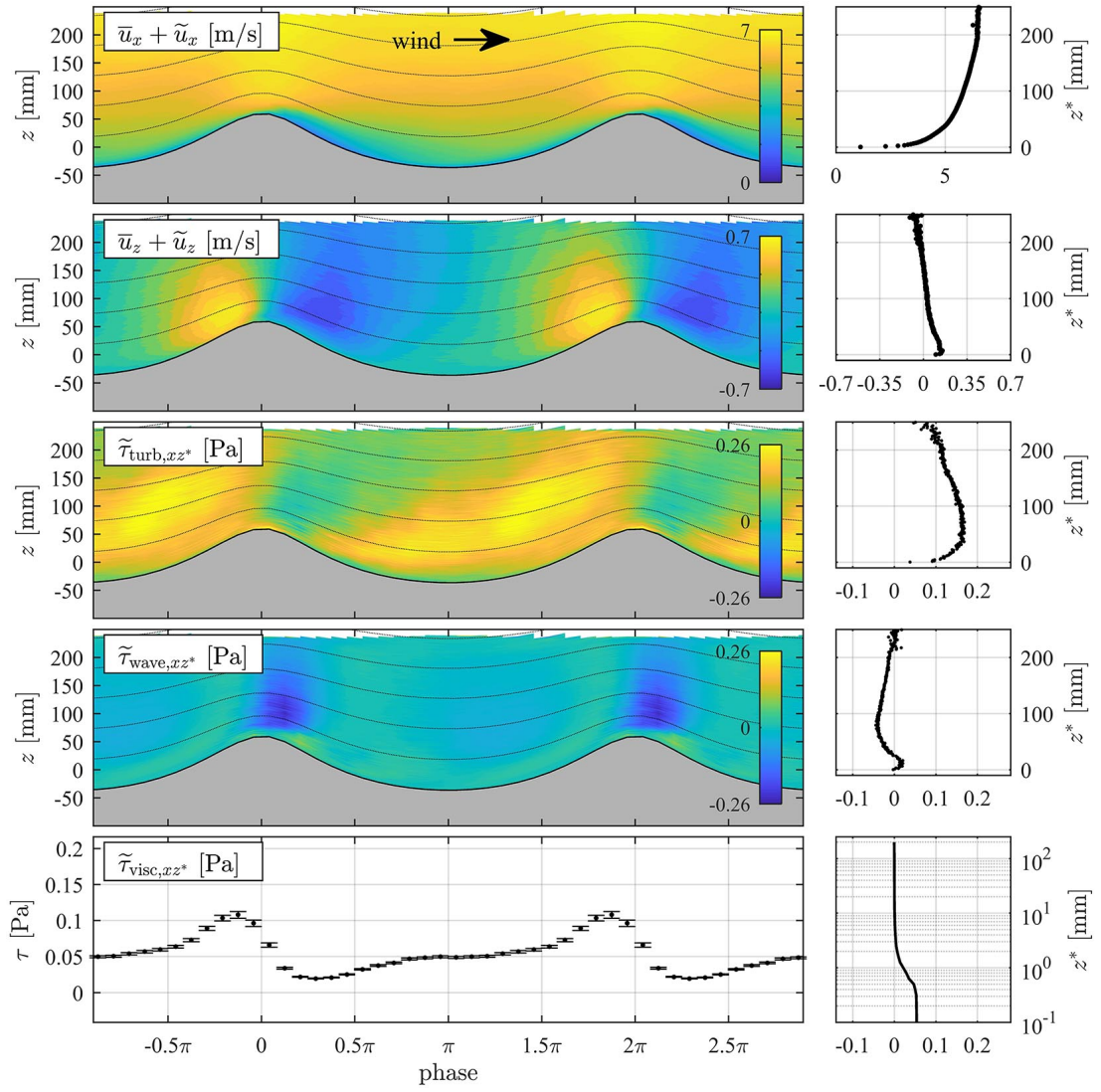

Figure A.7: Overview plot for condition 14 – 8 m/s, long paddle waves. Phase dependent velocity and stress distributions on the left and phase averaged profiles on the right.

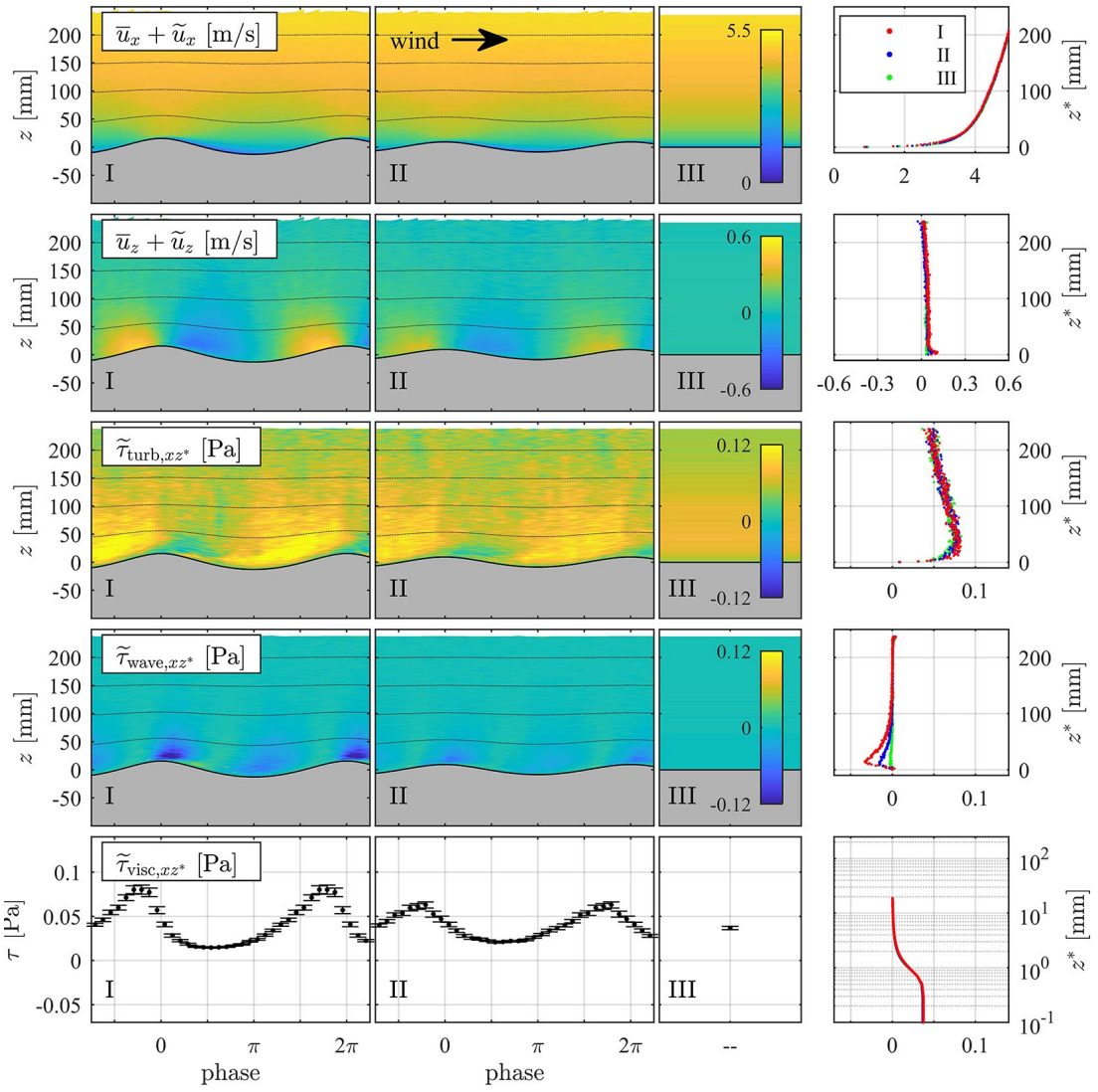

Figure A.8: Overview plot for condition 15 – 6 m/s, pure wind waves. Phase dependent velocity and stress distributions on the left and phase averaged profiles on the right. All data are separated into the three wave amplitude classes.

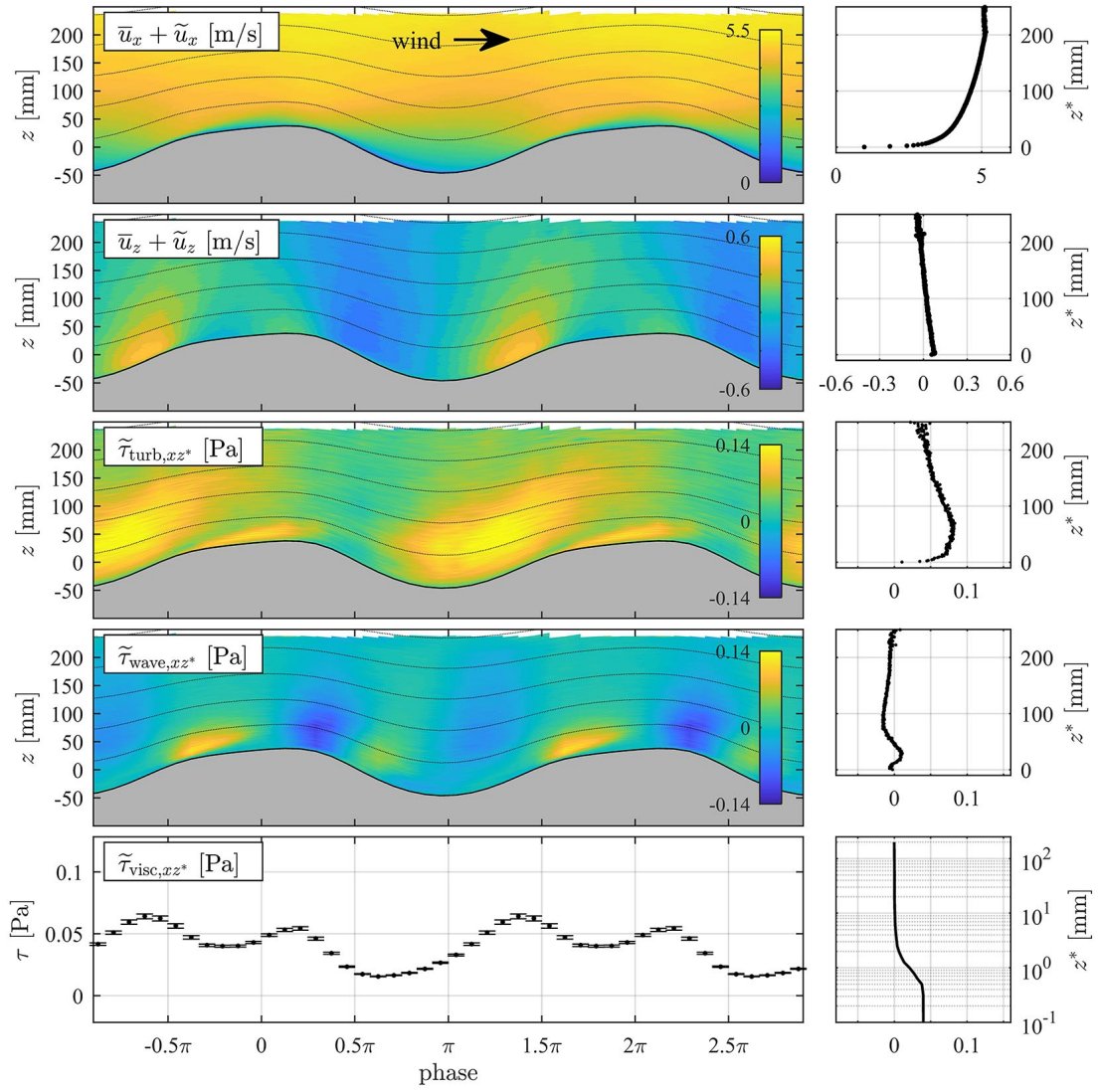

Figure A.9: Overview plot for condition 17 – 6 m/s, long paddle waves. Phase dependent velocity and stress distributions on the left and phase averaged profiles on the right.

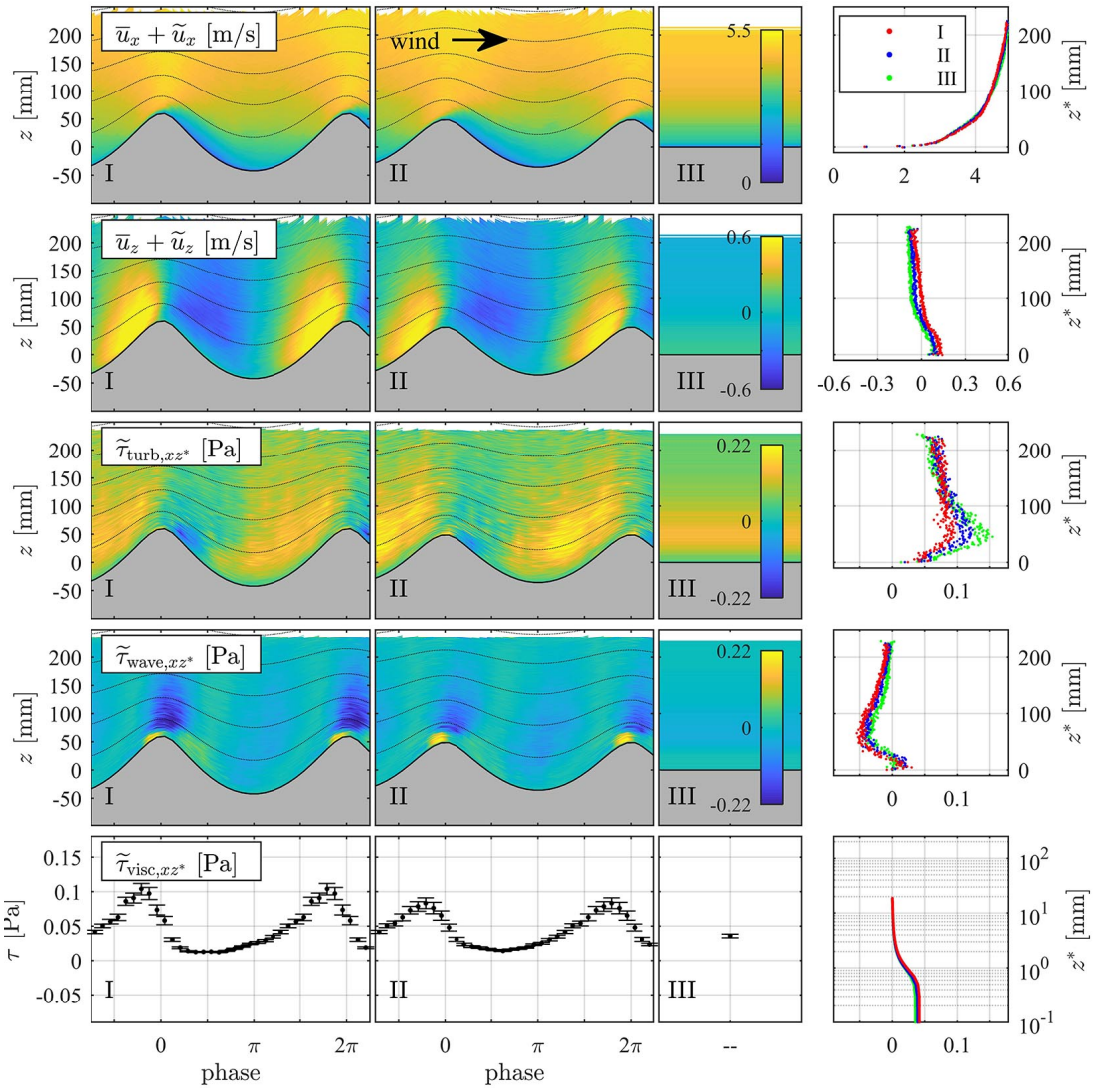

Figure A.10: Overview plot for condition 18 – 6 m/s, short paddle waves. Phase dependent velocity and stress distributions on the left and phase averaged profiles on the right. All data are separated into the three wave amplitude classes.

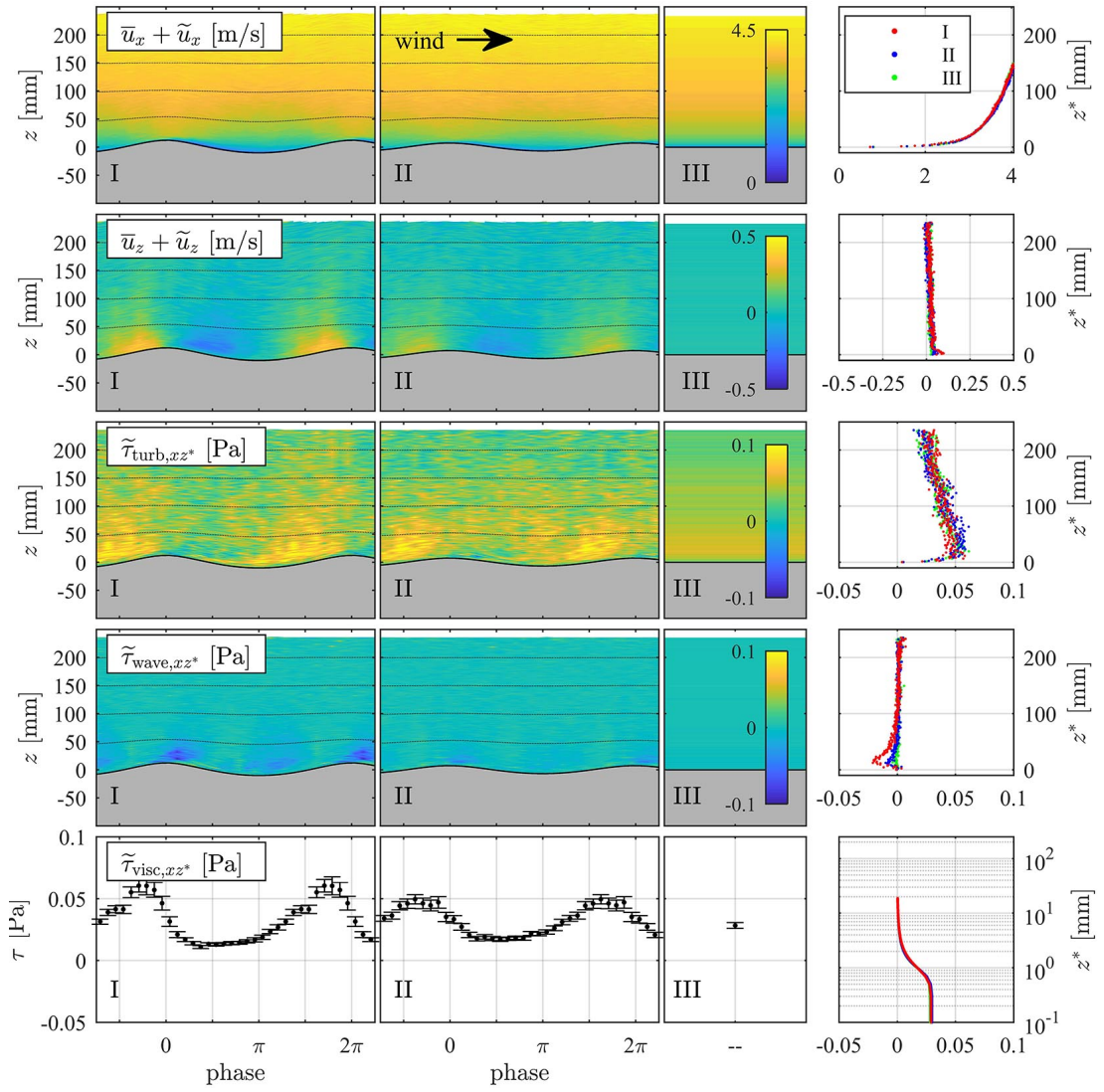

Figure A.11: Overview plot for condition 20 – 5 m/s, pure wind waves. Phase dependent velocity and stress distributions on the left and phase averaged profiles on the right. All data are separated into the three wave amplitude classes.

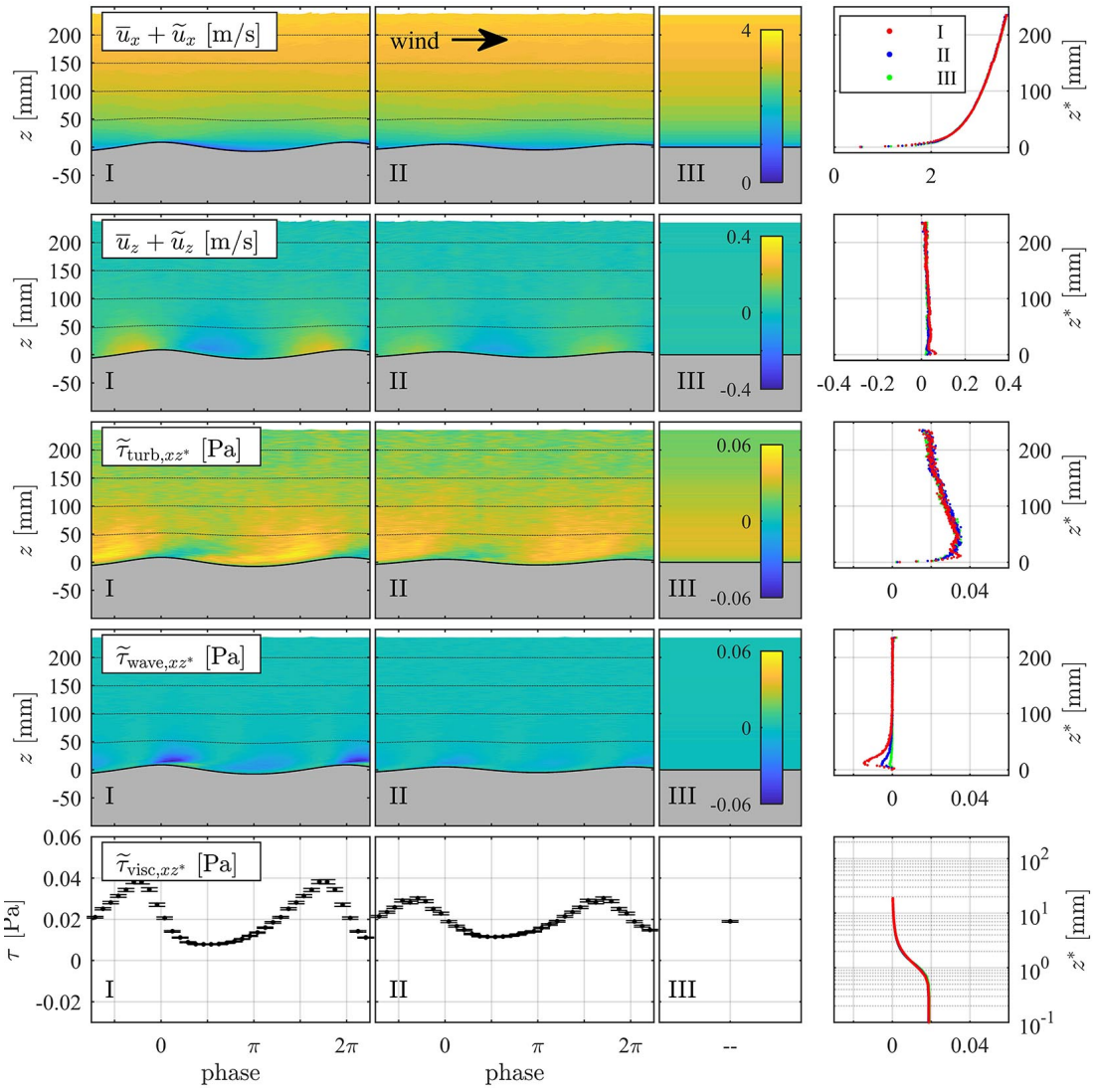

Figure A.12: Overview plot for condition 21 – 4 m/s, pure wind waves. Phase dependent velocity and stress distributions on the left and phase averaged profiles on the right. All data are separated into the three wave amplitude classes.

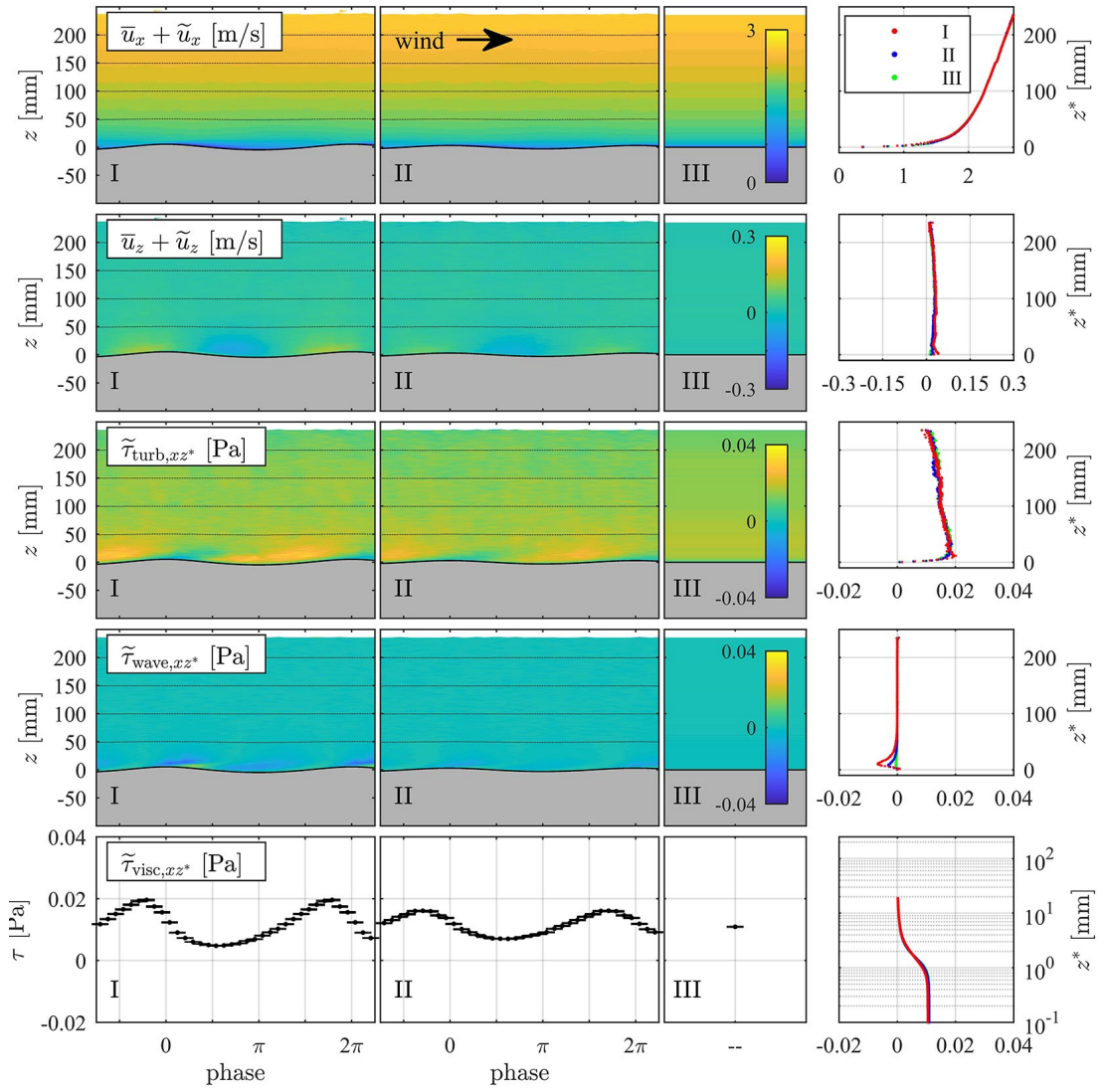

Figure A.13: Overview plot for condition 22 – 3 m/s, pure wind waves. Phase dependent velocity and stress distributions on the left and phase averaged profiles on the right. All data are separated into the three wave amplitude classes.

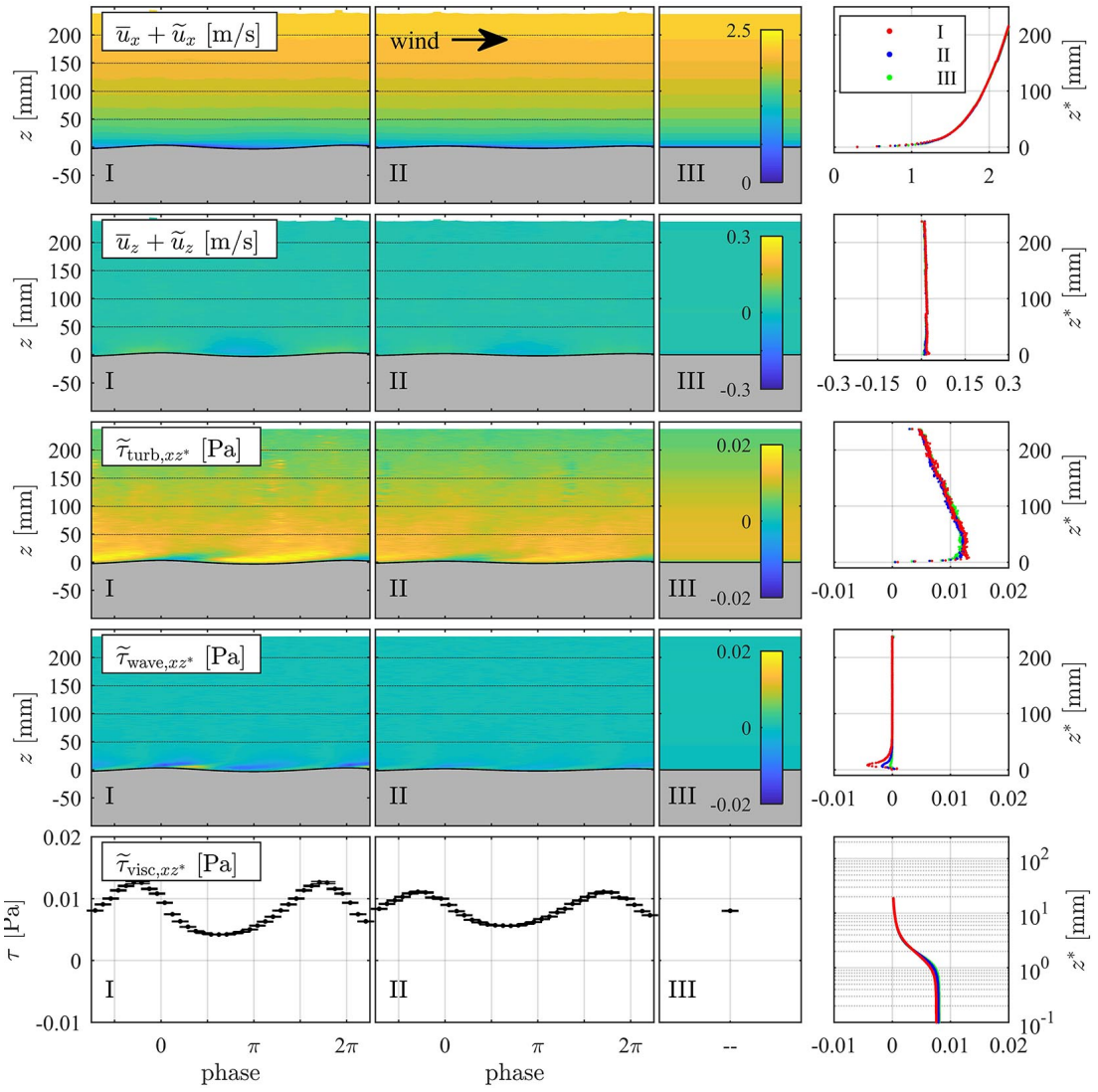

Figure A.14: Overview plot for condition 23 – 2.5 m/s, pure wind waves. Phase dependent velocity and stress distributions on the left and phase averaged profiles on the right. All data are separated into the three wave amplitude classes.

A.4 Signal- and image processing

This section briefly addresses some methods of signal- and image processing, which were used in this work. For more details it is referred to textbooks like Jähne (2012) and Oppenheim and Schafer (2010).

A.4.1 Sampling theorem

During digitalization processes continuous signals are sampled in finite steps. Thereby only structures of a certain size can be resolved. For representing a periodical structure with no aliasing effects correctly, at least two points per wavelength/period have to be sampled:

$$\text{in space:} \qquad \Delta\lambda \geq 2\,\Delta x \tag{A.4}$$

$$\text{in time:} \qquad \Delta T \geq 2\,\Delta t, \tag{A.5}$$

where Δx is the sampling width in case of spacial sampling (e.g. for images), Δt is the sampling width in case of temporal sampling (e.g. time series) and $\Delta\lambda$ and ΔT are the wavelength/period of the sampled structure.

A.4.2 Fourier transform

For analyzing signals, if periodical or not, the Fourier transform is a very powerful tool. The Fourier transform $\widehat{f}$ of a continuous function f is defined as:

$$\widehat{f}(k) = \int_{-\infty}^{\infty} f(x) e^{-2\pi i k x} \mathrm{d}x \tag{A.6}$$

and in inverse direction as:

$$f(x) = \int_{-\infty}^{\infty} \widehat{f}(k) e^{2\pi i k x} \mathrm{d}k, \tag{A.7}$$

where x is the coordinate in spacial domain and k is is the coordinate in wavenumber domain.

For discrete signals f_n the discrete Fourier transform (DFT) is:

$$\widehat{f}_k = \frac{1}{N} \sum_{n=0}^{N-1} f_n e^{-2\pi i k n/N}, \qquad 0 \leq k < N \tag{A.8}$$

and in inverse direction:

$$f_n = \sum_{n=0}^{N-1} \widehat{f}_n e^{2\pi i k n/N}, \qquad 0 \leq k < N, \tag{A.9}$$

where N is the length of the signal, n is the index in spacial domain and k in wavenumber domain. Here the notation is given for x as the spacial coordinate, the same can be written for time signals. Also extending the Fourier transform to more dimensions is commonly used especially in image processes, as images have usually two dimensions. A fast implementation of a DFT is the fast Fourier transform (FFT), which uses recursive calculation steps.

A.4.3 Hilbert transform

While the Fourier transform leads to a lost of the spacial information, by the Hilbert transform the phase $\phi(x)$ of a periodical signal $f(x)$ can be retrieved (see also Oppenheim and Schafer, 2010). The Hilbert transform is:

$$f_{\mathrm{h}}(x) = \frac{1}{\pi} \int_{-\inf}^{\inf} \frac{f(x^{'})}{x^{'} - x} \mathrm{d}x^{'}. \tag{A.10}$$

The local phase of the signal may then be calculated by:

$$\phi(x) = \arctan\left(\frac{-f_{\mathrm{h}}(x)}{f(x)}\right). \tag{A.11}$$

The local wavenumber k (here considered in 1D) then can be retrieved by the gradient of the phase:

$$k(x) = \frac{\partial \phi(x)}{\partial x}. \tag{A.12}$$

A.4.4 Structural tensor

By the structural tensor the local orientation in an image can be determined. For two dimensional images $g(x, y)$ it is defined as:

$$S_{ij} = \int_{-inf}^{\inf} w(x - x^{'}) \left(\frac{\partial g(x^{'}, y^{'})}{\partial x_i^{'}} \frac{\partial g(x^{'}, y^{'})}{\partial x_j^{'}}\right) \mathrm{d}x\mathrm{d}y, \tag{A.13}$$

where w is the tapering function defining the environment of a point, in which the orientation is determined. This can be expressed by an angle θ, which is calculated by:

$$\tan(\theta) = \frac{2S_{12}}{S_{11} - S_{22}}. \tag{A.14}$$

A.4.5 Cross correlation

The cross-correlation function R can be used to find the displacement of the two signals or images g and $g^{'}$. In two dimensions (x, y) it is (Raffel et al., 2007):

$$R_{gg'}(x, y) = \sum_{n=-K}^{n=K} \sum_{m=-L}^{m=L} g(n, m) g^{'}(n + x, m + y). \tag{A.15}$$

Here K and L define the correlation area. By finding the maximum of $R_{gg'}(x, y)$ the displacement of two images (or two signals, if regarded in two dimensions) can be determined. A much faster implementation can be realized by using the alternative calculation in the Fourier space by a complex conjugate multiplication:

$$R_{gg'} = \widehat{g} \cdot \widehat{g}^{'\,*}. \tag{A.16}$$

Danksagung

Bei allen, die mich bei dieser Arbeit unterstützt und begleitet haben, möchte ich mich herzlich bedanken.

Ein großes Dankeschön richte ich an Herrn Prof. Dr. Bernd Jähne für die Ermöglichung dieser Arbeit in diesem spannenden Bereich. Ohne die finanziellen Mittel für das technische Equipment und für das vierwöchige Experiment in Marseille, wäre diese Arbeit nicht realisierbar gewesen. Während der langjährigen Mitarbeit in seinem Team habe ich sehr viel gelernt und konnte meinen wissenschaftlichen Interessen nachgehen. Durch seine kompetente Betreuung sowie die Einbringung von Ideen hat er maßgeblich zum Erfolg dieser Arbeit beigetragen.

Auch bei Herrn Prof. Dr. Kurt Roth möchte ich mich bedanken für das Interesse an meiner Arbeit und die Bereitschaft das Zweitgutachten zu erstellen. Genauso gilt mein Dank Herrn Prof. Dr. Markus Oberthaler und Herrn Prof. Dr. Georg Wolschin für die Bereitwilligkeit Teil meines Prüfungskomitees zu sein.

For many hours of very valuable discussions I would like to thank Yuliya Troitskaya, whose professional competence was a big benefit for me. Many thanks go to Alexander Kandaurov and Daniil Seergev for all the experiments and their preparation we performed together. I learned much from their experimental experience.

I would like to express my thanks also to Guillemette Caulliez for the opportunity to perform all the measurements in the large IRPHE-Luminy wind-wave facility in Marseille. She never hesitated in discussing technical or physical aspects. Additionally, I want to thank Christopher Luneau, who supported the experiments by his technical work.

Einen großen Dank richte ich auch an alle Mitglieder der Windis-Arbeitsgruppe in Heidelberg. Ich konnte jederzeit auf große Unterstützung jeglicher Art zurückgreifen. Besonderer Dank gilt dabei Kerstin Krall, Günther Balschbach, Sonja Friman und Angelika Klein, die in den letzten Wochen viel Zeit mit Korrekturlesen meiner Arbeit verbracht haben. Ich möchte mich auch bei Katja Schwarz für die sorgfältige Auswertung der Höhenkamera im Rahmen ihrer Bachelorarbeit bedanken. Genauso möchte ich mich bei den ehemaligen Mitgliedern unsrer Arbeitsgruppe Daniel Kiefhaber, Christine Kräuter, Nils Krah, Felix Friedel, Jakob Kunz und Roland Rochholz bedanken.

Mein Dank gilt auch meinen Freunden und meiner Familie, die mich jederzeit in meinem Vorhaben unterstützt und bekräftigt haben. Ganz besonders möchte ich mich bei meiner Frau bedanken, die mich die letzten Jahre begleitet hat und mir bei allem zur Seite stand.